



HAL
open science

Development of a robust methodology for the design assessment of bonded reinforcements on steel structures

Quentin Sourisseau

► To cite this version:

Quentin Sourisseau. Development of a robust methodology for the design assessment of bonded reinforcements on steel structures: Use of cohesive zone model and distributed optical fiber for characterization. Engineering Sciences [physics]. Nantes Université, 2022. English. NNT: . tel-04282217

HAL Id: tel-04282217

<https://hal.science/tel-04282217>

Submitted on 16 Nov 2023

HAL is a multi-disciplinary open access archive for the deposit and dissemination of scientific research documents, whether they are published or not. The documents may come from teaching and research institutions in France or abroad, or from public or private research centers.

L'archive ouverte pluridisciplinaire **HAL**, est destinée au dépôt et à la diffusion de documents scientifiques de niveau recherche, publiés ou non, émanant des établissements d'enseignement et de recherche français ou étrangers, des laboratoires publics ou privés.

Public Domain

THESE DE DOCTORAT DE

NANTES UNIVERSITE

ECOLE DOCTORALE N° 602

Sciences pour l'Ingénieur

Spécialité : Mécanique des Solides, des Matériaux, des structures et des surfaces.

Par

Quentin SOURISSEAU

Development of a robust methodology for the design assessment of bonded reinforcements on steel structures

« Use of cohesive zone model and distributed optical fiber for characterization »

Thèse présentée et soutenue à Nantes, le 21/10/2022

Unité de recherche : Département Matériaux et Structures (MAST), Université Gustave Eiffel

Rapporteurs avant soutenance :

Evelyne Toussaint Professeur, Polytech Clermont Ferrand, Université Clermont-Auvergne
Emmanuel Ferrier Professeur, Université Lyon I

Composition du Jury :

Président :	Pascal Casari	Professeur, IUT St Nazaire, Nantes Université
Jury :	Evelyne Toussaint	Professeur, Polytech Clermont Ferrand, Université Clermont-Auvergne
	Emmanuel Ferrier	Professeur, Université Lyon I
	De Barros Silvio	Professeur, Ecole Technique de Rio de Janeiro
	Peter Davies	Ingénieur HDR, Ifremer
Dir. de thèse :	Sylvain Chataigner	Ingénieur-chercheur IPEF-HDR, Université Gustave Eiffel
Encadrants :	Emilie Lepretre	Ingénieur-chercheur ITPE, Université Gustave Eiffel
	Xavier Chapeleau	Chargé de recherche, Université Gustave Eiffel – I4S team Inria

Titre : Développement d'une méthodologie robuste pour l'évaluation et la conception des renforts collés sur acier

« Utilisation des modèles de zone cohésive et de mesures réparties de déformation par fibre optique pour la caractérisation »

Mots clés : collage, éléments cohésifs, méthode aux éléments finis, capteurs continus à fibre optique, méthode de la J-intégrale, corrélation d'images numériques.

Résumé :

Ce travail de thèse porte sur le développement et l'évaluation de méthodes de dimensionnement adaptées aux renforts collés sur structures métalliques en milieu offshore en se concentrant sur des assemblages métal-métal. Les méthodes proposées reposent sur l'utilisation de mesures par fibre optique continue pour l'étape de caractérisation basée sur des investigations de mécanique de la rupture, et sur les modèles de zone cohésive pour la modélisation de l'assemblage collé. Elles ont été éprouvées à travers plusieurs investigations expérimentales en mode I, mode II et mode mixte, et des études numériques via l'utilisation d'éléments finis dédiés. L'ensemble des méthodologies a ensuite été appliqué sur des assemblages collés de taille réelle afin de vérifier leur capacité prédictive. Les résultats des investigations expérimentales ont été comparés aux prédictions numériques des méthodes développées ainsi qu'à une autre approche reposant sur l'utilisation de critères couplés contrainte-énergie.

Title: Development of a robust methodology for the design assessment of bonded reinforcements on steel structures

« Use of cohesive zone model and distributed optical fiber for characterization »

Keywords: adhesive bonding, cohesive zone modeling, finite element method, distributed optical fiber sensor, J-integral method, digital image correlation.

Abstract:

This thesis work focuses on the development and the assessment of design methods adapted to reinforcements bonded on steel structure in offshore environment, and more specifically to steel-to-steel bonded joints. The proposed methodologies rely on the use of continuous optical fiber measurement during the characterization step based on fracture mechanics investigations, and the use of cohesive zone modeling for the bonded joint modeling. They were proven through several experimental investigations in mode I, mode II and mixed mode, and through numerical investigations using finite elements. The developed methodologies were then applied to real-scale samples in order to verify their predictive capacities. Experimental results were compared to numerical predictions and to an alternative approach from the literature relying on the use of coupled stress-energy criteria.

Remerciements

Il existe plusieurs citations qui mériteraient de trouver une place dans le préambule de ce paragraphe pour résumer l'aboutissement de ce travail de thèse. Cependant la conclusion de monsieur De la Fontaine retraçant l'histoire d'un charretier mal en point semble très à propos : « aide-toi et le ciel t'aidera ». Cette phrase est en effet la directe expression du difficile contexte dans lequel ces trois ans de travaux ont été effectués. À savoir, que s'il fallait attendre les actes d'un grand barbu pour avancer, on n'aurait pas été bien loin...

Le document qui suit revêt la signature d'une seule personne, mais c'est le résultat de travaux effectués par plusieurs qu'il est nécessaire de faire apparaître dans ces quelques lignes pour rendre honneur aux qualités humaines, techniques et scientifiques qu'ils ont déployés pour permettre l'aboutissement de ces recherches, et la rédaction de ce manuscrit.

Pour ne pas déroger à l' ancestrale coutume dictant l'ordre d'apparition de ces personnes, j'adresse un sincère remerciement à Sylvain Chataigner, Emilie Leprêtre, Xavier Chapeleau, ainsi qu'à Stéphane Paboef et Luc Mouton. Le fait que ces lignes existent, prouvent que vous avez su canaliser le turbulent et pas toujours très rigoureux doctorant des premiers mois, et que vous m'avez donné l'opportunité de travailler et apprendre à mon rythme. Merci de la confiance que vous m'avez accordée pour mener ce doctorat au bout et de la qualité du cadre de travail que vous m'avez fourni malgré les innombrables difficultés contextuelles.

Je remercie également les membres du jury, le président Pascal Casari, les rapporteurs Evelyne Toussaint et Emmanuel Ferrier et enfin les examinateurs Silvio de Barros et Peter Davies, ainsi que le membre de mon CSI Romain Créac'hcadec. Je leur suis reconnaissant du temps qu'ils ont bien voulu consacrer à l'analyse de mes travaux.

Ce travail a été réalisé conjointement entre le laboratoire Structures Métalliques et à Câbles (SMC) de l'Université Gustave Eiffel et l'équipe Matériaux Composites du département de recherche de Bureau Veritas, j'adresse mes remerciements à ces deux équipes pour leurs accueils et moments passés ensemble. Plus précisément, je remercie, Jean-François David, Richard Michel, Pauline Bochereau, Yannick Falaise et Ludwig Battais pour leurs disponibilités permanentes et aide à la réalisation de la partie expérimentale de ce doctorat. Je remercie Benjamin Collier et Jean-Christophe Petiteau sur la transmission de leur savoir technique et théorique lié aux problématiques du collage. Je remercie aussi Jean-Philippe Terrier et Vincent Gaudrefroy du laboratoire MIT pour leur aide lors de la réalisation de l'étude sur les propriétés des préparations de surface de la campagne expérimentale de la thèse. Et finalement, pour clore la partie professionnelle de ce paragraphe, un remerciement particulièrement appuyé à Maxime Deydier pour la qualité et l'efficacité de son travail produit au cours de ce doctorat, sans qui et sans quoi, les résultats et analyses présentés dans ce document n'auraient pas pu être aussi approfondis.

Je remercie aussi ma famille, les frangins/frangines, Fabien et Manon, tonton Michel, Mamie et plus particulièrement mes parents, Raphaëlle et Jean-François, qui m'ont toujours soutenu et sans qui, évidemment, je ne serais pas celui que je suis aujourd'hui. Merci maman pour ta permanente gentillesse et abnégation dont seule une mère est capable et qui a permis mon développement personnel. Merci papa, scientifique jusqu'au bout des ongles pour tes conseils toujours avisés et soutien permanent quand il y en a eu besoin.

Finalement, un pensé aux copains qui si un jour, lisent ces lignes, se reconnaitrons. Et plus particulièrement Gabrielle pour m'avoir accompagné pendant cette dernière année de thèse et qui a contribué, à sa façon, à la réussite de ce doctorat.

Résumé en français

Cette thèse s'inscrit dans le cadre du projet Strength Bond Offshore dédié au développement d'une réparation de tôles d'acier corrodées à l'aide d'un patch composite pour augmenter la durée de vie de structures offshore. Le développement d'une réparation composite pour ce type de structures semble particulièrement approprié pour diverses raisons. Premièrement, ces matériaux présentent des performances élevées, peuvent être facilement adaptés à diverses géométries tridimensionnelles, et sont faciles à transporter et à installer. Ils sont en outre non corrodables et donc particulièrement bien adaptés au milieu offshore. Enfin, cette technique ne nécessite aucun travail dit "à chaud" tel que la technique de réparation commune : le découpage (généralement au plasma) des tôles corrodées et le soudage de nouvelles tôles. Ceci est particulièrement important dans le cas de la réparation ou du renforcement des FPSO (Floating Production, Storage and Offloading).

Cependant, l'absence d'approches de dimensionnement communément adoptées et validées pour ce type de renforcement conduit à un surdimensionnement des joints collés dans les applications industrielles diminuant l'intérêt de la méthode, voire limitant le recours à cette technique dans le cas de géométries complexes. Une meilleure compréhension des techniques de dimensionnement est donc nécessaire ainsi qu'une évaluation de leur robustesse. Une méthodologie de caractérisation et de conception des joints collés est donc proposée dans cette étude. Elle a été validée sur le cas d'assemblages collés métal-métal représentatifs d'applications industriels. Elle pourrait servir par la suite de base pour développer une méthodologie adaptée au cas des renforts composites collés.

La première partie du document s'attache à la réalisation d'un état de l'art sur les joints collés structuraux. Des éléments généraux sur le sujet du collage structural sont tout d'abord rappelés. On retiendra en particulier la notion d'adhésion dépendante des opérations de préparation de surface et impactant les modes de rupture obtenus.

Une revue des différents modèles mécaniques existants pour représenter le comportement d'assemblage collé est ensuite réalisée. Les principaux modèles analytiques sont ainsi rappelés : les modèles de Volkersen et de Goland et Reissner dans le cas d'un adhésif ayant un comportement élastique, et de Hart-Smith dans le cas d'un adhésif élasto-plastique. Ces modèles permettent d'obtenir de façon directe l'état de contraintes au bord d'un joint collé dans le cadre de géométries simples. Cependant, avec des assemblages collés de géométries plus complexes ou constitués de matériaux ayant un comportement mécanique fortement non linéaire, il est souvent nécessaire de recourir à l'utilisation de méthodes numériques. Plusieurs approches sont également présentées dont celle des éléments finis qui sera utilisée dans la suite de l'étude. On retiendra que dans ce cas, l'étude des assemblages collés présente une difficulté liée à la présence de singularités physiques responsables de problèmes de convergence des modèles.

Ensuite, une revue des critères de rupture utilisés pour le dimensionnement des assemblages collés est réalisée. Trois familles principales de critères sont identifiées : les critères en contrainte ou déformation relevant de la mécanique des milieux continus, les critères en énergie relevant de la mécanique de la rupture, et les approches couplées. Ces dernières présentent l'avantage de pouvoir s'intéresser à la fois à des structures continues et fissurées. Pour cette raison, elles semblent être un bon compromis pour le dimensionnement des joints collés. Elles seront ainsi utilisées dans le cadre de notre étude. Deux méthodes principales sont exposées : la méthode couplée contrainte-énergie et la méthode des modèles de zone cohésive qui implique

l'identification des lois d'interface. C'est cette dernière méthode qui sera plus particulièrement utilisée dans notre travail. Elle repose sur des investigations expérimentales visant à déterminer la ténacité ou énergie de déformation à rupture, et sur l'utilisation d'outils de modélisation aux éléments finis cohésifs.

Le second chapitre de la thèse porte sur l'amélioration des investigations expérimentales visant à caractériser la ténacité des assemblages collés via des mesures réparties de déformation par fibre optique. Celles-ci doivent permettre de suivre la propagation d'une fissure dans un assemblage collés en étant complètement indépendante de l'opérateur. Cette mesure est effectuée de manière continue pendant l'essai, et permet de connaître la longueur de fissure au milieu du joint collé. Plusieurs stratégies d'instrumentation sont présentées et évaluées via des investigations expérimentales, des modèles analytiques et des modèles numériques. Cette étude est réalisée pour les deux modes principalement rencontrés dans les applications offshore (mode I et mode II) et pour le mode mixte. L'essai DCB (Double Cantilever Beam) a été utilisé pour le mode I. L'essai ENF (End Notched Flexure Test) a été utilisé pour le mode II. L'essai MMB (Mixed Mode Bending) avec deux ratios de mode différents a été utilisé pour le mode mixte. Pour ces trois essais, les géométries d'éprouvettes et de bâtis d'essai sont inspirées des normes existantes pour ces différents tests et adaptées au cas étudié. Le suivi du front de fissure par fibre optique a été validée avec des éprouvettes métal-métal collés avec une résine époxy (désignée par la référence A pour une raison de confidentialité vis-à-vis du projet Strengthbond).

L'utilisation d'une fibre optique continue collée en surface des éprouvettes et le développement d'un post-traitement adapté des mesures de déformation a permis de réaliser pour ces trois essais un suivi de la propagation de fissure. Les résultats ont été comparés à des modèle numériques et des mesures visuelles après rupture et une bonne corrélation a été constatée. L'intérêt de la méthode au regard de la forme du front de fissure a également été montrée. Une limitation existe cependant dans le cas d'une propagation de fissure trop rapide (ou incontrôlée) avec les moyens de mesure à notre disposition. L'utilisation d'une fibre optique continue insérée au sein de la couche de colle a également été étudiée. Les résultats ont été moins satisfaisants et il semble que davantage d'investigations soient nécessaires pour mieux relier les profils de déformation aux phénomènes physiques se produisant dans la colle lors de la propagation d'une fissure. Cette étude a également mis en avant que les capteurs à fibre optiques continus peuvent être utilisés pour d'autres type de chargements, ou de géométrie d'éprouvettes.

Le troisième chapitre de la thèse porte sur la détermination des ténacités d'un assemblage collé métal-métal lors d'essais de mécanique de la rupture (essais DCB, ENF et MMB) par des méthodes normalisées ou en utilisant la méthode précédemment développée pour le suivi de propagation de fissure à l'aide de fibre optique continue. Cette étude a été réalisée avec des éprouvettes métal-métal collés avec une résine époxy B qui a été utilisée pour toute la suite des travaux de thèse. En utilisant la fibre optique pour le suivi de fissure au cours des essais, les méthodes de détermination de la ténacité ont été adaptées à partir des normes et comparées à une autre méthode non normalisée : la méthode de l'intégrale J. Cette dernière permet d'obtenir l'état énergétique aux abords d'une pointe de fissure via des mesures de déplacements locaux (mesures réalisées à l'aide de la corrélation d'images numériques).

Les méthodes CCM (Compliance Calibration Method) et MBTM (Modifier Beam Theory Method) proposée par les normes se sont avérées efficaces pour obtenir la ténacité « à l'amorçage » de la fissure pour les essais DCB, ENF et MMB. Cependant, ces valeurs de ténacité dite d'« amorçage » sont connues comme étant faibles (ou conservatrices) par rapport à la ténacité dite de « propagation » qu'il est possible de mesurer avec l'instrumentation par fibre optique. Toutefois, du fait du choix de la résine pour cette étude, seuls les essais DCB ont

permis d'avoir une propagation de fissure contrôlée et donc de pouvoir appliquer les méthodes développées de mesure de ténacités à l'aide du suivi de fissure par fibre optique.

L'approche de l'intégrale J constitue également un moyen efficace d'obtenir la ténacité de propagation. Les résultats obtenus par cette méthode sont proches des résultats précédents obtenus par les méthodes CCM et MBTM modifiées dans le cas d'une instrumentation par fibre optique. La dérivation de la courbe de l'intégrale J a permis, en outre, d'évaluer directement les lois d'interface (modèles de zones cohésives) pour les modes I et II.

Le quatrième chapitre étudie deux approches de détermination des modèles de zone cohésive (pouvant être implémentées par éléments finis) ainsi que la démarche de modélisation associée. La première méthode est une calibration directe du modèle, basée sur l'analyse de l'intégrale J décrite précédemment. La deuxième méthode est une méthode indirecte basée sur la ténacité et s'appuyant sur l'utilisation itérative de modélisations aux éléments finis. La première partie de ce chapitre présente plus en détails la stratégie de modélisation par éléments finis et plus particulièrement la modélisation dans le cas de modes mixtes. Elle permet en particulier de mettre en exergue pour l'outil utilisé, les interdépendances des lois cohésives en mode I et en mode II et le rôle du coefficient de couplage α . La deuxième partie décrit plus précisément les méthodes directes (lois cohésives obtenues avec l'intégrale J) et indirectes (par minimisation) utilisées dans ce travail pour déterminer les lois cohésives en mode I, II et en mode mixte. Ces deux méthodes sont ensuite appliquées aux résultats des trois séries d'essais, DCB, ENF et MMB, présentées dans le chapitre 3. Pour la forme de loi cohésive, la loi bilinéaire a été retenue dans cette étude car elle correspond assez bien à celle obtenue par la méthode directe. De plus, d'un point de vue numérique, elle présente l'avantage de ne nécessiter que deux paramètres à déterminer (la contrainte critique et la ténacité critique) dans le cas de la méthode indirecte, ce qui permet de limiter le nombre d'itérations par rapport à d'autres lois cohésives de formes plus complexes.

Néanmoins, les paramètres de la loi bilinéaire obtenus par la méthode indirecte sont assez différents de ceux obtenus par la méthode directe. Bien que les rigidités initiales soient similaires, les valeurs de la ténacité critique et la contrainte critique pour la méthode indirecte sont supérieures à celles obtenues par la méthode directe. Cela génère donc une différence dans la forme de la loi cohésive. D'un point de vue physique, la loi cohésive de la méthode directe semble plus réaliste car elle représente davantage le comportement fragile identifié pour l'adhésif étudié lors des essais. La forme de la méthode indirecte semble en contradiction avec cette observation puisqu'elle présente une partie dédiée à l'endommagement plus importante et donc moins représentative d'un adhésif fragile. Le coefficient de couplage reste cependant proche entre les deux méthodes.

Les modèles cohésifs déterminés par les méthodes directes et indirectes ont ensuite été implémentés dans les modèles aux éléments finis pour simuler les essais de mécanique de la rupture réalisés (présentés au chapitre 3). Les comparaisons entre modèles numériques et mesures expérimentales ont montré peu de différences entre les deux approches. Il semble donc que, dans le cas d'essais quasi-statique, la forme de la loi cohésive a peu ou pas d'impact sur le comportement et sur la prédiction de la charge à rupture des assemblages collés avec la résine B. Ceci est en accord avec plusieurs résultats de la littérature. Dans le cas d'une étude de la durabilité des assemblages collés, des études additionnelles seraient néanmoins nécessaires concernant le choix de la forme de ces modèles cohésifs.

Par ailleurs, il est important de souligner que la méthode indirecte nécessite un temps de calcul assez important par rapport à la méthode directe (via l'intégrale J). La méthode directe a permis de prédire plus précisément (erreur <10%) la charge à rupture des essais DCB, ENF et MMB. Elle implique néanmoins l'utilisation de davantage d'instrumentation, comme par exemple, dans notre cas, un système de corrélation d'images.

Suite à ces investigations portant sur les essais de mécanique de la rupture (pré-fissurés), le dernier chapitre s'est concentré à évaluer la capacité des méthodes développées pour prédire le comportement et la capacité d'assemblages collés plus réalistes (représentatif de solutions industrielles). Des essais sur assemblages à plus grande échelle ont donc été réalisés avec des conditions de chargement proches de la réalité (situations de chargement les plus couramment rencontrées pour les ponts de navires). Afin d'évaluer la pertinence de la méthodologie proposée et d'étudier sa robustesse, il a été décidé de comparer les résultats obtenus avec les méthodes directe et indirecte à ceux obtenus avec une méthodologie alternative s'appuyant à la fois sur la mécanique continue et la mécanique de la rupture : la méthode couplée contrainte-énergie.

Les essais ont été instrumentés par des jauges de déformation et une fibre optique continue afin de bien identifier l'amorçage du décollement et de suivre la propagation de la fissure. La fibre optique continue a effectivement pu suivre la propagation de la fissure. Ce résultat valide que ce moyen d'instrumentation peut aussi être appliqué en conditions réelles dans le cadre de monitoring ou de suivi qualité. Les résultats des essais se sont en outre avérés relativement répétables. Une capacité moyenne de l'assemblage collé pour les deux situations étudiées (traction et flexion) a ainsi pu être déterminée.

L'application de la méthode couplée contrainte-énergie a ensuite été réalisée. Son application, en particulier le critère en contrainte, s'est heurtée à plusieurs difficultés : le choix de la contrainte, la détermination du critère associé et le choix de la localisation. De fortes hypothèses ont été réalisées sur ce sujet, tendant à limiter l'applicabilité de la méthode pour des géométries plus complexes. Les deux méthodes indirectes et directes ont ensuite été appliquées à l'aide des résultats du chapitre 4.


Les résultats obtenus ont permis de valider la capacité des modèles cohésifs (avec la méthode directe et indirecte) et de la méthode couplée à prédire la charge à rupture de l'assemblage et son comportement local et général. La seule méthodologie dont les résultats sont conservateurs est la méthode directe. Le Tableau 0.1-1 compare les trois méthodes étudiées dans cette étude.

	<i>Tests requis</i>	<i>Temps de calcul (essais standard)</i>	<i>Temps de calcul (essais réels)</i>	<i>Données des modèles</i>	<i>Prédiction de la rupture</i>
<i>Méthode directe</i>	<i>DCB/ENF/MMB Avec instrumentation spéciale (DIC)</i>	<i>2 jours</i>	<i>4 jours</i>	<i>Comportement complet du patch et effort à rupture</i>	<i>Conservative</i>
<i>Méthode indirecte</i>	<i>DCB/ENF/MMB Avec instrumentation standard</i>	<i>5-8 jours</i>	<i>4 jours</i>	<i>Comportement complet du patch et effort à rupture</i>	<i>Non conservative</i>
<i>Critère couplé</i>	<i>TAST/DCB/ENF/MMB</i>	<i>∅</i>	<i>5-6 jours</i>	<i>Effort à rupture</i>	<i>Non conservative</i>

Tableau 0.1-1: Comparaison des méthodes de dimensionnement étudiées

Ce travail a permis d'établir et d'évaluer différentes méthodologies de dimensionnement des renforts collés sur acier pour des chargements typiquement rencontrés en conditions réelles. Ces méthodes se sont avérées prédictives pour le dimensionnement lors d'un chargement monotone, montrant que dans notre cas (avec la résine B), la forme des lois cohésives choisies avait peu d'impact sur cette prédictivité.

Les capacités prédictives des méthodes étudiées dans cette thèse doivent encore être évaluées vis-à-vis de la fatigue. De plus, dans le cadre du développement de renforts composites collés,



il sera nécessaire d'étendre une des méthodologies développées au cas d'interfaces multi-matériaux. Des plis de fibre de verre sont en effet très souvent intégrés entre le renfort composite à fibre de carbone et la structure métallique renforcée pour des raisons de corrosion galvanique. Celui-ci peut avoir un impact non négligeable sur les propriétés d'interface.

Details on StrengthBond Offshore JIP project



Leading by Stéphane Paboeuf of Bureau Veritas (head of composite materials section research department).

Bureau Veritas has initiated the Strength Bond Joint Industrial Project (JIP), on the assessment of bonded repairs for offshore units. FPSO's have been around for the last forty years, with a large development in the early 1990's. About two hundred are now operated around the world. The offshore environment is extremely severe to these steel structures that are required to operate twenty years without dry docking. Corrosion is a permanent threat to FPSO's and maintenance is a challenge. The current crop and renew repair techniques imply welding, thus:

- emptying, cleaning and inerting the surrounding tanks,
- opening a floating structure,
- rewelding the stiffeners, thus setting up large scaffoldings.

Mechanically, crop and renew repairs imply large costs and down time. Composites and steel bonded repairs overcome these problems by being a non-intrusive and "cold" repair. It can be found surprising that such repairs have not been more developed in the industry. Offshore installation and durability are obvious problems to be treated. However, engineering face problems as basic as strength qualification. Analysis and design of a composite bonded repairs require tests that are delicate to translate to specific offshore design as there is a lack of guidance or reference. It makes difficult the qualification of a design of repair, and the evaluation of the safety margin.

Based on the experience gathered during the last twenty years, in research or certification of bonded repairs and composite projects, Strength Bond Offshore JIP has been initiated to overpass the limitation to qualification of bonded repairs. A clear objective of the JIP is to enable a first level of certification of bonded repairs. The workflow of the project is articulated between characterization and strength tests, to be compared to a large modelling work investigating the failure predictions techniques. Fatigue tests are to be performed as it is a necessary step to enable qualification of bonded repairs. Improved definition of failure criteria will allow the evaluation of the margin between the strength and the regulatory loads, hence definition of safety factors. Hence, bonded repairs design can follow classical offshore engineering routines. Approval of design will not require systematic tests and its duration will be shortened to allow acceptable time frames.

Consortium of SBO JIP project :



Contact: Stephane.paboeuf@bureauveritas.com

Web page: <https://marine-offshore.bureauveritas.com/strength-bond-offshore-assessing-strength-bonded-repairs>

Contents

Remerciements	3
Résumé en français.....	4
Details on StrengthBond Offshore JIP project.....	9
Contents.....	10
Table of figures	15
Table of tables.....	21
General Introduction	24
Chapter 1: State of the art regarding the design of adhesively bonded joints	27
1.1. Generalities about adhesive bonding	27
1.1.1. Historical background	27
1.1.2. Adhesion theories	27
1.1.3. Failure modes	28
1.1.4. Load and geometries of adhesively bonded joint.....	29
1.2. Mechanical state analysis of bonded lap joints	30
1.2.1. Models based on analytical solutions.....	30
1.2.2. Models based on numerical approaches	40
1.3. Design approach and failure prediction	43
1.3.1. Continuum mechanics approach	43
1.3.2. Fracture mechanics.....	45
1.3.3. Coupled stress-energy method	49
1.4. Damage mechanics and cohesive zone modeling.....	53
1.4.1. Description and concept	53
1.4.2. Cohesive law shape	56
1.4.3. Determination of the critical energy release rate in mode I according to standardized tests	59

1.4.4.	Determination of the critical energy release rate in mode II according to standardized tests	62
1.4.5.	Determination of the critical energy release rate in mixed mode according to standardized tests	63
1.4.6.	Non-standard test G_c determination.....	65
1.5.	Conclusion.....	68
2.	Chapter 2: A new methodology for fracture mechanics investigations on adhesively bonded joints relying on the use of distributed optical fiber sensor.....	71
2.1.	Justification of the developpement of the new crack propagation measurement methodology	71
2.2.	Optical fiber crack front measurement methodologies.....	72
2.2.1.	Theoretical ENF crack front measurement	73
2.2.2.	Theoretical DCB crack front measurement.....	74
2.2.3.	Theoretical MMB crack front measurement	74
2.3.	Description of the experimental protocol	76
2.3.1.	Studied samples.....	76
2.3.2.	DCB, ENF and MMB test bed geometries.....	77
2.3.1.	Monitoring system by distributed optical fiber sensor.....	78
2.4.	DCB test investigations	81
2.4.1.	Load/displacement curve analysis and failure mode.....	81
2.4.2.	Exterior optical fiber	81
2.4.3.	Crack length visual validation.....	83
2.5.	ENF test investigations	83
2.5.1.	Load vs time curve analysis and failure mode	83
2.5.2.	Exterior optical fiber analysis and crack propagation determination.....	84
2.5.3.	Crack length visual validation.....	86
2.5.4.	Embedded optical fiber curve analysis.....	87
2.5.5.	Numerical validation of the crack length measurement.....	88
2.6.	MMB test investigations.....	90
2.6.1.	Load vs time curve analysis and failure mode	90

2.6.2.	Optical fiber analysis and crack propagation determination	91
2.6.3.	Crack length visual validation	92
2.7.	Conclusion	92
3.	Chapter 3: Critical toughness and cohesive law experimental determination methodology	95
3.1.	Realized experimental investigations	95
3.1.1.	Samples and experimental program	95
3.1.2.	Additional monitoring system: Digital Image Correlation	97
3.2.	Determination of critical toughnesses using standard procedures.....	98
3.2.1.	Obtained failure mode	98
3.2.2.	Obtained results in mode I (DCB investigations)	99
3.2.3.	Obtained results in mode II (ENF investigations).....	102
3.2.4.	Obtained results in mixed mode (MMB investigations)	105
3.3.	Determination of critical toughnesses and cohesive laws using J integral for mode I and II.....	106
3.3.1.	J-integral expression for DCB and ENF tests	106
3.3.2.	Cohesive law expression for DCB and ENF tests	110
3.3.3.	Analysis of the DIC strategy to monitor local displacement	111
3.3.4.	Obtained results for DCB investigations.....	115
3.3.5.	Obtained results for ENF investigations	116
3.4.	Conclusion and discussion.....	118
4.	Chapter 4: Description and evaluation of the adopted cohesive zone modeling strategy	121
4.1.	Presentation of the used finite elements models.....	121
4.1.1.	Cohesive elements.....	121
4.1.2.	Finite element model hypothesis.....	123
4.1.3.	Mode I and II cohesive laws determination methods.....	125
4.2.	Cohesive zone model determination using indirect method.....	127
4.2.1.	Calibration method	127
4.2.2.	Cohesive laws reference parameters	129

4.2.3.	Model results in mode II	129
4.2.4.	Model results in mode I.....	135
4.2.5.	Model results in mixed mode	140
4.3.	Cohesive zone model determination using direct method.....	142
4.3.1.	Model results in mode II	143
4.3.2.	Model results in mode I.....	144
4.3.3.	Model results in mixed mode	145
4.3.4.	Resulting cohesive law parameters	146
4.4.	Discussion.....	146
5.	Chapter 5: Robustness appraisal of the proposed methodology	149
5.1.	Experimental campaign at real scale and under most commonly encountered loading situations.....	149
5.1.1.	Studied samples and instrumentation	149
5.1.2.	Test protocols	151
5.1.3.	Strain measurement and load at failure	152
5.2.	Stress/energy criteria application to full size model.....	155
5.2.1.	Hypothesis for FE model.....	156
5.2.2.	Stress criteria and mesh sensitivity	157
5.2.3.	Energy criteria	160
5.2.4.	Load at failure prediction analysis using coupled stress-energy criteria.....	163
5.3.	Application of the developed methodologies: direct and indirect method failure prediction.....	165
5.3.1.	Hypothesis for FE model.....	165
5.3.2.	Load/displacement curves	166
5.3.3.	Strain measurements analysis during tension tests	167
5.3.4.	Strain measurements analysis during bending tests	171
5.3.5.	Crack front shape	174
5.4.	Conclusion.....	175
6.	General conclusion.....	177

7. **References** 180

8. **Appendix**..... 190

 A1: ENF specimens with primer – observations after failure..... 190

 A2: TAST test of the resin B with primer..... 191

 A3: Surface preparation analysis 192

 A4: Tensile test result on resin B (bulk samples) 198

 A5: VCCT routine..... 199

 A6: Full size tension and bending tests – observations after failure..... 200

Table of figures

Figure 1.1-1: Failure modes of an adhesively bonded assembly.	28
Figure 1.1-2: Main types of loads applied on bonded joints.	29
Figure 1.1-3: Most commonly encountered bonded assemblies.	29
Figure 1.2-1: Constant shear model.	30
Figure 1.2-2: TAST Test [16].	31
Figure 1.2-3: Volkersen’s model for the single lap joint.	31
Figure 1.2-4: Infinitesimal free-body-diagram of the Volkersen’s model.	32
Figure 1.2-5: Shear stress along the bonded length according to Volkersen’s theory for different values of ku/ka versus constant shear model.	33
Figure 1.2-6: Shear stress along the bonded length according to Volkersen’s theory for different bonded length versus constant shear model.	34
Figure 1.2-7: Typical relation between ultimate capacity and overlap length [18].	34
Figure 1.2-8: Deformed state of a single lap joint in the case of the Goland and Reissner model [22].	35
Figure 1.2-9: Infinitesimal free-body-diagram of the Goland & Reissner model in the adherent out of the bonded area.	35
Figure 1.2-10: Infinitesimal free-body-diagram of the Goland & Reissner model in the joint.	35
Figure 1.2-11: Stresses predicted by Volkersen and Goland & Reissner models [22].	37
Figure 1.2-12: Application case of the Hart-Smith model.	38
Figure 1.2-13: Perfect plastic law of the adhesive.	39
Figure 1.2-14: Hart-Smith’s shear stress distribution.	39
Figure 1.2-15: Relation between the overlap length and the adhesive shear stress distributions for Hart-Smith model, for a) short overlap and b) long overlap.	39
Figure 1.2-16: Scheme presenting the relationship between the ultimate capacity and the bonded length.	40
Figure 1.2-17: Bonded joint possible singularities.	41
Figure 1.2-18: Schemes of the M4 approaches.	43
Figure 1.3-1: The three modes of loading of a crack.	45
Figure 1.3-2: Energy released with the crack propagation.	46
Figure 1.3-3: a) Cracked plate at initial state, b) Cracked plate after fixed displacement Δ or fixed loading P . ..	47
Figure 1.3-4: J-integral contour path Γ around a crack tip in two dimensions.	48
Figure 1.3-5: Typical analytical stress state and stress criteria curve.	50
Figure 1.3-6: Energy release rate and energy criteria along the bonded length.	51
Figure 1.3-7: Two-steps VCCT overview.	52
Figure 1.3-8: Coupled stress-energy criterion at critical load level (the extent of the damaged zone is equal to the minimum propagation of the crack).	52
Figure 1.4-1: Representation of the fracture process zone and a bilinear cohesive zone law for mode I.	53
Figure 1.4-2: Four-node linear cohesive elements separation in FEM.	54
Figure 1.4-3: Models: a) with thick cohesive zone model representing the adhesive layer between the adherents, b) with zero thickness cohesive elements with adhesive volume elements.	55
Figure 1.4-4: Dugdale cohesive law.	56

Figure 1.4-5: Needleman cohesive law.....	56
Figure 1.4-6: Trapezoidal cohesive law.	57
Figure 1.4-7: Bilinear cohesive law.....	57
Figure 1.4-8: Peterson cohesive law.....	57
Figure 1.4-9: Mixed mode cohesive law surface (Power law criterion, [83]).	59
Figure 1.4-10: DCB test ([87]).	60
Figure 1.4-11: Exemple of DCB $P(\delta)$ curve.....	60
Figure 1.4-12: Typical DCB $C(\alpha_3)$ curve.....	60
Figure 1.4-13: $G(\alpha)$ curve.....	62
Figure 1.4-14: ENF sample.	62
Figure 1.4-15: Exemple of ENF $P(\delta)$ curve.....	63
Figure 1.4-16: MMB test bed and sample.....	63
Figure 1.4-17: MMB Test configuration.....	64
Figure 1.4-18: MMB exemple $P(\delta)$ curve.....	65
Figure 1.4-19: Blister test sample.....	65
Figure 1.4-20: 4ENF sample.	66
Figure 1.4-21: ELS sample.	66
Figure 1.4-22: Single lap test.....	66
Figure 1.4-23: Spelt test.	67
Figure 1.4-24: DCB-UBM test frame.....	67
Figure 1.4-25: Arcan test.....	68
Figure 2.2-1: Scheme representing strain distributions for two characteristic cross-sections into the ENF sample during loading.....	73
Figure 2.2-2: Strain into the DCB sample during loading.....	74
The MMB test can be analyzed as the sum of an ENF and a DCB test. Upstream from the crack front (on the right in Figure 2.2-3), the MMB sample corresponds to a beam of thickness $2hs + ha$ while downstream from the crack front (on the left in Figure 2.2-4), the sample is equivalent to the superposition of two beams of thickness hs	74
Figure 2.2-5: Theoretical outer strain profiles on the lower and upper surface of an MMB sample.....	75
Figure 2.3-1: Photo of the DCB sample and DCB test bed.....	77
Figure 2.3-2: Photo of the ENF sample and ENF test bed.....	78
Figure 2.3-3: Photo of the MMB sample and MMB test bed.....	78
Figure 2.3-4: Tested positions for the optical fiber on the sample (flank, transverse, embedded and on the top).	79
Figure 2.3-5: a) Example of optical fiber application on a specimen: option 3, b) DCB specimen with surface bonded optical fiber with Araldite-2014-1.....	79
Figure 2.3-6: Scheme of the two studied optical fiber technologies and connection to the samples.....	80
Figure 2.3-7: Local strain measurement during an ENF test with polyimide and acrylate optical fiber coating... ..	80
Figure 2.4-1: DCB resin A load/time curve.....	81
Figure 2.4-2: DCB exterior optical fiber continuous strain measurements along lap length for different times... ..	82
Figure 2.4-3: Crack propagation curve for the DCB test - data processing via local mean approximation.....	82
Figure 2.4-4: Visual measurement of the crack length of the DCB test, a) in the middle and b) at the border. ...	83
Figure 2.5-1: ENF resin A load / time curve, a) test 1 and b) test 2.....	84

Figure 2.5-2: Exterior optical fiber distributed strain measurements between times 154.76 s and 203.0 s.	85
Figure 2.5-3: Shift of the first peak of the strain profiles measured during the ENF test.	85
Figure 2.5-4: Crack propagation curve for the ENF test – raw data processing via local mean approximation. ...	86
Figure 2.5-5: Visual measurement of the crack length at the end of the ENF test.	86
Figure 2.5-6: Embedded distributed optical fiber strain measurements before crack propagation.	87
Figure 2.5-7: Embedded distributed optical fiber strain measurements after crack propagation.	88
Figure 2.5-8: Finite element mesh and strain measurement area.	88
Figure 2.5-9: Comparison of strain profiles along lap length: elastic FEM analysis vs experimental measurements at 39 s, a) exterior measurement, b) embedded measurement.	89
Figure 2.5-10: Comparison of strain profiles along lap length: elastic FEM analysis vs experimental measurements at $t_b=58$ s, a) exterior measurement, b) embedded measurement.	90
Figure 2.6-1: MMB test load/displacement curve.	90
Figure 2.6-2: Optical fiber continuous strain measurements between time 100s and 174s.	91
Figure 2.6-3: Crack propagation curve for the MMB test.	91
Figure 2.6-4: a) Visual measurements of the crack length at the end of the MMB test, a) at mid width, b) on the border.	92
Figure 3.1-1: a) Primer application with the lint free cloth, b) Primer applied in thin layer.	96
Figure 3.1-2: ENF Samples bonding.	96
Figure 3.1-3: Resin flow during the bonding process.	97
Figure 3.1-4: Example of speckle and initial crack front.	97
Figure 3.2-1: DCB resin B fracture surface.	98
Figure 3.2-2: Resin B fracture surface for different modes.	98
Figure 3.2-3: DCB tests load/displacement curves.	99
Figure 3.2-4: a) II-I test load/time curve, and b) crack propagation curve.	100
Figure 3.2-5: a) Linear approximation of the $C^{1/3}=f(a)$ curve for the Δ computation, b) Linear approximation of $\ln(C)=f(\ln(a))$ for n computation.	100
Figure 3.2-6: Critical toughness in mode I at initiation and stabilization for the II-1 test.	101
Figure 3.2-7: Critical toughness computation results in mode I.	102
Figure 3.2-8: ENF tests load/displacement curves with primer.	103
Figure 3.2-9: ENF tests load/displacement curves without primer.	103
Figure 3.2-10: Linear approximation of the $C=f(a^3)$ curve with primer.	104
Figure 3.2-11: Linear approximation of the $C=f(a^3)$ curve without primer.	104
Figure 3.2-12: ASTM Critical toughness computation.	105
Figure 3.2-13: MMB load/displacement curves.	105
Figure 3.2-14: Critical toughness average value in function of the mode II ratio for the resin B.	106
Figure 3.3-1: Adhesive joint and J-integral integration path.	107
Figure 3.3-2: ENF J-integral integration path A+B+C+D.	107
Figure 3.3-3: ENF local sliding at the crack front.	109
Figure 3.3-4: DCB J-integral integration path A+B+C.	109
Figure 3.3-5: Cohesive zone ahead of the crack tip.	110
Figure 3.3-6: DIC measurement point on test samples.	111
Figure 3.3-7: ENF test DIC speckle showing difficulties to have a precise initial crack front position based on the marking.	112

Figure 3.3-8: DCB test DIC X displacement map.....	112
Figure 3.3-9: DCB test DIC X displacement profiles through the sample thickness.	112
Figure 3.3-10: Example of ENF test DIC X displacement map and local profiles.	113
Figure 3.3-11: ENF test DIC X displacement profiles through sample thickness at the crack front position.	113
Figure 3.3-12: ENF SV-1 test, J-integral computation depending of the error of position of the X displacement profile.	114
Figure 3.3-13: Impact of the position of the profile on the Jc computation for ENF tests.	114
Figure 3.3-14: Impact of the position of the profile on the Jc computation for DCB tests.	115
Figure 3.3-15: J-integral computation curves for the DCB tests.....	115
Figure 3.3-16: Cohesive laws in mode I based on the J-integral curves derivation.	116
Figure 3.3-17: J-integral computation curves for the ENF tests without primer.	116
Figure 3.3-18: J-integral computation curves for the ENF tests with primer.....	117
Figure 3.3-19: Cohesive law in mode II based on the J-integral curves derivation.....	118
Figure 4.1-1: Graphic showing all the parameters defining the bilinear cohesive law in mode I.....	123
Figure 4.1-2: Cohesive element implementation on the bonded area, contact definition of the initially not bonded area.	124
Figure 4.1-3: DCB model representing the adhesive layer with cohesive elements only.	124
Figure 4.1-4: ENF model representing the adhesive layer with cohesive elements only.	124
Figure 4.1-5: MMB model representing the adhesive layer with cohesive elements only.	125
Figure 4.1-6: Direct method flowchart.	126
Figure 4.2-1: Indirect method flowchart.	128
Figure 4.2-2: Mesh of an ENF for an element size of 1 mm.....	129
Figure 4.2-3: Load/displacement curves for different mesh sizes for the ENF model with an initial crack length of 74 mm.	130
Figure 4.2-4: Comparison between experimental and numerical load/displacement curves for different cohesive stiffness for ENF models.	130
Figure 4.2-5: Comparison between experimental ($a_0 = 74$ mm) and numerical load/displacement curves for different critical shear stress for ENF models.	131
Figure 4.2-6: Cohesive parameters in mode II obtained for indirect method for resin B steel-to-steel bonding.	132
Figure 4.2-7: Comparison of experimental and numerical load/displacement curves obtained for ENF tests and models, with initial crack lengths of 59 mm and 90 mm.	132
Figure 4.2-8: 3D Model of the ENF (the contact zones are highlighted).	133
Figure 4.2-9: Load/displacement curves for the 2D and 3D model of the ENF test.....	134
Figure 4.2-10: Plot of the cohesive element damage during the ENF test showing a planar crack propagation.	134
Figure 4.2-11: Crack front observations on an ENF sample at the end of the test.....	134
Figure 4.2-12: Load/displacement curves for different mesh sizes for the DCB model.	135
Figure 4.2-13: Numerical load/displacement curves for different cohesive stiffness for DCB models.	136
Figure 4.2-14: Comparison of load/displacement curves for different critical peel stresses for DCB models.	137
Figure 4.2-15: Comparison of experimental and numerical load/displacement curves of DCB resin B.	138
Figure 4.2-16: Resulting indirect cohesive law in mode I for steel-to-steel bonded assembly with resin B.	138
Figure 4.2-17: 3D DCB model.	139
Figure 4.2-18: Comparison of load/displacement curves for DCB model in 2D and 3D with a 2mm mesh size.	139

Figure 4.2-19: Fracture surface along the width for the 3D DCB model.	140
Figure 4.2-20: Indirect cohesive laws obtained in mode I and mode II.	140
Figure 4.2-21: Comparison of load/displacement curves for MMB experimental test and model with a 1mm mesh size, a mixed mode ratio of 0.7 and different values of the coupling parameter α	141
Figure 4.2-22: Comparison of load/displacement curves for MMB experimental test and model with a 1mm mesh size, a mixed mode ratio of 0.5 and different values of the coupling parameter α	141
Figure 4.3-1: Experimental and proposed numerical cohesive laws in pure Mode II for ENF test.	143
Figure 4.3-2: Experimental and proposed numerical cohesive laws in pure Mode I for DCB test.	143
Figure 4.3-3: Numerical and experimental ENF load/displacement curves for different initial crack lengths. ...	144
Figure 4.3-4: Numerical direct method and experimental DCB load/displacement curves.	144
Figure 4.3-5: Comparison of numerical and experimental load/displacement curves for MMB test with 50% of mode II, for different values of the coupling parameter, using direct cohesive law.	145
Figure 4.3-6: Comparison of numerical and experimental load/displacement curves for MMB test with 70% of mode II, for different values of the coupling parameter values, using direct cohesive law.	146
Figure 4.4-1: Final DCB cohesive laws.	147
Figure 4.4-2: Final ENF cohesive laws.	148
Figure 5.1-1: Full-size test geometries for tension and bending/tension loadings.	149
Figure 5.1-2: Full size tension and bending samples instrumentation.	150
Figure 5.1-3: a) Initial tension test without instrumentation, b) Tension sample lower end with optical fiber and gauge instrumentation.	151
Figure 5.1-4: Bending test with instrumentation.	152
Figure 5.1-5: Adhesive failure and crack front shape of the samples.	152
Figure 5.1-6: Tension test load/displacement curves.	153
Figure 5.1-7: Gauges 3 and 4 strain measurement for the three samples in tension.	154
Figure 5.1-8: Load/displacement curves of the bending tests.	155
Figure 5.1-9: Gauges 3 and 4 strain measurements during the bending tests.	155
Figure 5.2-1: Stress- energy coupled criteria.	156
Figure 5.2-2: Finite element model boundary conditions for tension test.	157
Figure 5.2-3: Finite element model boundary conditions for bending test.	157
Figure 5.2-4: Stress analysis meshing.	157
Figure 5.2-5: Mesh sensitivity analysis for the tension test: shear stress.	158
Figure 5.2-6: Mesh sensitivity analysis for the tension test: peel stress.	158
Figure 5.2-7: Mesh sensitivity analysis for the tension test: principal stress.	159
Figure 5.2-8: Mesh sensitivity analysis for the bending test: shear stress.	159
Figure 5.2-9: Tension and bending model shear stress.	160
Figure 5.2-10: Illustration of the energy criteria with a critical interface ERR G_c and a characteristic length a_c	160
Figure 5.2-11: Example of the definition of the critical ERR with the B-K criterion for a resin C.	161
Figure 5.2-12: Resin B fracture test results and B-K criterion fitting.	162
Figure 5.2-13: VCCT energy release rate for the tension model.	162
Figure 5.2-14: VCCT energy release rate for the bending model.	162
Figure 5.2-15: VCCT G_{II}/G_{tot} mode ratio for the tension and bending model.	163

<i>Figure 5.2-16: Tension test coupled stress-energy criterion computation for: a) experimental failure load, b) 1.15 * experimental failure load , c) 1.22 * experimental failure load and d) 1.4 * experimental failure load.</i>	<i>164</i>
<i>Figure 5.2-17: Bending test coupled stress-energy criterion computation for: a) experimental failure load and b) 1.13 * experimental failure load.</i>	<i>164</i>
<i>Figure 5.3-1: Cohesive model meshing.....</i>	<i>165</i>
<i>Figure 5.3-2: a) Bending test load/displacement curves, b) Tension test load/displacement curves.</i>	<i>166</i>
<i>Figure 5.3-3: Experimental and numerical gauge 1 measurements for the tension tests,.....</i>	<i>167</i>
<i>Figure 5.3-4: Zoom on the non-linear part of the curves for gauge 1 measurements for the tension tests.....</i>	<i>168</i>
<i>Figure 5.3-5: Experimental and numerical gauge 5 data for the tension test.....</i>	<i>168</i>
<i>Figure 5.3-6: Experimental and numerical gauge 3 measurements for the tension test.</i>	<i>169</i>
<i>Figure 5.3-7: Experimental optical fiber strain measurements for tension test n°3 and numerical strain profile results.....</i>	<i>170</i>
<i>Figure 5.3-8: Experimental and numerical gauge 1 measurements for the bending tests.</i>	<i>171</i>
<i>Figure 5.3-9: Experimental and numerical gauge 5 measurements for the bending tests.</i>	<i>172</i>
<i>Figure 5.3-10: Experimental and numerical gauge 3 measurements for the bending tests.</i>	<i>173</i>
<i>Figure 5.3-11: Experimental optical fiber strain measurements for the bending test n°2 and numerical strain profile results.....</i>	<i>174</i>
<i>Figure 5.3-12: Experimental crack front shape and FE method crack front shape prediction.</i>	<i>175</i>
<i>Figure 5.4-1: Normalized failure load predictions of direct, indirect and coupled stress-energy criteria methods compared to experimental results.</i>	<i>176</i>

Table of tables

<i>Table 2.1-1: Comparison (advantage and limitations) of several techniques for crack front measurement.</i>	<i>72</i>
<i>Table 2.3-1: Resin A mechanical properties in tension.</i>	<i>76</i>
<i>Table 2.7-1: Crack length from the experimental investigations using exterior optical fiber and visual inspection.</i>	<i>92</i>
<i>Table 3.1-1: Resin B mechanical properties in tension.</i>	<i>95</i>
<i>Table 3.1-2: Fracture tests nomenclature.</i>	<i>96</i>
<i>Table 3.2-1: DCB test nomenclature and crack propagation information.</i>	<i>99</i>
<i>Table 3.2-2: Standard critical toughness characterization with optical fiber crack length measurement.</i>	<i>101</i>
<i>Table 3.2-3: ENF test nomenclature.</i>	<i>102</i>
<i>Table 3.2-4: Critical toughness computation following the ASTM D7905 standard.</i>	<i>104</i>
<i>Table 3.2-5: Critical toughness computation of the mixed mode test.</i>	<i>106</i>
<i>Table 3.3-1: DCB test J-integral polynomial approximation.</i>	<i>115</i>
<i>Table 3.3-2: Critical toughness computation in mode I based on the J-integral curves.</i>	<i>116</i>
<i>Table 3.3-3: ENF test J-integral polynomial approximation.</i>	<i>117</i>
<i>Table 3.3-4: Critical toughness computation in mode II based on the J-integral curves.</i>	<i>117</i>
<i>Table 3.4-1: Critical toughness computation in mode I.</i>	<i>118</i>
<i>Table 3.4-2: Critical toughness computation in mode II.</i>	<i>119</i>
<i>Table 4.2-1: Comparison of experimental and numerical failure forces for different critical shear stress for ENF model with an initial crack length of 74mm.</i>	<i>131</i>
<i>Table 4.2-2: Cohesive parameters in mode II obtained for indirect method for Resin B steel-steel for indirect method.</i>	<i>131</i>
<i>Table 4.2-3: Comparison of failure forces obtained numerically and experimentally for ENF tests and models with different initial crack lengths.</i>	<i>132</i>
<i>Table 4.2-4: Failure forces for different mesh sizes for DCB model.</i>	<i>135</i>
<i>Table 4.2-5: Comparison of experimental and numerical failure forces for different critical peel stresses for DCB models.</i>	<i>137</i>
<i>Table 4.2-6: Cohesive parameters in mode I for indirect method.</i>	<i>138</i>
<i>Table 4.2-7: Comparison of experimental and numerical failure loads for MMB test for a mode mixity of 50% and 70% and for different coupling parameter values.</i>	<i>142</i>
<i>Table 4.3-1: Cohesive parameters using direct method for mode I and II.</i>	<i>142</i>
<i>Table 4.3-2: Comparison of failure loads in mode II obtained numerically by the direct method and experimentally by ENF tests.</i>	<i>144</i>
<i>Table 4.3-3: Comparison of numerical and experimental failure loads for the DCB direct method.</i>	<i>145</i>
<i>Table 4.3-4: Comparison of experimental and numerical failure loads for MMB test with 50% of mode II, for different values of the coupling parameter, using direct cohesive law.</i>	<i>145</i>
<i>Table 4.3-5: Comparison of experimental and numerical failure loads for MMB test 70% of mode II, for different values of the coupling parameter, using direct cohesive law.</i>	<i>146</i>
<i>Table 4.3-6: Resulting parameters of cohesive laws using direct method.</i>	<i>146</i>
<i>Table 5.1-1: Strain and load at failure for the tension test.</i>	<i>154</i>

<i>Table 5.1-2: Strain and load at failure of the bending tests.</i>	155
<i>Table 5.3-1: Resulting parameters of cohesive law for resin B steel-to-steel assembly characterization using direct method.</i>	166
<i>Table 5.3-2: Resulting parameters of cohesive law for resin B steel-to-steel assembly characterization using indirect method.</i>	166
<i>Table 5.3-3: Several characteristic values determined through experimental and numerical analyses using the developed cohesive zone approaches (direct and indirect methods) for gauges 1 and 5, for the tension tests.</i>	169
<i>Table 5.3-4: Several characteristic values determined through experimental and numerical analyses using the developed cohesive zone approaches (direct and indirect methods) for gauge 3, for the tension tests.</i>	170
<i>Table 5.3-5: Several characteristic values determined through experimental and numerical analyses using the developed cohesive zone approaches (direct and indirect methods) for gauge 1 and 5, for the bending tests.</i>	172
<i>Table 5.3-6: Several characteristic values determined through experimental and numerical analyses using the developed cohesive zone approaches (direct and indirect methods) for gauge 3, for the bending tests.</i>	173
<i>Table 5.4-1: Failure load prediction of direct, indirect methodologies and coupled stress-energy criteria compared to experimental results for real-scale investigations.</i>	176



General Introduction

The maintenance of marine steel structures installed in harsh offshore environment (like tropical areas) is a great challenge. Vessels and mobile offshore units can be maintained and repaired onshore in shipyards, units such as Floating Production Storage and Offloading platforms (FPSO) are permanently moored at sea and shall be maintained on site. Similarly, naval ships may also be faced with the need to perform repairs in short period of time at sea to maintain operability. On FPSO units, the corrosion is a permanent threat due to high temperature and high humidity conditions. Bonded repair solutions which present several advantages (short down-time and non-intrusively process) are actually in development. However, repairing corroded areas on large marine structures by bonding patch imposes important constraints on the design. The patch lies in fully stressed area (for instance area subject to hull girder flexibility), causing high stresses in the bond line edges. Thus, a fine apprehension of adhesion mechanics and strength is critical for designing highly reliable patch repairs.

This study is part of a project called Strength Bond aiming at developing a bonded composite repair for corroded steel plate for offshore applications. The development of a composite repair in such conditions seems particularly appropriate for various reasons. Composite materials show high performance, can be easily adapted to various 3-dimensional shape, and are easy to transport and install. In addition, the use of adhesive bonding is particularly adapted as it limits local stress concentrations, and may avoid operations at high temperatures. Yet, the lack of commonly adopted design approach for adhesively bonded joints still limits the use of such techniques.

One of the main issues encountered in bonded assemblies is the risk of brittle failure. Consequently, due to safety considerations, it is often required that adhesively bonded structures (particularly those employed in primary load/bearing applications) include mechanical fasteners to limit this type of failure (welding, bolts, ...). These practices generally result in heavier, more expensive and less efficient assembly. Moreover, this is not relevant in our application case, as it would require « hot works » that may damage the existing structure, raise safety issues or limit the operation during the repair/reinforcement application.

Better understanding of the failure of bonded joint and the development of reliable design methodologies are thus necessary to increase confidence and to lead to more efficient application of composite bonded repairs in offshore applications. It is also a necessary step for further damage tolerance assessment and ageing assessment. It was therefore decided to focus in this work on adhesively bonded joints design.

When designing adhesively bonded joints, several steps are generally required. The first step aims at assessing the adhesive or the joints capacities through standardized experimental investigations. It allows obtaining failure criteria data and sometimes mechanical behavior information. It may also give information related to surface preparation and failure modes. The second step requires having access to mechanical analysis tools that may be analytical or numerical. Their use provides information related to design predictions. Comparison of both results (failure criteria and design predictions) is then carried out, and, if needed, design is modified.

Several design approaches have been developed for adhesively bonded joints (relying on continuous mechanics, fracture mechanics or both). This work intends to develop a methodology

assessing at each step (characterization and design assessment) the precision of the obtained results and the sensitivity of the approach.

First chapter will be dedicated to a literature review on adhesively bonded joints and their design. After general information related to the specific case of bonded joints, and the issue of adhesion, main existing design strategies (stresses and energy approaches) are developed giving for each the advantages and the drawbacks. A focus is then done on the use of the cohesive zone approach that was chosen for the developed methodology. The associated standard fracture mechanics experimental investigations and critical toughness computation methods are also described.

The second chapter will intend at improving the experimental characterization through fracture mechanics investigations. In order to improve the robustness and precision of the measurement, it was decided to study if the use of continuous optical fiber measurement for crack monitoring could be suitable. Several experimental investigations are presented in mode I, II and mixed mode. Obtained optical fiber crack length measurement are compared to visual and numerical measurement and a precise methodology for the obtention of the critical toughnesses is proposed and assessed.

The third chapter presents the application of this methodology to a wider experimental campaign. Both standards and J-integral approaches are carried out in order to determine the critical toughnesses and, for the J-integral approach, the cohesive zone model. The obtained results are commented and compared.

Chapter fourth is dedicated to the presentation of the modeling strategy relying on the use of finite element models. The cohesive elements are presented and different strategies aiming at obtaining the cohesive zone models are also presented. Two main methods are being considered and compared for mode I and II: the direct and the indirect methods. The mixed mode case is also deeply studied.

The last chapter intends at applying the developed methodology on real scale adhesively bonded joints, using the improved mechanical investigations, the obtained critical toughnesses and the cohesive zone models using the different strategies. The experimental results, load at failure, local and general samples behavior are compared to design predictions. In order to assess the precision of the methodology, an alternative design methodology is carried out (the coupled stress energy approach). Conclusion are express on the efficiency and robustness of each methodology to predict behavior of bonded patch.



Chapter 1: State of the art regarding the design of adhesively bonded joints

In the first part, some generalities regarding the use of structural adhesive bonding will be described. This will allow to address main issues related to this assembly technique and the corresponding glossary. In the second part, the different strategies available to determine the adhesively bonded joints mechanical state will be presented. At first, main analytical developments will be detailed. Then, different numerical strategies will be described. In the third part, the different failure criteria that were developed and used for the considered application will be listed. A classification is proposed and allows distinguishing the classical criteria used in continuum mechanics, the fracture mechanics criteria and the mixed criteria. Finally, the cohesive zone model approach, comprising a modeling strategy and failure criteria, will be described. The main methodologies used to determine the parameters of the cohesive zones will also be highlighted.

1.1. Generalities about adhesive bonding

A bonded assembly consists in two adherents (substrates) which are the elements to be assembled, linked by an adhesive which transmits the load from one element to the other.

1.1.1. Historical background

The first use of bonded assembly was in 8000 years BC with the use of animal and vegetable adhesives (fish and bones glue) for the assembly of tools and wood structures. Synthetic adhesives were created only around 1850 with the industrialization [1]. During the 20th century, their development is related to the newly born aeronautics industry. The Fokker company started using adhesive bonding in 1915 for wood-to-wood and wood-to-fabric assembly leading the way for other manufacturers [2]. In 1940, adhesive bonds were used on wood spars, on the De Havilland DH 98 Mosquito aircraft. In the 1960s, the aerospace industry also started using adhesive bonding technology, convinced that it was an optimal solution for the manufacture of lightweight and resistant structures. Today, it tends to be more and more extensively used in other areas: sailing, building and civil engineering [3] [4] [5] [6] [7].

1.1.2. Adhesion theories

The link between the adherent and the adhesive mainly depends on the adhesion at the interface, which remains a research topic. Adhesion includes all the physico-chemical phenomena that occur when intimate contact is realized between two materials. There is no single model to explain this phenomenon and several theories in different fields have been proposed to explain the adhesion. Main ones are listed here:

- physical adsorption: effect of forces of attraction between atoms and molecules of different nature, acting on the surfaces in contact. The molecules of the adhesive are retained on the surface, thanks to the adsorption forces, which act as soon as the molecules are within 5×10^{-8} cm [8],
- chemical absorption: chemical reaction between the atoms and the molecules of the surfaces in contact [9],

- mechanical anchorage: comes from the creation of geometrical anchorage on rough surfaces. This theory links directly the surface geometry with the resistance of the assembly [10].

Adhesion is therefore closely related to the properties of the surfaces of the two adherents. For this reason, the process of surface preparation prior to adhesive bonding is an important issue. This will determine directly the level of surface wettability and the final level of adhesion forces. Surface energy (or surface tension, or wettability) is a physical quantity used to characterize the state of cohesion of a solid (or liquid). The molecular force of attraction between different materials is related to their surface properties (surface energy and/or surface tension) and conditions their adhesion. For a solid, a high surface energy means a strong molecular attraction, while a low surface energy results in lower forces of attraction. For optimum bonding of two materials, it is necessary to have good wettability (liquid on solid). This results in higher surface energy of the solid (substrate to be bonded) than of the liquid (adhesive) [11].

Either mechanical or chemical surface preparations can be carried out. The most commonly encountered mechanical surface preparation processes are the following:

- sandblasting, that consists in projection of an abrasive powder. The surface may then be covered with a protective film before adhesive bonding (like anti-corrosion film),
- abrasion, that consists in removing the external adherent layer with a specific brush or tool,
- ultrasound treatment, that is an expensive method of cavitating water by overpressure – depression. It cleans the surface without modifying its wettability characteristics.

Regarding the chemical surface preparation, it consists mainly in:

- degreasing with solvents: in that case, derivatives of hydrocarbons or chlorine are generally used. The solvent is chosen according to the contaminating elements,
- using primer agent on the surface prior to bonding to improve chemical compatibility.

1.1.3. Failure modes

In the assembly of two materials, the overall resistance depends on the strength of the adherents, the adhesive and the interfaces between adherents and adhesive. Three failure modes of a bonded assembly can be distinguished (Figure 1.1-1):

- cohesive failure, in the adhesive or in the substrates,
- adhesive failure, at the interfaces,
- or a mix of cohesive and adhesive failure.

A cohesive failure is generally preferred to an adhesive failure as it relies on the properties of the materials and not the quantification of the adhesion forces that are strongly related to the surface preparation and the application quality.

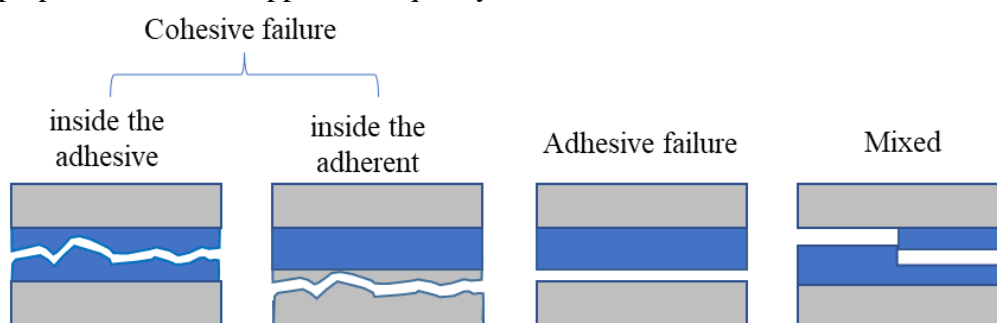


Figure 1.1-1: Failure modes of an adhesively bonded assembly.

1.1.4. Load and geometries of adhesively bonded joint

Adhesively bonded joints can be submitted to several types of mechanical stresses. Figure 1.1-2 shows the four main types of loads experienced by a bonded assembly: shear, peel, cleavage and traction/compression. An adhesively bonded assembly is generally more efficient in shear and compression [12].

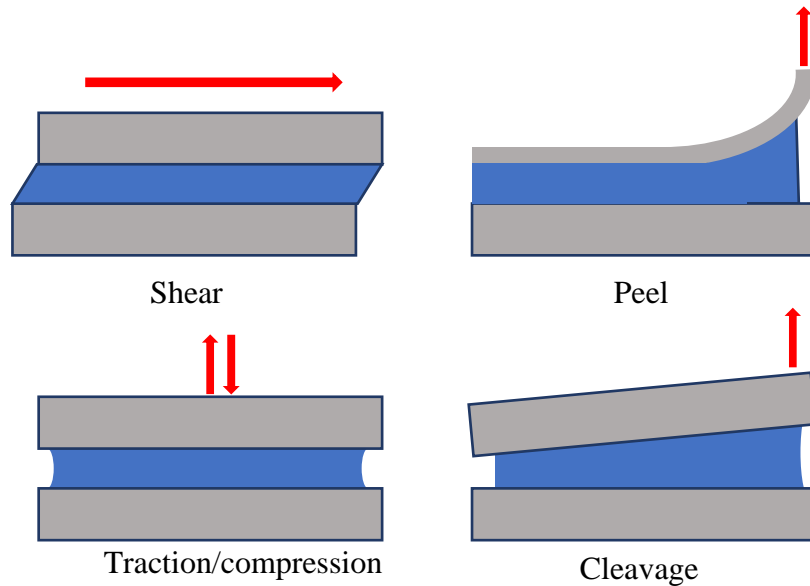


Figure 1.1-2: Main types of loads applied on bonded joints.

Depending on the application, various geometries have been proposed for improving the strength (increase shear loading or reduce geometrical singularities) of a bonded assembly. Figure 1.1-3 presents the main encountered geometries of bonded assembly that were studied in the literature. Among those geometries, the butt joint is not well adapted to bonded assembly as it does not induce any shear or compressive stresses. The single lap joint is the most encountered geometry and will therefore be more deeply studied in next part [13].

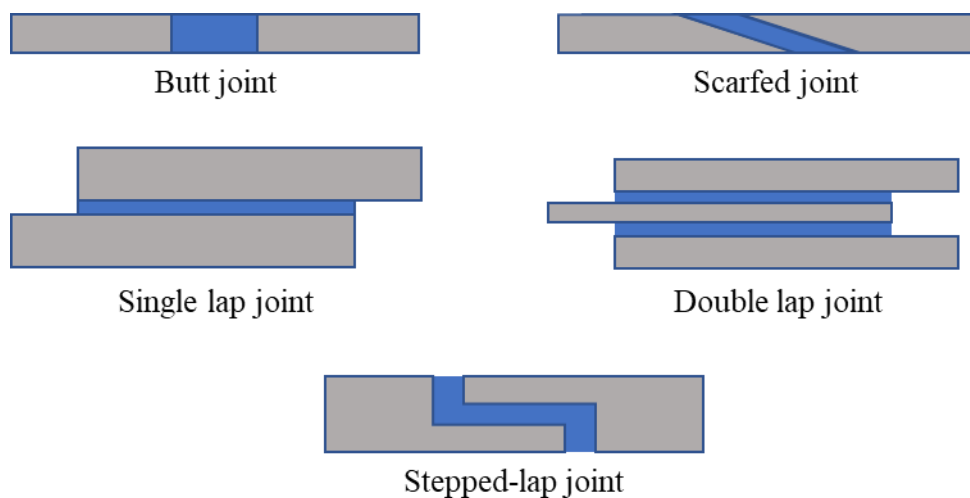


Figure 1.1-3: Most commonly encountered bonded assemblies.

1.2. Mechanical state analysis of bonded lap joints

To be able to express and use adapted criteria for the design of the assembly, it is necessary to have access to the internal stress or strain states.

Existing analytical modeling developed for single or double lap joints will be first reviewed. Then an overview of the main numerical approaches available for the designers will be presented.

1.2.1. Models based on analytical solutions

It is not possible to exhaustively describe all the proposed analytical models in this part. Only the most recognized and used approaches will be raised with increasing complexity and in order to highlight the main phenomena associated to the design of adhesively bonded joints.

1.2.1.1. Constant shear model

Regarding single lap joints, the simplest analysis that can be applied considers that the shear stress is constant over the entire bonded surface [14]. For that case, only the shear stress is considered and the adherents are considered as rigid (Figure 1.2-1).

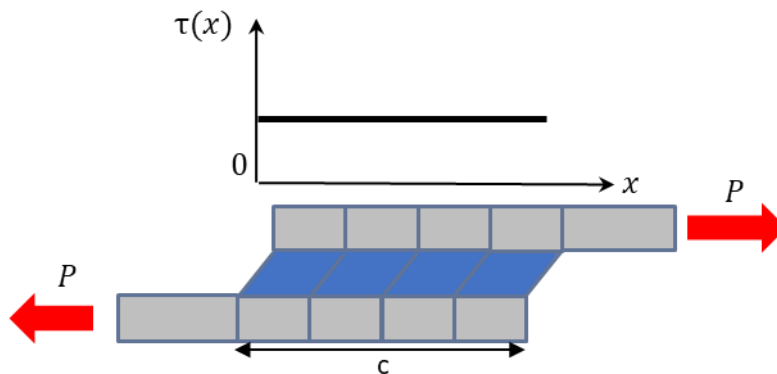


Figure 1.2-1: Constant shear model.

This rigidity involves the adhesive shear stress τ to be constant over the overlap length, and it can be expressed by the equation (1).

$$\tau(x) = \frac{P}{bc} \quad (1)$$

Where, P is the applied load to the adherent, b is the joint width, and c is the overlap length.

Such hypothesis is only relevant when the overall stiffness of the bonded joint (depending on the thickness, the Young's modulus of the adhesive, width and length of overlap), k_a , is low, in comparison with the stiffness of the upper adherent, k_u , and lower adherent, k_l . These parameters are detailed in equation (2), by unit width.

$$k_u = \frac{t_u E_u}{c}, k_l = \frac{t_l E_l}{c}, k_a = \frac{G_a c}{t_a} \quad (2)$$

E_u, E_l being the Young modulus of the upper and lower adherent, G_a the shear modulus of the adhesive, and t_u, t_l, t_a the thicknesses of respectively the upper adherent, lower adherent and the adhesive, respectively.

The main advantage of this model is its ease of use. It is used to define the adhesive shear strength in several standards such as TAST (thick adherent shear test), described in ISO 11003–2 [15] and ASTM D 5656 [16] standards (Figure 1.2-2). In these standards, a specific geometry is adopted, in particular thick adherents and short overlap, in order to obtain shear stress profiles as constant as possible. This is however difficult to obtain in the case of structural adhesives (as their stiffness is high) and as there exists actually edge effects.



Figure 1.2-2: TAST Test [16].

1.2.1.2. Volkersen analysis or “shear lag” model

The first historical model that considers the flexibility of the adherents was proposed in 1938 by O. Volkersen [17] in 1938, and is called “shear lag” model. Using a 1D model of pure shear, it assumed that the adhesive layer was loaded only in shear and that the adherents followed a purely longitudinal strain. It also assumes that the behavior of the adhesive is linear elastic. The shear stress in the adhesive (Figure 1.2-3) is maximum at $x = 0, x = c$ (c is the overlap length).

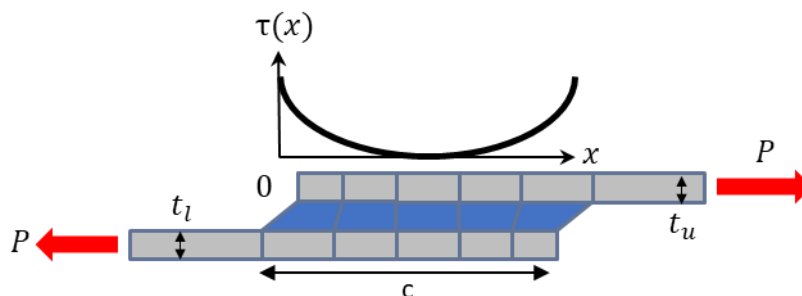


Figure 1.2-3: Volkersen’s model for the single lap joint.

The stress distribution in the adhesive is obtained in that case using the free-body-diagram of an infinitesimal section of the joint (Figure 1.2-4). σ_u is the axial stress in the upper adherent, and σ_l is the axial stress in the lower adherent.

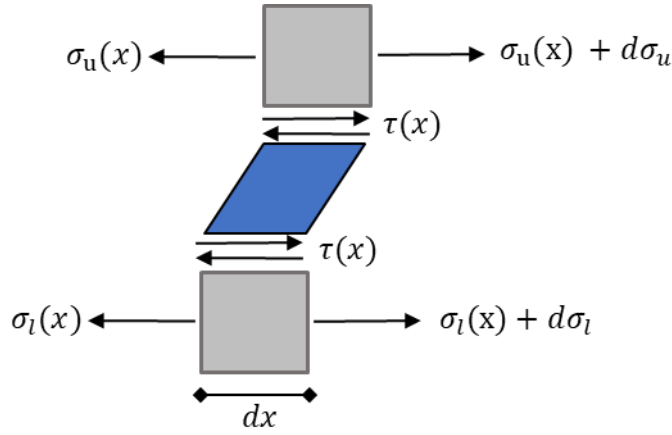


Figure 1.2-4: Infinitesimal free-body-diagram of the Volkersen's model.

Firstly, equilibrium equation for each adherent can be written to obtain a direct relation between the shear stress and tensile stress in the two adherents.

$$\tau(x) = -t_u \frac{d\sigma_u(x)}{dx} \quad (3)$$

$$\tau(x) = t_l \frac{d\sigma_l(x)}{dx} \quad (4)$$

Following the Hooke equations, the overall shear in the adhesive can also be expressed by equation (5).

$$\frac{d\tau(x)}{dx} = \frac{G_a}{t_a} \left(-\frac{\sigma_l(x)}{E_l} + \frac{\sigma_u(x)}{E_u} \right) \quad (5)$$

Using equations (3), (4) and (5), equation (6) can be obtained.

$$\frac{d^2 \left(-\frac{\sigma_l(x)}{E_l} + \frac{\sigma_u(x)}{E_u} \right)}{dx^2} = \omega^2 \left(-\frac{\sigma_l(x)}{E_l} + \frac{\sigma_u(x)}{E_u} \right) \quad (6)$$

With

$$\omega = \sqrt{\frac{G_a}{t_a} \left(\frac{1}{t_l E_l} + \frac{1}{t_u E_u} \right)} \quad (7)$$

Based on these equations, an expression of the shear stress distribution along the adhesive layer can be obtained. The unique solution of this equation with the boundary conditions of a single lap joint: $\sigma_l(x=0) = -\frac{P}{bt_l}$, $\sigma_l(x=c) = 0$, $\sigma_u(x=0) = 0$, $\sigma_u(x=c) = \frac{P}{bt_u}$ are given in equation (8).

$$\tau(x) = \frac{G_a}{\omega t_a} \frac{P}{bE_l t_l} \left(\frac{\cosh(\omega x)}{\sinh(\omega c)} \left(\cosh(\omega c) + \frac{k_l}{k_u} \right) - \sinh(\omega x) \right) \quad (8)$$

This equation (8) can be simplified if the lower and upper adherents have an equivalent rigidity $k_u = k_l$. In that case, the adhesive joint is balanced and equation (9) is obtained.

$$\tau(x) = \frac{k_a}{\omega k_l c} \frac{P}{bc} \left(\frac{\cosh(\omega x)(1 + \cosh(\omega c))}{\sinh(\omega c)} - \sinh(\omega x) \right) \quad (9)$$

In Figure 1.2-5, the obtained shear stress was plotted for a fixed bondline length of 20 mm and k_u/k_a (representing the stiffness ratio) ranging from 0.005 to 0.5. For the curve corresponding to $k_u/k_a = 0.2$, the part in the middle does not transfer any shear stress. This result illustrates an important phenomenon related to bonding: the existence of a characteristic anchorage length also called effective bond length. The effective bond length corresponds to the length over which the majority of the bond stress is transferred.

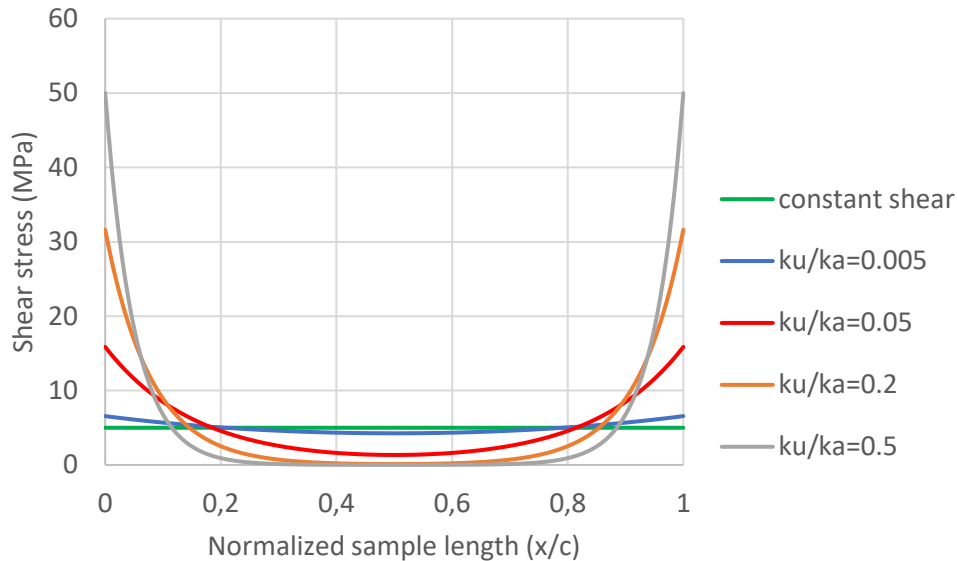


Figure 1.2-5: Shear stress along the bonded length according to Volkersen's theory for different values of k_u/k_a versus constant shear model.

In Figure 1.2-6, the obtained shear stress according to Volkersen's theory given by equation (8) was plotted for four different bonded lengths: 20 mm, 50 mm, 250 mm and 1 000 mm and for the following geometry and properties: $t_u = t_l = 20$ mm, $t_a = 1$ mm, $G_a = 2$ GPa, $E_u = E_l = 200$ GPa and $F = 1000$ N.. We can observe for the curve with $c \geq 250$ mm that any shear stress is transferred in the middle of the bondline. It is the same phenomenon as described in the previous paragraph. In addition, it can be noted that the ultimate shear values are obtained at the edges. For a given applied load level, it can be stated that once the bonded length is greater than the characteristic anchorage length (250mm), those values do not decrease anymore.

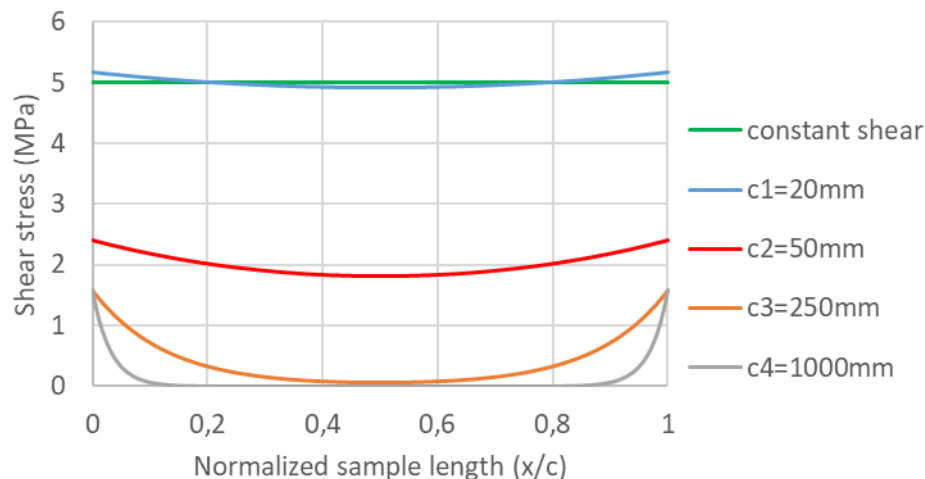


Figure 1.2-6: Shear stress along the bonded length according to Volkersen's theory for different bonded length versus constant shear model.

The characteristic anchorage length expresses the fact that, in the condition of validity of the model (the adhesive is assumed to have linear elastic behavior), above a long enough length (depending on the material properties), the ultimate strength and the overlap length are independent (Figure 1.2-7). Therefore, the presence of a bond defect outside the area of characteristic anchorage length should not induce a reduction of the ultimate strength of the bonding.

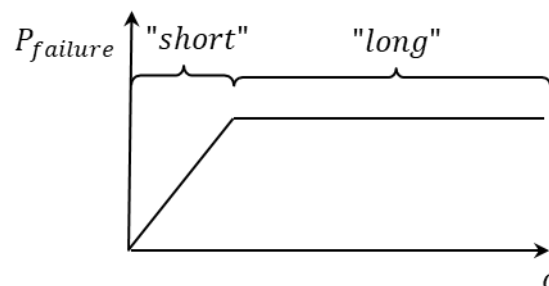


Figure 1.2-7: Typical relation between ultimate capacity and overlap length [18].

The model of Volkersen allows an easy understanding of the main phenomenon related to the use of bonded joints. However, it has some problems inducing restrictions in its use. The main issue with the theory of Volkersen is that the eccentricity of the loads is neglected. In that case, bending moments in the adherents is introduced, and thus peel stresses in the adhesive, that may cause premature damage. The Volkersen model cannot predict this phenomenon. Additionally, this model is limited to linear material, whereas a large range of bonded joints uses nonlinear adhesives. Finally, it is interesting to note that the model proposed by Volkersen does not fulfill the generalized beam theory free edge null shear strain fundamental assumption [19].

1.2.1.3. Goland and Reissner approach

To improve the Volkersen model on the stress analysis of bonded joints, Goland & Reissner [20] [21] proposed another approach, based on plates theory, to express the stress state along the bondline for linear elastic material, including the effect of the bending of the adherent resulting in shear and peel stresses along the bonded length (Figure 1.2-8). Their analysis was only developed for the case of balanced joints (similar top and bottom adherends).

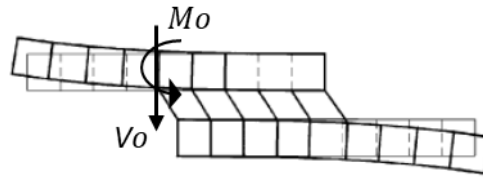


Figure 1.2-8: Deformed state of a single lap joint in the case of the Goland and Reissner model [22].

The single lap joint problem defined by Goland & Reissner is divided into two different studies:
 - the analysis of the bending moment and the rotation of the adherents out of the bonded area, following the plate theory;
 - the analysis of the bonded area.

The stress in the assembly of the Goland & Reissner model can be summarized into two free-body-diagram of infinitesimal section of the joint, and adherent (Figure 1.2-9, Figure 1.2-10).

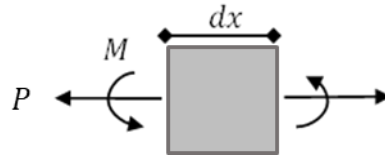


Figure 1.2-9: Infinitesimal free-body-diagram of the Goland & Reissner model in the adherent out of the bonded area.

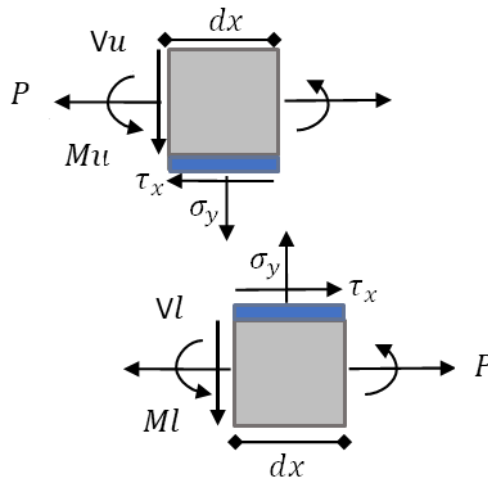


Figure 1.2-10: Infinitesimal free-body-diagram of the Goland & Reissner model in the joint.

For the adherent (out of the bonded area) under bending load, two sets of differential equations can be obtained using the plate theory and the Hooke's law stress/strain: equations (10), (11) and (12).

$$\frac{d^3 \tau(x)}{dx^3} = \frac{8G_a t_u}{E t_a} \frac{d\tau(x)}{dx} \quad (10)$$

$$\frac{d^2 \tau(x)}{dx^2} = \frac{E_a}{t_u} \frac{M_l - M_u}{R} \quad (11)$$

$$\frac{d^4 \sigma_y(x)}{dx^4} = -\frac{E_a \sigma_y}{t_u R} \quad (12)$$

With M_u is the applied bending moment to the upper adherent, M_l is the applied bending moment to the lower adherent, σ_y is the normal stress in the adhesive, t_u the thickness of the adherent, t_a the thickness of the adhesive, E the Young modulus of the adherents, E_a the Young modulus of the adhesive, R the flexural rigidity of the adherend and G_a the shear modulus of the adhesive.

The following boundary conditions are considered: equations (13) and (14).

$$\text{at } x = c, M_u = V_u = 0 \text{ and } M_l = M_o, V_l = V_o \quad (13)$$

$$\text{at } x = 0, M_l = V_l = 0 \text{ and } M_u = -M_o, V_u = V_o \quad (14)$$

M_o and V_o are respectively the bending moment and the shearing force at the joint edge defined by:

$$M_o = k \frac{F t_u}{2} \quad (15)$$

$$\text{and } V_o = kF \sqrt{\frac{3(1-\nu^2)F}{t_u E}} \quad (16)$$

Where F is the applied tensile load per unit width ($F = P/b$) and k is the bending moment factor expressed as:

$$k = \frac{\cosh \Lambda}{\cosh \Lambda + 2\sqrt{2} \sinh \Lambda} \quad (17)$$

$$\text{with } \Lambda = \frac{C}{2t_u} \sqrt{\frac{3F(1-\nu^2)}{2t_u E}} \quad (18)$$

In the above equations, b corresponds to the width of the bondline and $c/2$ to the distance from the middle of the bondline to the extremity of the bonded joint (half the overlap length).

With ν the Poisson coefficient of the adherent, b the width, $c/2$ the distance from the middle of the bondline to the extremity of the bonded joint (half the overlap length).

For the overlap region, the authors obtained two equations, one for the adhesive shear stress (equation 19), and another one for peel stress distributions (equation 22).

Adhesive shear stress distribution:

$$\frac{\tau(x)}{\tau_s} = -\frac{1}{8} \left[(1 + 3k) \frac{\delta}{\sinh(\delta)} \left(\cosh \frac{\delta x}{c} \right) + 3(1 - k) \right] \quad (19)$$

$$\text{With } \delta = \frac{c}{t_u} \sqrt{\frac{8G_a t_u}{Et_a}} \quad (20)$$

$$\text{With the average shear stress } \tau_s = \frac{2F}{c} \quad (21)$$

Adhesive peel stress distribution:

$$\frac{\sigma_y(x)}{Ft_u} \left(\frac{c}{2}\right)^2 = \frac{1}{\Delta} [A + B] \quad (22)$$

$$\text{With } A = \left(K_2 \lambda^2 \frac{k}{2} + \lambda k' \cosh(\lambda) \cos(\lambda) \right) \cosh\left(\lambda \frac{2x}{c}\right) \cos\left(\lambda \frac{2x}{c}\right) \quad (23)$$

$$\text{With } B = \left(K_1 \lambda^2 \frac{k}{2} + \lambda k' \sinh(\lambda) \sin(\lambda) \right) \sinh\left(\lambda \frac{2x}{c}\right) \sin\left(\lambda \frac{2x}{c}\right) \quad (24)$$

$$\text{With } K_2 = \sinh(\lambda) \cos(\lambda) - \cosh(\lambda) \sin(\lambda) \quad (25)$$

$$\text{With } K_1 = \cosh(\lambda) \sin(\lambda) + \sinh(\lambda) \cos(\lambda) \quad (26)$$

$$\text{With } \Delta = \frac{1}{2} (\sinh(2\lambda) + \sin(2\lambda)) \quad (27)$$

$$\text{With } \lambda = \frac{c}{2t_u} \sqrt[4]{\frac{6E_a t_u}{E_u t_a}} \quad (28)$$

$$\text{With } k' = \frac{V_0 c}{2Ft_u^3} = kF \sqrt{\frac{3(1-\nu^2)Ft_u}{E}} = \text{the transverse factor} \quad (29)$$

Compared to the models that have been discussed so far, the Goland & Reissner's model is the first to consider an important phenomenon that can cause the failure of a bonded assembly: the peel stress. The obtained shear profile is closed to the one from Volkersen. The peel is in tension at the edge and compression in the central part. It is much more complete than the previous model derived from the Volkersen's approach but remains limited to linear elastic adhesives. As it can be seen in Figure 1.2-11, the Goland & Reissner model predicts higher adhesive shear stresses at the end of the overlap, mainly because of the peel stresses that cause additional shear stress [17].

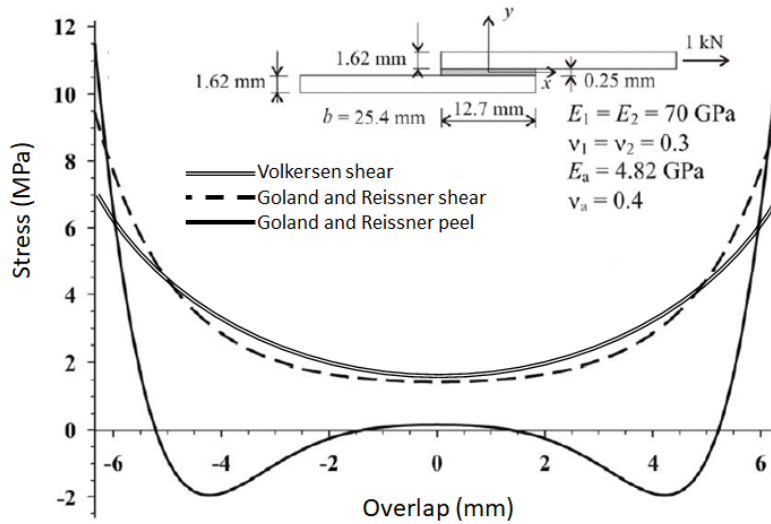


Figure 1.2-11: Stresses predicted by Volkersen and Goland & Reissner models [22].

The study of this model seems entirely appropriate in the case of application of bonded patches. However, a physical problem common to these analytical models (Volkersen and Goland and Reissner) is that they do not fulfill the zero-stress condition at the edges. This result can introduce error in the design of the ultimate capacity of bonded patches.

In addition, the limitation to linear elastic materials which may be not adapted for some structural adhesives.

1.2.1.4. Hart-smith approach

In 1973, Hart-Smith [18] proposed an improvement of the Volkersen's theory including the elasto-plastic (with perfect plasticity) behavior of the adhesive. As in Volkersen's model, the adhesive is supposed to remain in pure shear strain and the adherents in pure tensile strain. Historically, this development was carried out on symmetric double lap joints (Figure 1.2-12).

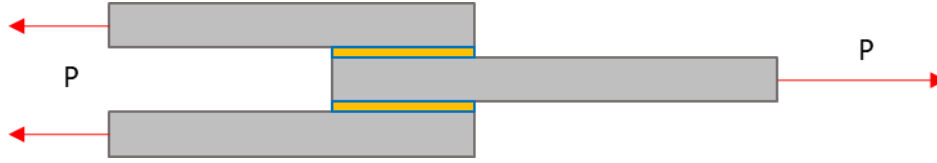


Figure 1.2-12: Application case of the Hart-Smith model.

Based on these assumptions and equilibrium, two differential nonlinear equations can be obtained:

- one specific equation for the shear stress in the elastic zone, which is the same than the one from Volkersen,
- another one for the adhesive shear strain, γ_p , in the plastic zone of length $(c - d)/2$, d being the elastic zone length.

As for the Volkersen's equation, the expression of the parameter ω remains similar (equation 30).

$$\omega = \sqrt{\frac{G_a}{t_a} \left(\frac{1}{t_l E_l} + \frac{1}{t_u E_u} \right)} \quad (30)$$

$$\gamma(\xi) = \left(\frac{\omega^2}{2G_a} \right) \tau_p \xi^2 + C\xi + H \quad (31)$$

$$\xi = x - \frac{d}{2} \quad (32)$$

$$C = \frac{\omega \tau_p}{G_a} \tanh \left(\frac{\omega d}{2} \right) \quad (33)$$

$$H = \frac{\tau_p}{G_a} = \gamma_e \quad (34)$$

$$\gamma_e = \gamma \text{ at } x = \frac{d}{2}, \quad (35)$$

With γ_e the adhesive elastic shear strain at yield, γ_p the plastic part of the shear strain and τ_p the adhesive yield shear stress (Figure 1.2-13).

The strain continuity condition and the overall force equilibrium allow obtaining two equations that need to be solved to get access to the final shear stress state (equations 36 and 38).

$$\left(\omega \frac{(c-d)}{2} \tanh \left(\frac{\omega d}{2} \right) \right)^2 = \tanh^2 \left(\frac{\omega d}{2} \right) + 2 \frac{\gamma_p}{\gamma_e} \quad (36)$$

$$\gamma_e + \gamma_p = \gamma \left(\xi = \frac{c-d}{2} \right). \quad (37)$$

$$\frac{\tau(x)}{\tau_p} = \left(1 - \frac{d}{c} \right) + \frac{\tanh \left(\frac{\omega d}{2} \right)}{\frac{\omega c}{2}} \quad (38)$$

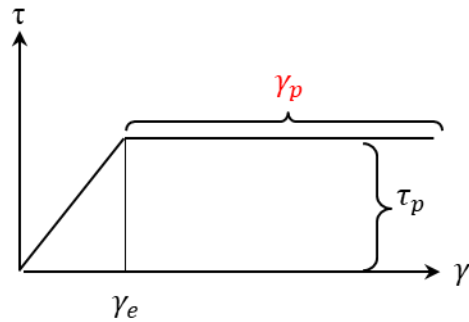


Figure 1.2-13: Perfect plastic law of the adhesive.

A common shape of the typical solutions for the shear stress along the lap length is described in Figure 1.2-14.

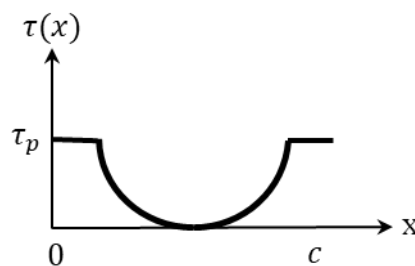


Figure 1.2-14: Hart-Smith's shear stress distribution.

The plateau corresponds to the plasticity around the edges of the bondline. The Hart-Smith model solved the main problem of the Volkersen and Goland & Reissner one, as it accounts for the plastic reduction of stresses around the free edges (Figure 1.2-15).

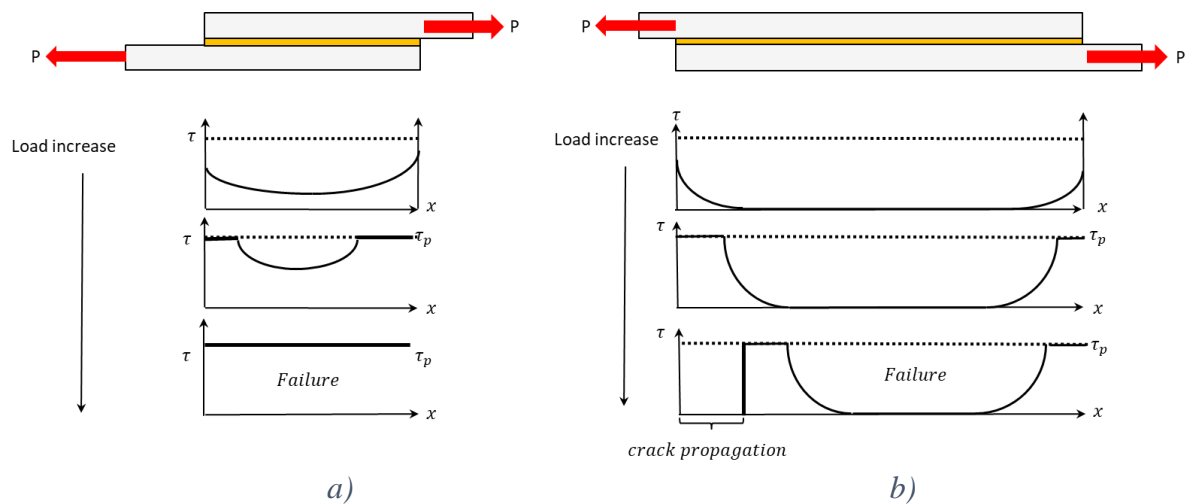


Figure 1.2-15: Relation between the overlap length and the adhesive shear stress distributions for Hart-Smith model, for a) short overlap and b) long overlap.

Considering a longer bondline, the behavior is different as described on Figure 1.2-15a and b. For a low load level, the response is elastic within the bonded length. With the load increase, the yield stress is reached at one end first and a plastic zone starts to develop before the second end reaches the yield stress. Then, the plastic zone will develop on each side of the assembly. As the plastic zone continues to grow, the adhesive strain increases at the edges up to a maximal

allowable strain value and a crack initiate near the border of the overlap. If the load remains constant, the crack propagates and leads to failure. It can thus be observed that above a certain length, the ultimate strength and the overlap length are independent (Figure 1.2-16). Any bond defect in the center area (adhesion, material defect), where the stresses are equal to zero, should therefore have a limited impact on the overall strength of the patch [18].

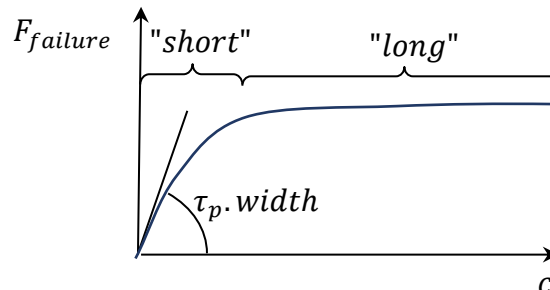


Figure 1.2-16: Scheme presenting the relationship between the ultimate capacity and the bonded length.

1.2.1.5. Summary of the analytical models

The models described in the previous parts represent the main analytical approaches used for the study of mechanical states in bonded assemblies. Others have been developed with the aim of increasing the representativeness of analytical models for other types of applications or solicitations. The state of the art realized by Da Silva et al. in [17] and Gleich in [25] proposed a synthesis of those existing analytical models on the basis of the materials behavior (adhesive and adherents), the resolution method and the obtained physical quantities. From this review, it is important to note that in most cases there exists a specific length called the characteristic anchorage length that is necessary to transfer the stresses through the bonded joint. This parameter must be considered during the design. It is also important to be aware that in the case of structural adhesives, the adhesive rigidity effect cannot be neglected. In that case, shear and peel stress concentrations arise at the assembly edges.

Several limits exist to the application of those models, the main ones being the inadequacy with more complex geometries, especially at the edges [26], the hypotheses of linear behavior and the absence of peel stress computation. To overcome these issues, numerical approaches have been developed to determine the internal mechanical stress state either in the adhesive or at the interfaces.

1.2.2. Models based on numerical approaches

Before to present numerical approaches, the first paragraph will be dedicated to the presentation of the singularity difficulty associated with the analysis of such assembly. Then, three numerical approaches will be detailed presenting some examples of their applications for the study of adhesively bonded joint: the finite element approach, the discrete element approach and the M4 models.

1.2.2.1. Singularities

In the case of adhesive bonding, there is a numerical difficulty due to the mathematical singularities at the joint edges either due to the geometry or due to the presence of two materials with different rigidity. This depends on the edge treatments. Some commonly encountered ones are presented in Figure 1.2-17 indicating the presence of geometrical singularity (blue circles). Singularity refers to a point where, in linear elastic analysis, stress will reach an infinite value. This induces a high dependence of the obtained maximum stress values with mesh refinement.

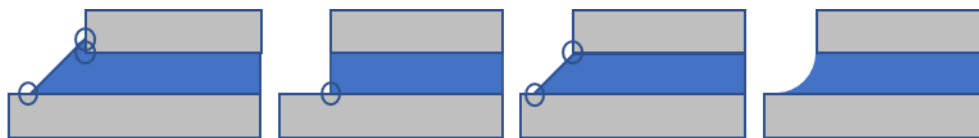


Figure 1.2-17: Bonded joint possible singularities.

To overcome this problem, adding a fillet of adhesive at the edge of the joint can help to reduce its impact. Such fillet exists naturally in most of the realized joint [26]. It was shown that the maximal stress value is dependent on the shape of this fillet. This effect was experimentally studied by Zhao et al. [28] for a ductile and a brittle adhesive. The main formulated conclusions are the following ones:

- joints bonded with a brittle adhesive are highly affected by the presence of a fillet and by its shape,
- joints bonded with a ductile adhesive present a better strength for sharp corners joints, when compared with round corner, indicating a lower sensibility to singularity.

1.2.2.2. Finite element method

Currently, the mostly used approach is the finite element method (FEM). It consists in a numerical method using an iterative algorithm allowing to search for an approximate solution of a partial differential equation $U'' = f$ on a compact discretized domain with boundary conditions. This method has been applied to adhesively bonded joints with success, depending on the application case. L. Mouton in [28] showed accurate maximal strength prediction for a single lap bonded tri-material (polyurethane/epoxy/steel) patch with FEM. You et al. [29] used an elasto-plastic finite element analysis and experimental investigations to study the effects of chamfer on the ultimate capacity of adhesively bonded steel single lap joints. The results showed that all the maximum stresses in the bondline were reduced with the increase of the chamfer angle. Additional review of the application of FEM on adhesively bonded joints have also been made by Xiaocong et al. in [30].

To summarize, FEM is particularly adapted for the computation of stresses and strains for complex geometries. There exist however some limitations in the case of adhesively bonded joint application:

- the thickness ratio within the adherents and the center to edge length requires a fine mesh in these areas. Consequently, the number of degrees of freedom necessary to model a joint is generally high [31],
- the singularity locations, where the stress value increases with the mesh refinement, inhibits the convergence towards a solution. Therefore, this analysis should be used with care,
- those refined FEM tend to take a lot of time to compute, especially in the case of multiple supposed crack propagation path.

1.2.2.3. Finite difference method

The finite difference method (FDM) is actually a way to solve a system of by approximating derivatives with finite differences. A series of equations, which can be numerically solved with matrix methods, are then created. It allows considering more complex boundary condition than with the closed-form solution.

This method implies determining the equations (an analytical model with assumptions) previously to the numerical calculations [32] [33].

This can be particularly adapted in the case of more complex geometries joint (tapered lap joint, scarf joint). The differential equations become more complex and the analytical solutions tend to become impossible to derive. The finite difference method (FDM) replaces the continuous variables in the differential equations by approximations. A series of equations, which can be numerically solved with matrix methods, are then created. It allows considering more complex boundary conditions than with the closed-form solution.

FDM has been used a lot before the massive development of commercial finite element software for the study of adhesively bonded joints. Thus, Bigwood et al. [34] compared the obtained stress profiles, in the case of a single lap joint, for both finite element and finite difference methods, and showed a good correlation.

To summarize, FDM seems to be highly relevant when a similar case is repeatedly encountered. In that case, it may limit computation time while accessing accurate results. It cannot however give access to very local information as FEM.

1.2.2.4. M4 model

M4 models stands for Multiparticle Models of Multilayered Materials and was specifically developed to analyze edge stress fields at interfaces in the case of road pavement structures or composite layered structures [35]. It consists in simplifying the mechanical problems in layers and interfaces (Figure 1.2-18). Several versions of the M4 model exist depending on the kinematics hypotheses, the most famous one being the one developed by Pagano [36]. The construction of those models relies on four main steps:

- a polynomial approximation of the 3D stress fields in the thickness direction in each layer of the studied structure is carried out. This allows expressing forces, moments and shear internal forces for each layer, and shear and normal stresses at the interfaces,
- the associated generalized displacement fields are then approximated using the Hellinger-Reissner functional,
- the equations of equilibrium on the generalized internal forces and the boundary conditions for each layer allow obtaining the equations linking the internal forces with the interface stresses,
- finally, the constitutive equations are used to express the internal forces and interface stresses in function of the compliance of the materials.

Such an approach has been used in the case of adhesively bonded joints with elastic interface [37] or elasto-plastic interface [38]. Good results were obtained and a comparison with finite element approaches showed that, provided a refined mesh (in the width and length only, as there is no mesh in the thickness) was used and that the order of the M4 model was sufficient, a good correlation could be found.

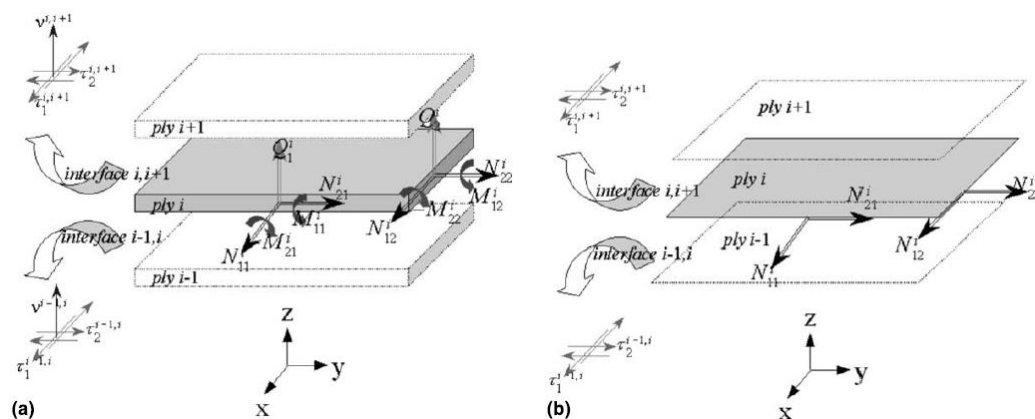


Figure 1.2-18: Schemes of the M4 approaches.

In conclusion on the numerical strategies review, it may be highlighted that, in the special case of bonded patch, special design with possible overlapping chamfer which allows optimized reduction of shear stresses at the interface and at the edge, the choice of the numerical strategy may be limited to the finite element method. However, cautions must be taken regarding the maximum stress values and their dependency with mesh size.

1.3. Design approach and failure prediction

There are few reliable failure criteria for bonded joints, and they generally depend on the application case. However, an accurate prediction of the strength of bonded joints is essential to reduce the number of costly tests at the design stage. Currently used approaches for predicting the strength of adhesively bonded joints are: the continuum mechanics approach (stress and strain based), fracture mechanics, and damage mechanics approach [31]. These approaches will be presented in more details in next paragraphs.

1.3.1. Continuum mechanics approach

Using the continuum mechanics hypothesis (material continuity), several authors got interested in critical stress or strain approaches. Of course, such approach is strongly related with the choice of the method used to determine those stresses or strains.

1.3.1.1. Critical stress approach

Initially, the critical stress approach was proposed for very brittle adhesive (linear elastic material) whose failure depends on the direction of maximum principal stresses [22]. With this approach, in the case of bonded joint, the maximal stresses are determined in the adherent, in the adhesive or close to the interfaces (depending on the observed failure mode) and then the values are compared to the maximal allowable ones.

Maximal shear stress has been widely used to predict ultimate joint strength (using closed-form analyses) under shear loading, considering the maximum allowable shear stress equal to the bulk adhesive shear strength. In a study led on single-lap joints, Da Silva et al. [39] have used the maximal shear stress determined with the Goland and Reissner model as a criterion. They showed that this criterion is only valid for brittle adhesives and for short overlaps. More recently, some designs based on such criteria have been done for the development of bonded

application, with low modulus thick adhesive and limited stress concentration, and showed good results [28]. Though the approach seems to be rather simple, some limitations may exist, especially the fact that the peel stress is ignored.

Mixed stress criteria have thus been developed to express the maximal allowable stress state considering multiaxial stress state.

Some studies have been made following standard continuous mechanics approach using the Von Mises yield criterion for an application case of GFRP scarf joint on steel [40]. The stress and strain distributions were obtained using elastic finite element analysis. It is important to note that the Von Mises stress is not dependent upon hydrostatic pressure part ($\sum_{i=1}^3 \sigma_{ii}/3$) of the stress tensor though this has a great influence on the adhesive's behavior [41].

The CIRIA Guideline (RP 645) and CNR Guideline (CNR_DT202) proposed therefore criteria expressions relying on the simplified Mohr's principal stress definition (Mohr circle), equations (39) and (40).

$$\frac{\sigma_x + \sigma_y}{2} + \sqrt{\frac{(\sigma_x - \sigma_y)^2}{4} + \tau_{xy}^2} \leq \frac{\sigma_p}{2} + \sqrt{\frac{\sigma_p^2}{4} + \tau_p^2} \quad (39)$$

$$\frac{\sigma_y^2}{2} + \sqrt{\frac{\sigma_y^2}{4} + \tau_{xy}^2} \leq \frac{F_{ak}}{\gamma_a \cdot \gamma_{rd}} \cdot \eta \quad (40)$$

With σ_x being the loading direction stress, σ_y being the normal direction stress, τ_{xy} the shear stress, τ_p being the adhesive yield shear stress and σ_p being the adhesive normal yield stress, F_{ak} the adhesive resistance evaluated through ISO standard single lap shear test, γ_a , γ_{rd} two parameters ("partial factors") taking into account the conditions of the bonding (quality of the application and type of loading) and η a compensating parameter depending of the type of loading and type of composite used.

In the particular case where σ_y is negative, the overall value of the criteria will be superior to traction case. This expresses well that bonding under compression and shear sustains higher load than in traction and shear.

As already mentioned, for the finite element approach, the encountered singularity at the edges may prevent from obtaining mesh independent stress values at those locations. Alternative methods have also been proposed to use an effective stress at a certain distance of the edge to limit the impact of the singularity.

1.3.1.2. Stress at distance

To overcome stress singularity, John et al. [42] used a critical distance combined with shear stresses to predict the maximal strength under linear elastic behavior. The main conclusion of these results is a global overestimation of the maximal strength of the bonding. This overestimation makes this criterion unusable in case of bonded patches with scarf design. Similarly, Crocombe [43] used a critical peel stress at a distance from the singularity with some success and concluded that the critical distance at which the criterion must be applied varies with the loading, since the type of loading will have an influence on the size of the plastic zone.

1.3.1.3. Critical strain approach

For the study of more ductile adhesives, stress criteria are not appropriate anymore (failure is governed by strain). Hart-Smith [18] proposed the use of the maximum shear strain as a failure criterion. The main limitation of this approach is the necessity to determine the plastic strain. Another analysis has been proposed by Adams & Harris in 1984 [45], which studies the use of maximum principal strain in the adhesive for aluminum plate bonded with different epoxies in single lap joint. The main advantage of this criterion is the ability, following the direction of the maximal principal strain, to predict the failure mode.

1.3.1.4. Critical plastic strain and energy density criteria

Critical plastic strain is a concept closed to the total strain energy criterion that states that failure (by yielding or by fracture) would occur when the total strain energy, or total strain energy density, reaches a critical value. The critical strain energy density U_t is generally expressed in cartesian coordinates by equation (41) [45].

$$U_t = \frac{1}{2} (\sigma_{xx}\epsilon_{xx} + \sigma_{yy}\epsilon_{yy} + \sigma_{zz}\epsilon_{zz} + \tau_{xy}\gamma_{xy} + \tau_{xz}\tau_{xz} + \tau_{yz}\tau_{yz}) \quad (41)$$

The critical plastic strain is restricting the analysis only to the plastic part of the strain ($\epsilon_{total} = \epsilon_{elastic} + \epsilon_{plastic}$). This approach has been used by Adams and Harris [26] as a failure criterion. This concept is closed to the critical plastic length proposed in [41]. Zhao et al. [27] also applied this criterion combined with a distance from the free edge to express a maximal allowable energy plastic density before the failure of the assembly. The advantage of the use of an energy density is the limited sensitivity to the mesh size. It is common knowledge that the accuracy of the Finite Element (FE) approach is more reliable when it is interpreted as an average, rather than in a local sense [22]. Using this criterion, Zhao et al. [27] used the adhesive thickness as an integration zone for the energy density computation of ductile adhesives. The main issue with this approach is an experimental issue, and is related to the difficulties to measure the plastic strain in samples especially for low thicknesses.

All the above criteria are applicable to continuous structures. When discontinuity such as crack occurs, it becomes necessary to define new criteria based on fracture mechanic approach.

1.3.2. Fracture mechanics

The Linear Elastic Fracture Mechanics (LEFM) is interested in the study of cracks in linear elastic isotropic materials. It assumes that its propagation is associated with 3 main modes: mode I that corresponds to opening effect, mode II that corresponds to in-plane shear effect, and mode III that corresponds to out-of-plane shear (Figure 1.3-1).

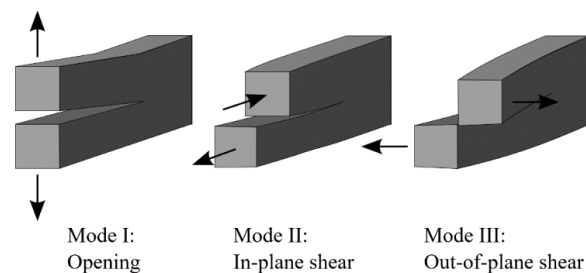


Figure 1.3-1: The three modes of loading of a crack.

The LEFM is valid when inelastic strains are small compared to the size of the crack. If large plastic strains are expected, the Non-Linear Fracture Mechanics (NLFM) might be used [46]. Two main approaches can be detailed in the LEFM:

- the direct method: the stress state around the crack tip is determined using the stress intensity factor K_i ($i = I, II, III$ regarding the loading mode of the crack). The stresses are defined, depending on the geometry and loading. In the case of bi-material joint, Golio et al. [47] showed the difficulties to define the amplitude of the singular field around the crack tip. Even more difficulties can be expected in the case of multiple material bonded joint with thin bondline,
- the energetical approach: this approach is based on the Griffith's theory and will be discussed in the following paragraph.

1.3.2.1. Griffith's theory

The fracture mechanics approach proposes to define the crack propagation by quantifying the energy released by an increment of crack length da (Figure 1.3-2). In 1920, Griffith [48] proposed an energy balance to explain crack propagation in the case of a linear elastic material under static load. In the vicinity of an equilibrium position, to allow the propagation of the crack, the energy released for an increment of crack extension ($b \cdot da$), $G(a)$, is equal to the variation of stored elastic energy (U) (red and blue triangles in Figure 1.3-2 represent the unloaded area before and after crack propagation) and the work of the boundary/external loads (F) for an increment of crack length (see equation (42)). The difference between the stored elastic energy and the work of the boundary load is noted $\Pi = U - F$.

$$G(a) = - \frac{d(U - F)}{b da} \quad (42)$$

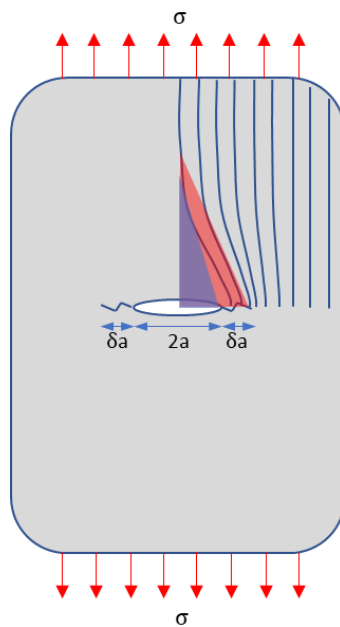


Figure 1.3-2: Energy released with the crack propagation.

Two cases can then be described for linear elasticity (Figure 1.3-3).

- In the case of a prescribed load, with Δ the general displacement at the loaded point:

$$F = P\Delta, U = \frac{P\Delta}{2} \rightarrow G(a) = - \frac{1}{b} \left(\frac{d\Pi}{da} \right)_P = \frac{P}{2b} \left(\frac{d\Delta}{da} \right)_P \quad (43)$$

The crack extension da results in a net increase in strain energy.

- For a fixed displacement:

$$F = 0, U = \frac{P\Delta}{2} \rightarrow G(a) = -\frac{1}{b} \left(\frac{dU}{da} \right)_{\Delta} = -\frac{\Delta}{2b} \left(\frac{dP}{da} \right)_{\Delta} \quad (44)$$

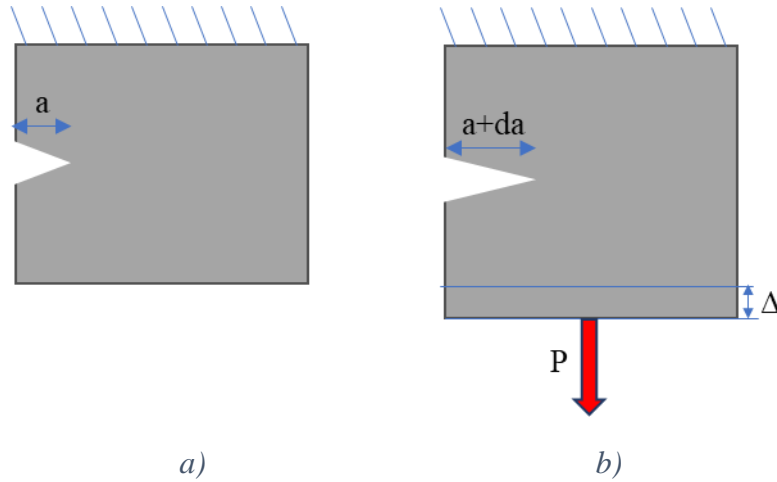


Figure 1.3-3: a) Cracked plate at initial state, b) Cracked plate after fixed displacement Δ or fixed loading P .

Thus, $U - F = -\frac{P\Delta}{2}$ for the fixed load case, or $U - F = \frac{P\Delta}{2}$ in fixed displacement case.

The energy release rate (ERR) can then be calculated using equation (45).

$$G(a) = \frac{1}{2b} \frac{d(\pm P(a)\Delta(a))}{da} = \frac{P^2}{2b} \frac{dC}{da} \quad (\text{Irwin-Kies equation [45]}) \quad (45)$$

With C the compliance ($C=\Delta/P$).

In case of nonlinear materials, if the non-linearity is confined to a small region near the crack tip (Small Scale Yielding assumption), the LEFM may be applied [41].

In conclusion, the propagation of an internal defect (such as crack) will occur when the available energy at the defect tip (G) equals the energy needed for the crack to propagate (G_c , the critical energy release rate, or critical toughness). The value G_c is directly linked to the material, type of failure (cohesive or adhesive) and the mode of loading. Many energetic failure criteria can be found in the literature for the combination of modes. Yet, using simple elastic hypotheses, it may be possible to have access to the value of G_c using the applied load and resulting displacement. However, the measurement of the crack propagation is, in most cases, a pre-requisite. This approach has one main limitation. To be used, a pre-crack must be specified to allow computing the energy release rate when the crack propagates from a to $a + da$.

1.3.2.2. J-integral

In 1967, Cherepanov [50] and Rice [51] developed a new method based on the determination of an energy flow through a surface. The concept of the J-integral is based on the independency of an energetic contour path integral with the path located around the crack tips for homogeneous elastic materials. The direct mathematical expression of the J-integral in 2D is given in equation (46). The coordinate system as well as an example of a contour path can be seen in Figure 1.3-4. The first term in the integral represents the elastic strain energy while the second term represents the work done by external loads on the outline.

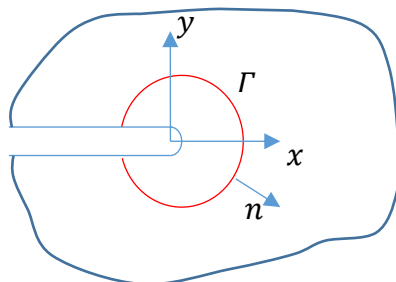


Figure 1.3-4: J-integral contour path Γ around a crack tip in two dimensions.

$$J = \int_{\Gamma} w(\varepsilon) dy - \sigma_{ij} \cdot n \frac{du_i}{dx} d\Gamma \quad (46)$$

With $w(\varepsilon)$, the strain energy density, σ_{ij} , the stress tensor, u_i the displacement vector, Γ the contour path and n the vector normal to the contour path.

The following main properties must be mentioned:

- the J-integral is independent of the contour path (as long as the contour embeds the crack tip),
- the path goes in the counter-clockwise direction from the lower crack surface to the upper crack surface,
- the crack must not be loaded.

The J-integral represents the energy release rate if the crack grows straight ahead (for planar crack grows) [52] [53]. In the case of elasto-plastic materials, Rice showed that if monotonic loading is assumed (with no crack propagation) then the J-integral can also be used to compute the critical energy release rate ($J_c = G_c$). Some good results have been found with the use of the J-integral method. Choupani [54] used it to determine the critical toughness G_c with J-integral approach in the case of thick adhesive and adhesive failure with Arcan test.

1.3.2.3. Mixed mode criteria

The physical quantities used to characterize the bonded joints often refer to the critical energy release rate (G_c) which has been abundantly used to characterize and predict failure of bonded joints [55], [56].

In design, some references consider only the mode I (DNV ST0376) indicating it is the worst-case situation and the most common type of failure.

For the studied application, the loading is mainly in shear. Therefore, the study of the fracture in only mode I should not be sufficient, and special attention should be provided to the effect of mode II. The necessity to define a fracture criterion that correctly establishes the fracture

toughness (G_c) in mixed mode is related to the incapacity to test every mixed-mode combination. Several mixed mode failure criteria have been used in the literature [54]. In the case of adhesively bonded joint, the most commonly used criteria are the Power law criterion [58] (equation 47) and the B-K criterion [59] (equation 48).

$$\text{The power law criterion: } \left(\frac{G_I(a)}{G_{Ic}}\right)^\alpha + \left(\frac{G_{II}(a)}{G_{IIc}}\right)^\beta \geq 1 \quad (47)$$

$$\text{The B-K criterion: } G(a) \geq G_{Ic} + (G_{IIc} - G_{Ic}) \left(\frac{G_{II}(a)}{G(a)}\right)^\eta \quad (48)$$

where G_{Ic} is the critical strain energy release rate in pure mode I, G_{IIc} is the critical strain energy release rate in pure mode II and α , β , η being values that are numerically fitted to the experimental data.

1.3.3. Coupled stress-energy method

The principle of the coupled criteria approach is to compensate the major problems of the main criteria of continuous and fracture mechanics applied to bonded area.

For continuous mechanics, the critical stress approach is relevant to express the mechanical state of materials following the conditions of the continuous mechanics. However, it is generally inefficient to express this state around geometrical singularity. The definition of a criteria following these values will systematically lead to an error on crack initiation prediction. For fracture mechanics, the definition of the critical value, that allows the propagation of a crack through the materials, cannot be applied to an uncracked assembly (fracture mechanics theory assumption). As defined by Leguillon [60], these two criteria are expressing a paradox, as the first one is nearly always fulfilled because of the stress concentration and the other cannot. Moreover, generally none of those criteria matches the results obtained from the experiment. The experiments of Parvizi et al. [61] followed by the analysis of Leguillon [60] proposed an explanation to this paradox. They defined a special traction test that correlated the crack initiation with the applied load and the stress state. They have proved that, while the crack develops, the stress criterion is not relevant anymore to describe the crack propagation. They also proved that, when the crack is opened, the energy criterion governs the process and the stress criterion remains always fulfilled.

The main conclusions of their work are that a crack initiation will occur when those criteria are fulfilled simultaneously, and both are needed to express a predictive global criterion. The method is detailed step by step in the following parts.

1.3.3.1. Stress criteria

The direct application of part 1.3.1.1 allows defining different stress criteria, depending on the type of loading. The stress criterion is here expressed as a function f depending on the set-up and the level of load. It is expressed all along the bonded joint for each x positions.

For mode II:

$$f(x) = \frac{\tau_p}{\tau(x)} \quad (49)$$

For mode I:

$$f(x) = \frac{\sigma_p}{\sigma(x)}, \quad \sigma(x) > 0 \quad (50)$$

τ_p being the adhesive yield shear stress and σ_p being the adhesive yield stress.

Criteria fulfillment corresponds to the fact that the stress at location (x) is equal or greater than the allowable stress, leading to $f(x)$ being inferior or equal to 1.

For mixed mode I and II, similar approach as the one detailed in part 1.3.1 can be defined for stresses application. For example, a power law type criterion depending on shear and peel stress can be used, equation (51).

$$f(x) = \frac{1}{\sqrt{\left(\frac{\tau(x)}{\tau_p}\right)^2 + \left(\frac{\sigma(x)}{\sigma_p}\right)^2}} < 1 \quad (51)$$

Other criteria could also be used for the mixed mode, as the Von Mises yield criteria or the CIRIA criteria, described in part 1.3.1.1.

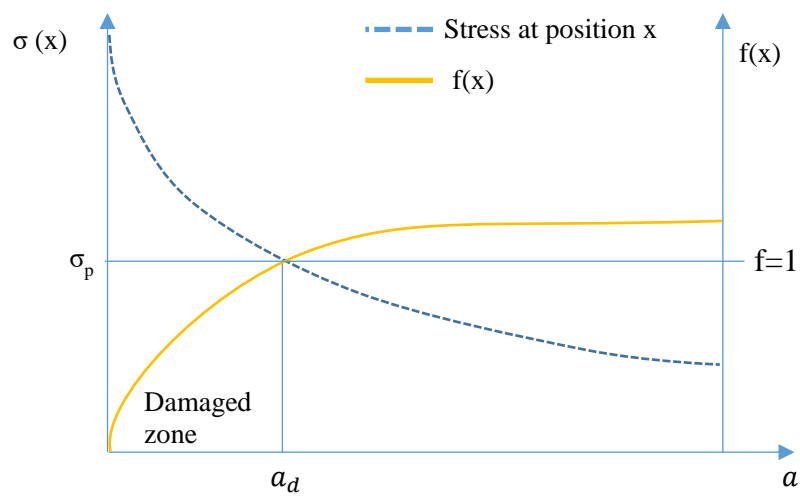


Figure 1.3-5: Typical analytical stress state and stress criteria curve.

On Figure 1.3-5, it can be seen that for a defined level of loading, all the area within $x =]0; a_d[$ experience stresses above the allowable limit. In this area the stress criterion is smaller than 1 corresponding to the damaged zone.

1.3.3.2. Energy criteria

The same kind of criteria can also be applied to the energetic analysis defined by a function h .

For mode I:

$$h(x) = \sqrt{\frac{G_{Ic}}{G_I(x)}} < 1 \quad (52)$$

$G_I(x)$ being the computation of the strain energy release rate in mode I.

For mode II:

$$h(x) = \sqrt{\frac{G_{IIc}}{G_{II}(x)}} < 1 \quad (53)$$

$G_{II}(x)$ being the computation of the strain energy release rate in mode II.

For mixed mode I and II, formulations detailed in previous part can be used, as for example, the Power law type criteria (equation (54)). Figure 1.3-6 presents an example of mixed mode criterion based on a power law. It can be seen that for a defined level of loading, all the area within $x =]0; a_c[$ has a lower energy level than the one required to have a crack propagation (the criterion is smaller than 1). Once the crack length is superior to this critical length, at this load level, the crack propagates.

$$h(x) = \frac{1}{\sqrt{\left(\frac{G_I(x)}{G_{Ic}}\right)^\alpha + \left(\frac{G_{II}(x)}{G_{IIc}}\right)^\alpha}} = 1 \quad (54)$$

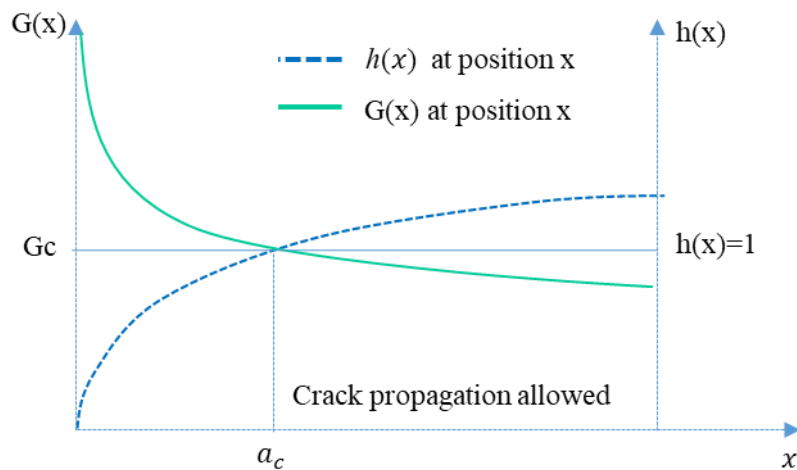


Figure 1.3-6: Energy release rate and energy criteria along the bonded length.

The use of this criterion allows defining a minimal allowable crack length before the crack propagates. Numerical modeling can be used to determine this energy for different crack lengths through the Crack Closure Technique (CCT) or Virtual Crack Closure Technique (VCCT).

In the crack closure method or technique, the crack is physically extended, or closed, during two complete finite element numerical steps. This approach is based on Irwin's crack closure integral [60] and on the assumption that the energy released $d\Pi$ when a crack is extended by a length da is identical to the energy required to close the crack around the crack tip. In the first step with a crack size a , the constraint forces at the crack tip will be retrieved. In the second step, the node at the crack tip will be separated and thus the crack size in the second model will be $a + da$. In the case of the VCCT, this step is automatically done. The displacements of the just separated nodes will then be retrieved in each direction, allowing to compute the energy release rate in each mode (Figure 1.3-7). In the case of the VCCT method, the determination of the internal forces necessary to keep the crack closed is carried out at the end of the second stage when the crack has propagated by the length da .

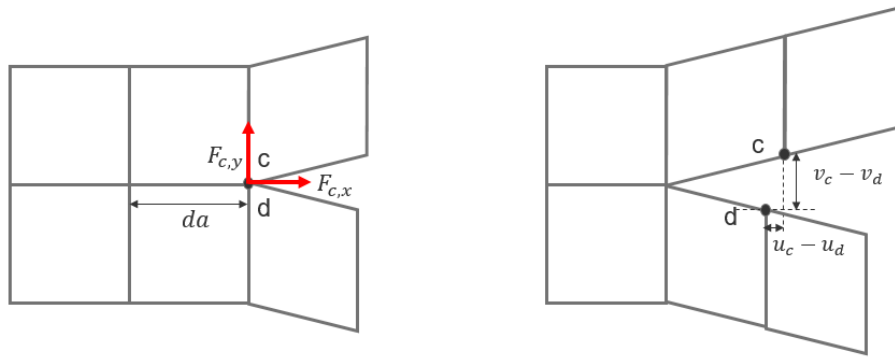


Figure 1.3-7: Two-steps VCCT overview.

Once these forces and displacements have been retrieved from the model, the total strain energy release rate as well as the contributions from mode I and mode II can be obtained by using the equation (55) [63].

$$G = \frac{1}{2\Delta_a} [F_{c,x}(u_c - u_d) + F_{c,y}(v_c - v_d)] = G_I + G_{II} \quad (55)$$

The first term corresponds to the mode II contribution and the second one corresponds to the mode I contribution.

1.3.3.3. Stress-energy criterion

For a given load level, the use of a coupled stress-energy criterion allows comparing the length of the damaged bonded joint, a_d (stress criteria), to the minimum crack length necessary for crack propagation, a_c (energy criteria). When the load is such that the crack length a_c equals the damaged length a_d , it corresponds to the critical load leading to failure (Figure 1.3-8).

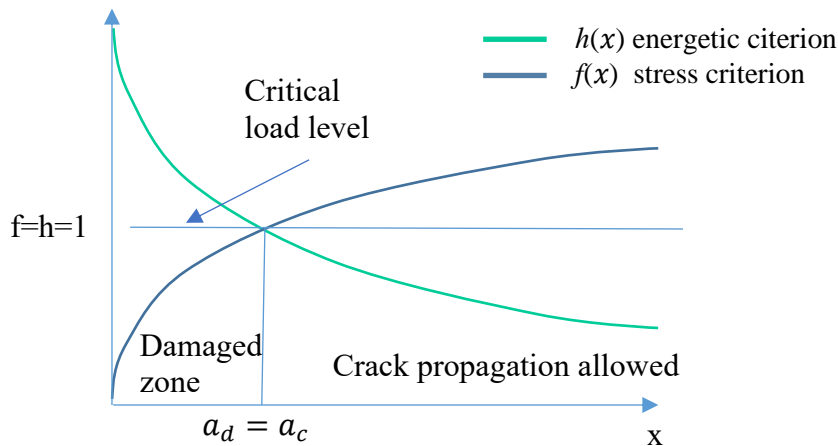


Figure 1.3-8: Coupled stress-energy criterion at critical load level (the extent of the damaged zone is equal to the minimum propagation of the crack).

The coupled approach requires several parameters to be characterized (τ_p , σ_p , G_{Ic} , G_{IIc}). It also requires the calculation of the energy release rate curve and the stress curve to completely define the criterion. However, it remains interesting as it both considers the uncracked structure state and its ability to sustain damages and cracks.

1.4. Damage mechanics and cohesive zone modeling

Some authors have proposed another approach that relies on the definition of an interfacial behavior and that combines both fracture mechanics and continuum mechanics failure criteria to overcome the main encountered difficulties and limits. It is called the Cohesive Zone Modeling (CZM). The CZM allows focusing only on the interface behavior (independently of the rest of the model) in order to simulate more precisely the behavior of the bonded joint and thus its resistance.

1.4.1. Description and concept

Historically, the first definition of a cohesive zone model has been proposed by Barenblatt [64], in 1962 and Dugdale [65] in 1960. This description was made to try to solve the problem of stress singularity around a crack tip in the case of brittle fracture mechanics to model the separation of atomic bonds at the tip of the crack.

These models assume that the damaged area in front of the crack (fracture process zone) can be described as an interface where the displacement field can admit discontinuities, while continuing to transmit load. This cohesive process area constitutes a transition zone between the undamaged material and the broken material where the damage can grow. Figure 1.4-1 shows the described zone and the resulting interfacial displacement.

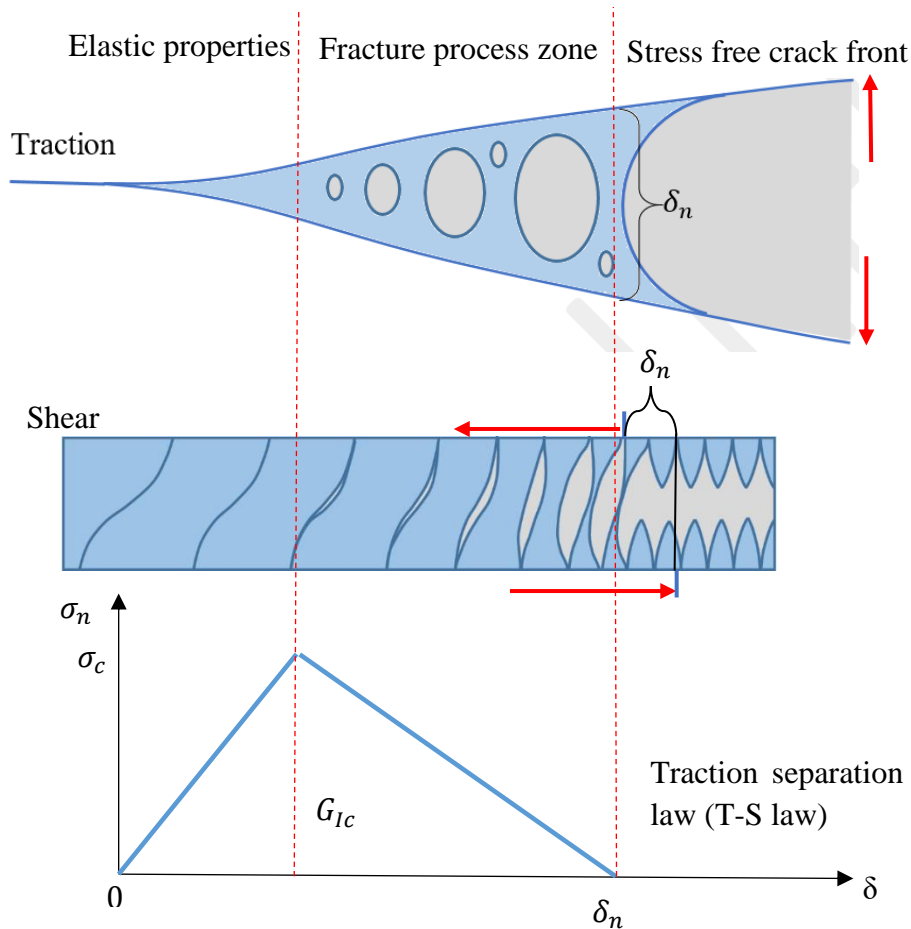


Figure 1.4-1: Representation of the fracture process zone and a bilinear cohesive zone law for mode I.

The cohesive zone model represents the cohesive stress versus the interface's relative displacement evolution. This corresponds to the traction separation law in mode I. The initiation of the damage is connected to the maximum values of the different stresses at the interface and to the creation of the process zone in the bondline. Damage then grows with interface's relative displacement. When the stored energy in the cohesive element is equal to the critical energy release rate of the material, the traction or shear forces are reduced to zero, and a crack front is created.

Hillerborg [66] introduced in 1976 a bilinear law with three main parameters expressing the interface law:

- σ_c the maximal material stress that the material can sustain,
- G_{Ic} the critical energy release rate, which is the energy needed for the separation of the interface,
- δ_n , the ultimate slip that the material can sustain before separation (for respectively peel and shear law).

Numerically, CZM laws are established between nodes of cohesive elements. Figure 1.4-2 presents the local displacement allowed by the cohesive law for each node at the interface (cohesive element) depending on the loading mode; δ_n for local opening (mode I), and δ_t for local sliding (mode II).

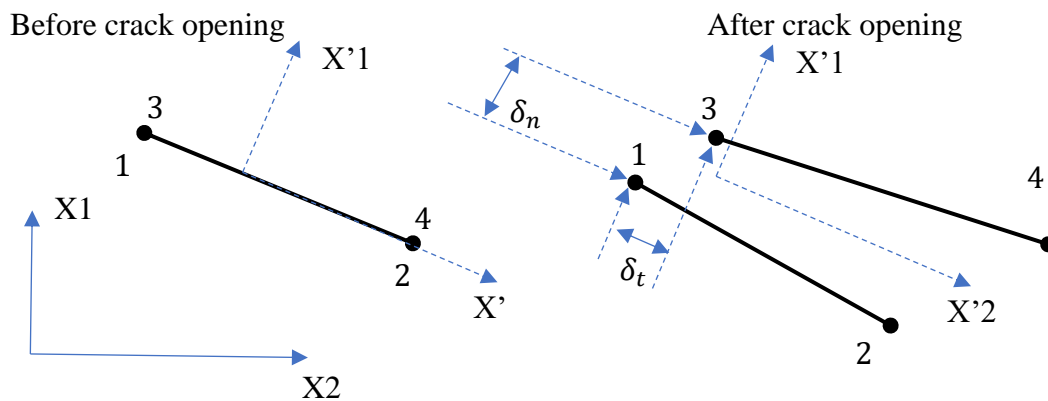


Figure 1.4-2: Four-node linear cohesive elements separation in FEM.

There are two options to define cohesive law between two materials:

- use the cohesive elements (with defined thickness) to represent the adhesive layer (Figure 1.4-3a),
- or represent the adhesive layer with volume elements and use interfacial cohesive element (with zero thickness) to model the interface's behavior (Figure 1.4-3b).

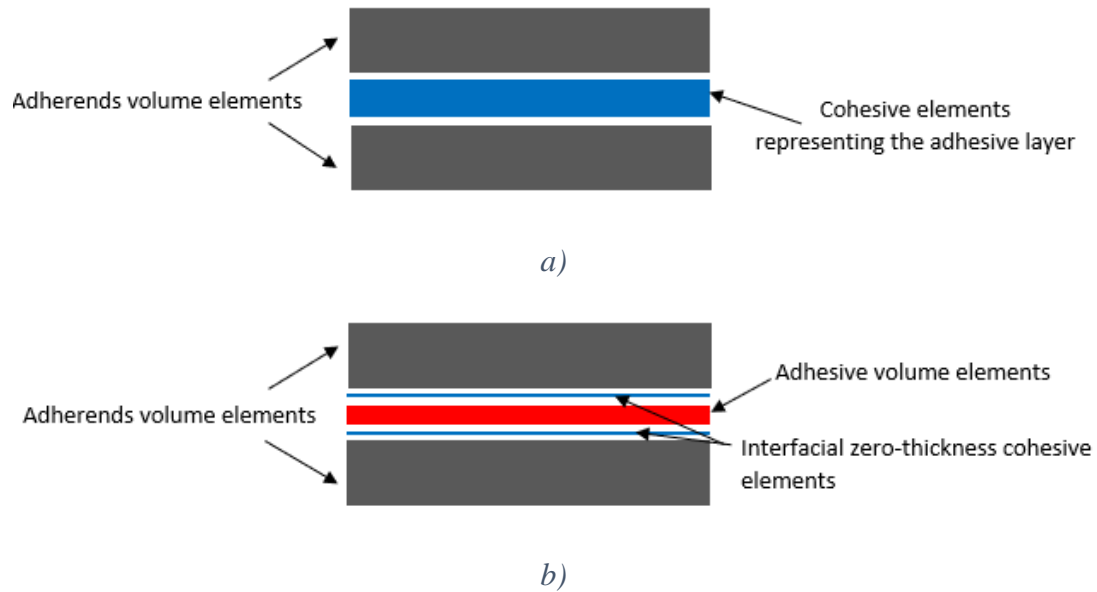


Figure 1.4-3: Models: a) with thick cohesive zone model representing the adhesive layer between the adherents, b) with zero thickness cohesive elements with adhesive volume elements.

Using the first methodology (cohesive elements with defined thickness), the elastic loading and the plastic dissipations of the adhesive bond are simulated by solid finite elements. In the case of highly ductile, or thick adhesive with cohesive failure, the introduction of 3D elasto-plastic element should be really efficient.

In this case, the stiffness of the interfacial cohesive elements can be defined as follows:

- stiffness in tension is given by (equation (56)):

$$k_I = \frac{ES}{t} \quad (56)$$

- shear stiffness is given by (equation (57)):

$$k_{II} = \frac{GS}{t} \quad (57)$$

With E , G being respectively the Young modulus and shear modulus of the material, S the surface of the element (distance between nodes 1 and 2 multiplied by width in Figure 1.4-2), and t its thickness. It is to be noted that these values are generally obtained through bulk test. However, in the case of thin bonded joint, tests such as Arcan test for multi axial properties, or TAST test for shear properties seem to be more appropriate to express the particular materials properties as described in [67].

A few works on CZM technique use the zero-thickness approach to model the bonded joint behaviour [68], [69]. This approach should be relevant in the case of thick bonded layer or multiple interfaces composites failure. In the other hand, Sorensen [70] and Yang [71] used the thick cohesive elements to accurately express the large plastic strain impact around the crack tip of ductile adhesive and to determine the resulting cohesive law without having to obtained directly G_c .

1.4.2. Cohesive law shape

The cohesive law shape contains information from underlying physical processes at the microscale. Thus, the stiffness of the cohesive elements is inversely proportional to their thicknesses. Therefore, the definition of the cohesive law will change, depending on the type of cohesive element. The first initial slope will be infinite for zero thickness cohesive element (Figure 1.4-4, Figure 1.4-5), and should be linked to adhesive's Young modulus, or shear modulus (depending on the mode) for thick cohesive element (Figure 1.4-6, Figure 1.4-7, Figure 1.4-8).

Its determination is important for accurate mechanical modeling. This is especially true when the fracture process zone is large [72]. There exist cohesive zone models with many different shapes for the cohesive law. The following examples are mostly dedicated to mode I. Yet, similar laws have been used for mode II.

The first introduction by Dugdale [65] of a cohesive law in 1960 followed a pure plasticity scheme (Figure 1.4-4). This model describes the relation between the tensile force and the normal displacement jump. This jump is null as long as the stress does not reach the critical value σ_c . Then, when the displacement or slip exceeds the threshold value, interaction between the lips is cancelled and thus no stress can be transmitted.

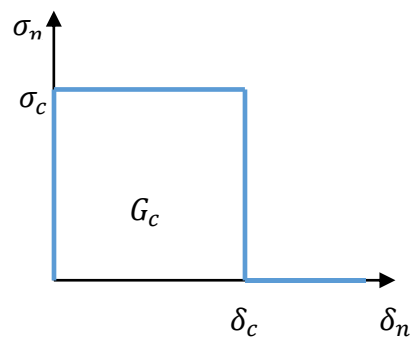


Figure 1.4-4: Dugdale cohesive law.

Needleman [73] suggested the introduction of cubic and polynomial laws to express accurately the failure of materials following nonlinear properties (Figure 1.4-5).

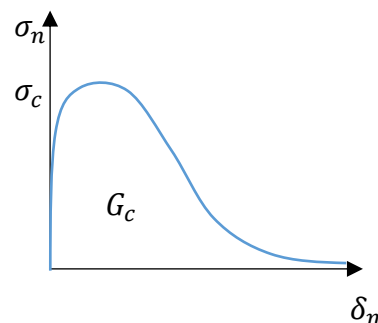


Figure 1.4-5: Needleman cohesive law.

Tvergaard [74] used a trapezoidal form to model the behavior of an elasto-plastic adhesive joint (Figure 1.4-6).

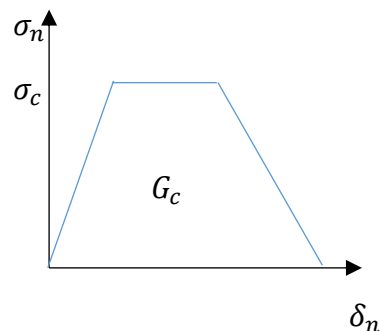


Figure 1.4-6: Trapezoidal cohesive law.

Camacho [75] (Figure 1.4-7) used a bilinear tensile-separation relationship applied to delamination problems in layered composite [76], [69]. This model is also commonly used to simulate the strength of bonded composite joints as it is accurate to express failure without plasticity, often encountered in adhesive failures [68].

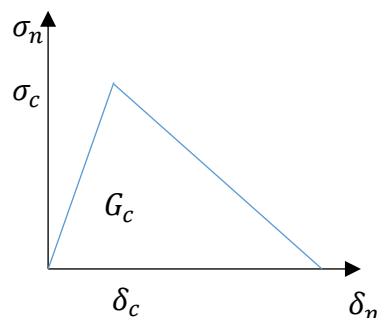


Figure 1.4-7: Bilinear cohesive law.

Petersson [77] defined a softened "bilinear" law which is frequently used to model concrete or wood failure because of its high accuracy to express delamination or bridging (in this case, some fibers remain attached to each adherent after the crack has already propagated) (Figure 1.4-8). This law needs at least one more parameter than the bilinear cohesive law, increasing the difficulty of its definition. However, the softened bilinear behavior seems to be a good compromise between the polynomial law and the bilinear one.

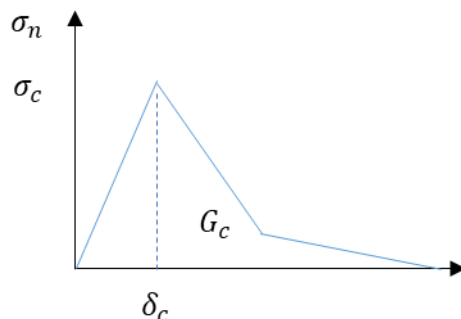


Figure 1.4-8: Peterson cohesive law.

The exact shape of the cohesive law can nowadays be extracted from experimental tests [78], although the tests are not standardized. If the cohesive laws have been obtained experimentally,

the available cohesive law shape and parameters of the model should be selected to best fit the experimental data. If the shape of the cohesive law is not known and there is no previous experience on the most appropriate selection, the simplest model is to assume linear softening. Additionally, the cohesive law shape may have an impact on the computational performance depending on the type of studied material [79].

For mixed mode cohesive law, several expressions have been proposed to express the impact of mode mixity on the interface properties. The simplest one is the power law expressed by equation (58).

$$1 = \frac{G_I}{G_{Ic}}^\alpha + \frac{G_{II}}{G_{IIc}}^\beta \quad (58)$$

Where the exponents α and β are determined by a curve fit to the fracture toughness data. For $\alpha=\beta=1$, this criterion becomes the linear interaction criterion, where the G_I component of the experimental data is simply plotted versus its G_{II} component.

Other criteria have been discussed in detail in several overview studies [80]. Today, the most often used 2D fracture criterion is the so-called B-K criterion proposed by Benzeggagh and Kenane [81] where a simple mathematical relationship between G_c and G_{II}/G_T is used in equation (59).

$$G_c = G_{Ic} + G_{IIc} - G_{Ic} \left(\frac{G_{II}}{G_c} \right)^\eta \quad (59)$$

With G_T the energy release rate in mixed mode. The exponent η is determined by a curve fit to the fracture toughness, G_c , plotted as a function of the mixed-mode ratio, G_{II}/G_c . The parameters G_{Ic} , G_{IIc} , and η are required inputs to perform modeling.

The surface of the cohesive law (depending of mixed mode ratio) can thus be obtained following a given criterion (power law, B-K) or a polynomial surface approximation as visible in Figure 1.4-9 [82].

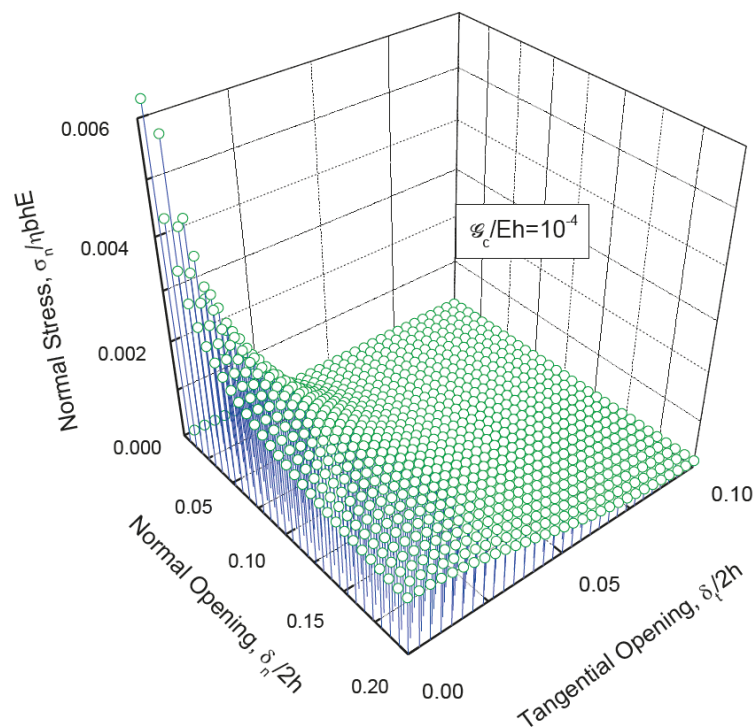


Figure 1.4-9: Mixed mode cohesive law surface (Power law criterion, [83]).

Several studies [84] [76] have been carried out on the expression of critical toughness in mixed mode, and it has been shown that the criterion B-K [81] and Power law could succeed in expressing G_c with composite (UD and angle-ply) test samples. More particularly, Camanho et al. [75] showed, for UD composites with different types of resin, that, with the correct choice of η for the B-K criterion, the critical toughness (for large mixed mode ratio) can be represented. A comparison between the Power law and the B-K criterion has also been done in [85] concluding that the Power law criterion, which is one of the most popular criteria, is not able to capture the rising mode I component in the low mode II ratio region for mixed mode test. The Power law criterion is also difficult to express in terms of the mixed-mode ratio (G_{II}/G). The B-K is then often used to produce criteria in accordance with experimental results. It has the advantage to use only 3 curve fitting parameters (G_{Ic} , G_{IIc} and η) (cf. equation (59)).

1.4.3. Determination of the critical energy release rate in mode I according to standardized tests

The double cantilever beam (DCB) test is the most commonly used method for measuring the initiation and propagation values of Mode I fracture energy G_{Ic} under static and cyclic loading conditions (see ASTM D5528 [87], ASTM D3433 [86], [88]) (Figure 1.4-10). A tensile load is applied to a DCB specimen with an embedded through-width insert at the specimen mid-plane which creates the initial crack of length a . The tensile force is applied perpendicular to the crack surface P and the local opening at the load application δ is monitored. Crack length is measured using either a travelling microscope or video camera. Building and testing of DCB specimens is straightforward and relatively inexpensive. Figure 1.4-11 presents a typical DCB test $P(\delta)$ curve which can be described in two parts. The first one is the elastic loading of the adherent in bending, which may finish with a non linear part because of the creation of the process zone near the crack tip. The second part, where the load decreases because of the crack propagation, leads to a increase of the length of the adherent in bending.

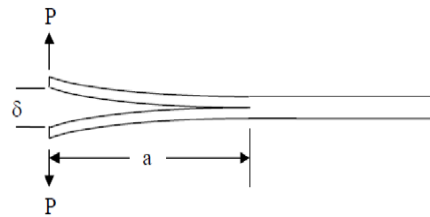


Figure 1.4-10: DCB test ([87]).

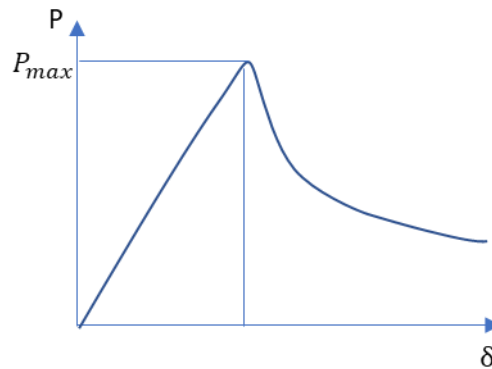


Figure 1.4-11: Exemple of DCB $P(\delta)$ curve.

Different methods were proposed to determine the energy release rate from such a test. Four of them are described here and are from two different standards: the modified beam theory method, the compliance calibration method, the modified compliance calibration method, and the shear corrected beam theory method.

- the Modified Beam Theory Method (MBTM):

This method, detailed in ASTM D5528 [87](for composite-to-composite delamination) follows the beam theory which tends to overestimate the critical toughness. In that case, the expression of the energy release rate is then described by equation (60).

$$G_I(a) = \frac{3P\delta}{2b(a + |\Delta|)} \quad (60)$$

With Δ a compensation factor (which is equal to 0 in the “normal” beam theory method) for the rotation of the adherent upstream of the crack front. It must be experimentally determined by generating a least square plot of the cube root of compliance ($C^{1/3}$), as a function of the crack length as shown in Figure 1.4-12 .

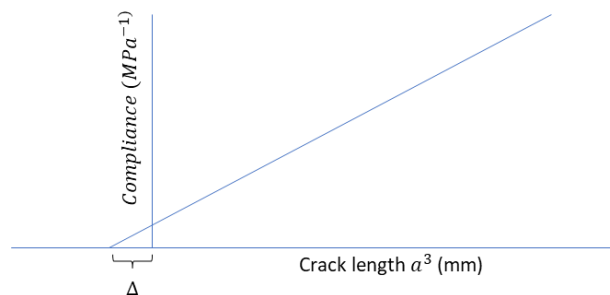


Figure 1.4-12: Typical DCB $C(a^3)$ curve.

- Compliance Calibration Method (CCM):

This second method, detailed in ASTM D5528 [87], gives the expression of the energy release rate in the equation (61).

$$G_I(a) = \frac{n\delta P}{2ba} \quad (61)$$

with n the slope of least square regression of the equation $\log(C) = f(\log(a))$.

- Modified Compliance Calibration Method (MCCM):

The last method detailed in ASTM D5528 [87] proposes another computation of $G_I(a)$ given in equation (62).

$$G_I(a) = \frac{3P^2 C^{\frac{2}{3}}}{2A_1 b h} \quad (62)$$

With A_1 the slope of the curve: $\frac{a}{h} = f(C^{\frac{1}{3}})$

- Shear Corrected Beam Theory Method (SCBTM):

This method is detailed in the ASTM D3433 [86] (for steel-to-steel bonding), and is derived from the LEFM and the beam theory. It proposes another expression of the relation between the variations of the compliance versus the crack length (equation (64)).

$$\frac{dC}{da} = \frac{8}{Eb} \left(\frac{3a^2}{t_u^3} + \frac{1}{t_u} \right) \quad (63)$$

$$G_I(a) = \frac{4P^2}{Eb^2} \left(\frac{3a^2}{t_u^3} + \frac{1}{t_u} \right) \quad (64)$$

E being the Young modulus of the adherents and t_u the thickness of the adherent.

Several initiation G_c values may be determined from the load/displacement curve as described by the ASTM standards. These values are based on the energy stored at the beginning of the non-linearity of the load/displacement curve, or at the maximal load (beginning of the crack propagation). However, they are highly dependent on the quality of the sample crack initiation process and tend to be lower (more conservative) than the material (or interface) crack propagation critical toughness. This value is obtained when G_{Ic} becomes independent on the crack length, therefore, when the critical toughness curve $G(a)$ becomes stable as visible in Figure 1.4-13.

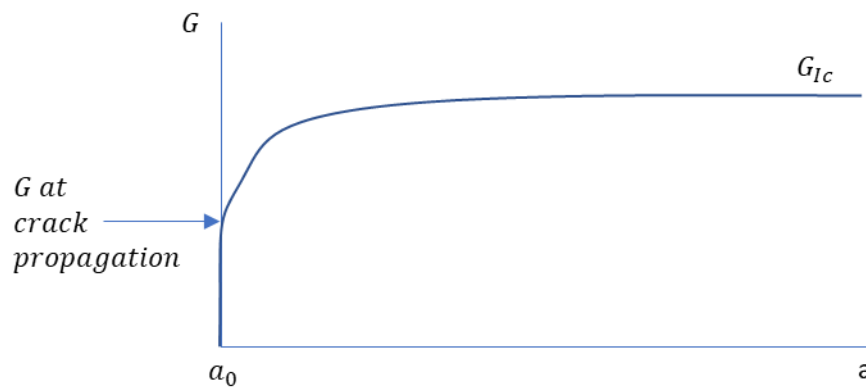


Figure 1.4-13: $G(a)$ curve.

1.4.4. Determination of the critical energy release rate in mode II according to standardized tests

The only standardized experimental setup for the mode II critical energy release rate is the End Notch Flexure (ENF), (ASTM D7905 [89], Figure 1.4-14). It is essentially a DCB specimen loaded under three-point flexure. The dimensions are similar to those employed for the DCB specimen.

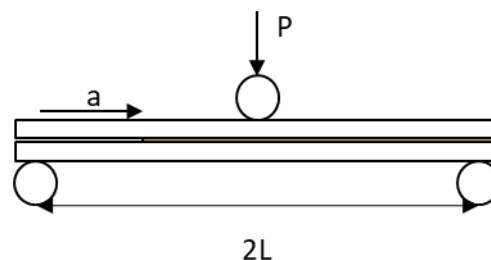


Figure 1.4-14: ENF sample.

The two methods previously exposed for mode I (Compliance Calibration Method CCM and modified beam theory method MBTM) can also be applied for mode II. The CCM method has been proved to be accurate and is recommended in the ASTM D7905 standard [90]. The alternative method, the MBTM, tends to underestimate G_{IIc} (depending on material properties) because of the absence of corrections to account for shear strain [14].

The following experimental issues with the ENF test have been listed:

- for brittle adhesives, or adhesive failure, uncontrolled crack propagation can be expected [14] [91],
- in [90], it has been shown that the ENF test does not guarantee the observation of pure mode II over its entire length. Indeed, there exists mixed mode that can decrease the obtained value of the critical strain energy release rate,
- too little crack propagation length might not be enough to observe a stabilized $G(a)$ curve into G_c , [14].

The ASTM standard (ASTM D7905 [89]), for composite-to-composite bonding, proposes simplifying hypothesis for the CCM approach as unstable crack propagation may occur during the ENF test. The same sample is used three times with different pre-cracked lengths a_0 .

After the preliminary investigations, for each a_0 , the three-point bending test is then performed until the crack propagates. The main hypothesis of this test is that the crack propagates when the maximum force (P_{max}) is reached, as visible in Figure 1.4-15 and G_{IIc} can therefore be computed from the equation (65).

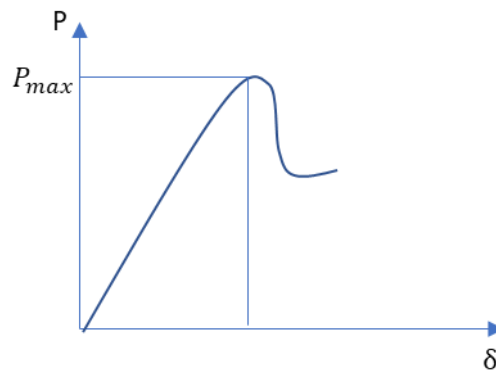


Figure 1.4-15: Example of ENF $P(\delta)$ curve.

$$G_{IIc} = \frac{3 m P_{max}^2 a_0^2}{2 b} \quad (65)$$

$$C = A + m a^3 \quad (66)$$

With m (slope) and A (intercept), being the coefficients of the linear least square regression analysis of the compliance curve determined by fitting (equation 66).

It is to be noted that the compliance curve must be obtained using a minimum of three points (three tests with one sample). The main interest of this approach is that G_{IIc} is directly obtained using equation (65), without precise measurement of the crack during the whole test.

1.4.5. Determination of the critical energy release rate in mixed mode according to standardized tests

The most frequently used experimental setup is the Mixed Mode Bending test (MMB) (Figure 1.4-16) which is described in standard ASTM D6671 [101]. It is based on a mix of DCB and ENF tests and allows testing under the full range of mixed mode ratio, from pure Mode I to pure Mode II. In MMB test, a lever is used to load the specimen. Loads are applied at the center of the specimen which creates mode II loading and at the upper bonded tabs position which creates mode I loading. The mixed mode ratio can be easily controlled through the displacement on the lever arm and the change of the length c (Figure 1.4-17).

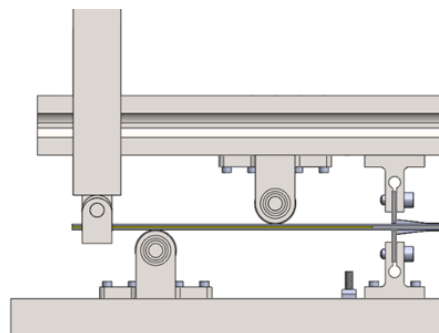


Figure 1.4-16: MMB test bed and sample.

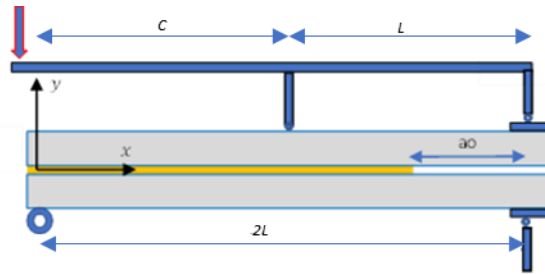


Figure 1.4-17: MMB Test configuration.

In the ASTM D6671 standard, the analytical solutions for the critical toughness computation are obtained using Corrected Beam Theory (CBT) proposed by Kinloch et al. [89]. In [90], Reeder proposed, based on the CBT, for only mode I and mode II loading conditions, the following equations to evaluate the critical toughness value for isotropic adherents, monitored during the crack propagation (blue curve in Figure 1.4-18):

$$GI = \frac{12P^2(3c - L)^2}{16b^2h^3L^2E} (a + \chi h)^2 \quad (67)$$

$$GII = \frac{9P^2(c + L)^2}{16b^2h^3L^2E} (a + 0,42\chi h)^2 \quad (68)$$

These equations connect the toughness to the lever length c , the loading P and the crack length a of the sample, the Young's modulus of the adherents E , and the shear modulus of the adherents G , the length of the sample L , its thickness and width, h and b .

$$\chi = \sqrt{\frac{E}{11G} \left\{ 3 - 2 \left(\frac{\Gamma}{\Gamma + 1} \right)^2 \right\}} \quad (69)$$

$$\Gamma = 1.18 \frac{E}{G} \quad (70)$$

$$G_{tot} = GI + GII \Rightarrow Gc \quad (71)$$

Where χ is the crack length correction parameter and Γ is the transverse modulus correction parameter.

Figure 1.4-18 shows typical load/displacement (P/δ) curves. The monitoring of these values must allow computing the toughness curve depending on the mode ratio. However, it is specified that in case of uncontrolled crack propagation (generally at high G_{II}/Gc ratio, see green curve on Figure 1.4-18), an approximation of G_{Ic} and G_{IIc} (initiation critical toughnesses) can be made using the critical toughness computation at crack initiation, using the maximal load P_{max} and the initial crack length a_0 . Nonetheless, it may cause an underestimation of Gc value.

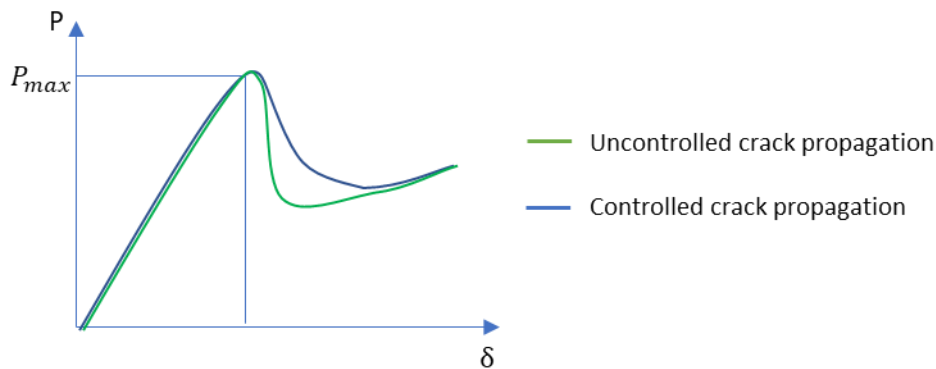


Figure 1.4-18: MMB exemple $P(\delta)$ curve.

1.4.6. Non-standard test G_c determination

1.4.6.1. In Mode I

The adhesion between thin surface and a flat metal surface is commonly made through the blister test. The setup is based on the formation of a blister by injecting gas under pressure between a film and a substrate as shown in Figure 1.4-19. The mode I critical toughness is determined by recording the pressure as a function of the variation of the blister radius. The blister shape is monitored in 2D to measure the radius at different increasing pressure. This approach has been extended to the bonding of composites on steel in some studies by de Barros [88] in the case of bonded CFRP on steel pipe for mode I failure prediction and critical toughness measurement.

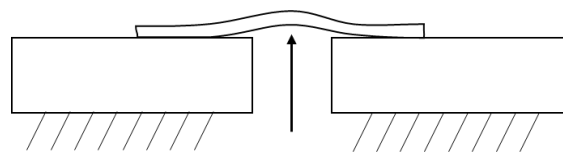


Figure 1.4-19: Blister test sample.

1.4.6.2. In Mode II

To compensate the issues of the ENF test, the study and development of other mode II test was made.

As exposed, the ENF test is prompt to uncontrolled crack propagation. An alternative mode II configuration, was proposed by Martin et al. [96], called the four-point end notched flexure (4ENF) test (Figure 1.4-20). This test is known as having a much more stable crack propagation so that CCM can be more commonly applied for the fracture toughness computation as described in [97]. The 4ENF test use a four-point flexure frame allowing similar rotation than the ENF test. However, this test, because of the crack being located between the two-load application points, is known as having issue related to overestimation of the critical toughness because of friction energy dissipation [91].

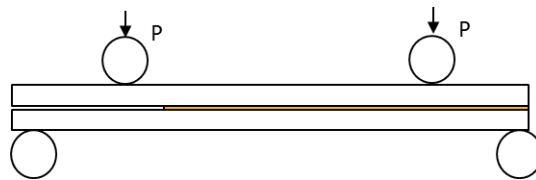


Figure 1.4-20: 4ENF sample.

The End Loaded Split (ELS) test has been lately pushed forward. This set-up allows avoiding friction between the upper and lower beams along the crack length. Wang et al. [98] argued that this test is the most suitable for measuring the strain energy release rate curve, which is justified by the longer allowable crack length which help to have a stabilized crack propagation. Blackman et al. [99] asserted that it was especially adequate in the case of stiff and toughened adherents because of the requirement of the adherents to remain elastic during the whole test. The only real limitation of this case has been shown by [101]: a minimal sample length of few decimeters might be required to ensure a correct computation and stabilization of G_{IIC} with the ELS samples. Figure 1.4-21 presents the overall geometry of the ELS test.

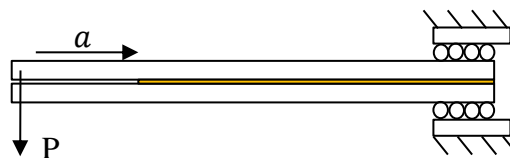


Figure 1.4-21: ELS sample.

ELS test is based on cantilever beam geometry. The two adherents are bonded together up to the point of the initial crack length (pre-crack). The applied load generates shear in the bondline around the crack position inducing mode II loading in the adhesive. In [13] da Silva et al. add the specification that the crack propagation should occur before large displacement takes place (before the maximum deflection of the beam is equal to 0.2 times the length of the sample). This should be the case, as described in [98], when the crack length is longer than the half length of the sample.

An alternative test might be used, the single lap shear test, that corresponds to a traction test on two bonded adherents with relatively long lap length compared to other samples dimensions (Figure 1.4-22). It is the easiest test to perform to obtain energy value. Yet, as raised previously, peel stress may exist in such a geometry that cannot always be neglected [13]. In some particular case, such as CFRP (Carbon Fiber Reinforced Polymer) bonded on concrete such as in [101], the peel effect remains limited, and the single lap shear tests can be used to obtain cohesive laws [102]. For this method, one adherend must present a great stiffness compared to the other.

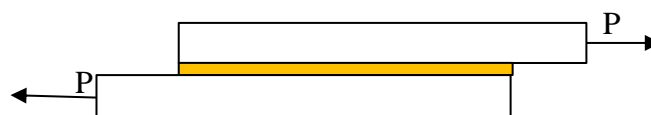


Figure 1.4-22: Single lap test.

1.4.6.3. Mixed mode

The Spelt test has been developed by Fernlund et Spelt [103]. Samples geometry is closed to the DCB and ENF ones as shown in Figure 1.4-23. Different loads can be achieved by changing the main distances on the test frame, thereby varying the mode-mixity. Changing the distances generates differential load applied to the upper and lower adherends. The main advantage of this test is that it also allows the realization of pure mode tests, DCB for mode I and the ENF for mode II.

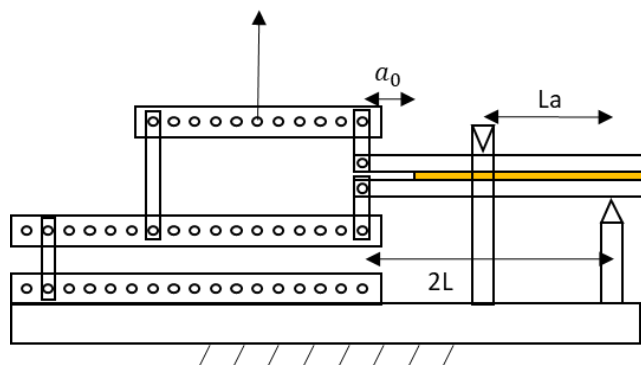


Figure 1.4-23: Spelt test.

Another test for mixed mode has been lately developed by Sørensen et al. [101], the Double Cantilever Beam with Uneven Bending Moments (DCB-UBM). As shown in Figure 1.4-24, the principle of this test is to generate two different bending moments at the free edges of the sample. The mixed mode ratio can be changed simply by changing one transverse arm length that modifies the applied bending moment. The main advantages of the DCB-UBM test is the direct analytical computation of the J-integral which is independent of the crack length [101]. The authors showed good correlation between the obtained critical value of the J-integral and literature results in the case of a GFRP beam bonded with a thick ductile adhesive (polyurethane adhesive, 10mm-thick). Another advantage is the absence of shear forces, reducing the energy lost by friction between the opening faces

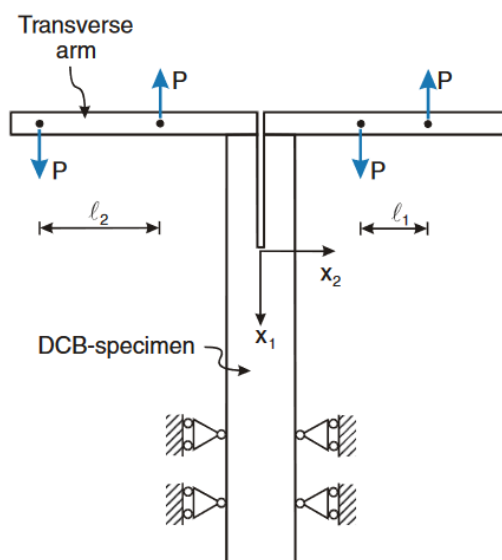


Figure 1.4-24: DCB-UBM test frame.

Other configurations have also been used. A promising one using modified Arcan specimens [54] has been tested with various types of bonded interface (CFRP, GFRP, steel) (Figure 1.4-25).

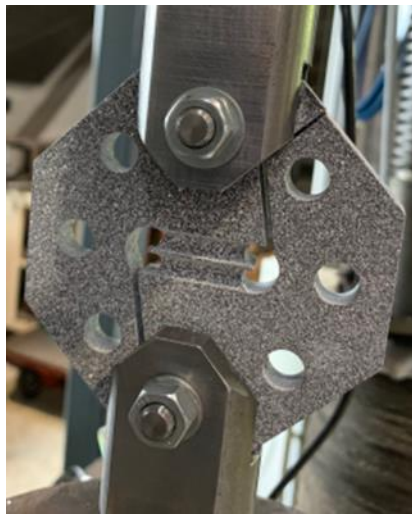


Figure 1.4-25: Arcan test.

The mixed mode ratio is controlled by the angle of loading in the Arcan sample from pure mode I to pure mode II. Choupani [54] was able to obtain Mode I, Mode II and mixed mode critical energy release rate values for crack propagation in the adhesive and perform numerical analyses of the experiments. He concludes that, for composite to steel bonding, peel tends to propagate the crack adhesively while shear tends to propagate the crack cohesively with a much higher critical toughness.

1.5. Conclusion

The objective of this bibliography was to identify the main methods to design structural adhesive joints. These methods should take into account the specificity encountered with bonded joints and propose a modeling approach with some failure criteria.

The review of the analytical models allowed highlighting the main mechanical phenomena associated with adhesively bonded joints (influence of the overlap length, existence of a characteristic anchorage length, peeling and shear concentrations at the free edges), and the main points requiring special attention in the design. This analysis also permits to identify the limits of these models for complex patch geometries and the need to use numerical approaches to obtain more consistent stress and strain fields (or energies) needed for the design of a bonded patch. Among the identified numerical tools, the finite element model seems to be the most convenient, given that the singularity effect can be considered.

The study of the available design criteria highlights the difficulties linked to their application to bonded reinforcement. Continuous failure criteria, in the elastic case, encounters some limits due to the singularities. The use of fracture mechanics approaches, on the other hand, needs to define a pre-existing initial defect length to be applicable. In the case of ductile adhesive, it seems that continuous mechanics may be used but the criteria will have to be properly defined choosing for example a critical strain approach. One approach therefore proposes to adopt coupled stress energy criteria to overcome these difficulties.

Several authors have also proposed a new approach combining both the modeling and the failure criteria of the bonded joint: the cohesive zone model. This approach couples the continuous mechanics approach as a stress criterion may be used (as the maximum stress of the cohesive law), as well as the fracture mechanics characteristics (the critical energy release corresponding to the area under the curve of the cohesive law). It is already implemented in finite element modeling and several approaches exist regarding its use in 3D.

The main methodologies used to determine the critical energy release rates in the mode I, mode II and mixed mode were then presented. It has been shown that a fine apprehension of adhesion mechanics and strength is critical for a good understanding of interface properties of bonding. Different critical toughness computation methods have been detailed such as the CCM and the MBTM. These methods propose relations between the strain energy release rate and the crack length of the samples through classical fracture mechanics investigations. However, issue to precisely monitor of the crack propagation may occur during these tests [87]. This is more deeply studied in the next chapter.

Chapter 2: A new methodology for fracture mechanics investigations on adhesively bonded joints relying on the use of distributed optical fiber sensor

The aim of this chapter is to present a new methodology based on the use of strain distributed optical fiber sensor for the characterization of bonded assemblies. This methodology has been developed to measure relatively precisely the crack propagation during fracture mechanics tests. First, the motivation of this development is discussed. Then, the experimental investigations done for the validation of this new methodology are detailed for ENF, DCB and MMB tests.

2.1. Justification of the developpement of the new crack propagation measurement methodology

According to the equations given in the standards ([87] and [104] for DCB and MMB tests), critical toughness is directly correlated to the crack length. As consequence, a precise measurement of the crack propagation during the entire test period is necessary to ensure a correct critical toughness determination.

Standards propose a visual monitoring (with a microscope) of the crack front position on one flank of the sample during the test. However, the measurements obtained by this technique are highly dependent on the operator. In the literature, automatization of the crack propagation measurement by DIC (Digital Image Correlation) is tested to improve the accuracy measurement. Nevertheless, this method can ensure good results if the crack propagates slowly with a straight front perpendicular to the direction of propagation. In some cases, depending on the mechanical and geometrical characteristics of the bonded assembly as well as the loading, the crack front shape may not be straight in the plane perpendicular to the direction of the crack propagation. In consequence, the measurement from the flank of the specimen can lead to underestimate of several millimeters the real crack propagation. The calculation of critical toughness from such biased measurements may therefore have a large uncertainty. Other methods have been developed lately, such as using acoustic emission to measure crack length in fracture mechanics tests [105]. However, limited precision (few millimeters) remains an issue for the critical toughness computation. Table 2.1-1 summarizes the advantages and the limitations of the different techniques mentioned above for crack propagation measurement.

For the reasons mentioned above, the use of alternative measurement techniques is required to ensure a precise, robust, with high spatial resolution and easy to use, crack front measurement. In 2011, Bernasconi et al. [106] has investigated the use of an array of optical fiber sensors. The array was composed of 5 Fiber Bragg Gratings (FBGs) of 6 mm long and positioned at 21 mm intervals on the side of a joint. With this instrumentation, he showed that it is possible to detect and monitor the crack propagation in a bonded joint during a fatigue test. The methodology consisted in monitoring strain variation for each FBG. Indeed, when a crack appears and propagates near the FBG, large variation of the strain may generally occur and as consequence, the crack can be detected and localized. However, this instrumentation relying on FBG for crack front measurement presents two limitations. First, the accuracy of the position

of the crack is limited by the length of the Fiber Bragg grating. The second limitation is that several Fiber Bragg gratings must be used to obtain different crack propagation measurements.

More recently, in 2017, Meadows et al. [107] has proposed to use high spatial distributed optical fiber sensor. As for the methodology based on FBG to detect the crack position, it consisted in monitoring strain variation due to the crack propagation. Yet, distributed optical fiber allow using the whole length of the fiber as a sensor. This means that the crack propagation can be monitored continuously (if the speed of propagation is sufficiency small compared to the frequency acquisition of the system). In the study of Meadows et al., a polyimide optical fiber was imbedded in a composite sample (Carbon Fiber Reinforced Polymer) around crack tip and an ODiSI-A was used for the measurements. This system has a maximum sample rate of approximately 1 Hz and, for the post-processing of data, the gauge length and spacing were fixed to be equal to 1 mm. The comparison between the true crack lengths (measured by a microscope) and those measured with the optical fiber showed a difference less than 3 millimeters for DCB and ENF tests.

The good results of these study and their limited application case to composite sample with embedded fibers (embedded in one ply of the composite in small thickness sample, difficult and fragile samples) has motivated the idea to extend this analysis to larger application and other materials to be able to follow crack propagation in all the different case of standardized fracture mechanics tests while simplifying the measurement process. More precisely, we aimed at extending the field of application of such sensors to the field of adhesive joint, for less favorable cases (thicker samples and bonding of the fiber on the surface of the adherents) and with more recent optical fiber technology. In our case, standardized fracture mechanics tests such as DCB, ENF and MMB tests will be tested with this new methodology.

	<i>Visual measurement</i>	<i>DIC measurement</i>	<i>Optical fiber</i>	<i>Acoustic emission</i>
<i>Operator dependent</i>	<i>Yes</i>	<i>No</i>	<i>No</i>	<i>No</i>
<i>Automatization</i>	<i>Difficult</i>	<i>Yes</i>	<i>Yes</i>	<i>Yes</i>
<i>Position of the measured crack front</i>	<i>Border</i>	<i>Border</i>	<i>Center and border</i>	<i>Center and border</i>
<i>Crack length monitoring</i>	<i>Few centimeters</i>	<i>Few centimeters</i>	<i>Few meters</i>	<i>Few centimeter</i>
<i>Precision</i>	<i><1mm</i>	<i><1mm</i>	<i>1-2mm (expected)</i>	<i>1-5mm</i>

Table 2.1-1: Comparison (advantage and limitations) of several techniques for crack front measurement.

2.2. Optical fiber crack front measurement methodologies

To determine the crack front position from strain profile measurement obtained with the optical fibers, a correct understanding of the expected strain state on the surface of the tested samples is required for mode I, mode II and mixed modes.

2.2.1. Theoretical ENF crack front measurement

The ENF test (mode II) corresponds to a three-point bending test (Figure 2.2-1). Upstream from the crack front (on the right in scheme), the ENF sample corresponds to a beam of thickness $2h_s + h_a$ (with h_s and h_a , the steel and adhesive thickness respectively), while downstream from the crack front (on the left in scheme), the sample is equivalent to the superposition of two beams of thickness h_s (neglecting the friction).

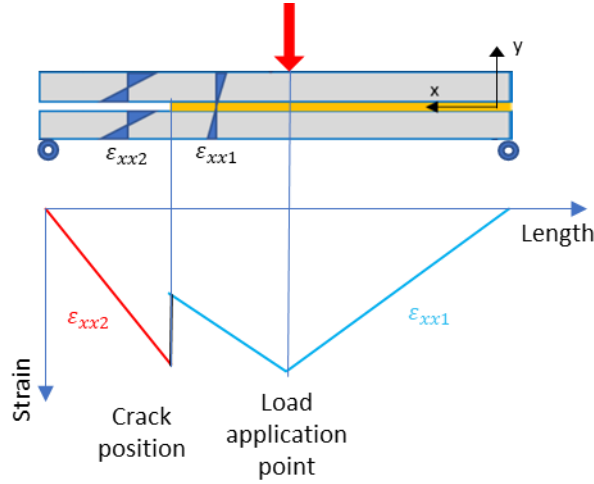


Figure 2.2-1: Scheme representing strain distributions for two characteristic cross-sections into the ENF sample during loading.

According to the beam theory, the strains ε_{xx1} and ε_{xx2} , respectively upstream and downstream from the crack front, that can be measured by an outer fiber (i.e. bonded on the surface of the lower plate), follow the equations (72) and (73).

$$\varepsilon_{xx1} = -\frac{M_{fz}(x)}{EI_{hz1}} \left(\frac{h_a}{2} + h_s \right) \quad (72)$$

$$\varepsilon_{xx2} = -\frac{M_{fz}(x) h_s}{E_s I_{hz2}} \frac{1}{4} \quad (73)$$

The equivalent stiffness of the bonded plate is given by:

$$EI_{hz1} = \frac{E_s b}{12} ((h_a + 2h_s)^3 - (h_a)^3) + \frac{E_a b}{12} h_a^3 \quad (74)$$

and the moment of inertia of the steel plate is written as:

$$I_{hz2} = \frac{bh_s^3}{12} \quad (75)$$

With E_a the adhesive Young's modulus, b the width of the sample/steel plate, M_{fz} the bending moment along the x axis, E_s the steel Young's modulus, h_s the steel plate thickness, h_a the adhesive thickness, EI_{hz1} the equivalent stiffness of the bonded plate and I_{hz2} the moment of inertia of the steel plate.

As shown in Figure 2.2-1, ε_{xx1} is maximal at the load application point, while ε_{xx2} is maximal at the junction of the bonded and un-bonded beams (corresponding to the location of the crack

tip). Therefore, the local maximum at the junction of ε_{xx1} and ε_{xx2} is set as the position of the crack front.

This analysis relies on two important assumptions:

- the supposed plasticity/damage inside the bondline (Fracture Process Zone – FPZ – size) remains limited (this assumption is very often adopted in fracture mechanics and should be verified if possible) and has limited impact on the strain measurement obtained with the optical fibers,
- the crack front is far enough (few centimeters) from the load application to ensure no interference.

Strain monitoring on top or bottom surface and determination of local maximum value's position may therefore provide a way to monitor crack propagation for ENF test.

2.2.2. Theoretical DCB crack front measurement

The same analysis has been performed with the DCB test by considering an optical fiber bonded on the top and bottom surfaces (no embedded fibers). The geometry of the DCB test is reminded in Figure 2.2-2.

Following the equation (76), the maximal local rotation variation ($\frac{d\omega}{dx}$) of the samples is supposed to occur closed to the crack tip, and thus the position of the maximal strain measured at the surface of the adherent should correspond to the position of the crack front.

$$\varepsilon_{xx3} = \frac{d\omega}{dx} = -\frac{M_{fz}(x) h_s}{E_s I_{hz2}} \frac{1}{2} \quad (76)$$

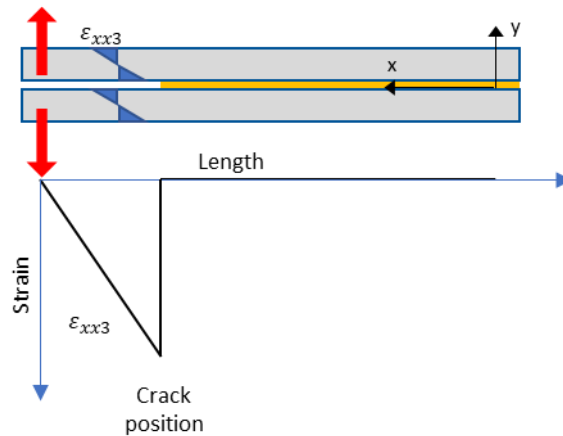


Figure 2.2-2: Strain into the DCB sample during loading.

Using an outer optical fiber (positioned on bottom or top surface) should then be sufficient to determine the crack front position.

2.2.3. Theoretical MMB crack front measurement

The MMB test can be analyzed as the sum of an ENF and a DCB test. Upstream from the crack front (on the right in Figure 2.2-3), the MMB sample corresponds to a beam of thickness $2h_s + h_a$ while downstream from the crack front (on the left in Figure 2.2-3), the sample is equivalent to the superposition of two beams of thickness h_s .

According to the beam theory, the strains ε_{xx4} , ε_{xx5} and ε_{xx6} shown in Figure 2.2-3 follow the equations (77) to (79).

$$\varepsilon_{xx4} = -\frac{M_{fz4}(x) h_s}{E_s I_{hz2}} \frac{h_s}{2} \quad (77)$$

$$\varepsilon_{xx5} = -\frac{M_{fz4}(x)}{EI_{hz1}} \left(\frac{h_a}{2} + h_s\right) \quad (78)$$

$$\varepsilon_{xx6} = -\frac{M_{fz6}(x) h_s}{E_s I_{hz2}} \frac{h_s}{2} \quad (79)$$

With M_{fz4} the bending moment along the x axis generated by the load F_4 , M_{fz5} the bending moment along the x axis generated by the load F_5 and M_{fz6} the bending moment along the x axis generated by the load F_6 , E_s the steel Young's modulus, h_s the steel plate thickness, h_a the adhesive thickness, EI_{hz1} the equivalent stiffness of the bonded plate given by the equation (74) and I_{hz2} the moment of inertia of the steel plate (75).

The strains ε_{xx4} and ε_{xx6} are maximal at the junction of the bonded and un-bonded beams (corresponding to the location of the crack tip) while ε_{xx5} is maximal at the load application point. As M_{fz4} and M_{fz5} have a similar effect, higher strains are generated on the top surface of the sample at the crack tip in comparison with the bottom surface (M_{fz5} and M_{fz6} have opposite effects). The disposition of the strain measurement instrumentation on the top surface is therefore recommended. Therefore, the local maximum at the junction of ε_{xx4} and ε_{xx5} is set as the position of the crack front.

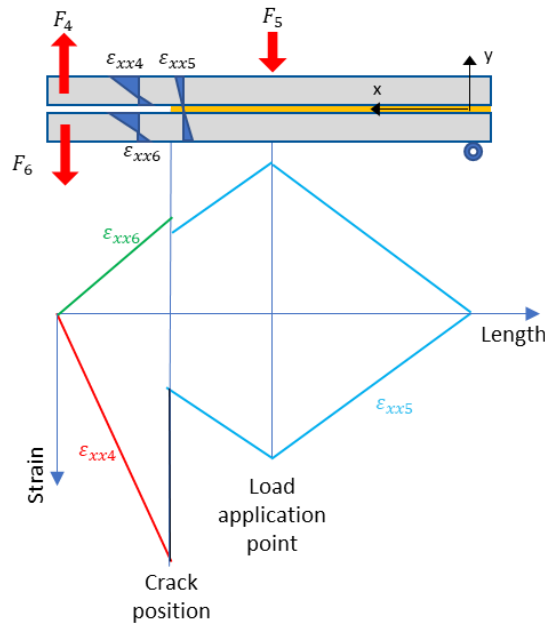


Figure 2.2-3: Theoretical outer strain profiles on the lower and upper surface of an MMB sample.

It is worth pointing out that the expected strain measurements are higher for MMB test than for the ENF test. Therefore, if the results of the ENF test are satisfying, using an outer optical fiber on the top surface, it should be sufficient to monitor the crack front position in the case of the MMB test.

2.3. Description of the experimental protocol

2.3.1. Studied samples

For mode I (DCB test), mode II (ENF test) and mixed mode (MMB test) investigations, it has been decided to use a custom geometry for the specimen, closed to the one given in the ASTM D7905 [104] standard related to the ENF test. The sample geometry has been fixed at 500x50x11mm³ and the substrates have been changed by steel plates. These dimensions, especially the thickness, have been chosen to assess the capabilities of the developed methodology on relatively thick (5 mm) and rigid adherents more representative of the considered application.

The initial crack length has also been increased compared to the ASTM standard to ensure that the crack propagation remains under control. Too little initial crack length can indeed tend to uncontrolled crack propagation for the ENF test as shown by Allix [109] or by de Barros [110]. The initial crack was made using a Teflon insert in contact with the steel adherent.

Steel surfaces were sanded and degreased prior to bonding. The bonding operation for all the specimens was processed as follows: a 1 mm steel plate was inserted at each end of the sample (out of the bonded zone); the resin was applied on the 2 surfaces prior to bonding; then the samples were assembled and pressured up to the point where the joint was 1 mm thick (the two adherents being in contact with 1 mm steel inserts). The sample was then cured at 20°C during seven days before being tested. Thickness measurements were made at several locations of the sample before testing and small variations, less than <10% of the thickness of the bondline, were seen along the length of the sample.

The adhesive used for the bonding of the sample is a cold curing epoxy (silicon toughened epoxy), called resin A. The main properties of the adhesive are given in Table 2.3-1 (from technical data sheet).

<i>Young modulus</i>	<i>Tensile strength</i>	<i>Strain at failure</i>
<i>11 GPa</i>	<i>25 MPa</i>	<i>1%</i>

Table 2.3-1: Resin A mechanical properties in tension.

The test frames for DCB, ENF and MMB tests were also inspired from the ones provided in the ASTM standards. The overall geometry and size were adapted to fit to the test sample geometries which are bigger than the ones in the standard. For the DCB and MMB test frame, the bonded tabs were increased in surface and thickness to avoid any debonding during the test.

2.3.2. DCB, ENF and MMB test bed geometries

This part presents the DCB, ENF and MMB test beds that were designed especially for the specimens described previously. The loading was carried out at a constant speed of 2 mm/min for each test.

The experiments were performed using customized devices on a Losen (300kN) testing machine. Since the expected loads were small, a secondary 5kN or 10kN load cell was used in order to provide a more accurate load measurement.

For the DCB test (Figure 2.3-1):

- the upper hinge was supported on a pull rod that had a greased loose bolt which allows to sample to self-align along the machine loading axis,
- the crack opening displacement was measured with a laser extensometer. The laser was fixed to the hinge fixture so that any rotation of the ends of the beams did not produce an error. An image of this setup can be seen in Figure 2.3-1 with the actuator located under the specimen and the secondary load cell mounted above.

For the ENF test (Figure 2.3-2):

- the upper part of the test frame was an assembly of the load cell, the push rod and fixture on the press clamp so that the load application point should only move in the vertical direction. The load application point's displacement was measured with a laser extensometer directly fixed to the push rod,
- the lower part was a two-point support consisting in two cylinders on bearing directly fixed on the floor of the press.

For the MMB test (Figure 2.3-3) the upper part consisted in the same upper assembly as for the ENF test with a different push rod shape,

- the lever part consisted in a thick I beam with a fixed hinge at one end, one cylinder on bearings in the center, and one device in the shape of horse shoe to transfer the vertical displacement from the upper part to the lever through bearings,
- the lower part was similar to the ENF device, with the left cylinder being replaced by a fixed hinge.

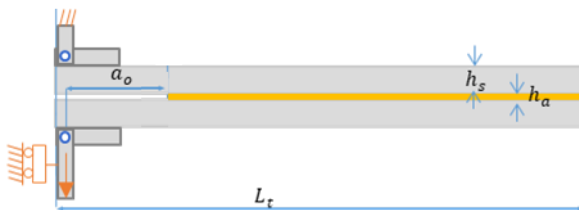


Figure 2.3-1: Photo of the DCB sample and DCB test bed.

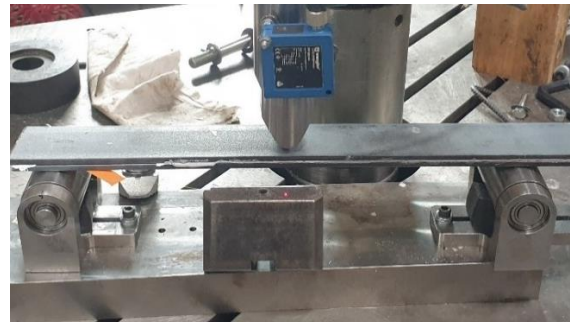
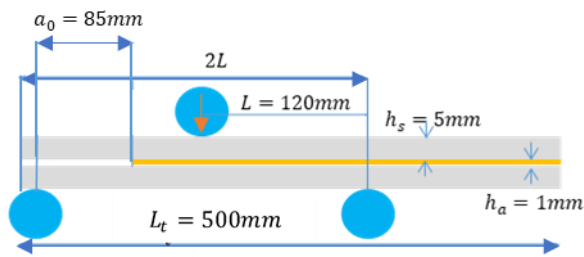


Figure 2.3-2: Photo of the ENF sample and ENF test bed.

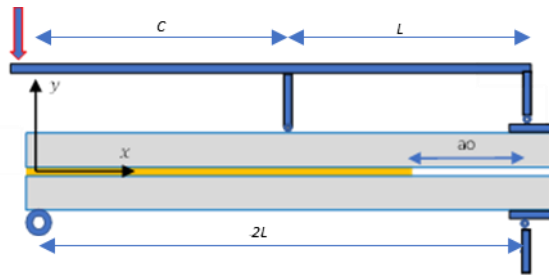


Figure 2.3-3: Photo of the MMB sample and MMB test bed.

During the tests, various physical quantities have been recorded. Applied force and displacements are monitored during the whole tests using adapted load cell (precision $\pm 0.145\%$, 2.5 to 10kN) and a laser displacement sensor (precision $10\mu\text{m}$). In addition, two local monitoring systems are used: high spatial strain distributed optical fiber sensor (Rayleigh technology) and digital image correlation.

2.3.1. Monitoring system by distributed optical fiber sensor

The used optical fiber distributed sensing system is a LUNA ODiSI-B. This system is based on the measurement of the Rayleigh backscattering that occurs when light propagates in the core of an optical fiber. This phenomenon is due to tiny variations of core refractive index and any changes resulting from elongation or contraction along the optical fiber modifies this signal. The technology patented by Luna relies on the use of an OFDR (Optical Frequency Domain Reflectometer) to detect these variations by comparing two Rayleigh backscattering measurements at different states. With this device, high spatial strain distributed measurement can be obtained along the entire length of an optical fiber (up to 10 m). Indeed, strain profiles can be measured with a gauge length of 1.2 mm and a gauge pitch of 0.6 mm. Moreover, the strain profile measurement can be sampled at a maximal rate of 23 Hz. It is also important to underline that this system needs no special optical fiber as sensor. Common mono-mode optical fiber with different coatings (acrylate, polyimide ...) can be used. Consequently, different types of fiber with different coatings have been studied to study the impact of this coating on the capacity of the fiber to monitor high strain gradient with high precision [111].

2.3.1.1. Optical fiber installation

The previous analytical analysis showed that bonded optical fiber on upper surface at the center of the sample (option 1 in Figure 2.3-4) should be sufficient to follow the crack propagation. Yet, it is supposed that, to better follow the real crack propagation, the crack measurement should be carried out in the center of the sample (plain strain).

Thus, several options have been studied in the case of ENF tests to be sure of the final choice of the location of the optical fiber:

- on the flank of the sample (option 2) in the direction of the crack propagation (Figure 2.3-4),
- on the flank of the specimen perpendicular to the direction of propagation (option 3), (Figure 2.3-4),
- inside the bond line (embedded optical fiber), at the center (option 4), (Figure 2.3-4).

For specimens with no embedded optical fiber in the bondline, the optical fiber was bonded with Araldite 2014-2 adhesive on the steel surface (Figure 2.3-5a), (Figure 2.3-5b).

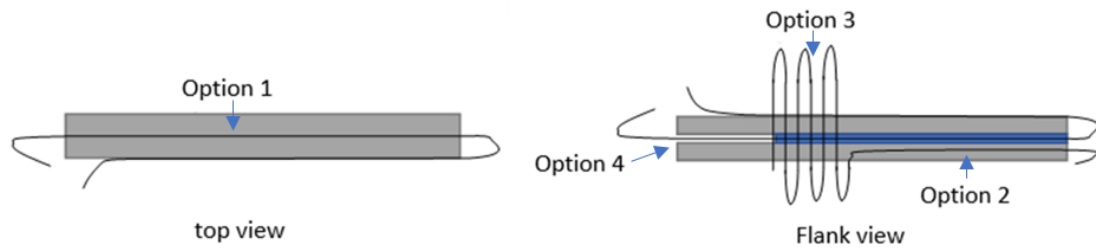


Figure 2.3-4: Tested positions for the optical fiber on the sample (flank, transverse, embedded and on the top).

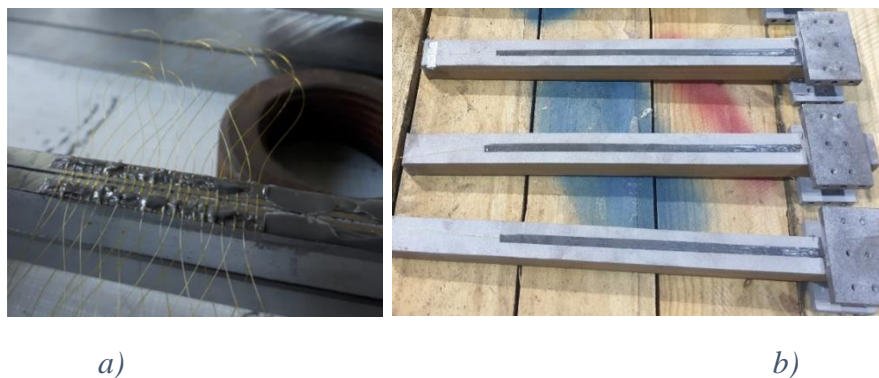


Figure 2.3-5: a) Example of optical fiber application on a specimen: option 3, b) DCB specimen with surface bonded optical fiber with Araldite-2014-1.

After initial tests which are not described here, two options (2 and 3) were not kept as crack front measurement solutions because they did not produce satisfactory results. Indeed, the option 2 revealed to be highly dependent on the position on the flank (near the top surface or near the bondline) possibly leading to misinterpretation of the results. Option 3 has presented relatively good results on the measurement of the crack front position on the border of the sample. However, it is proved to be not suitable for DCB and MMB test. Indeed, as the crack propagates, and the local opening increases, the measured local strains exceed the measurement capacity of the fiber (10 000 $\mu\text{m}/\text{m}$), and the optical fiber breaks after only few centimeters of crack propagation. The next analysis will be performed only with options 1 (also called exterior optical fiber) and 4 (also called embedded optical fiber).

2.3.1.2. Choice of the optical fiber technology

According to the theoretical analysis, the crack propagation monitoring should be possible with optical fiber through the recording of the position of the local maximal strain on the surface of the sample. The strains on the surface are transmitted to the core of the optical fiber through the used adhesive and through the coating of the fiber (Figure 2.3-6). The thickness and the material of the coating is critical on the capacity to determine high strain gradient. Thus, a thicker and less rigid coating may reduce this capacity.

An ENF test has been conducted using the previously described sample (with an initial crack length of 6 cm) to study the impact of the choice of the fiber on the strain measurement. Two different optical fibers were bonded with the Araldite A-2014-1 adhesive, centered on the surface of the sample with a 1 mm gap between them. The two studied coatings were polyimide and acrylate. The main geometrical properties of these two different fibers are summarized in Figure 2.3-6.

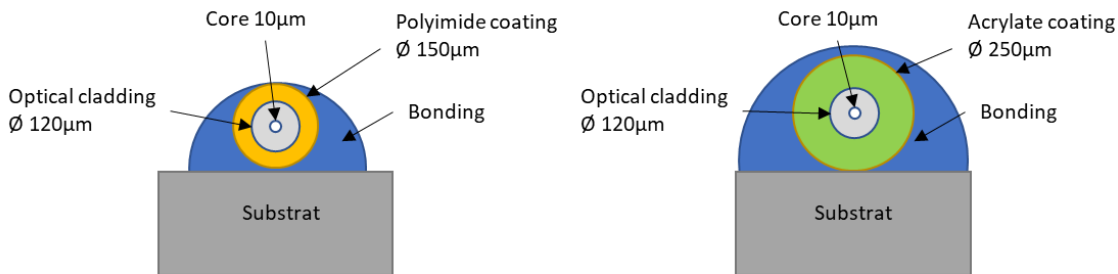


Figure 2.3-6: Scheme of the two studied optical fiber technologies and connection to the samples.

Figure 2.3-7 presents the resulting strain profiles obtained during this test for one load level with the two different studied optical fibers (with polyimide and acrylate coating).

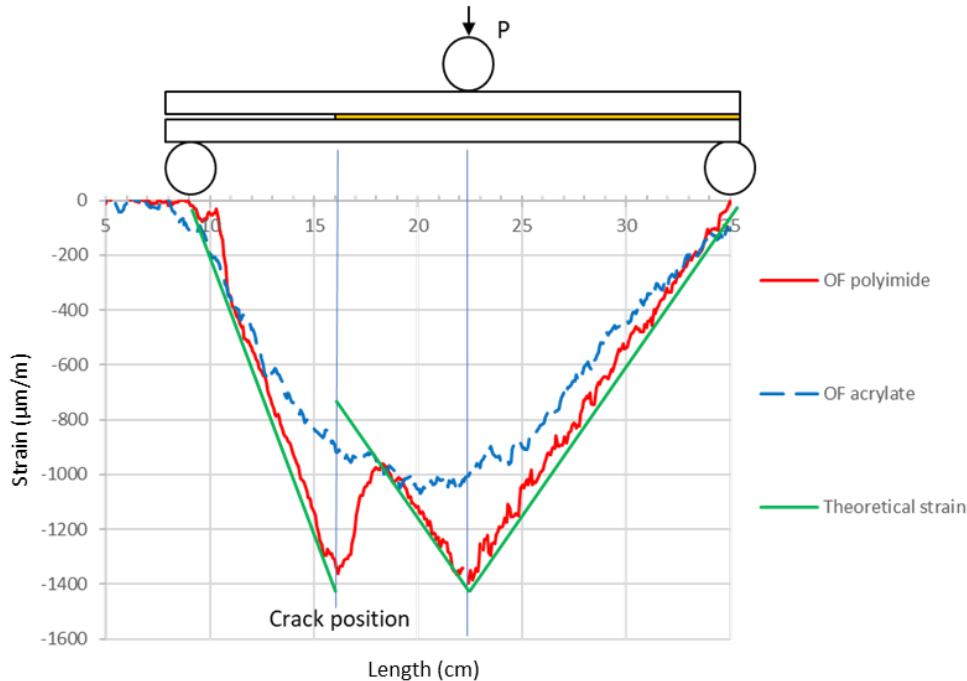


Figure 2.3-7: Local strain measurement during an ENF test with polyimide and acrylate optical fiber coating.

The curves show that depending on the type of fibers, the results are very different. The polyimide fiber shows distinct strain peak at the load application point and at the crack front position, while the acrylate fiber results show no visible peak. This may be explained by the thickness of the coating and the rigidity of the coating or/and the coating-adhesive interface (Figure 2.3-6). The impact of the coating on the smoothing of the strain gradient is easily visible from these results. To be able to follow the crack propagation during DCB, ENF and MMB tests, it seems, in our case, that the use of polyimide coated optical fiber is absolutely essential. Next parts will present the detailed analysis of the crack position monitoring during complete DCB, ENF and MMB tests using the polyimide optical fiber.

2.4. DCB test investigations

2.4.1. Load/displacement curve analysis and failure mode

The obtained load/displacement curve for the DCB test is shown in Figure 2.4-1. Three stages can be observed. The first one is a linear elastic stage up to point A ($t_A=85s$). Once the load exceeds the point of non-linearity, damage appears in the bondline, extends and forms the fracture process zone (FPZ). This leads to a slope decrease, and an increase of the compliance C ($C=\delta/P$, δ the opening at the load application point, P the Load). When the FPZ is fully developed, the load/displacement curve reaches its maximum point (point B, $t_B=115s$). The crack propagation is assumed to occur after the first load decrease, since the sample cannot store more elastic energy. Consequently, the upcoming analysis will be focused on the results computed after point B. The failure mode for this test was cohesive in the bondline.

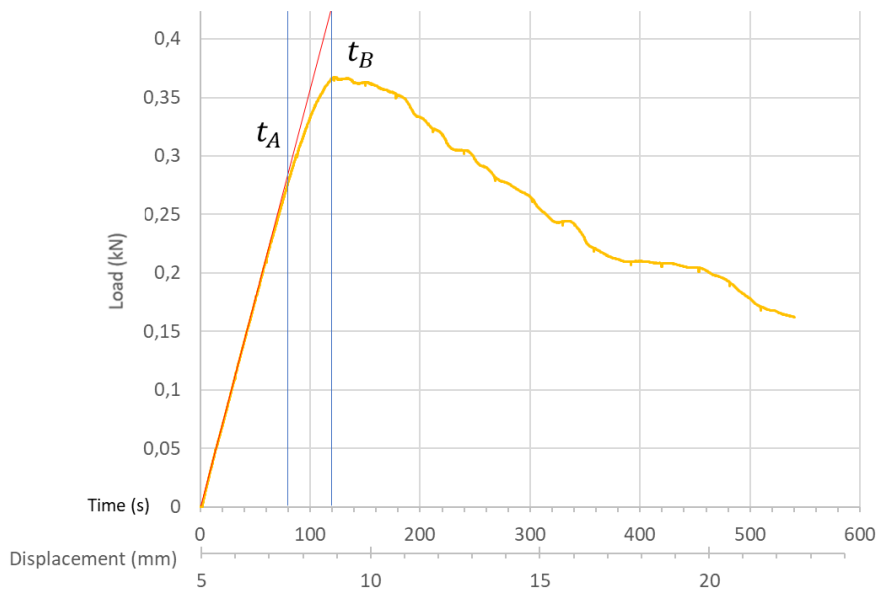


Figure 2.4-1: DCB resin A load/time curve.

2.4.2. Exterior optical fiber

For the DCB test, according to the theoretical analysis, an optical fiber on the upper surface of the sample seems sufficient to measure the crack propagation. Figure 2.4-2 presents the obtained experimental strain profiles along the lap length with the optical fiber, before and during the crack propagation. Each curve corresponds to a different time. Note also that all

successive strain profiles were shifted in abscissa by the same amount to match the initial crack propagation of 85 mm.

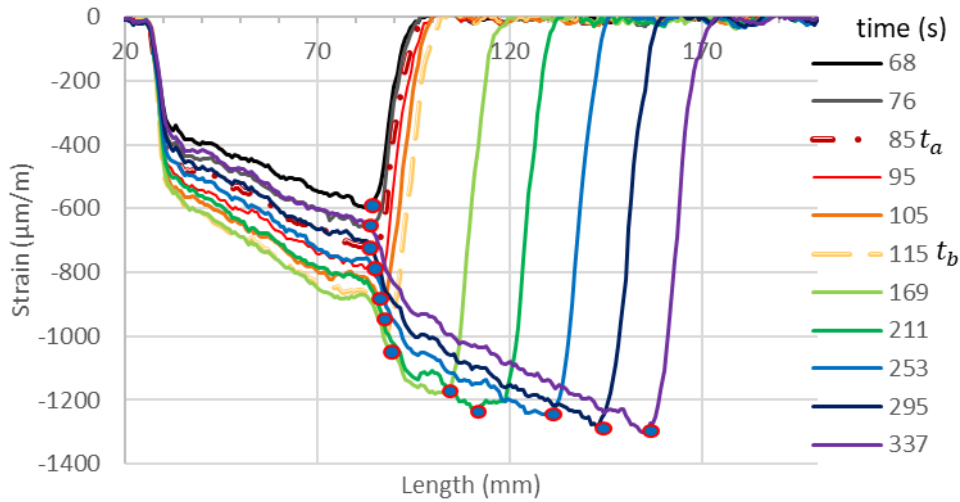


Figure 2.4-2: DCB exterior optical fiber continuous strain measurements along lap length for different times.

As proposed from the theoretical analysis described in the section 2.2.2, the position of the peak (red dots in Figure 2.4-2) is used to monitor the crack propagation. A limited shift of the maximum of the curve to the right can be observed at t_A , which is supposed to be linked to the beginning of the creation of the process zone in the bondline. The main propagation is supposed to happen after t_B as visible in Figure 2.4-2. After this time, it can be shown that the maximal strain value remains stable at a value of around $1250\mu\text{m/m}$. Thus, the local stress state remains similar at the crack tip during the crack propagation.

Figure 2.4-3 presents the crack propagation curve obtained from the optical fiber measurements. A smoothing of the data with the use of local mean has been made to reduce the raw crack front computation noise (each raw data value is converted to average of the 5 data points centered on the original value). It shows that the main crack propagation (macro-crack) occurred after the time t_B . The initial shift between t_A and t_B measures 3 mm. Two artefacts measurement can be seen at around 150 s which generate local error in the crack length measurement, but without compromising the validity of the measurement.

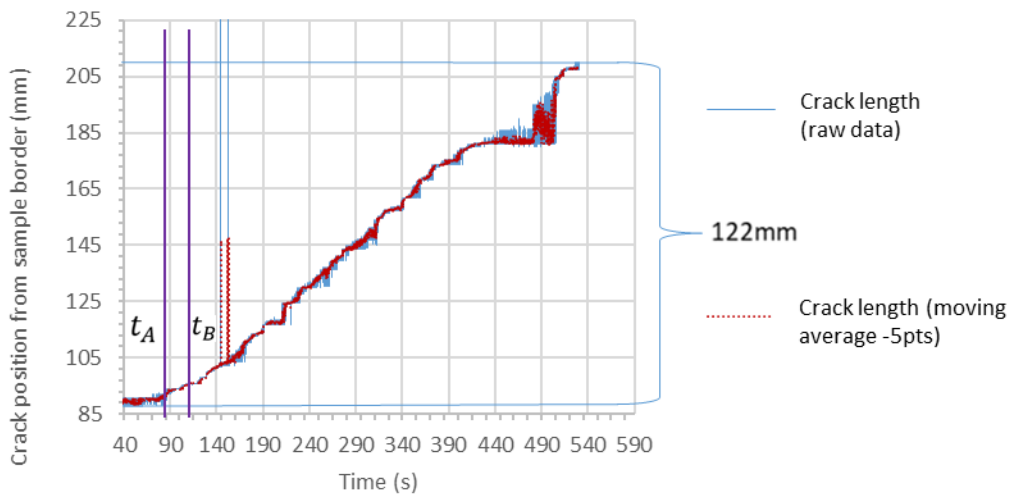


Figure 2.4-3: Crack propagation curve for the DCB test - data processing via local mean approximation.

The resulting curve shows that, as visible in Figure 2.4-1, the crack has propagated in a stable manner during the whole test. The peak of maximal strain has been correctly defined during nearly the whole crack propagation. The overall crack propagation length at the end of the test was 122 mm.

2.4.3. Crack length visual validation

After the end of the test, a dye penetrant was used to highlight the area between the initial crack front and the final crack front (colored by the product) marking the cracked area of the sample. The measurement of the length of this area at the middle of the sample is set as the crack length at the end of the test as visible in the Figure 2.4-4a.

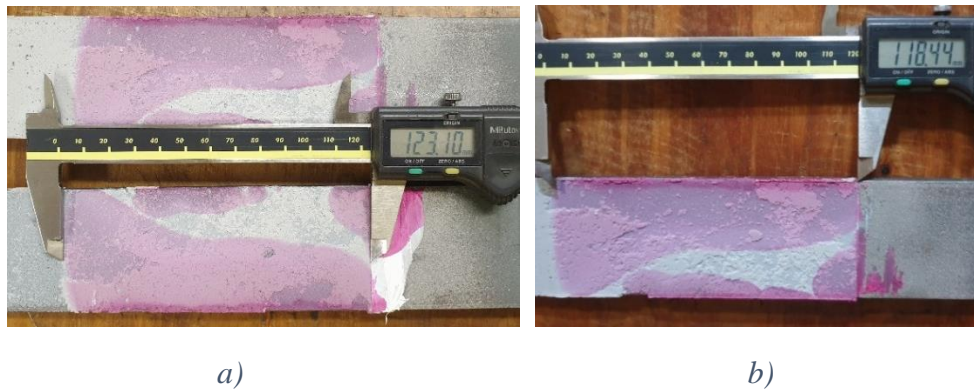


Figure 2.4-4: Visual measurement of the crack length of the DCB test, a) in the middle and b) at the border.

The result shows that the final crack length obtained by the optical fiber (122 mm) is really close to the value measured with a caliper (123.1 mm). This result confirms that the exterior optical fiber is able to monitor the crack propagation for DCB test.

It is worth noting that the maximal difference between the crack front position at the center of the sample and on the edges (where visual inspection and DIC are normally carried out) is equal to 4.7 mm. This difference is important in regards with the studied propagation distance of 122 mm. This result shows clearly that the crack propagation on the flank on the specimen can lead to underestimate the crack propagation. Thanks to the distributed optical fiber, a better measurement could be achieved.

2.5. ENF test investigations

2.5.1. Load vs time curve analysis and failure mode

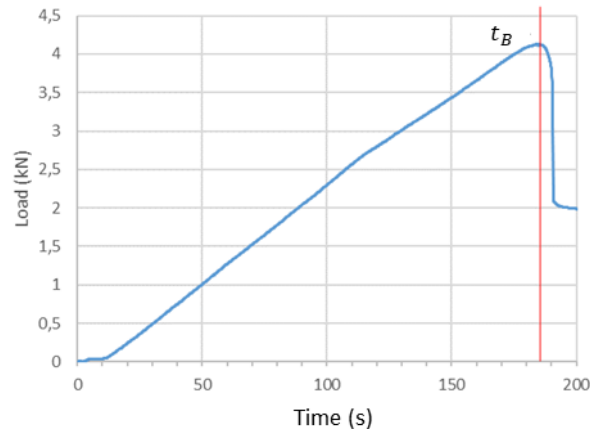
Two ENF tests were conducted:

- the first one with only the exterior optical fiber, to validate if the strain peak measured on the surface could be used to measure the crack front position,
- the second one, with an embedded optical fiber, to study the local strain in the adhesive and compare it to a finite element model, prior to the crack propagation.

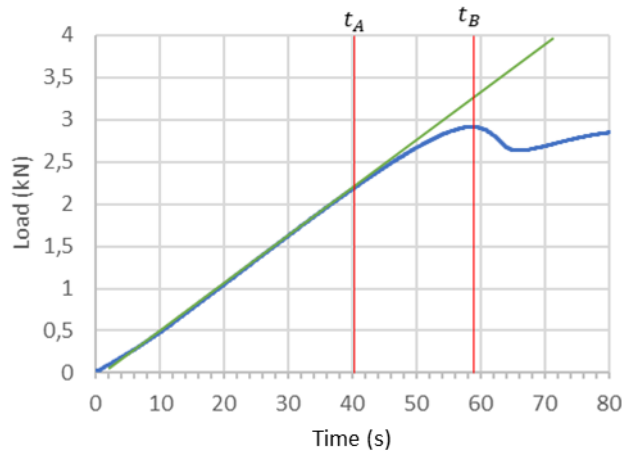
The obtained load vs time curve for the first ENF test (test 1) is shown in Figure 2.5-1a. To limit the crack propagation speed and help to monitor the displacement of the strain peak, the loading of the sample was stopped (fixed displacement) when the maximum load was reached.

However, the crack propagation still occurred as can be observed with the rapid decrease of the load. The resulting load/displacement curve can be decomposed in two stages. The first one is a linear elastic stage up to time $t_B = 189$ s. Once the load exceeds this limit, the crack propagation has occurred up to the local minimum after the first load decrease. Note that, no nonlinear loading correlated to the creation of the fracture process zone in the bondline is clearly observed for the test 1.

For the test 2, three stages can be observed: a linear loading up to time $t_A = 40$ s, a nonlinear loading which is correlated to the creation of the fracture process zone in the bondline, and the crack propagation after time $t_B = 58$ s (Figure 2.5-1b). Consequently, the upcoming analysis will be focused on the results computed after time t_B . The failure mode for this test was cohesive in the bondline.



a)



b)

Figure 2.5-1: ENF resin A load / time curve, a) test 1 and b) test 2.

2.5.2. Exterior optical fiber analysis and crack propagation determination

Figure 2.5-2 presents the obtained strain measurements along the length of the sample for the exterior optical fiber during the crack propagation of the test 1. Each curve corresponds to a different time. The two initial peaks described in part 2.2.1 (theoretical analysis) are clearly visible before the crack propagation. For the first peak (on the left in Figure 2.5-2), it can be observed that its position remains stable in the beginning of the loading. changed during the test (related to the crack propagation). This position corresponds to the initial crack front

position. Note that all strain profiles were shifted in abscissa by the same amount to correspond to the initial crack length of 85 mm (vertical blue line in Figure 2.5-2). When the crack propagates, the first peak shifts in direction of the load application peak point. Once the crack propagation is finished, the two peaks have merged near the position of the load application point. The strain loss on the right side of the curve is associated with the load decrease after the crack propagation.

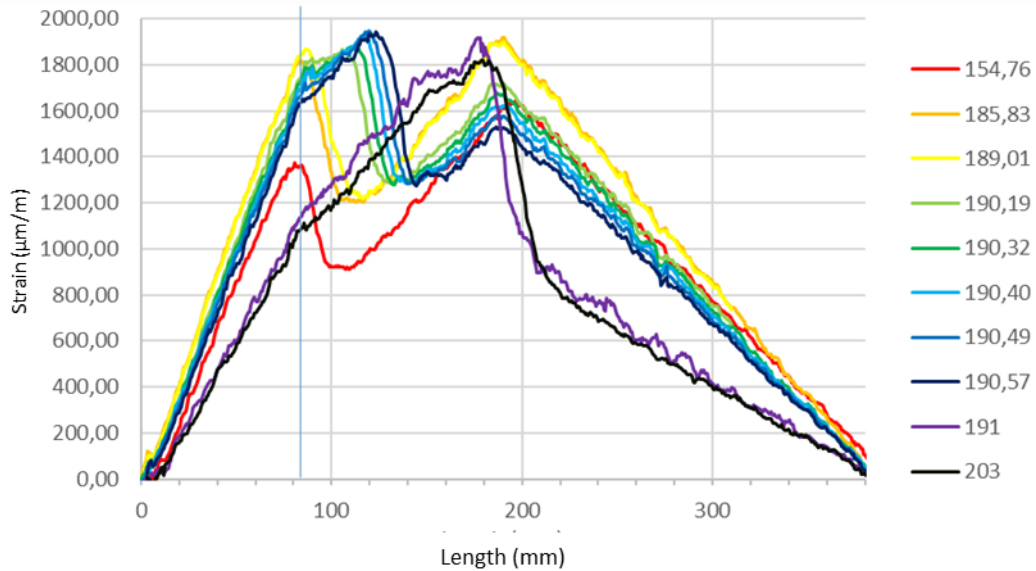


Figure 2.5-2: Exterior optical fiber distributed strain measurements between times 154.76 s and 203.0 s.

Figure 2.5-3 represents the maximal values of the optical fiber strain measurements versus the axial length for different times after the crack propagation. We can observe a shift of the maximum of the curve to the right, indicating a displacement of the crack tip. We can also observe that the main crack propagation occurs between $t = 189.01$ s and $t = 191.0$ s with a fast propagation between $t = 190.57$ s and $t = 191.0$ s.

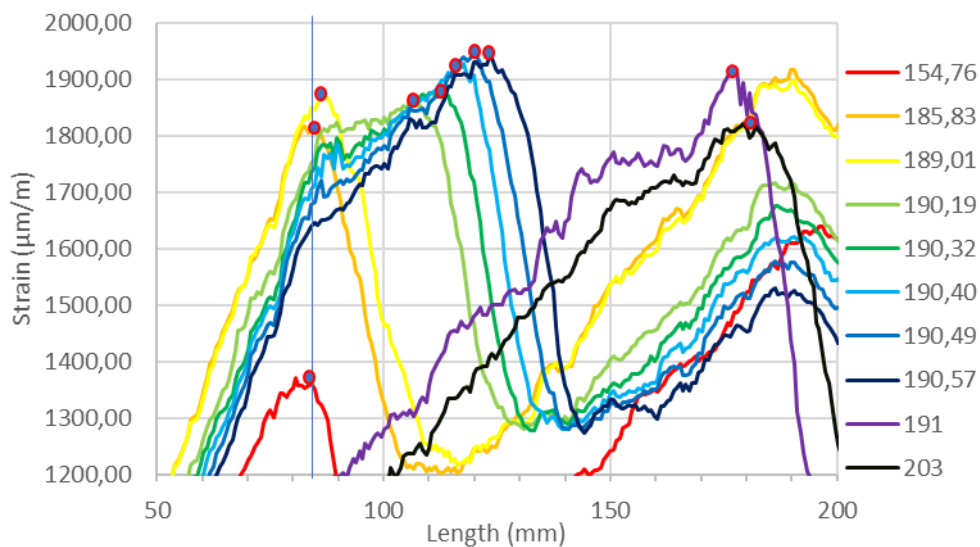


Figure 2.5-3: Shift of the first peak of the strain profiles measured during the ENF test.

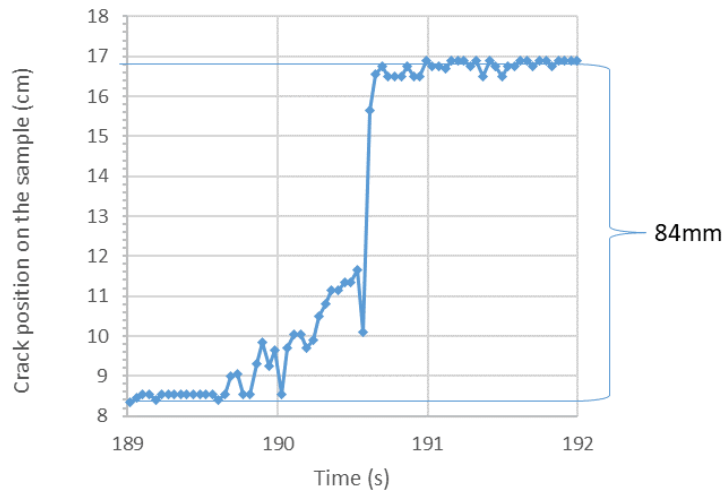


Figure 2.5-4: Crack propagation curve for the ENF test – raw data processing via local mean approximation.

Figure 2.5-4 shows the crack propagation curve obtained with the distributed optical fiber sensor. From this curve, it can be confirmed that the crack propagated very quickly at starting at about 190.6 s. Unfortunately, the frequency of the interrogator ($\sim 20\text{Hz}$) was insufficient to obtain a relatively high number of points during the fast part of the crack propagation ($\sim 50\text{cm/s}$). As consequence, no local meaning computation could be done. In spite of this, the final crack length can be measured by the optical fiber. A value of $84 \pm 1\text{ mm}$ is found.

2.5.3. Crack length visual validation

After the end of the test, dye penetrant was used to highlight the initial and final crack front. The measurement of the length of this area at the middle of the sample is set as the crack length at the end of the test as visible in Figure 2.5-5.



Figure 2.5-5: Visual measurement of the crack length at the end of the ENF test.

In the case of the ENF test, the result shows that the final crack length obtained by the optical fiber is 84 mm which is really close to the value measured with a caliper (86 mm). This result seems to confirm that the exterior optical fiber is able to monitor the crack propagation for the ENF test. It must be noted that, in this case, the crack front has remained straight at the end of the test. It is consistent with the results presented in [107] in the case of ENF tests realized on composite samples. In this study the crack front has been monitored during the test showing that it may change in orientation (non-perpendicular to the propagation direction), but remains always straight.

2.5.4. Embedded optical fiber curve analysis

Figure 2.5-6 and Figure 2.5-7 present the obtained strain profiles along the lap length for the embedded optical fiber of the second sample. Different measurement times were chosen and each profile corresponds to one of these moments before and during the crack propagation. Before the crack propagation ($t_B=58s$), the resulting curves present a visible peak. This is supposed to correspond to the position of the initial crack front. During the test, this initial strain jump remains at the initial crack front position, but the strain profile is modified along the joint. The experimental results show a strain plateau with a length of up to 2cm at the beginning of the crack propagation (Figure 2.5-6). This is supposed to be linked to damage near the crack tip before its propagation and could thus be used as a measurement of the fracture process zone (FPZ) length. This length being bigger than 1.5 cm, discussion could be opened on the assumption commonly made in the linear elastic fracture mechanics theory (generally used to compute the critical toughness), that requires that the process zone size remains confined to the crack tip area and with a length being shorter than the adhesive thickness. Östlund and Nilsson [109] have further investigated this recommendation for crack propagation in a double cantilever beam specimen with a cohesive zone heading the crack tip. Crack propagation was analyzed both with beam theory and continuum theory. Letting PZI the process zone length, and h_s the adherent thickness, the results of Östlund and Nilsson indicate that the ratio $\frac{PZI}{h_s}$ should not be greater than 10 as a reasonable limit for the applicability of beam theory. In our case, the adherent being 5 mm thick, and the process zone being supposed to be 15 mm long, this recommendation is fulfilled.

After the initial crack propagation (Figure 2.5-7), no clear indication of the position of the crack front is observed using optical fiber measurements. The use of embedded optical fiber may therefore require more complex strain state analysis tools to be able to monitor the crack front position.

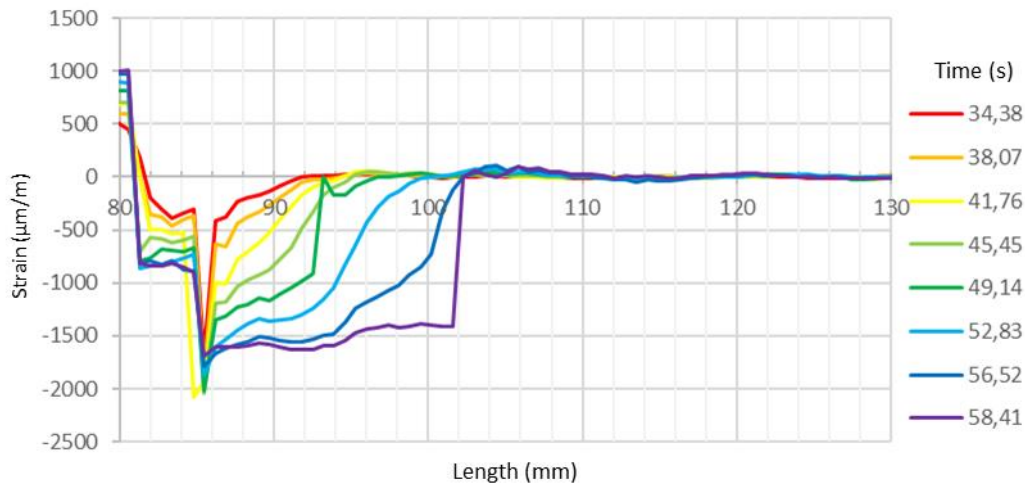


Figure 2.5-6: Embedded distributed optical fiber strain measurements before crack propagation.

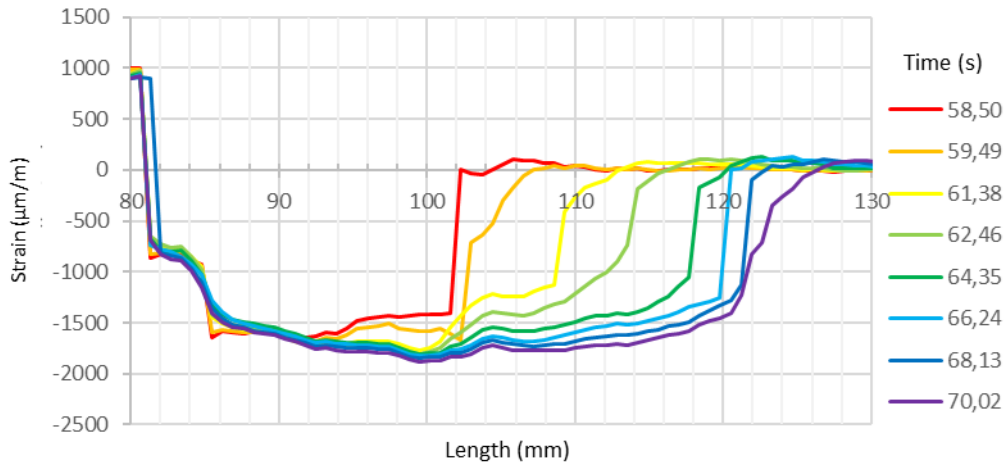


Figure 2.5-7: Embedded distributed optical fiber strain measurements after crack propagation.

2.5.5. Numerical validation of the crack length measurement

For the ENF test, a finite element model (FEM) has been built with the software Femap NX Nastran [110] using the same geometry and boundary conditions as the real one. It aimed at understanding the optical fiber strain measurements, having information on the strain state in the adhesive and validating the crack length measurement. The number of elements in the adhesive thickness is 3 and the mesh was set as in Figure 2.5-8 with linear quadrilateral elements (Q8). The model was 3D. The adhesive thickness was defined at 1 mm, with one element in the z direction. The boundary conditions definition was to block all the out of plane displacements (z direction) to simulate plane strain condition. A displacement in the y direction was applied at the center of the sample to simulate the load application point (x and z displacements were blocked). The displacement in the y direction were blocked at the position of the supports. A pure elastic behavior was considered for all materials. The Young modulus of the adhesive was set at 11 GPa, based on the adhesive datasheet and the steel modulus was defined at 210 GPa.

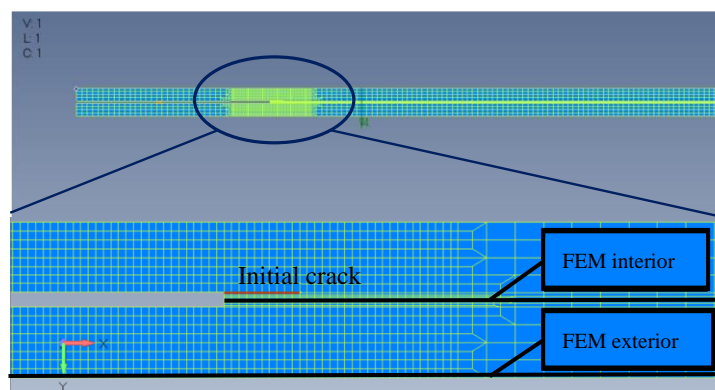


Figure 2.5-8: Finite element mesh and strain measurement area.

A comparison of the strain profiles obtained from experimental and numerical works is carried out in Figure 2.5-9 and Figure 2.5-10. Two moments before crack propagation are analyzed: $t_A = 39$ s and $t_B = 58$ s.

For the time $t_a = 39$ s, Figure 2.5-9a shows that the model validates the assumption that the initial crack front position is correlated to the position of the local maximal strain measured at the surface of the specimen. Concerning the embedded measurement in the bondline, Figure 2.5-9b shows that, prior to the non-linear part of the load/displacement curve (before t_A), the internal behavior of the bonding is well modeled (with linear elastic modeling) with an initial peak at the position of the initial crack front, and a parabolical increase of the strain upstream of the crack front. It indicates that in the real case, the process zone creation has not started yet, and that the bondline is only elastically loaded, as supposed from the load/displacement curve shape.

For the time $t_A = 58$ s, the Figure 2.5-10a, presents the strain at the surface of the specimen obtained by FEM and and the optical fiber. The results show that the numerical maximum strain location is situated right above the crack front. A slight shift of the position (< 2 mm) of the maximal point of the strain measured by the exterior optical fiber (blue curves) can be noted just before the crack propagation. It indicates (compared to the numerical result) that, in the real case, the creation of the process zone has generated a shift of the maximal strain peak upstream of the crack front. Concerning the embedded measurement in the bondline, Figure 2.5-10b shows that the linear FEM continues to predict a fast strain increase (absolute value) upstream of the crack front with a similar shape than for t_A . On the contrary, the experimental result shows a strain plateau around the value $-1500 \mu\text{strain}$. This is supposed to be linked to the local plasticity (or damage), and may thus correspond to the fracture process zone length, occurring in the bondline, which is not considered in the elastic FEM model.

For the strain profiles measured by the exterior optical fiber, it must be noted that thicker adherent, and consequently higher rigidity of the sample may create a flatter maximal strain peak. Because of the fiber measurement noise, it could involve higher error in the crack front position measurement.

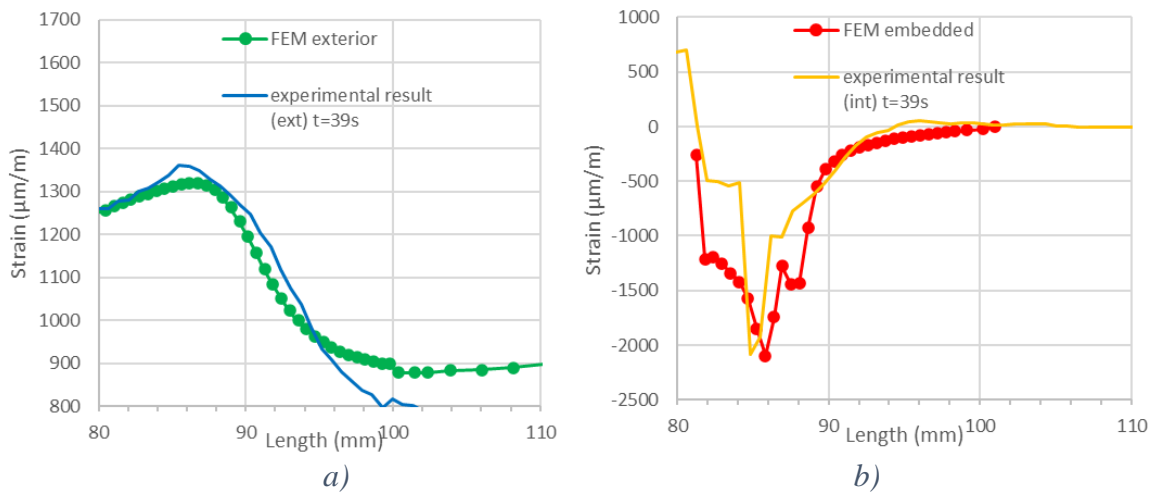


Figure 2.5-9: Comparison of strain profiles along lap length: elastic FEM analysis vs experimental measurements at 39 s, a) exterior measurement, b) embedded measurement.

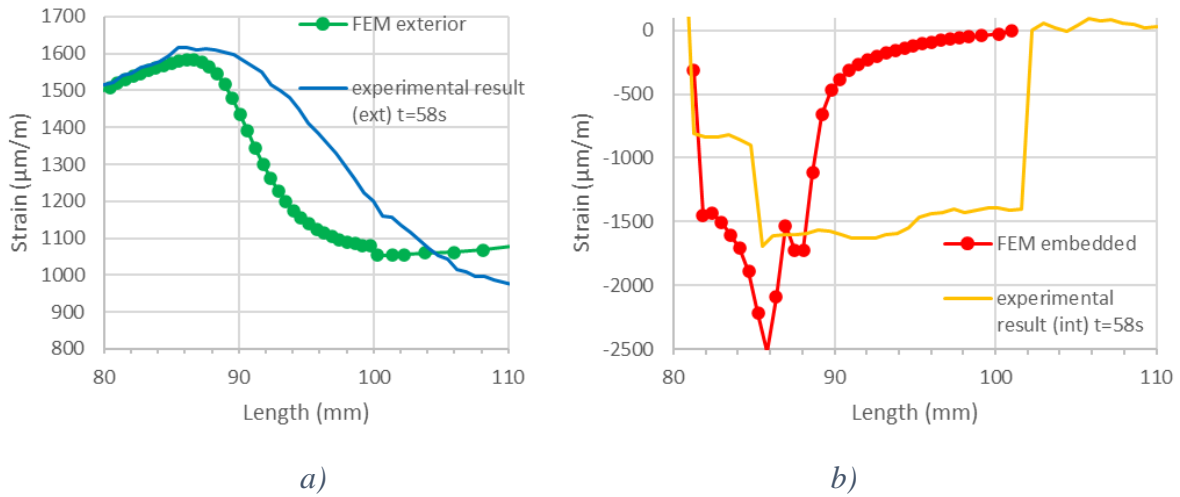


Figure 2.5-10: Comparison of strain profiles along lap length: elastic FEM analysis vs experimental measurements at $t_B = 58$ s, a) exterior measurement, b) embedded measurement.

2.6. MMB test investigations

2.6.1. Load vs time curve analysis and failure mode

Finally, to validate the theoretical approach exposed in section 2.2.3, with mixed mode loading, an MMB test was conducted. The crack front position was monitored using only the exterior optical fiber.

The obtained load vs time curve for the MMB test is shown in Figure 2.6-1. Three stages can be observed. The first one is a linear elastic stage up to time point A ($t_A = 140$ s). Once the load exceeds the point of non-linearity, damage appears in the bondline, extends and forms the fracture process zone (FPZ). This leads to a slope decrease, and an increase of the compliance. When the FPZ is fully developed, the load vs time curve reaches its maximum at time $t_B = 165$ s. The crack propagation is assumed to occur after the first load decrease. The failure mode for this test was cohesive in the bondline, similar to the DCB and ENF results.

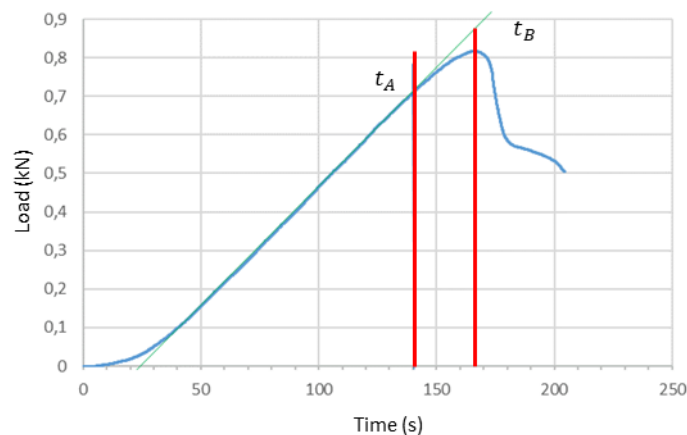


Figure 2.6-1: MMB test load/displacement curve.

2.6.2. Optical fiber analysis and crack propagation determination

2.6.2.1. Exterior optical fiber

The crack front position was monitored using only the exterior optical fiber. Figure 2.6-2 presents the strain measurements along the length of the sample for the optical fiber during the crack propagation. Each curve corresponds to a different time. It can be verified that a maximum strain value can be measured initially (corresponding to the initial crack front position) and that the position of this maximum is shifted during the test (related to the crack propagation).

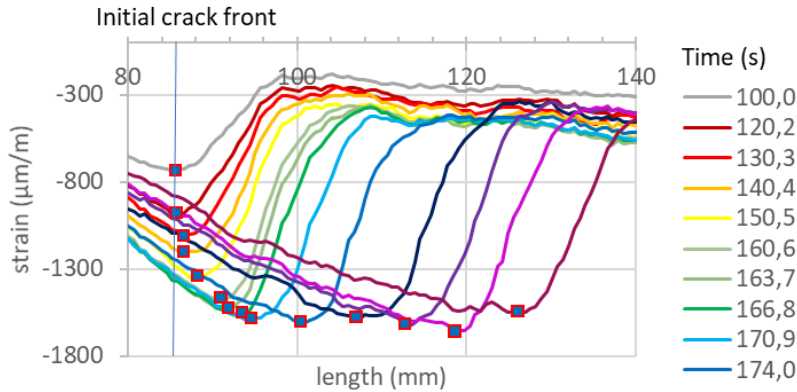


Figure 2.6-2: Optical fiber continuous strain measurements between time 100s and 174s.

At the beginning of the test, the position of the maximal strain value (at $x=86$ mm) corresponds to the initial crack length. A shift of the maximum of the curve can be observed, indicating a displacement of the crack tip after $t=140$ s.

The displacement of this peak is post-treated to obtain the crack propagation (Figure 2.6-3). A smoothing of the data with the use of local mean has been made to reduce the raw crack front computation noise (each raw data value is converted to average of the 5 data points centered on the original value).

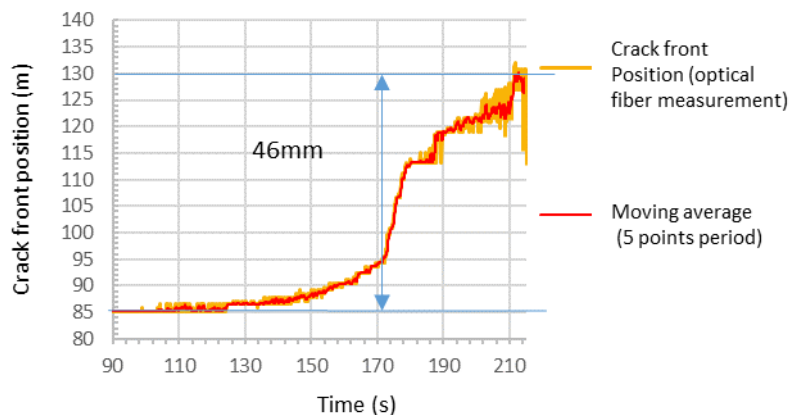


Figure 2.6-3: Crack propagation curve for the MMB test.

2.6.3. Crack length visual validation

The final crack front length was measured at mid-width of the sample as shown in Figure 2.6-4a for the MMB test. In this case, the result shows that the final crack length obtained by the optical fiber is 45.67 mm which is very close to the value measured with a caliper (45.5 mm).

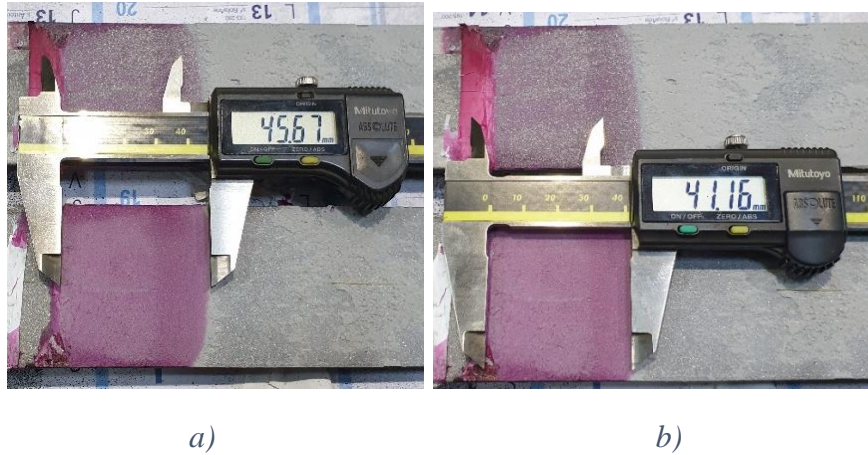


Figure 2.6-4: a) Visual measurements of the crack length at the end of the MMB test, a) at mid width, b) on the border.

In the MMB test, the crack length on the border of the sample, where visual inspection and DIC are normally carried out, was also measured as described in Figure 2.6-4b. The maximal difference between the crack front position at the center of the sample and on the edges is 4.5 mm which seems to be important in regards with the studied propagation distance of 45 mm.

2.7. Conclusion

This chapter has investigated the use of distributed optical fiber sensor to measure the crack propagation for steel-to-steel adhesively bonded joints in mode I, mode II and mixed mode (using DCB, ENF and MMB tests). It was shown that the high spatial resolution and the accurate strain measurement of the used optical fiber can greatly improve the monitoring of the crack propagation. The results obtained for the three tests are summarized in Table 2.7-1, showing a comparison of the visual measurement versus the optical fiber measurement. The results highlight a really good correlation between the optical fiber crack position measurement and the visual validation post-test, with an error equal or inferior to the millimeter.

	<i>DCB</i>	<i>ENF</i>	<i>MMB</i>
<i>Optical fiber measurement (mm)</i>	122 ± 1	84 ± 1	46 ± 1
<i>Post-failure visual measurement (mm)</i>	123 ± 1	86 ± 1	46 ± 1

Table 2.7-1: Crack length from the experimental investigations using exterior optical fiber and visual inspection.

The exterior optical fiber proved to give access to consistent crack propagation data during the tests in mode I, II and mixed mode. The only limitation has been proved to be the acquisition frequency of the Luna interrogator in the case of uncontrolled crack propagation (ENF). As far

as the embedded optical fiber was concerned, it was not possible to use it as crack length sensor. Additional development would be required for this.

Several advantages can be highlighted regarding the use of distributed optical fiber sensor:

- the central position of the exterior optical fiber is supposed to reduce error in crack front position compared to more commonly used methods such as DIC or visual inspection that are highly dependent on the crack front shape (both those methods are carried out on the flank of the sample).
- in regards with visual inspection, the use of the optical fiber seems more robust and independent of operators. In comparison with DIC, post-processing appears to be easier to carry out and several optical fibers could be used to improve crack propagation monitoring reliability.

It must be noted that these conclusions have been obtained with relatively thick steel-to-steel bonded samples. This methodology could be used on other samples with different materials (fiber reinforced composites or metals) or different samples shape. It may even be used for crack monitoring of full size CFRP reinforcement patches. It can also be highlighted that the final procedure does not require any embedment of the optical fiber, simplifying the realization of the samples.

The next chapter will study how the critical toughness can be computed using the optical fiber to monitor the crack propagation. This method will be compared to existing ones.

Chapter 3: Critical toughness and cohesive law experimental determination methodology

This chapter intends to study the options to obtain the critical toughness with the help of crack length monitoring using optical fiber and DIC local surface displacement measurement on the edge of the assembly. The first part presents the realized investigations in mode I, mode II, and mixed-mode (DCB, ENF and MMB) on steel-to-steel bonded assembly using epoxy resin B. During these investigations, critical toughnesses were determined using different methods. For mode I and II, methodologies proposed by standards with slight modifications were applied in order to use the proposed crack length propagation measurement with continuous optical fiber. Then, a new methodology is tested to obtain the critical toughness and cohesive laws using J-integral method. The different methodologies are finally compared in order to identify the ones that will be used for the modeling.

3.1. Realized experimental investigations

3.1.1. Samples and experimental program

The specimens chosen for this analysis are similar to the ones described in part 2.3.1. The overall size of the samples remains the same in length, width and adhesive thickness. Only the adherent thickness was increased to 6 mm. The adhesive was a resin that can be used for infusion (called resin B) (Table 3.1-1, Appendix A4).

<i>Young modulus</i>	<i>Tensile strength</i>	<i>Poisson coefficient</i>	<i>Strain at failure</i>
<i>3.2 GPa</i>	<i>58 MPa</i>	<i>0.43</i>	<i>2,5%</i>

Table 3.1-1: Resin B mechanical properties in tension.

For each series of test (DCB, ENF, MMB), two samples were made with a pre-crack being made at each end of the samples, leading to two possible tests for one sample (number #1 or #2 was specified corresponding to the tested side of the specimen). The pre-crack was initiated with the same manner as described in part 2.3.1. The adhesive thickness was controlled with 1 mm insert at each end of the samples.

During the ENF investigations, specific tests were carried out related to the use of primer. Two sets of samples were made. One was prepared with primer. The second one was prepared without primer and was used as a reference.

The DCB (4 tests) and MMB (6 tests) tests were made using the samples with primer.

The samples were made following the preparation procedure already described previously. The steel plates have been sandblasted (rugosity was measured, $5 \mu\text{m} < \text{Ra} < 10 \mu\text{m}$), then solvent cleaned. The straightness of the substrate was checked after sandblasting to ensure a thickness of the adhesive as constant as possible along the sample length. The primer has been applied with a lint free cloth in thin layer (Figure 3.1-1a and b). The samples were then bonded (Figure 3.1-2). In comparison with the procedure described in chapter 2, because of the change in the resin choice, the resin application protocol was modified. The resin B viscosity being much lower than the one of the resin A, the resin application was made by “resin flow” technique.

The samples were prepared and set in place on the flank with the 1 mm gap between the adherents remaining empty. The resin was then introduced inside the sample by gravity at the center of the sample (Figure 3.1-3). This manufacturing process prevents from any bubble in the bondline and ensures good quality of the bondline (in particular, close to the pre-crack). Following the results obtained in chapter 2, an optical fiber was bonded on the surface of all the samples to monitor the crack propagation during the tests.

Table 3.1-2 summarizes the nomenclature of all the samples made for this study. Note that the sample V-2 broke during the manipulation of the sample and could not be studied.

	<i>Samples with resin B with primer</i>	<i>Samples with resin B and without primer</i>
<i>DCB test</i>	<i>DCB I -1 + DCB I -2</i> <i>DCB II -1 + DCB II -2</i>	-
<i>ENF test</i>	<i>ENF V -1 + ENF V -2</i> <i>ENF VI -1 + ENF VI -2</i>	<i>ENF III -1 + ENF III -2</i> <i>ENF IV -1 + ENF IV -2</i>
<i>MMB test</i>	<i>MMB I -1 + MMB I -2</i> <i>MMB II -1 + MMB II -2</i>	-

Table 3.1-2: Fracture tests nomenclature.

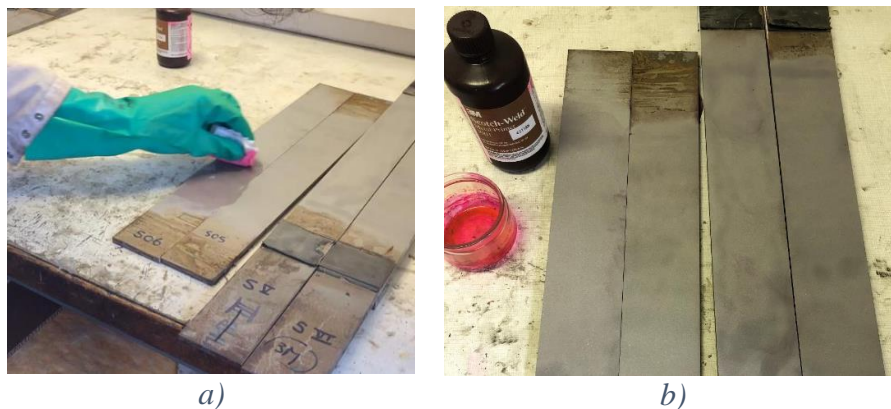


Figure 3.1-1: a) Primer application with the lint free cloth, b) Primer applied in thin layer.



Figure 3.1-2: ENF Samples bonding.

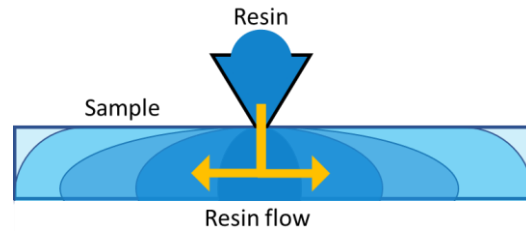


Figure 3.1-3: Resin flow during the bonding process.

3.1.2. Additional monitoring system: Digital Image Correlation

A DIC system was used in addition to the already described optical fiber monitoring system to measure the local displacement fields (local sliding, opening or rotation) at crack tip (initial crack front) on one flank of the specimens. The use of DIC was only limited to the local displacement measurement and it was not used for the crack position monitoring, as it was already performed by the optical fiber.

For each test, a black and white speckle is deposited on the specimen by non-homogeneous spraying of paint in three successive layers (white / black / white) with an approximative pattern size of around 0.2 mm.

The used optical set-up was the following: two 5 Mpx Basler acA2440-75um cameras installed with two Kowa LR1015WM52 lenses (50mm) at an angle of 15 degrees, placed at a certain distance of the sample depending on the required surface measurement. The acquisition rate was set at 5 Hz. The monitoring is made by a commercial system (CorreliSTC by Corelli Solution) to carry out digital image stereo-correlation on the flank of the specimen, at crack tip, as visible in Figure 3.1-4. The cameras were adjusted following the Corelli© software procedure (brightness / sharpness / calibration / synchronization). The distance between the sample and the cameras depends on the suited measurement area. This area called region of interest (ROI) remains in our case close to 6cm x 2cm around the initial crack location. The choice of the resolution is made following the recommendation of the Correli software speckling analysis tool that proposes the best mesh size compromise between spatial resolution and measurement accuracy (set at 16x16 pixels for all tests).

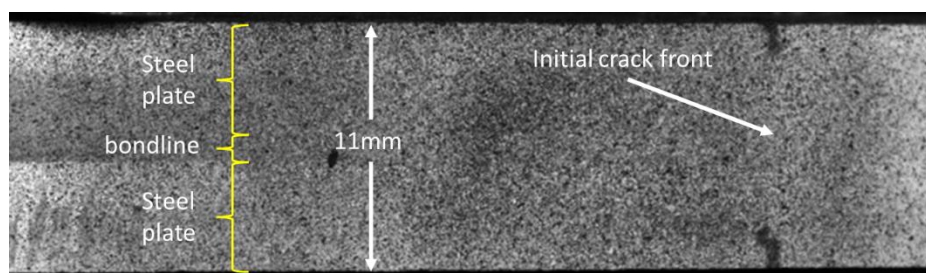


Figure 3.1-4: Example of speckle and initial crack front.

3.2. Determination of critical toughnesses using standard procedures

3.2.1. Obtained failure mode

The failure mode of all the samples were registered to determine the weak link of the bonding. All the pictures of the ENF tests are visible in Appendix A1. For the DCB tests, the failure is fully cohesive in the adhesive layer (Figure 3.2-1). For each DCB test, two parts were visible in the failure pattern: a first one corresponding to the initial unstable crack propagation in the shape of a wave (crack front shape is also visible); and a second one, with a much more disturbed pattern for the stable crack propagation step. This strange behavior has already been described for thick (10mm) epoxy steel-to-steel bonding in [115] where the authors conclude that this phenomenon should be expected when adhesive's critical toughness is lower than the interfacial toughness.

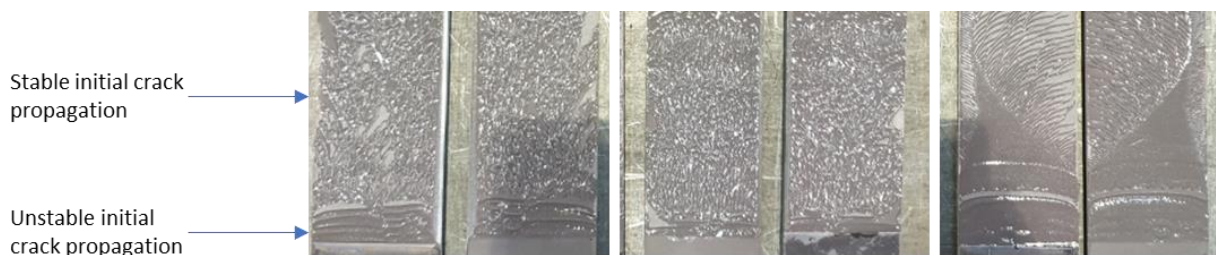


Figure 3.2-1: DCB resin B fracture surface.

For the ENF case, the bonding without primer (configuration 1) shows a perfect adhesive failure (the interface is thus considered as the weak point). When using the primer, the failure seems also to be adhesive. Nonetheless, it appears not clear if it is the primer/steel interface, or the primer/resin interface that has broken. The difference can hardly be made due to the really thin layer of primer.

For the MMB test, at the 50% mode ratio, the failure is mixed adhesive and cohesive (in adhesive layer). Whereas at the ratio 75%, the failure is 100% adhesive (Figure 3.2-2). These results tend to prove that for this resin, the analysis of the failure mode can give information on the loading mode ratio in the bondline when it is initially unknown.

The analysis of the failure mode allowed us validating the quality of the bonding procedure, as no bubble in the bondline are visible and as the initial crack front is well defined.

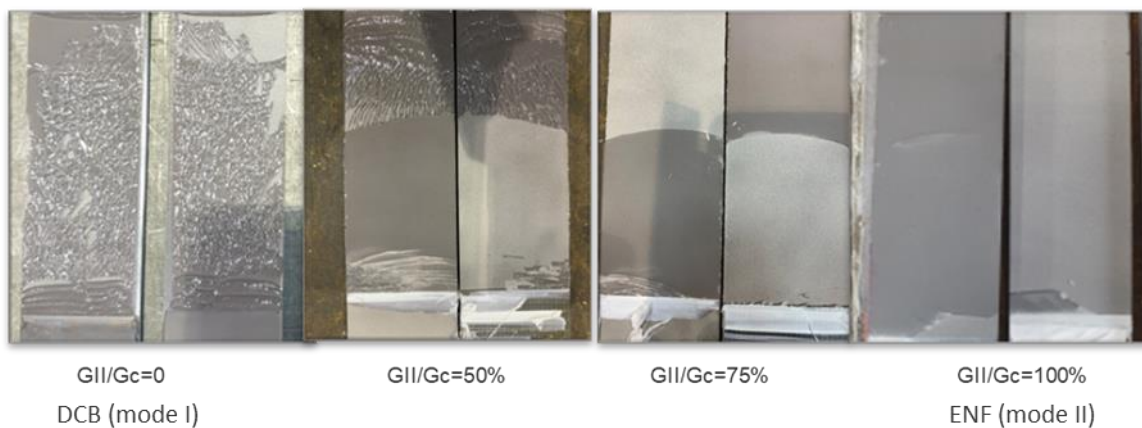


Figure 3.2-2: Resin B fracture surface for different modes.

3.2.2. Obtained results in mode I (DCB investigations)

Following the ASTM standard test analysis, with the help of the optical fiber for crack length measurement, the three methods (BTM, MBTM and CCM), described in part 1.4.3, were used to compute the critical toughness G_{Ic} . The standard proposes two main critical value computation. The first one, which can be called the critical toughness at initiation, is computed with the value of the crack just before the crack propagation occurred, where the loading P is maximum. As expressed in part 1.4.3, this value is supposed to be the more conservative, compared to the second one, after crack propagation. The strain energy release rate curve after crack propagation should stabilize at a higher value of critical toughness (the propagation critical toughness).

3.2.2.1. Load/displacement

The analysis of the load/displacement curves visible in Figure 3.2-3 shows that for the four performed tests, the load at failure ranges between 720N and 828N. The first part of the curves shows non-linearity for displacement of ~1 mm. This is supposed to be related to defaults in the samples manufacturing (adhesion of the normally unbonded part of the sample) but not to the material behavior.

The post-peak behavior seems to be very different between the four samples. For the tests I-1, II-1 and II-2, crack propagates continuously after a certain crack length, and tends to stabilize, while for the test I-2, an uncontrolled crack propagation pattern can be observed (series of violent load decrease during all the test), complexifying the determination of propagation critical toughness (Table 3.2-1).

	<i>Initial crack propagation</i>	<i>Crack propagation stabilization</i>
DCB I-1	<i>unstable</i>	<i>Stable (when displacement >4mm)</i>
DCB I-2	<i>unstable</i>	<i>Unstable</i>
DCB II-1	<i>unstable</i>	<i>Stable (when displacement >5mm)</i>
DCB II-2	<i>unstable</i>	<i>Stable (when displacement >3mm)</i>

Table 3.2-1: DCB test nomenclature and crack propagation information.

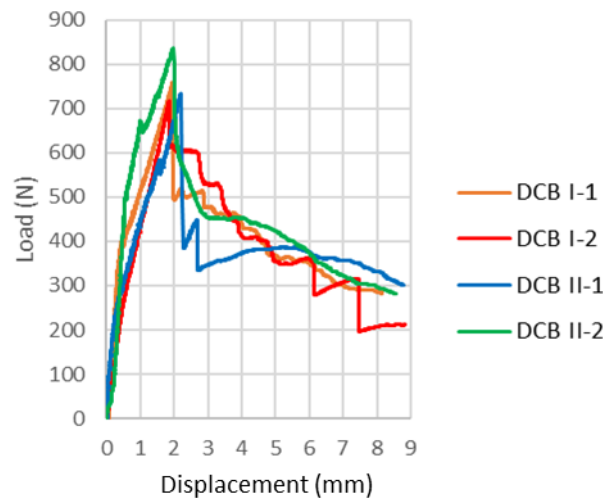


Figure 3.2-3: DCB tests load/displacement curves.

3.2.2.2. Critical toughness

In the next paragraph, the computation of the critical toughness following the three methods (BTM, MBTM and CCM) will be described for the typical case of the test II-I. For this test, an initial unstable crack propagation is observed (Figure 3.2-4a), followed by a stable crack propagation. For the critical toughness determination, only the stable propagation is considered. The crack propagation curve obtained thanks to the exterior optical fiber is shown in Figure 3.2-4b.

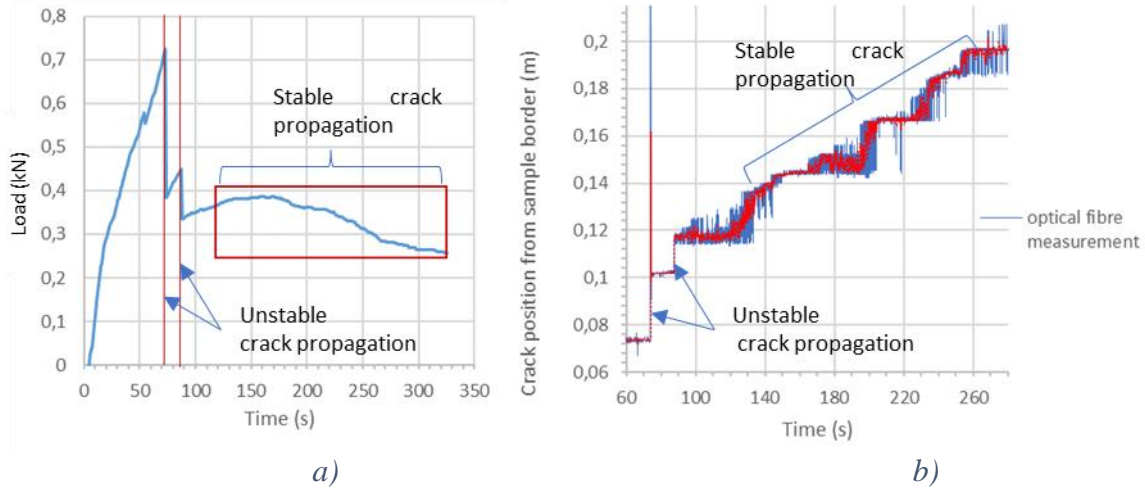


Figure 3.2-4: a) II-I test load/time curve, and b) crack propagation curve.

The two unstable crack propagations, occurring at $t=73s$ and $t=87s$, are clearly visible on the crack propagation curve (violent jump of the curve), and the reloading of the bondline and stable crack propagation occurring after $t=125s$ are also clearly visible.

Figure 3.2-5a displays the linear regression curve of $C^{1/3}=f(a)$. This curve allows the computation of the Δ parameter (crack length compensation factor) in the MBTM. The obtained value is $\Delta=-2.92$.

Figure 3.2-5b shows the linear regression curve of $\ln(C)=f(\ln(a))$ used in the CCM. The parameter value $n=2.62$ is obtained. It can be noted that, in both cases, these linear approximations are relatively accurate with a correlation coefficient R^2 superior to 0.94.

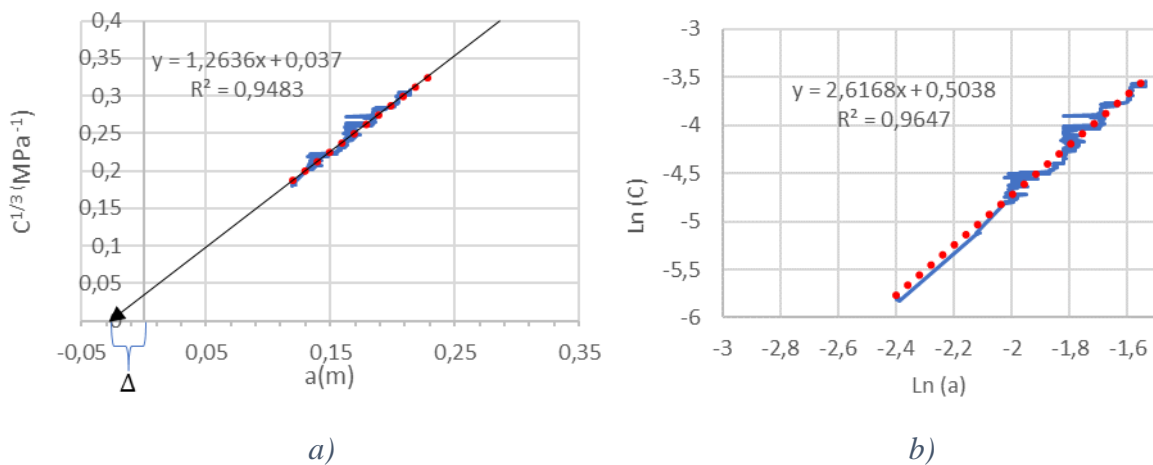


Figure 3.2-5: a) Linear approximation of the $C^{1/3}=f(a)$ curve for the Δ computation, b) Linear approximation of $\ln(C)=f(\ln(a))$ for n computation.

Based on the equations detailed in part 1.4.3 (equation 60 and 61) the BTM, MBTM and CCM toughnesses can be computed. The resulting curves are displayed in Figure 3.2-6. The crack initiation critical toughness is displayed with colored star at the beginning of the curves, while the stabilization values (mean) are displayed as colored line on the stabilized part of the curves. We can see, as expected, that the initiation values are much lower than the stabilization values. It can also be concluded, that the BTM values are much higher than the ones obtained with the two other theories, the MBTM being the more conservative for the stabilized value and for the initiation value.

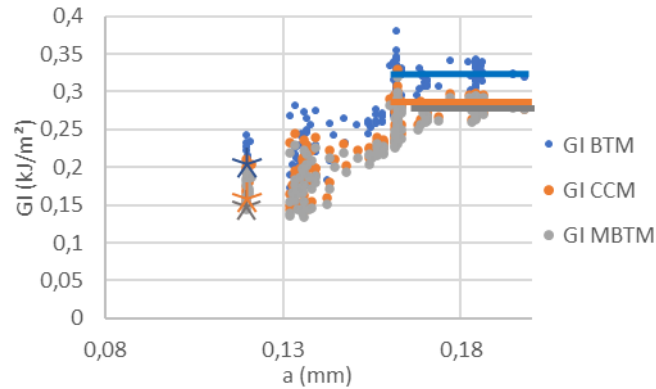


Figure 3.2-6: Critical toughness in mode I at initiation and stabilization for the II-1 test.

All the critical toughness computations performed for the DCB tests are summarized in the Table 3.2-2. Figure 3.2-7 compares average values of the critical toughness obtained for the BTM, MBTM and CCM methods.

G_{Ic} (kJ/m ²)	<i>BTM at initiation</i>	<i>MBTM at initiation</i>	<i>CCM at initiation</i>	<i>BTM at stabilization</i>	<i>MBTM at stabilization</i>	<i>CCM at stabilization</i>
Test I-1	0.25	0.18	0.18	0.3	0.22	0.25
Test I-2	0.28	0.24	0.23	No stabilization	No stabilization	No stabilization
Test II-1	0.24	0.23	0.21	0.32	0.25	0.24
Test II-2	0.21	0.15	0.16	0.32	0.28	0.28
Average	0.25	0.20	0.20	0.31	0.25	0.26
Standard deviation /average (%)	10%	21%	20%	5%	12%	8%

Table 3.2-2: Standard critical toughness characterization with optical fiber crack length measurement.

The critical toughness at initiation is the lower critical toughness for all the tests by 20-30% independently of the chosen computation methods (Figure 3.2-7). The dispersion of the stabilized results for the BTM, MBTM and CCM remains inferior to 12%, while the dispersion for the critical toughness at initiation tends to be much higher (9%-21%). The limited number of tests allows limited confidence into the values of standard deviation. The differences in values of the BTM, MBTM and CCM is consistent with the description of the ASTM standard [87]. The difference between the MBTM and the CCM is minor at initiation and stabilization

values which indicates that the choice of one of the two methods should provide similar results for brittle adhesives (our case).

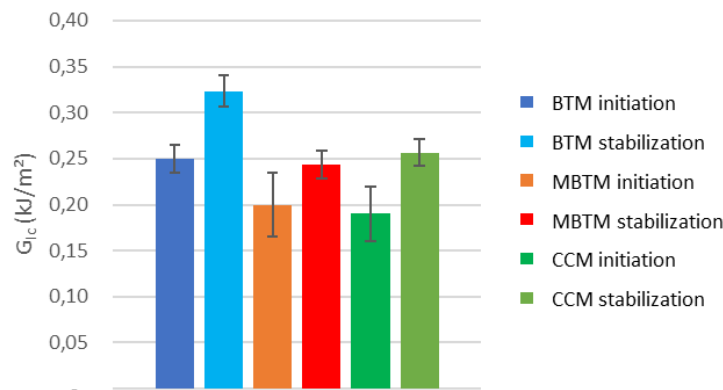


Figure 3.2-7: Critical toughness computation results in mode I.

3.2.3. Obtained results in mode II (ENF investigations)

For the methodology of computation of the critical toughness in mode II, it has been detailed in part 1.4.4, that the MBTM and CCM can be applied [113] in case of controlled crack propagation. This was not the case in this study with all of tests ending with uncontrolled crack propagation. The analysis had therefore to be performed following the ASTM standard proposal. This ASTM standard [110] proposes approximations based on the measurement of the compliance of the ENF samples and the load at failure (as described in part 1.4.4).

The studied samples were tested with different initial crack length a_0 (between 59 mm and 90 mm). The three-point bending tests were performed up to the failure load value. The compliance was computed following the standard recommendations. The nomenclature of the specimens is as follows: specimens III and IV for configuration without primer; specimens V and VI for configuration with primer (Table 3.2-3).

	<i>Surface preparation</i>	<i>a₀ (mm)</i>
<i>ENF III-1</i>	<i>Without primer</i>	73
<i>ENF III-2</i>	<i>Without primer</i>	90
<i>ENF IV-1</i>	<i>Without primer</i>	74
<i>ENF IV-2</i>	<i>Without primer</i>	91
<i>ENF V-1</i>	<i>With primer</i>	59
<i>ENF VI-1</i>	<i>With primer</i>	74
<i>ENF VI-2</i>	<i>With primer</i>	90

Table 3.2-3: ENF test nomenclature.

The post-test analysis of the sample has shown that the ENF VI-1 sample was already broken before the beginning of the test, thus this test was not considered in the analysis.

In the next paragraph, the computation of the critical toughness in mode II, G_{IIc} , is detailed.

3.2.3.1. Load/displacement

Figure 3.2-8 displays the load/displacement curves for tests V-1, VI-1 and VI-2 (samples with primer) and III-1, III-2, IV-1 and IV-2 (sample without primer), corresponding to different initial crack length a_0 . A difference in compliance between the samples is visible (difference in the initial slope of the curves). The uncontrolled crack propagation (fast decrease of the curve after the maximal load) and absence of non-linearity before the crack propagation are also visible.

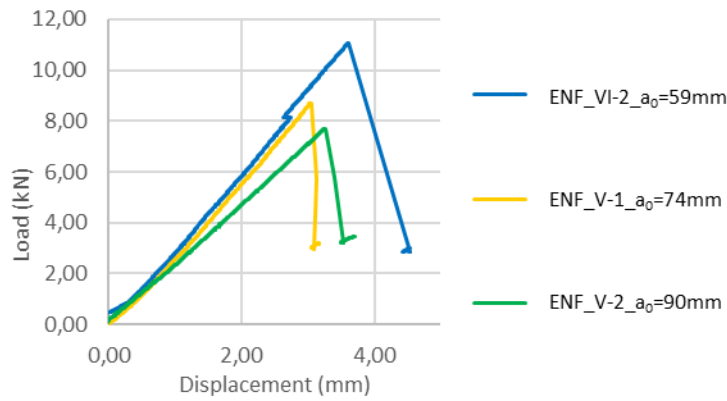


Figure 3.2-8: ENF tests load/displacement curves with primer.

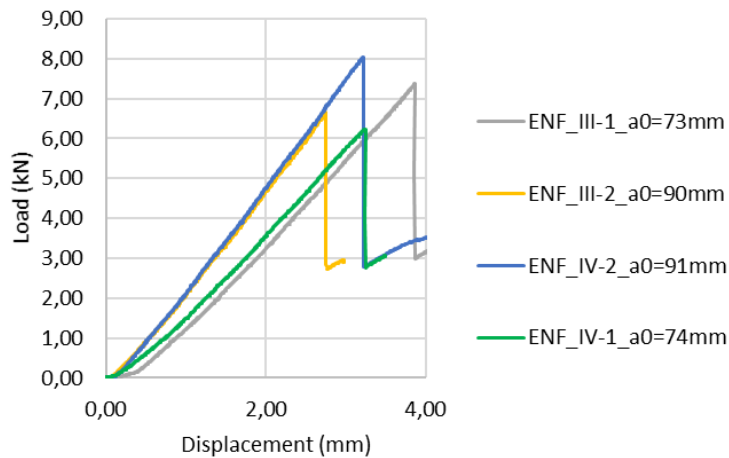


Figure 3.2-9: ENF tests load/displacement curves without primer.

3.2.3.2. Critical toughnesses

In the next paragraphs, the computation of the critical toughness for the specimens with and without the primer is detailed. The compliance was computed following the standard recommendations. The compliance value is computed as a linear regression of the load/displacement curve between the load $P1=P_{max}/10$ and $P2=P_{max}/2$. This is supposed to help to avoid non-linear part in the curve. Figure 3.2-10 displays the computed regression parameter of the $C=f(a^3)$ curve computed following the ASTM standard. It shows relatively good correlation between the linear approximation and the results (compared to result obtained without primer, Figure 3.2-11).

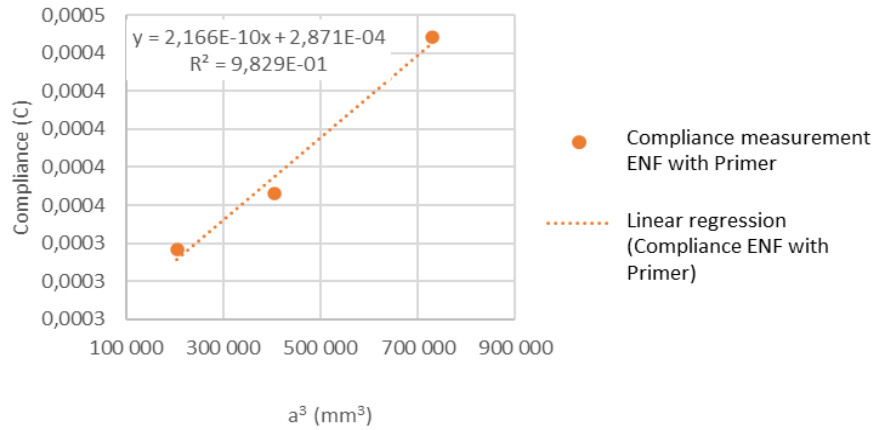


Figure 3.2-10: Linear approximation of the $C=f(a^3)$ curve with primer.

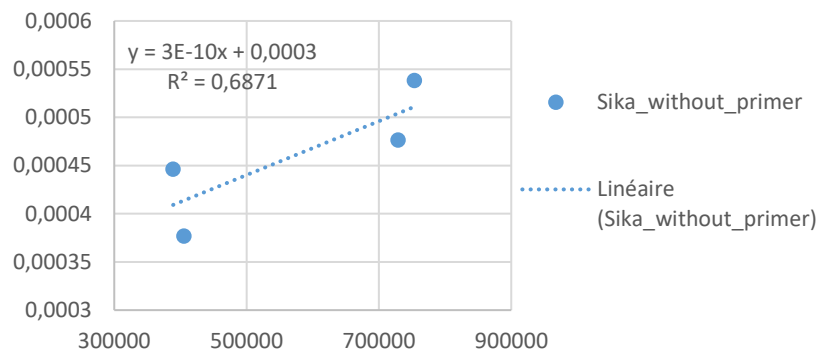


Figure 3.2-11: Linear approximation of the $C=f(a^3)$ curve without primer.

It is to be noted that a minimum of three tests is required. The critical toughness's results obtained for each series of ENF test are summarized in the Table 3.2-4.

	<i>Load at failure</i> P_{max} (N)	<i>Initial crack length</i> a_0 (mm)	<i>Compliance</i> C	<i>Slope of the linear regression</i> m	<i>Intercept of the linear regression</i> A	<i>Resulting critical toughness</i> G_{IIc}
Resin B without Primer						
III-2	6 680	73	0.00040	3.04×10^{10}	0.0003	1.73
III-1	7 450	90	0.00047			3.28
IV-1	8 090	74	0.00038			2.62
IV-2	6 260	91	0.00052			2.37
					<i>Mean</i>	2.50
					<i>Standard deviation</i>	25%
Resin B with primer						
VI-1	8 700	74	0.00037	2.16×10^{10}	0.00028	2.15
VI-2	7 710	90	0.00045			2.50
V-1	11 060	59	0.00034			2.21
V-2	<i>unexpected failure</i>					
					<i>Mean</i>	2.29
					<i>Standard deviation</i>	8%

Table 3.2-4: Critical toughness computation following the ASTM D7905 standard.

The limited number of tests does not allow a high confidence into the values of standard deviation. However, the results with primers seem to have a lower dispersion compared to the results without primer.

The results show that the results with the primer (2.3 kJ/m²), and without any primer (2.5 kJ/m²) are similar (Figure 3.2-12). In addition, we observe that the primer does not decrease the critical toughness of the resin B interface on steel.

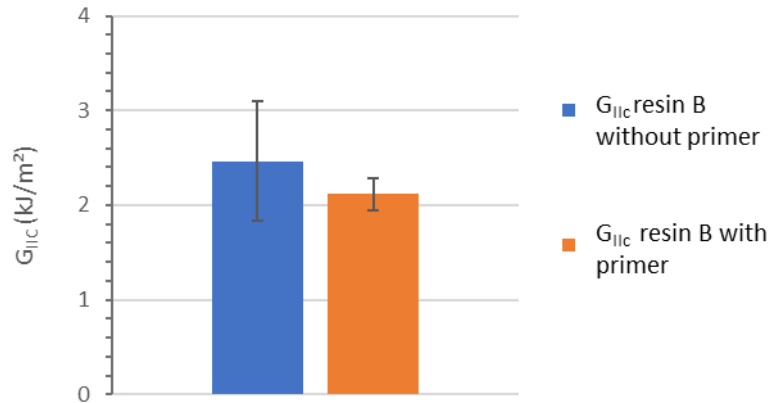


Figure 3.2-12: ASTM Critical toughness computation.

3.2.4. Obtained results in mixed mode (MMB investigations)

3.2.4.1. Load/displacement

To obtain the final critical toughness ratio curve, a series of 4 MMB tests was performed. The load/displacement curves obtained for these tests are shown in Figure 3.2-13.

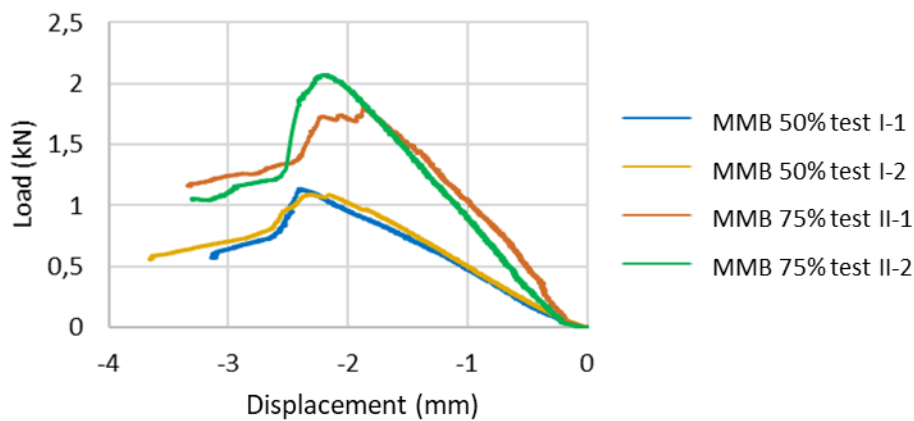


Figure 3.2-13: MMB load/displacement curves.

3.2.4.2. Critical toughness

The critical toughness determination was realized following the standard ASTM D6671 [101] as described in the part 1.4.5. It is specified that in case of uncontrolled crack propagation, an approximation of G_{Ic} and G_{IIc} can be made using the maximal load P_{max} , and the initial crack length a_0 . Nonetheless, it may cause an underestimation of G_c value. In our case, crack propagation is very different for the 50% and 75% G_{IIc}/G_c ratios as visible in the load/displacement curves in Figure 3.2-13. The final results are summarized in Table 3.2-5.

Ratio (G_{II}/G_c)	50%	75%
Critical toughness (kJ/m^2)	0.18	0.22
	0.17	0.28
Average	0.17	0.25

Table 3.2-5: Critical toughness computation of the mixed mode test.

Figure 3.2-14 shows the resulting critical toughness in function of the mode ratio. It can be seen that the results are in accordance with the failure mode analysis, as, the critical toughness in mixed mode between 0% and 50% of mode II remains similar and corresponds to a cohesive failure. Then, between 50% and 100% of mode II, the critical toughness increases by a coefficient 10 up to more than 2kJ/m^2 .

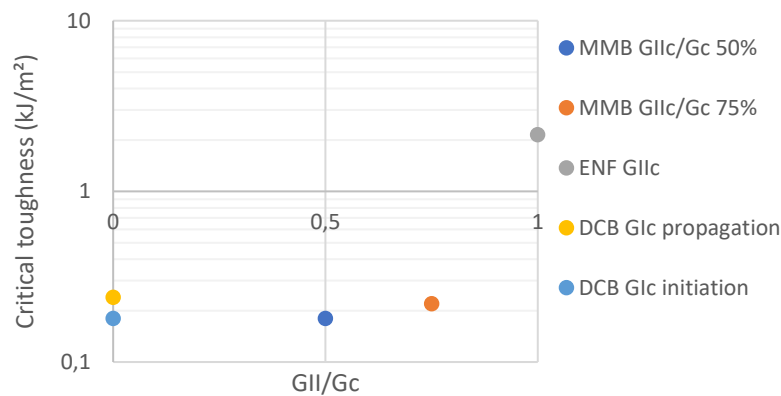


Figure 3.2-14: Critical toughness average value in function of the mode II ratio for the resin B.

3.3. Determination of critical toughnesses and cohesive laws using J integral for mode I and II

Main methods (described in part 1.4.4, 1.4.5, 1.4.3) to obtain the critical toughness in mode I and II have been described previously: the beam theory method, the modified beam theory method and the compliance calibration method [113]. These methods have been adapted to the crack propagation monitoring with optical fiber (compare to the standard visual measurement) and will be in this part, compared to the J-integral analysis performed for the DCB and ENF tests.

3.3.1. J-integral expression for DCB and ENF tests

For adhesive bonding loaded in mode II, Leffler et al. [114] proposed a formulation of the J-integral considering an integration path in the bondline, as shown in Figure 3.3-1. This path can be shrunk to a straight line in the y -direction at the crack tip, and $\sigma_{ij} \cdot n$ has to be null since the crack tips is a free surface.

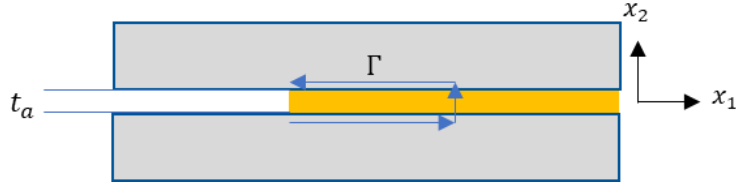


Figure 3.3-1: Adhesive joint and J-integral integration path.

From the equation (45), the equation (80) can then be obtained.

$$J = \int_{t_a} w(\varepsilon) dy \quad (80)$$

With $w(\varepsilon)$, the strain energy density which can be divided in two parts, with the elongation, ε_1 , and the shear deformation, ε_2 , and the conjugated stresses σ and τ , resulting in the equation (81).

$$J = \int_0^{\varepsilon_1} \sigma dy + \int_0^{\varepsilon_2} \tau dx = J_I + J_{II} \quad (81)$$

In the particular case of the ENF test, numerical analyses led by the authors showed that almost no normal stress appears in the adhesive layer except at the loading point. Thus, the equation can be simplified into equation (82).

$$J = \int_0^{\varepsilon_2} \tau dx \quad (82)$$

In order to solve the equation (82), Leffler et al. considered a closed integration path as shown in Figure 3.3-2.

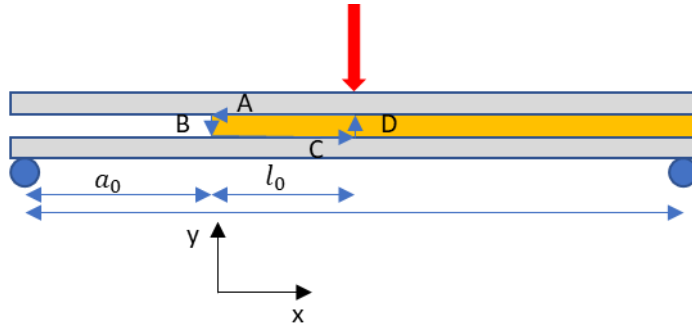


Figure 3.3-2: ENF J-integral integration path A+B+C+D.

Based on this integration path, the expression of J can be partitioned as in equation (83).

$$0 = J_A + J_B + J_C + J_D \quad (83)$$

With:

$$-J = J_B \quad (84)$$

$$J_D = \int_{t_a} w(\varepsilon(x = l_0, y)) dy - \int_{t_a} \tau \frac{du_y}{dx} \Big|_{x=l_0, y} dy \quad (85)$$

In the case of the distance l_0 , between the crack tip and the loading point, being long enough, the adhesive can be assumed to be in a linear elastic state, and thus the shear in the thickness of

the adhesive can be considered as independent on the thickness. Moreover, $\frac{du_i}{dx} = \theta$ is equal to the local rotation at the loading point. This leads to the equation (86) for the expression of J_D .

$$J_D = w(\varepsilon(x = l_0))t_a + \tau(x = l_0) \cdot \theta(x = l_0) \cdot t_a \quad (86)$$

Due to horizontal integration paths for J_A and J_C only the second term contributes:

$$J_A = \int_0^{l_0} \tau \frac{du_u}{dx} dx \quad (87)$$

And

$$J_C = - \int_0^{l_0} \tau \frac{du_l}{dx} dx \quad (88)$$

With u_u and u_l the horizontal displacement of the upper and the lower interface.

In the case of the addition of $J_A + J_C$ the equation (89) can be obtained.

$$J_A + J_C = - \int_0^{l_0} \tau \frac{d(u_u - u_l)}{dx} dx \quad (89)$$

Alfredsson et al. in [118], based on Euler-Bernoulli beam theory, gives an expression of the shear stress in the adhesive layer for $a < x < l_0$.

$$\tau = \frac{Eh_s}{8} \frac{d^2(u_u - u_l)}{dx} + \frac{3}{8} \frac{P}{h_s b} \quad (90)$$

With P the load, h_s the adherent thickness, b the sample width and E the adherent Young's modulus. This expression allows to directly compute the integrals as described in equation (91).

$$J_A + J_C = - \frac{Eh_s}{16} [U'(x = l_0)^2 - U'(x = 0)^2] - \frac{3}{8} \frac{P}{bh_s} [U(x = l_0) - U(x = 0)] \quad (91)$$

With $\frac{d(u_u - u_l)}{dx} = U'$ and $u_u - u_l = U$

At $x = 0$, Alfredsson et al. proposed the boundary condition (based on beam theory) [118]:

$$U'(x = 0) = - \frac{3Pa_0}{Ebh_s^2} \quad (92)$$

With a_0 the initial crack length.

Finally, the addition of all terms leads to the equation (93):

$$J = \frac{9}{16} \frac{P^2 a_0^2}{Eb^2 h_s^3} - \frac{Eh_s}{16} [U'(x = l_0)^2] + \frac{3P(\delta_s - U(x = l_0))}{8bh_s} + w(\varepsilon(x = l_0)) \cdot t_a + \tau(x = l_0) \cdot \theta(x = l_0) \cdot t_a \quad (93)$$

With $\delta_s = U(x = 0)$, the local sliding as explained in Figure 3.3-3.

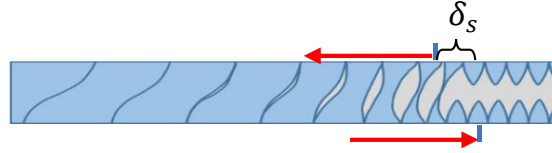


Figure 3.3-3: ENF local sliding at the crack front.

The first term of the equation (94) corresponds to the case of a rigid adhesive layer (beam theory) while the next ones give the influence of a flexible adhesive layer.

If a large distance between the crack tip and the loading point, l_0 , is considered, $U(x = l_0)$ can be neglected compared to $U(x = 0) = \delta_s$. Moreover, $w(\varepsilon(x = l_0))$ can also be neglected compared to the strain energy at the crack tip. Finally, the two last terms of the equation (94) have a very low contribution that may be neglected. It is thus assessed to be around 0,1% by Leffler et al. [117].

Therefore, a simplified expression of the J-integral can be considered (equation 94):

$$J_{ENF} \approx \frac{9 (Pa_0)^2}{16 E h_s^3 b^2} + \frac{3P\delta_s}{8h_s b} \quad (94)$$

For adhesive bonding loading in mode I (DCB tests), a simplified analytical expression of the J-integral was proposed by Högberg et al. [117] based on the same type of analysis led by Leffler et al. [114]. In that case, the considered integration path is described in the Figure 3.3-4. Högberg et al. act that, on this integration path, only the paths A and C contribute to J_B . Thus, the J-integral can be expressed directly using the adherends properties and the load following the equation (95). It must be specified that the first term corresponds to the beam theory considering a rigid adhesive, while the second term corresponds to the effect of the flexibility of the adhesive and the local rotation of the adherent.

$$J_{DCB} \approx \frac{12(Pa_0)^2}{Eb^2h_s^3} + \frac{P}{b} |\theta_{sup} - \theta_{inf}| \quad (95)$$

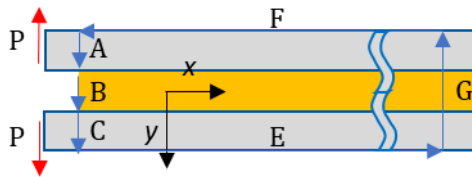


Figure 3.3-4: DCB J-integral integration path A+B+C.

For our DCB and ENF tests, the digital image correlation system was used to measure the displacement fields at crack tip (local sliding and local rotation of the upper and the lower adherent, δ_s and $|\theta_{sup} - \theta_{inf}|$ respectively) on the side of the specimens, and thus to compute the J-integral.

3.3.2. Cohesive law expression for DCB and ENF tests

Rice produced two alternative expressions of J [118], [51]. He used the Barrenblatt approach which considers a cohesive zone ahead of the crack tips in which the restraining stress $\sigma(\delta_n)$ is represented as a function of the opening δ_n . If the J -integral is evaluated along contour $\Gamma = \sum_1^3 \Gamma_i$ (example in Figure 3.3-5 for mode I loading) which runs along the cohesive zone, Γ_2 is upstream of the crack front. Therefore, there is no stress, $\sigma_{ij} \cdot n$ and dy are equal to zero. In addition, Γ_1 can be taken at distance long enough from the crack tip, and therefore $J_1 \approx 0$. On the contour Γ_3 , $dy = 0$, $\sigma_{ij} \cdot n = \sigma(\delta_n)$ because $n = y$ and $d\Gamma = dx$.

The equation (96) can then be obtained.

$$J = \oint_{\Gamma_3} \sigma(\delta_n) \frac{d\delta_n}{dx} dx \quad (96)$$

This expression can be explained as follows. If the crack opening, or sliding, at each point in the cohesive zone increases by an amount $d\delta$, then the profile of the cohesive zone boundary extends of a distance dx . The quantity $\sigma(\delta_n)dx$ is the load over each infinitesimal area and $\sigma(\delta_n) d\delta_n dx$ is the energy absorbed for a separation increase of $d\delta_n$. Then J , in the equation (97), is defined as a rate of energy absorption, respecting the cohesive zone propagation.

$$J = \int_0^{\delta_t} \sigma(\delta_n) d\delta_n \quad (97)$$

With δ_t the local opening at the crack tips which has to be measured.

When the critical opening is achieved, at crack propagation, $J = J_c$, which is the area under the $\sigma(\delta_n)$ curve and can be seen as the rate of energy absorption in the cohesive zone.

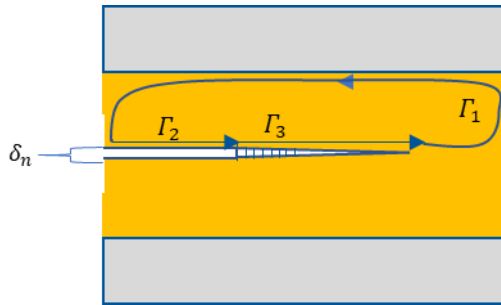


Figure 3.3-5: Cohesive zone ahead of the crack tip.

The relation between the J -integral expression and the cohesive law $\sigma(\delta_n)$, is expressed in the equation (98), with δ_n the local opening of the sample at the crack tip.

$$\sigma(\delta_n) = \frac{dJ_{DCB}}{d\delta_n} \quad (98)$$

Consequently, with a limited data (load/displacement curve and local displacement measurement), the complete cohesive law shape should be obtained from the experimental data. As for the DCB test, the relation between the J -integral expression and the cohesive law, $\tau(\delta_s)$ can be obtained for the ENF test. It is expressed in the equation (99). Following the same analysis in shear loading, with δ_s the local sliding of the sample at the crack tips.

$$\tau(\delta_s) = \frac{dJ_{ENF}}{d\delta_s} \quad (99)$$

3.3.3. Analysis of the DIC strategy to monitor local displacement

The Leffler and Högberg expressions of the J-integral for ENF and DCB tests, require to measure the local displacement (sliding, adherent rotation and opening) at the crack tip. Using the data provided by the DIC, the local measurements are used to obtain, for the J-integral computation, $|\theta_{sup} - \theta_{inf}|$, δ_n and δ_s . Figure 3.3-6 presents the 4 positions of the required measurement points (A, B, C, D) to compute the local rotations. For the local opening and local sliding, only the points B and C should be required.

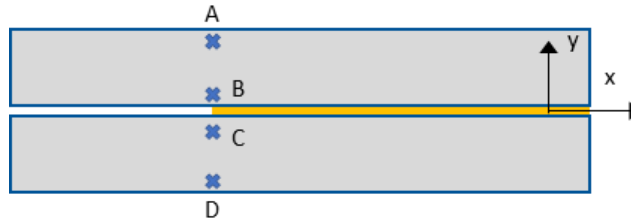


Figure 3.3-6: DIC measurement point on test samples.

The local sliding is obtained following the equation (100).

$$\delta_s = |DX_B| - |DX_C| \quad (100)$$

With DX_i the local displacement in the x direction of the point i compared to the initial position
The local opening is obtained following the equation (101).

$$\delta_n = |DY_B| - |DY_C| \quad (101)$$

With DY_i the local displacement in the y direction of the point i compared to the initial position
Local rotations are obtained following the equation (102).

$$|\theta_{sup} - \theta_{inf}| = \left| \frac{|DX_A| - |DX_B|}{Y_A - Y_B} - \frac{|DX_D| - |DX_C|}{Y_D - Y_C} \right| \quad (102)$$

The measurements should be carried as close as possible to the adhesive layer and the initial crack position. However, because of technical limitations of the use of the DIC, positions of measurement points, A, B, C and D, may experimentally vary according to the type of tests and also from one to another.

It must be noted that the use of DIC as the measurement device for these values may have some limitation:

- DIC meshing may not be aligned with the different materials. Actually, most of the time, at the steel-adhesive interface, one element represents this interface. Therefore, the local displacement measurement at this point is not accurate,
- the definition of the exact numerical position of the experimental initial crack front is not easy. Figure 3.3-7 presents an ENF test speckle for which the initial crack front was marked with a thin black pen. The pencil thickness is large and thus introduces incertitude on the exact initial crack front position.

The next paragraphs will detail how these problematics were solved.

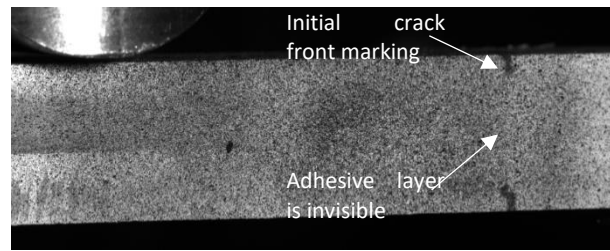


Figure 3.3-7: ENF test DIC speckle showing difficulties to have a precise initial crack front position based on the marking.

Figure 3.3-8 presents the X displacements map for a DCB test prior to the crack propagation. The white line represents a chosen measurement profile in Correli software used to obtain the required X displacement values for the computation of $|\theta_{sup} - \theta_{inf}|$ and the Y displacement values for the computation of δ_n .

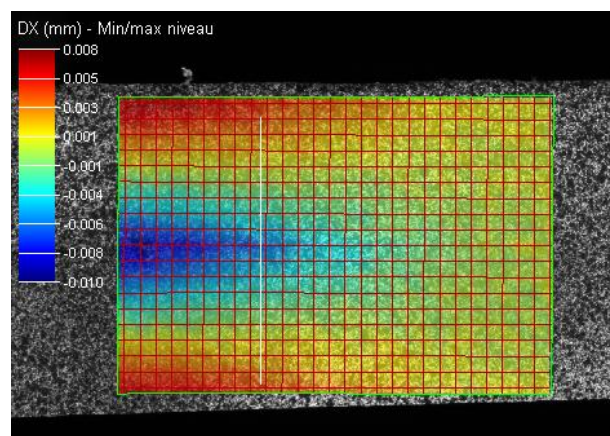


Figure 3.3-8: DCB test DIC X displacement map.

Figure 3.3-9 presents the obtained X displacement corresponding to the chosen profile. The figure shows that the curve is divided in two linear parts for the two adherents plus the bondline. It has been decided to use the maximum and minimum local displacement as the values for the calculation of the adherent rotations following the equation (103).

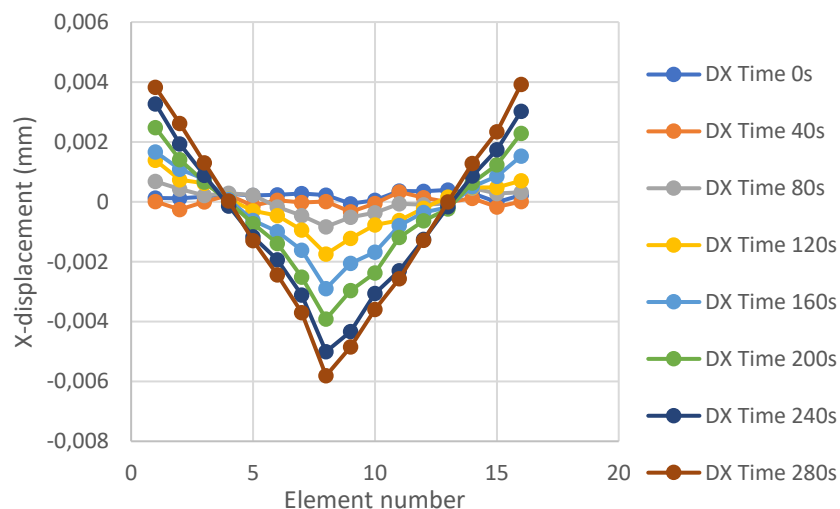


Figure 3.3-9: DCB test DIC X displacement profiles through the sample thickness.

Figure 3.3-10 displays the X displacement map for an ENF test, prior to the crack propagation. The white line displays the measurement profiles where the local displacements through the thickness of the sample are registered. They are then used to obtain the required δ_s values. The Figure 3.3-11 presents the resulting profiles through the sample thickness.

Note also in Figure 3.3-10 that the initial crack is partially visible on the right side of the figure. However, its exact position is not clearly defined (on few elements).

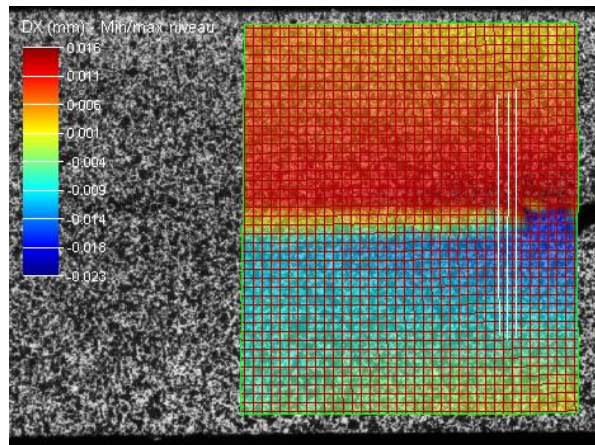


Figure 3.3-10: Example of ENF test DIC X displacement map and local profiles.

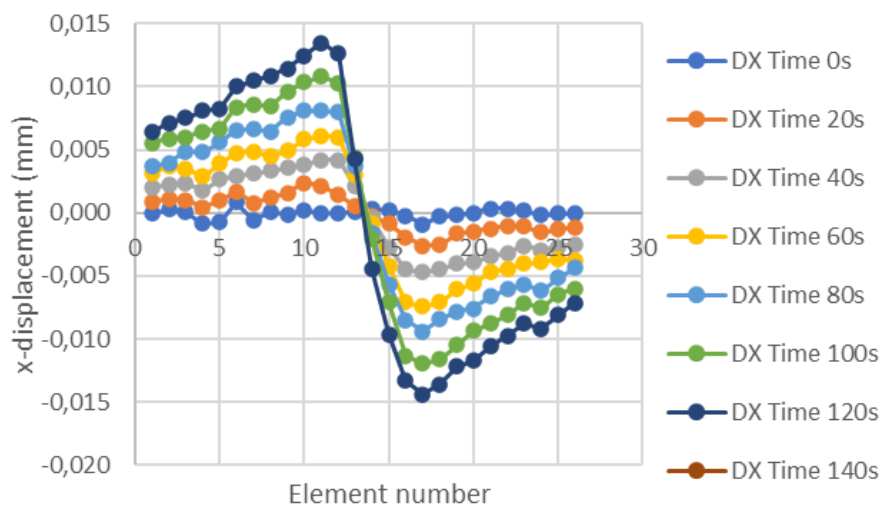


Figure 3.3-11: ENF test DIC X displacement profiles through sample thickness at the crack front position.

Based on the assumption that the maximal displacement should occur at the bonded surface of the adherents, it has been decided to use the maximum (for the upper adherent) and minimum (for lower adherent) local displacements as the value of interfaces local displacements (local sliding, equation (100)).

The issue related with the determination of the exact position of the displacement measurement profile (which should be at the same position as the crack front) was studied assessing the impact of an error of this position on the critical J-integral, J_c . Figure 3.3-12 presents an example of the computation of J-integral curves obtained for one ENF test (V-1). The blue curve is set

as the reference at the initial crack position. The three other curves are obtained with measurement point shifted in the direction of the bondline from 0.7 to 3.3 mm.

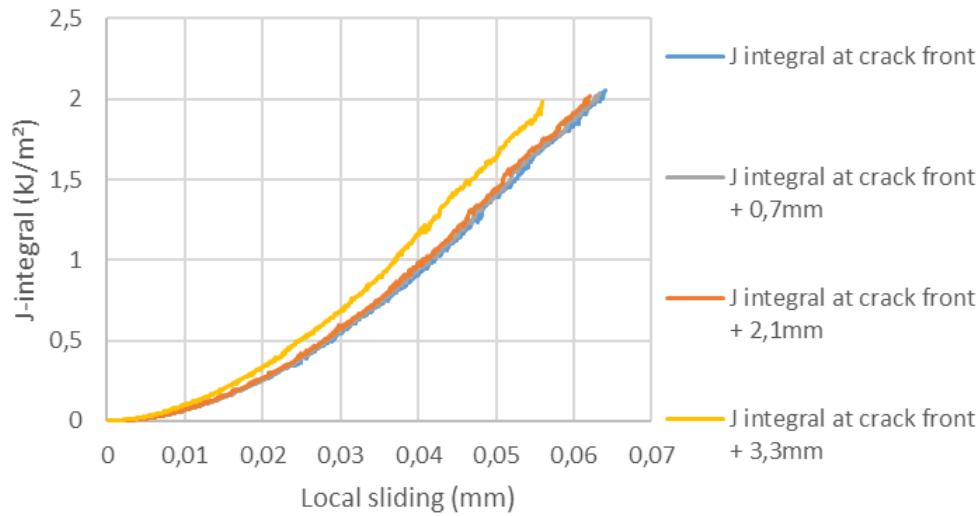


Figure 3.3-12: ENF SV-1 test, J-integral computation depending of the error of position of the X displacement profile.

It can be seen that higher is the error, lower are the local sliding measurement and the J_c value. Figure 3.3-13 and Figure 3.3-14 present the resulting absolute values of the error in critical toughness computation variation for some ENF and DCB tests. It can be seen that this error of position always induces a diminution of the J_c values (conservative error).

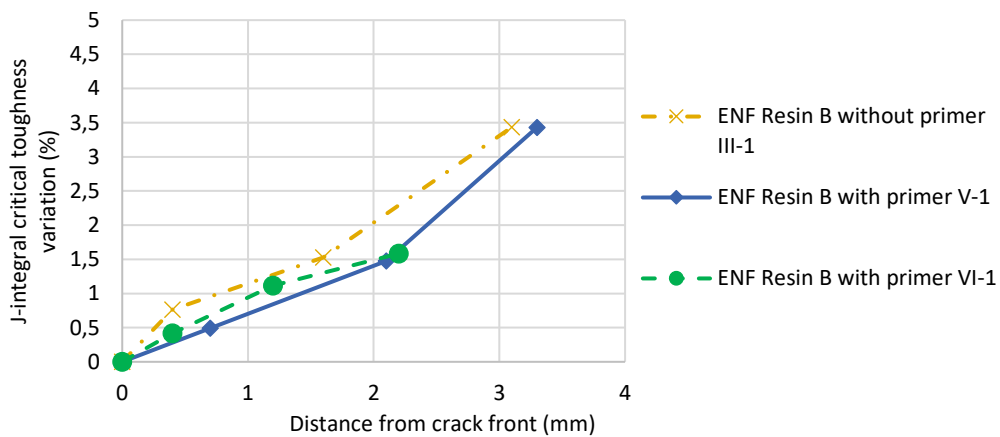


Figure 3.3-13: Impact of the position of the profile on the J_c computation for ENF tests.

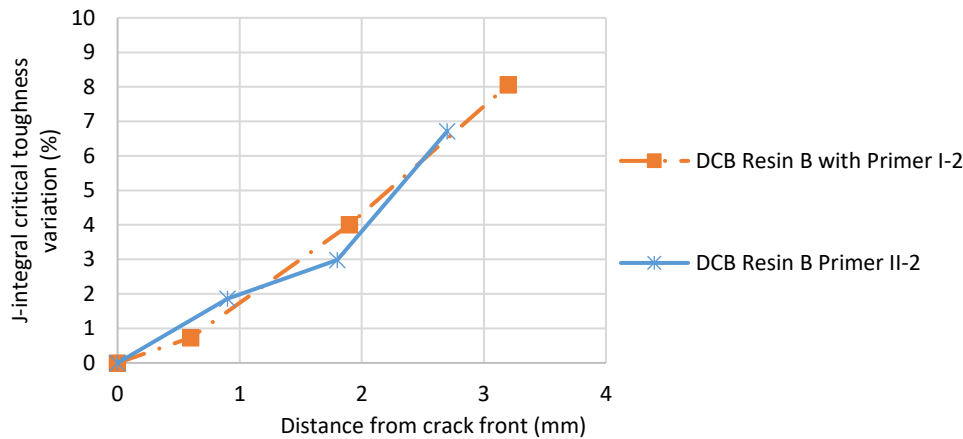


Figure 3.3-14: Impact of the position of the profile on the J_c computation for DCB tests.

3.3.4. Obtained results for DCB investigations

The J-integral analysis has been performed using the DIC data on the previously described tests. In mode I, the local rotations have been monitored, as well as the load and the local opening to obtain the J_c value. The cohesive laws are directly obtained by computation of a derivative curve of the polynomial approximation of degree 3 of the J-integral curve (equation 95) based on the equation (95). Figure 3.3-15 presents the resulting curve for three of the four tests and Table 3.3-1 the polynomial approximations of the J-integral curves. A problem with the DIC monitoring during the II-1 test preventing us from obtaining data for this test.

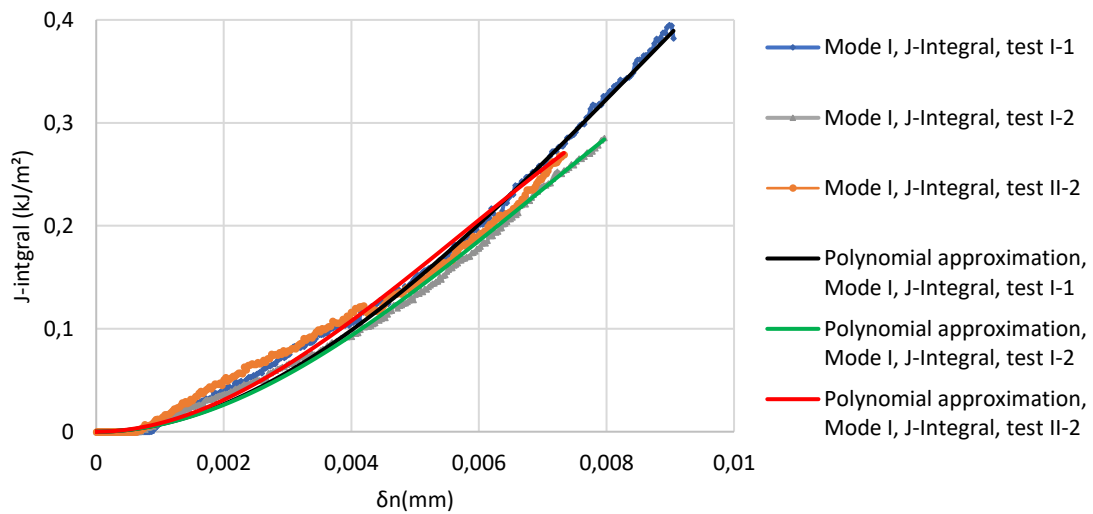


Figure 3.3-15: J-integral computation curves for the DCB tests.

Test I-1	$-277895x^3+7268x^2$
Test I-2	$-344055x^3+7615x^2$
Test II-2	$-507536x^3+8957x^2$

Table 3.3-1: DCB test J-integral polynomial approximation.

The curves show a direct increasing J-integral computation up to the failure value. The lack of stabilization of the curve shows that the failure is brittle with no plasticity in the bondline. The critical values J_c are obtained as the maximum of the curves. These values are reported in the Table 3.3-2.

<i>J_c</i> (kJ/m ²)	0.38
	0.28
	0.27
<i>Average</i>	0.31
<i>Standard deviation / Average</i>	20%

Table 3.3-2: Critical toughness computation in mode I based on the J-integral curves.

The cohesive laws are then directly obtained by computation of a derivative curve of the polynomial approximation of the J-integral curves (equation 99), see Figure 3.3-16.

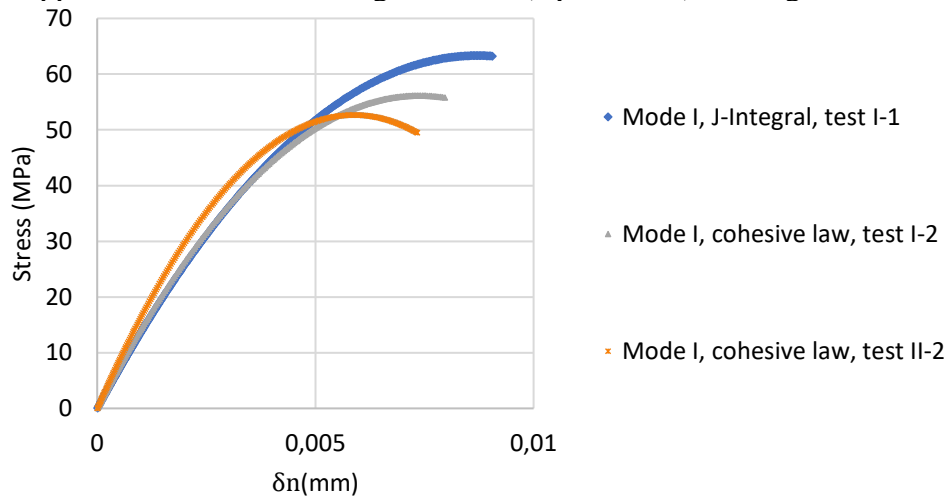


Figure 3.3-16: Cohesive laws in mode I based on the J-integral curves derivation.

The curves obtained from the J-integral polynomial approximation show a lack of damage and nearly no plasticity, which is in accordance with the brittle behavior of the adhesive observed during the tests.

3.3.5. Obtained results for ENF investigations

The J-integral analysis has been performed with the DIC data for all the ENF tests. The local sliding was determined for each test. With the monitoring of the load, the J-integral curves are obtained for the tests without primer (Figure 3.3-17) and with primer (Figure 3.3-18) and the polynomial approximation of the J-integral curves are described in Table 3.3-3. A problem with the DIC monitoring during the V-2 test preventing us from obtaining data for this test. The obtained curve from the J-integral polynomial approximation was a polynomial of degree 3.

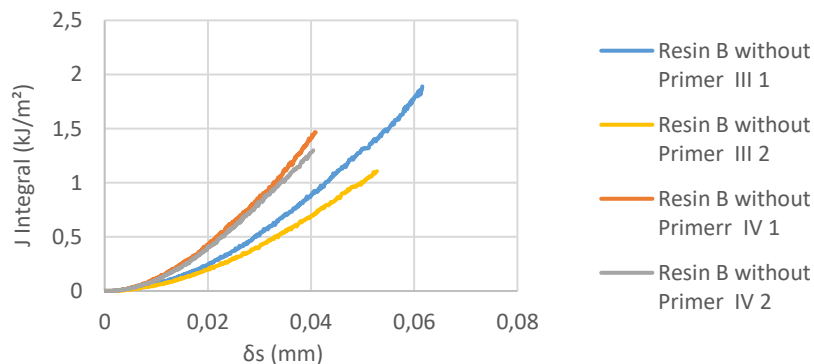


Figure 3.3-17: J-integral computation curves for the ENF tests without primer.

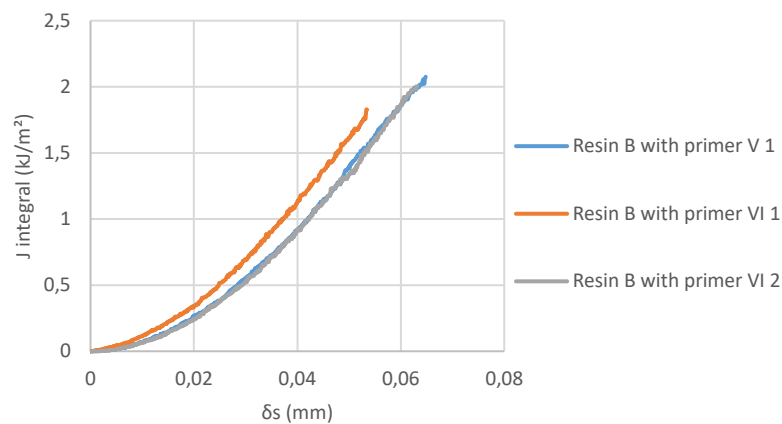


Figure 3.3-18: J-integral computation curves for the ENF tests with primer.

	Polynomial approximation
Test III-1	$-2949x^3 + 661x^2$
Test III-2	$-2702x^3 + 535x^2$
Test IV-1	$-6797x^3 + 1093x^2$
Test IV-2	$-12019x^3 + 1324x^2$
Test V-1	$-3394x^3 + 728x^2$
Test VI-1	$-3839x^3 + 765x^2$
Test VI-2	$-2645x^3 + 679x^2$

Table 3.3-3: ENF test J-integral polynomial approximation.

As for the DCB tests, the curves show a direct increasing J-integral computation up to the failure value. It shows that the failure is brittle. The critical values J_c are obtained as the maximum of the curves. These values are reported in Table 3.3-4.

	Without primer	With primer
J_c (kJ/m²)	1.9	2.1
	1.1	1.9
	1.5	1.75
	1.4	
Average	1.5	2
Standard deviation	0.3	0.1
Standard deviation / Average	23%	5%

Table 3.3-4: Critical toughness computation in mode II based on the J-integral curves.

The computation of the cohesive laws from the J-integral curve is displayed on Figure 3.3-19. It shows that the three obtained curves are really similar in shape, and in term of maximal stresses.

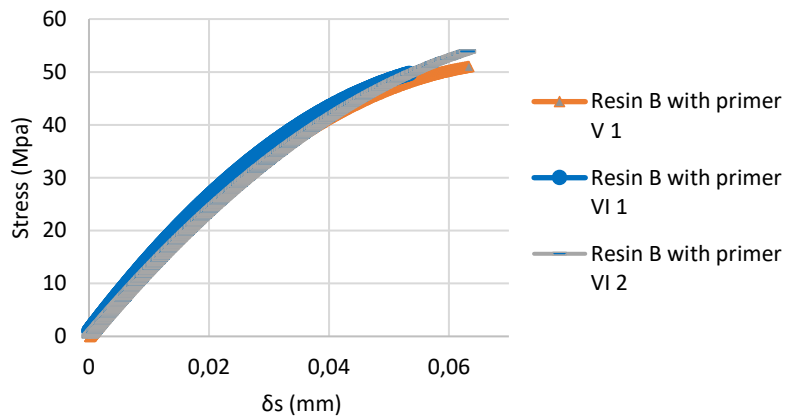


Figure 3.3-19: Cohesive law in mode II based on the J-integral curves derivation.

3.4. Conclusion and discussion

The tests performed during this study have shown that, in this particular case, the approximation of the CCM and MBTM methods proposed by the standard proved to be efficient to obtain crack initiation critical toughnesses for MMB and ENF tests with limited instrumentation and expertise. However, these initiation values are known as being low (or conservative) compared to “propagation” critical toughness. Therefore, their use for modeling might lead to too conservative prediction.

Despite being used for only one of the three test computation (DCB), the propagation critical toughness determination with optical fiber crack front measurement had a major advantage compared to standard visual crack front measurement (or DIC). It can be easily automated, leading to fast data analysis and critical toughness computation (few seconds) and avoiding any operator misjudgments. Despite the really good capacity of the optical fiber to follow crack propagation, its use might be limited in real critical toughness test application when uncontrolled crack propagation might be encountered with fragile adhesive (such as the resin B).

The J-integral approach also proved to be an efficient way to obtain the critical toughness with a different monitoring strategy and relatively easily. It must be pointed out that, despite being computed before the crack propagation occurs (as the critical toughness at initiation), the J_c computation leads to similar results to the ones obtained with the “propagation critical toughness” (CCM and MBTM) (Table 3.4-1 and Table 3.4-2). The J-integral derivation also proved to be effective in obtaining cohesive laws directly from tests. The obtained laws shapes are consistent with the brittle behavior of the studied adhesive.

<i>Mode I critical toughness (kJ/m²)</i>	<i>G_{Ic} (CCM)</i>	<i>G_{Ic} (MBTM)</i>	<i>J_{Ic} with primer</i>
	0.25	0.22	0.38
	<i>No stabilisation</i>	<i>No stabilisation</i>	0.28
	0.24	0.25	0.27
	0.28	0.28	
<i>Average</i>	0.26	0.25	0.31
<i>Standard deviation</i>	8%	12%	20%

Table 3.4-1: Critical toughness computation in mode I.

<i>Mode II critical toughness (kJ/m²)</i>	<i>G_{IIc} Without primer</i>	<i>G_{IIc} with primer</i>	<i>J_{IIc} without primer</i>	<i>J_{IIc} with primer</i>
	1.73	2.15	1.9	2.1
	3.28	2.50	1.1	1.9
	2.62	2.21	1.5	
	2.37		1.4	1.75
<i>Average</i>	2.5	2.29	1.5	2
<i>Standard deviation</i>	25%	8%	23%	5%

Table 3.4-2: Critical toughness computation in mode II.

Parts 3.2.2 and 3.2.3 have provided critical toughness values obtained based one the ASTM standard test procedure for the DCB and ENF test with the optical fiber crack propagation monitoring. These results will be used in chapter 4 as initial parameters of the indirect method for cohesive law modeling. The results obtained in part 3.2.4 for the MMB result will be used to fit mixed mode parameter of the model in chapter 4.

Part 3.3 with the J-integral analysis has provided cohesive laws in mode I and II. These laws will be implemented into the direct method of the cohesive analysis with some approximations to fit the data required by the FEM software used in chapter 4.

The results obtained in this chapter for the cohesive law calibration show that bilinear law should be sufficient to express the interface properties. These results are consistent with literature such as in [120] for DCB test or [123] for single-lap test which conclude that the cohesive law shape has little impact on the behavior and the failure load prediction of such bonded assemblies. For those reasons and for simplicity, only bilinear cohesive laws will be used in numerical models.

Chapter 4: Description and evaluation of the adopted cohesive zone modeling strategy

In this chapter, two different methods are used to determine the cohesive laws that may be implemented in numerical FEM (finite element models) to design adhesively bonded assembly. The first method is a direct cohesive law calibration, based on the previously described J-integral analysis. The second method is an indirect method based on the critical toughness and relying on the iterative use of FEM to determine the cohesive law. For both methods, it was decided that the cohesive law represents the behavior of the entire assembly (adhesive and both interfaces). The load/displacements curves obtained for the three types of tests (DCB, ENF and MMB) presented in chapter 3 will be used for those determinations and to verify the suitability of the proposed methodologies.

First part will present more deeply the finite element modeling strategy and especially the mixed-mode cohesive zone modeling. The second part will describe more precisely the direct and indirect methods used in this work to determine the cohesive laws in mode I, mode II and in mixed mode. Then, both methods were applied on the results of the three types of tests (DCB, ENF and MMB) presented in chapter 3. In conclusion, the two approaches are compared and discussed.

4.1. Presentation of the used finite elements models

4.1.1. Cohesive elements

Cohesive elements are used to model delamination and adhesive failure by predicting both crack initiation and propagation. These elements can be included in the model at an interface or adhesive bond while allowing load to be transferred between the adherends. The formulation of these elements is based on the Cohesive Zone Model (CZM) associated with a local mechanical behavior that may describe ongoing processes close to the crack tip. This allows avoiding the issues related to stress singularities. This behavior is also referred as cohesive laws (traction-separation relationship).

It was chosen to use Simcenter FEMAP which is a finite element calculation software for pre/post processing for the Simcenter Nastran solver. FEMAP integrates the choice of solvers. In our case, Non-Linear (SOL402 - SAMCEF Solver) was used.

The cohesive law, called "Damage Interface" in SAMCEF, is assigned to specific elements called elements of interface (or cohesive elements), to which a thermodynamic potential E_d (the density surface of elastic strain energy) is associated ([115]). This parameter is more precisely developed in equation (103).

$$E_d = \frac{1}{2} \left(\frac{\langle \sigma_{33} \rangle_-^2}{K_I} + \frac{\langle \sigma_{33} \rangle_+^2}{K_I(1-d_1)} + \frac{\langle \sigma_{32} \rangle^2}{K_{II}(1-d_2)} + \frac{\langle \sigma_{31} \rangle^2}{K_{III}(1-d_3)} \right) \quad (103)$$

With:

- d_1, d_2, d_3 : damages due to respectively peeling mode, plane shear mode, out-of-plane shear mode,

- K_I, K_{II}, K_{III} , the pseudo-stiffnesses (different from the stress intensity factor from the Griffith theory) for each mode.

The term $\frac{\langle \sigma_{33} \rangle^2}{K_I}$ designates the strain energy due to the compression forces. It is considered that compressive stresses tend to close cracks which is why no damage variable is associated with the compression in the peel direction. The term $E_{dI} = \frac{\langle \sigma_{33} \rangle_+^2}{K_I(1-d_1)}$ designates the strain energy due to the peeling forces. This term is associated with the variable of damage d_I which transcribes the degradation of the mechanical properties of the material when the damage evolves according to mode I. Terms $E_{dII} = \frac{\langle \sigma_{32} \rangle^2}{K_{II}(1-d_2)}$ and $E_{dIII} = \frac{\langle \sigma_{31} \rangle^2}{K_{III}(1-d_3)}$ designate the strain energies associated with the in-plane and out-of-plane shear loads and express the decrease of the mechanical properties in shear when damage is due to modes II and III. The pseudo-stiffnesses are the ratio between the peel or shear stiffnesses divided by the numerical thickness of the cohesive element.

In FEMAP, cohesive damage in mode I, II or III for bi-linear cohesive law will always be equal ($d_i = d$), even in pure mode I. Indeed, it is based on an equivalent thermodynamic force Y_{eq} , that is based on the loadings of each mode (equation (104)).

$$Y_{eq} = (Y_I^\alpha + (\gamma_{II} Y_{II})^\alpha + (\gamma_{III} Y_{III})^\alpha)^{\frac{1}{\alpha}} \quad (104)$$

Y_I, Y_{II} and Y_{III} can then be defined by differentiating the density surface of strain energy from strain compared to the three variables of damage. They are analogous to energy release rate. They are obtained with:

- Y_i is the thermodynamic force for each mode i , and is equal to $Y_i = \frac{\partial E_d}{\partial d_i}$,
- $\gamma_{II} = \frac{G_{IIc}}{G_{IIIc}}, \gamma_{III} = \frac{G_{Ic}}{G_{IIIc}}$, is a ratio of the critical toughness which reflects the state of stress in a point of the structure,
- α is the coupling parameter, that must be calibrated. This can be carried out in our case using the MMB tests.

In the model used in FEMAP solver, the elastic energy absorbed before damage is described using only one parameter $y0s$ (in mode I) and $y0s \cdot \frac{G_{IIIc}}{G_{Ic}}$ (in mode II). This explains why only the stiffness and this parameter $y0s$ are needed, and not the interface strength for each mode. Thus, in pure mode, it is equal to the area below the first linear part (for bilinear law) of the curve, as shown in Figure 4.1-1.

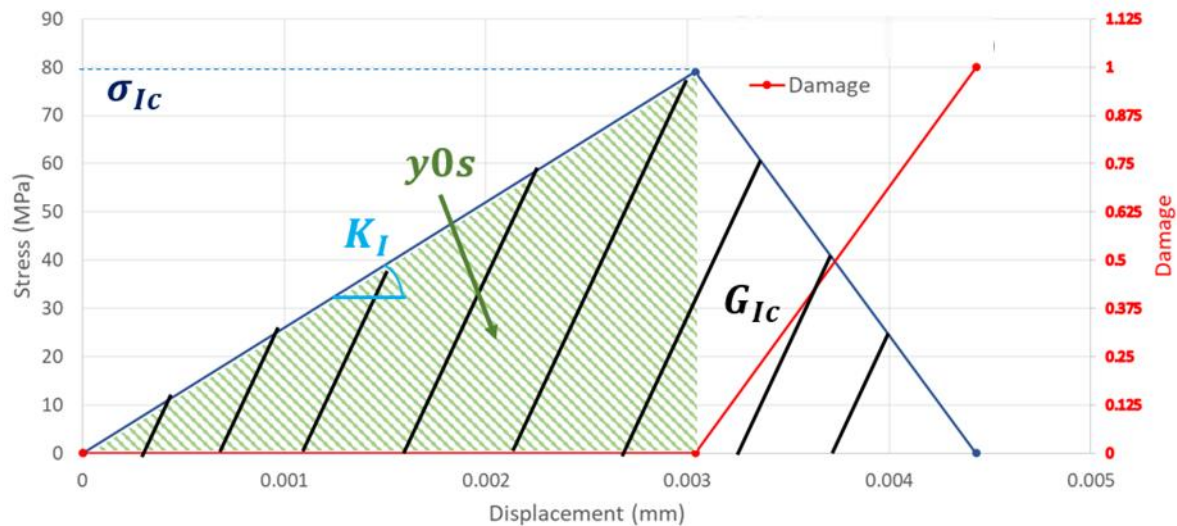


Figure 4.1-1: Graphic showing all the parameters defining the bilinear cohesive law in mode I.

It must be noted that, in this description, the shear strength is dependent on the peel strength. If the stiffnesses are fixed, it can be described by equation (105).

$$\tau_c = \sigma_c \sqrt{\frac{G_{IIc} K_{II}}{G_{Ic} K_I}} \quad (105)$$

In the FEMAP software (and more specifically for the SOL 402 solver), the parameters (apart from purely numerical parameters such as numerical damping) that are needed for the bilinear law for transverse isotropic material for which the influence of the mode III ($G_{IIc} = G_{IIIc}$) can be neglected, are:

- K_I and K_{II} , the pseudo-stiffnesses for mode I and II,
- G_{Ic} and G_{IIc} , the fracture toughnesses for mode I and II,
- $y0s$, the thermodynamic force,
- α , a mixed mode coupling coefficient.

4.1.2. Finite element model hypothesis

It was chosen that the cohesive laws in mode I and II describe the global behavior of the bonded assembly, i.e. the adhesive and its interfaces with both adherends. Thus, cohesive elements using these laws are placed directly between the two adherends. A picture of the implementation of the cohesive elements in a model of ENF test is given in Figure 4.1-2. The geometric thickness of the cohesive elements is set to zero to simplify the creation of the contact condition of the unbonded area. Contact condition is not needed in the part with cohesive elements as this type of elements does not allow compression below their initial geometric thickness. The contact of the debonded area was therefore not modeled. In the part with no cohesive elements (initial crack length) for ENF and MMB tests, contact conditions had to be applied on the surfaces of the adherends. The default parameters from FEMAP were used defining a minimal distance between nodes. Friction was not modeled.

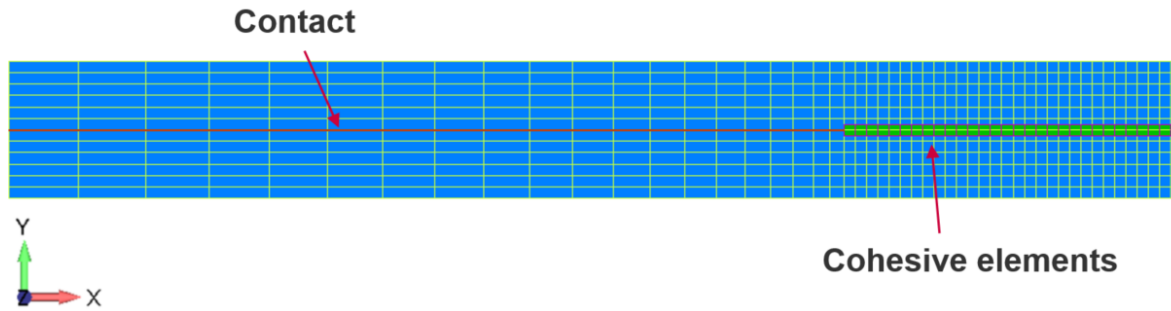


Figure 4.1-2: Cohesive element implementation on the bonded area, contact definition of the initially not bonded area.

The models are presented in Figure 4.1-3 for DCB test, in Figure 4.1-4 for ENF test and in Figure 4.1-5 for MMB test. The used geometries for the model are the geometries described in part 2.2. For all these models, the mesh size in the crack propagation direction, which is the most important and the one that will be studied in the mesh convergence analysis, is 1mm. In all numerical models (DCB, ENF and MMB), only one 3D element is modeled in the width and its width is 1 mm. The cohesive elements are defined with a layer of one element between the two adherents of zero thickness (green elements on Figure 4.1-3). To apply plane strain conditions to the models, the displacements in the width were blocked, this was applied for each model (DCB, ENF, MMB). To validate that this choice does not interfere with the quality of the prediction of the model, full 3D models have been made for ENF and DCB tests.

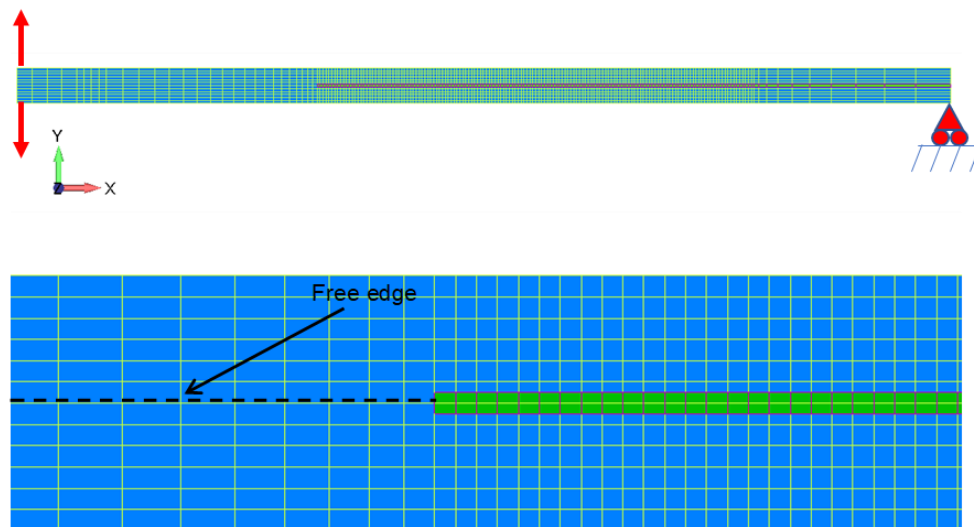


Figure 4.1-3: DCB model representing the adhesive layer with cohesive elements only.

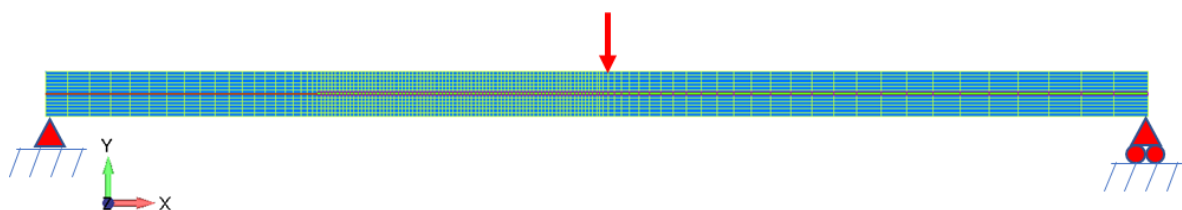


Figure 4.1-4: ENF model representing the adhesive layer with cohesive elements only.

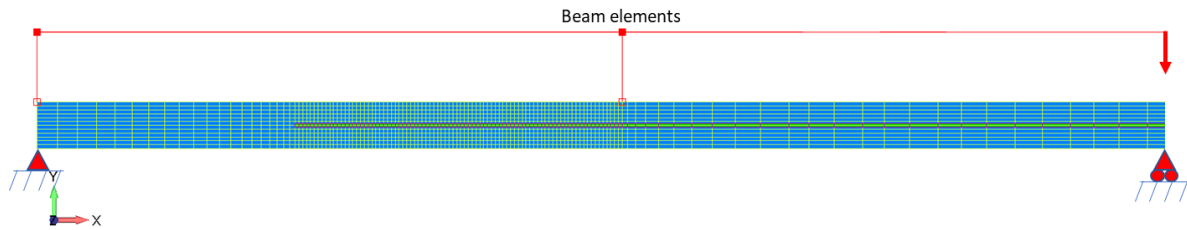


Figure 4.1-5: MMB model representing the adhesive layer with cohesive elements only.

The applied loading for all models was realized through displacement. The displacement values were determined from the experimental investigations. The boundary conditions were applied accordingly with the experimental investigations with the same boundary conditions (same fixed displacement).

For the DCB model:

- x displacements are blocked at the load applications points,
- y and z displacements are blocked, on the sliding pivot,

For the ENF model:

- y and z displacements are blocked, on the sliding pivot,
- x and y displacements are blocked, on the left support,

For the MMB model:

- same boundary conditions as the ENF model are applied for the left support and the sliding pivot.
- beam elements were added in order to model the loading frame and get the correct mode ratio. The beam elements used a rigid material ($E = 1.10^{10}$ MPa) and were linked to the adherends with rigid elements. At the load application points, y displacements are defined as the load of the sample.

The values for the time steps were densified around the crack propagation time to help converging and obtain more data during propagation (especially at the failure loads). The first timesteps had also to be really small for convergence reasons. All the model hypotheses were valid for our specific case (thin adhesive, thick adherend layers). The described models will be used for both the direct and indirect methods.

4.1.3. Mode I and II cohesive laws determination methods

4.1.3.1. Indirect method

The indirect method consists in testing a large number of cohesive laws until the numerical and experimental load/displacements curves coincide. This method can be performed purely numerically. More precisely:

- the toughness is obtained experimentally from tests,
- the mesh sensitivity is assessed for the models,
- the cohesive law in mode II is determined,
- the cohesive law in mode I is determined,
- Finally, the resulting cohesive laws in mode I and II are implemented in MMB models and the sensibility to the coupling parameter is assessed to determine its value.

4.1.3.2. Direct method

In the direct method, the cohesive laws are determined experimentally in pure mode I (DCB test) and pure mode II (ENF test), based on the J-integral computation from the local displacement measurements by DIC. From these laws, the parameters (in mode I: K_I , G_{IC} and y_0s and in mode II: K_{II} and G_{IIc}) needed by FEMAP for the numerical finite elements models can be directly obtained. However, as stated in previous part, in the FEMAP software, there is a relation between stiffness and critical stresses (peel or shear) based on the thermodynamic force that fixes y_0s . To overcome this issue, it was chosen to fix the critical stress based on measured laws and calculate the resulting stiffness.

Though the experimentally determined cohesive laws are used in the finite elements models, it is important to validate the numerical simulations results in mode I and II through a comparison of the obtained load/displacement curves (experimental and numerical).

In mixed mode, no cohesive law was measured during the MMB test. Only the load/displacement curves as well as the critical toughness G_c related to the studied mode ratio are known. The MMB tests are modeled numerically with a coupling parameter (α) that drives the cohesive laws in mixed mode. In FEMAP, the default value is 1. This parameter must be calibrated until numerical and experimental load/displacement curves coincide, and more specifically, the failure load. Figure 4.1-6 summarizes the overall method.

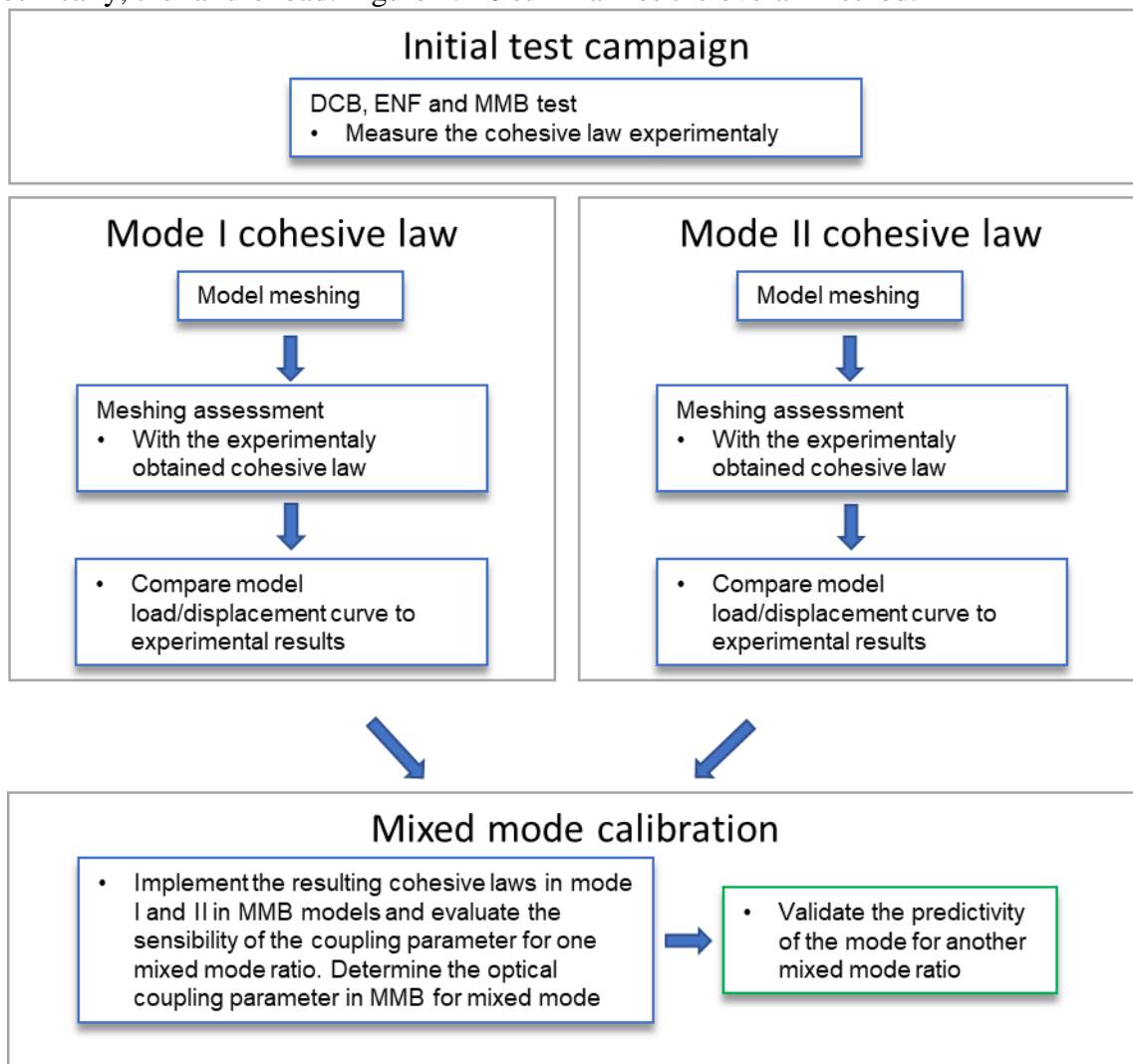


Figure 4.1-6: Direct method flowchart.

4.2. Cohesive zone model determination using indirect method

4.2.1. Calibration method

The inverse method to determine the cohesive law using Femap and its particular implementation is described in Figure 4.2-1. Several steps are carried out:

- measure the toughness experimentally from DCB and ENF tests, G_{Ic} and G_{IIc} ,
- assess the mesh sensitivity for all models,
- determine the cohesive law in mode II, with the only given value being G_{IIc} , by:
 - o evaluating the pseudo-stiffness sensitivity for ENF models (K_{II}),
 - o evaluating the critical shear stress sensitivity for ENF models,
 - o determining the cohesive law in mode II with optimal pseudo-stiffness and critical shear stress (determination of the parameter y_0 s),
- determine the cohesive law in mode I, with the only given value being G_{Ic} , by:
 - o evaluating the stiffness sensitivity in DCB models (K_I),
 - o evaluating the critical peel stress sensitivity in DCB models,
 - o determine the cohesive law in mode I with optimal pseudo-stiffness and critical peel stress and updated y_0 s. Indeed in FEMAP, one value will be dependent on all the others (either the stiffness in mode I or the critical peel stress),
- implement the resulting cohesive laws in mode I and II in MMB models and evaluate the sensibility of the coupling parameter (α),
- determine the optimal coupling parameter α in MMB models for mixed mode.

In our case, the determination of the law in mode II was done in a first step as the data was available. The same procedure with the cohesive law in mode I being obtained firstly can also be done.

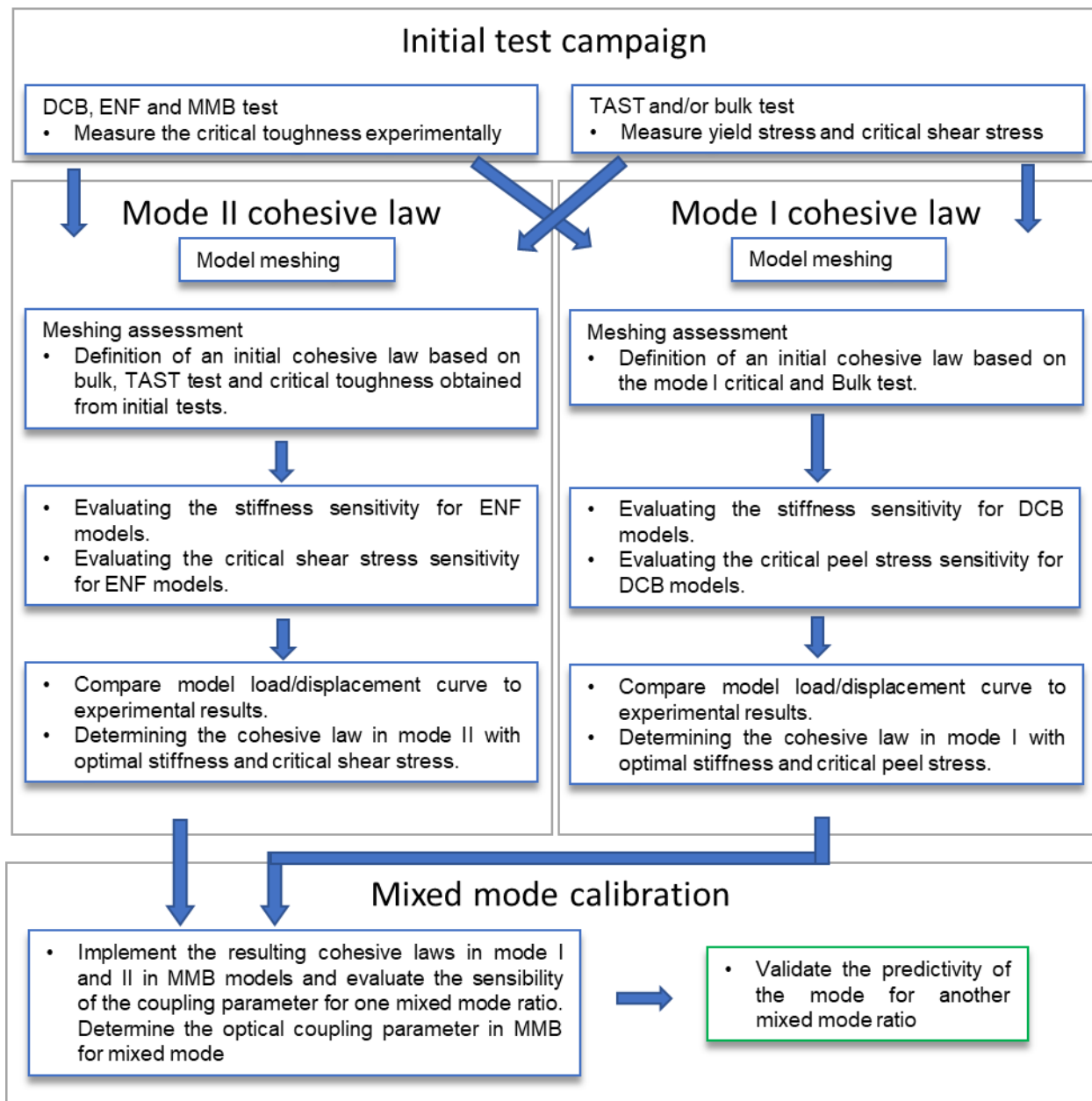


Figure 4.2-1: Indirect method flowchart.

As explained previously, in Femap, the interface strengths τ_c and σ_c of the different modes are not independent. Thus, the complete method consists in determining preliminary stiffnesses in mode I and II, and then calibrating the interface strength in mode I. After this, the parameter y_0 is set (as well as interface strength and stiffness in mode I). Then, the calibration of the interface strength in mode II is carried out modifying stiffness in mode II.

4.2.2. Cohesive laws reference parameters

The critical toughness was obtained from the experiments and is set as the average values obtained in part 3.2.2.

$$G_{Ic} = 0.25 \text{ kJ/m}^2 \text{ and } G_{IIc} = 2.15 \text{ kJ/m}^2$$

Based on TAST results (Appendix A2), initial values of $\tau_c = 35 \text{ MPa}$ and $K_{II} = 1100 \text{ MPa/mm}$ were chosen (close to TAST test results) for the interface strength in pure mode II. Preliminary values of $\sigma_c = 50 \text{ MPa}$ and $K_I = 18500 \text{ MPa/mm}$ were chosen for pure mode I loading based on Bulk test (Appendix A4). These values are initial values. During the sensibility study, they will be modified in order to obtain the best fitting cohesive laws.

4.2.3. Model results in mode II

4.2.3.1. Mesh convergence study

To validate that the model is mesh independent, a mesh convergence study was done by changing the mesh size in the crack propagation direction. The reference mesh uses an element size of 1 mm in the crack propagation direction. The other mesh sizes that were tested were 0.5 mm and 2 mm. In each case, the element size in the x -direction was increased or decreased by twofold for all elements (not just in the crack propagation part). The mesh with element size of 1 mm for the ENF model with an initial crack size of 74 mm is presented in Figure 4.2-2.

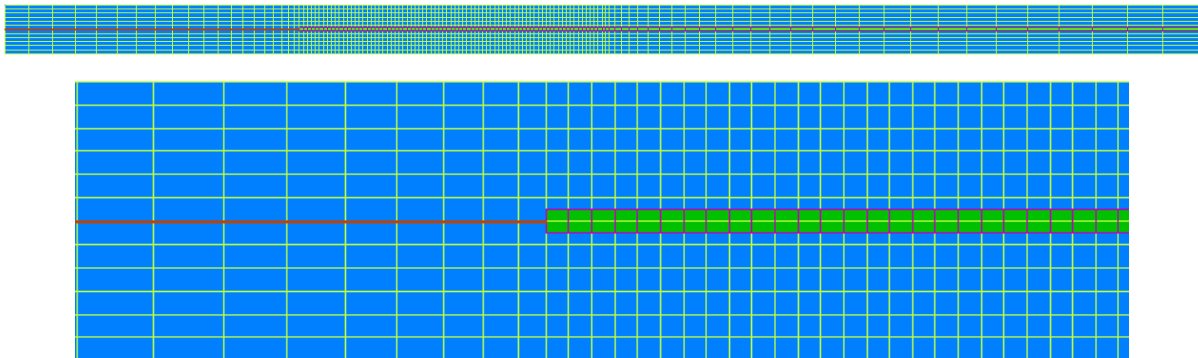


Figure 4.2-2: Mesh of an ENF for an element size of 1 mm.

The load/displacement curves for the three mesh sizes can be seen in Figure 4.2-3. In order to quantitatively compare the different mesh sizes, the failure loads (here the maximum load) were compared. For the ENF tests, the failure load is defined as the maximum stress of the first linear part, before the first decrease. The 1 mm and 0.5 mm mesh showed no difference of the failure load prediction compared to the 2 mm mesh. The 1 mm mesh will be used for the assembly characterization described in the next parts.

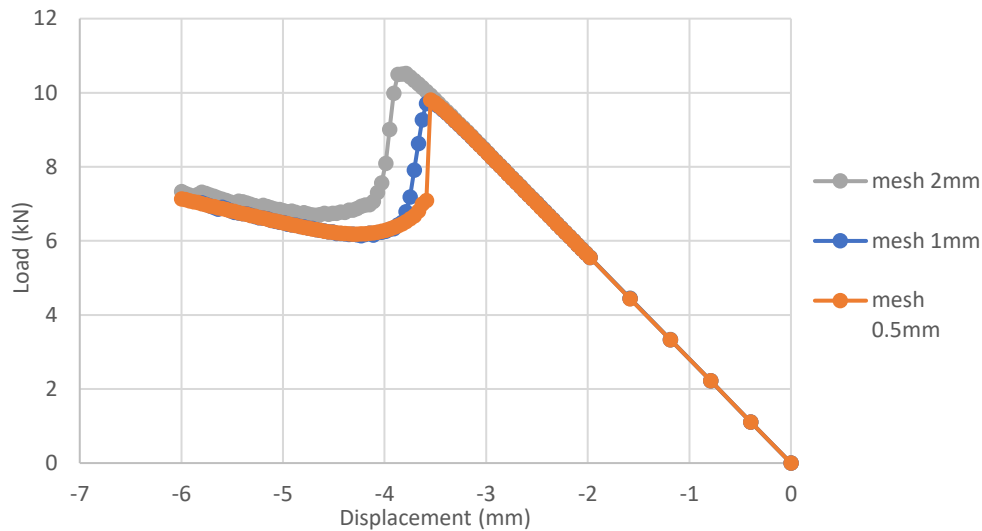


Figure 4.2-3: Load/displacement curves for different mesh sizes for the ENF model with an initial crack length of 74 mm.

4.2.3.2. Stiffness sensitivity analysis

The sensitivity analysis was performed on the model with a mesh size of 1 mm and an initial crack length of 74 mm based on one of the performed tests. The cohesive parameters used in this analysis are:

- $G_{IIc} = 2.15 \text{ kJ/m}^2$, obtained from the ENF tests results,
- $\tau_c = 35 \text{ MPa}$,
- $K_{II} = 800 \text{ MPa/mm}$, 1100 MPa/mm and 1500 MPa/mm .

The load/displacement curves for each tested stiffness are shown in Figure 4.2-4. This figure highlights that the stiffness barely influences the results and especially the failure force, the difference being inferior to 1% for all the three models. The stiffness for the cohesive law was $K_{II} = 1500 \text{ MPa/mm}$ since the slope before crack propagation was the closest to the experimental results.

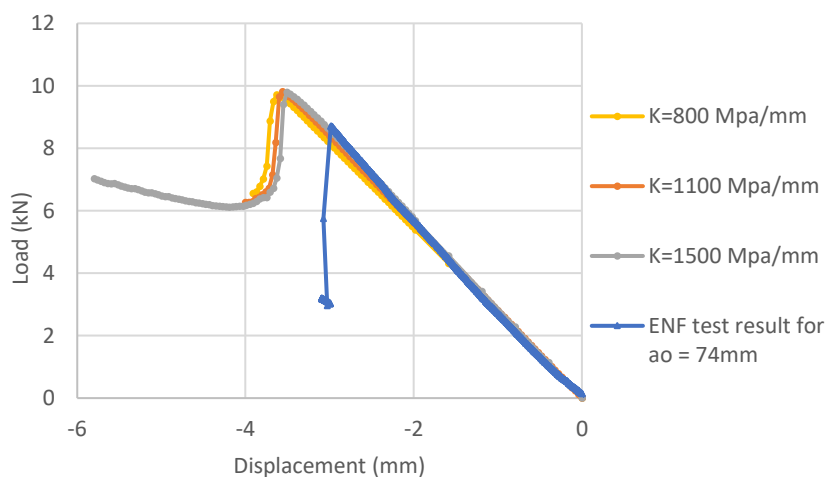


Figure 4.2-4: Comparison between experimental and numerical load/displacement curves for different cohesive stiffness for ENF models.

4.2.3.3. Critical shear stress sensitivity analysis

The critical shear stress sensitivity analysis was also performed on the model with a mesh size of 1mm and an initial crack length of 74mm. The cohesive parameters used for this analysis are as follows:

- $G_{IIc} = 2.15 \text{ kJ/m}^2$
- $K_{II} = 1500 \text{ MPa/mm}$
- $\tau_c = 31 \text{ MPa}, 35 \text{ MPa}, 50 \text{ MPa}, 57 \text{ MPa}$ and 70 MPa

The comparison between the numerical and the experimental load/displacement curves for each critical shear stress is shown in Figure 4.2-5.

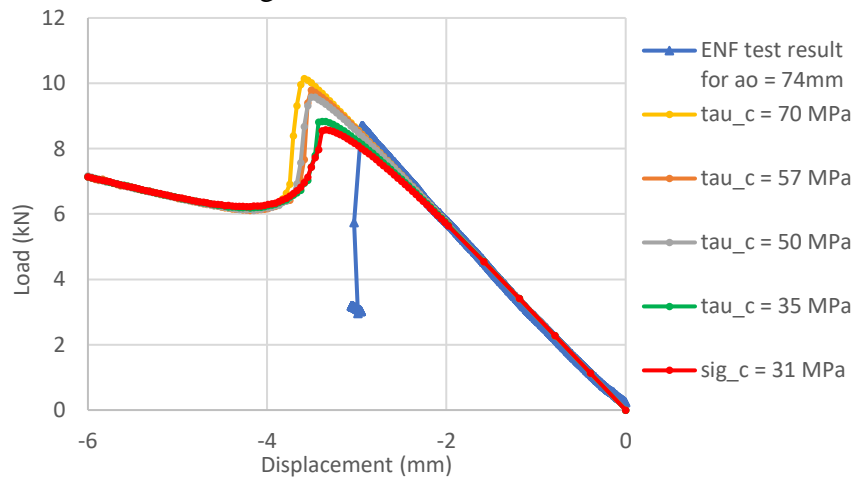


Figure 4.2-5: Comparison between experimental ($a_0 = 74 \text{ mm}$) and numerical load/displacement curves for different critical shear stress for ENF models.

The comparison of failure forces (to the experimental average failure load of 8.60 kN) for each critical shear stress is presented in Table 4.2-2. The results show a high dependency to the value of the critical shear stress. Based on these results and the lowest difference between experimental failure and numerical prediction, the critical shear stress of $\tau_c = 35 \text{ MPa}$ was kept for the cohesive law in mode II.

$\tau_c \text{ (MPa)}$	31	35	50	57	70
Failure force (kN)	8.576	8.834	9.580	9.791	10.151
Difference to exp failure force (%)	-1.46	1.50	10.08	12.50	16.64

Table 4.2-1: Comparison of experimental and numerical failure forces for different critical shear stress for ENF model with an initial crack length of 74mm.

4.2.3.4. Resulting cohesive law in mode II

The final cohesive parameters for the indirect cohesive law in mode II is given in Table 4.2-2 and the cohesive law is shown in Figure 4.2-6.

Fracture toughness	Cohesive stiffness	Critical shear stress
$G_{IIc} = 2.15 \text{ kJ/m}^2$	$K_{II} = 1500 \text{ MPa/mm}$	$\tau_c = 35 \text{ MPa}$

Table 4.2-2: Cohesive parameters in mode II obtained for indirect method for Resin B steel-steel for indirect method.

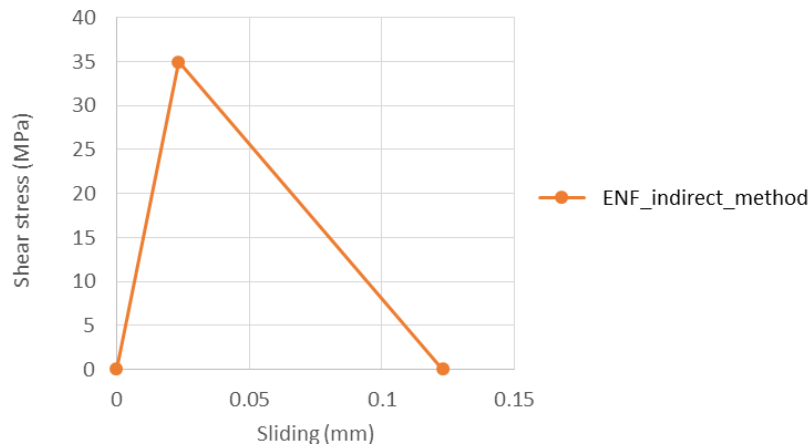


Figure 4.2-6: Cohesive parameters in mode II obtained for indirect method for resin B steel-to-steel bonding.

This cohesive law was implemented in the other two ENF models with initial crack lengths of 59 mm and 90 mm. The comparison of load/displacement curves for both experimental and numerical tests is shown in Figure 4.2-7. The numerical and experimental failure forces for each crack length are compared in Table 4.2-3. The results show that the cohesive law obtained for a model with an initial crack length $a_0 = 74$ mm can well predict the general behavior of ENF models with initial crack lengths $a_0 = 59$ mm and $a_0 = 90$ mm. The load at failure’s prediction error remains under 6%. The unstable crack propagation for the specimen with an initial crack length $a_0 = 59$ mm is well represented by the model whereas it is not the case for the specimen with an initial crack length $a_0 = 90$ mm, for which a stable crack propagation is predicted by the model. However, it is important to underline that the failure forces are well predicted by the models for both initial crack lengths.

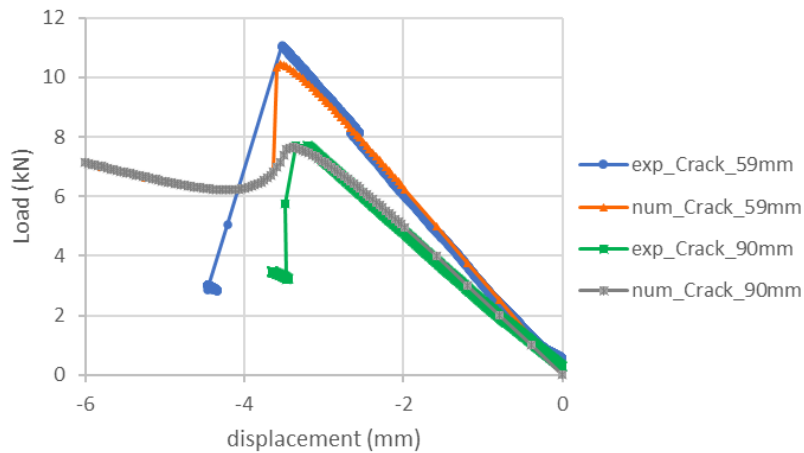


Figure 4.2-7: Comparison of experimental and numerical load/displacement curves obtained for ENF tests and models, with initial crack lengths of 59 mm and 90 mm.

Crack length (mm)	59	74	90
Numerical failure force (kN)	10.453	8.834	7.648
Experimental failure force (kN)	11.060	8.703	7.711
Difference (%)	-5.49%	1.51%	-0.82%

Table 4.2-3: Comparison of failure forces obtained numerically and experimentally for ENF tests and models with different initial crack lengths.

The cohesive law, calibrated with the model with an initial crack length of 74 mm, seems thus validated with the other two models presenting different initial crack lengths. Indeed, errors on the failure force are less than 6%. However, it must be noted that only three tests were used for comparison and only one for each crack length. More tests would have allowed to improve the estimations of the parameters by the indirect method.

4.2.3.5. Comparison with 3D model

A comparison was made with a 3D model and a mesh size of 2mm in the x-direction. Instead of boundary conditions on nodes as in the 2D model, an effort was made to be as close as possible to the experiment and thus, cylinders were used to model the supports. The 3D model is shown in Figure 4.2-8.

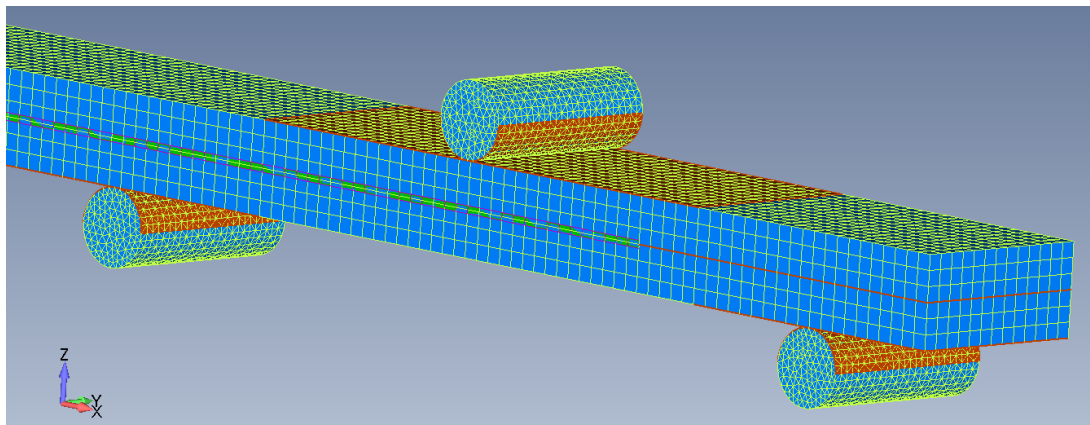


Figure 4.2-8: 3D Model of the ENF (the contact zones are highlighted).

The comparison of the load/displacement curves is shown in Figure 4.2-9. It can be seen that the difference between the 2D and 3D models is quite low, the difference of 2D and 3D numerical failure load being less than 3%. The hypothesis made for the 2D, i.e. plane strain model can therefore be considered as verified. Moreover, the planar crack propagation in the 3D model is illustrated in Figure 4.2-10 showing the cohesive element damage during crack propagation. Figure 4.2-11 presents the resulting experimental flat crack front shape also observed during one ENF test. Both results are therefore in agreement.

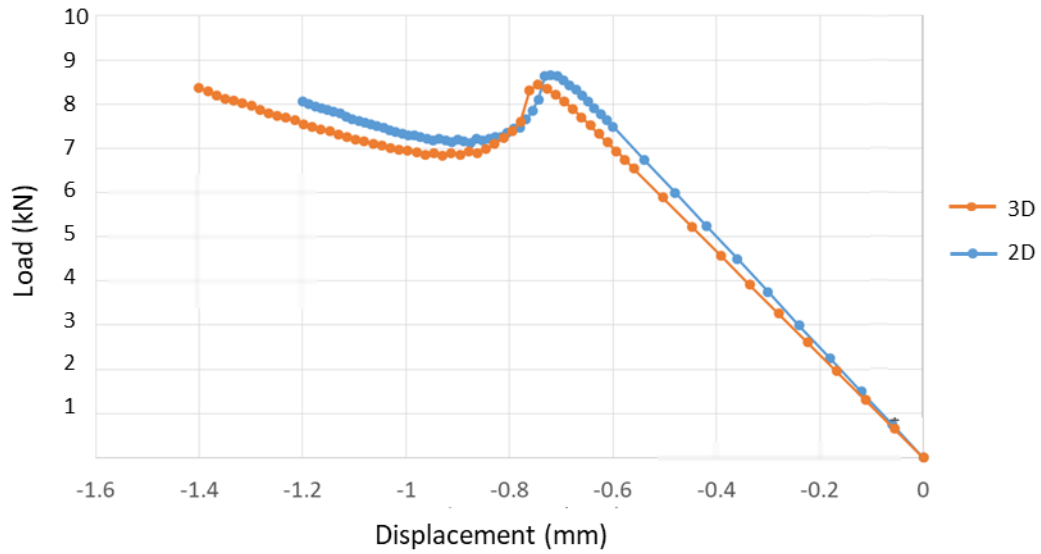


Figure 4.2-9: Load/displacement curves for the 2D and 3D model of the ENF test.

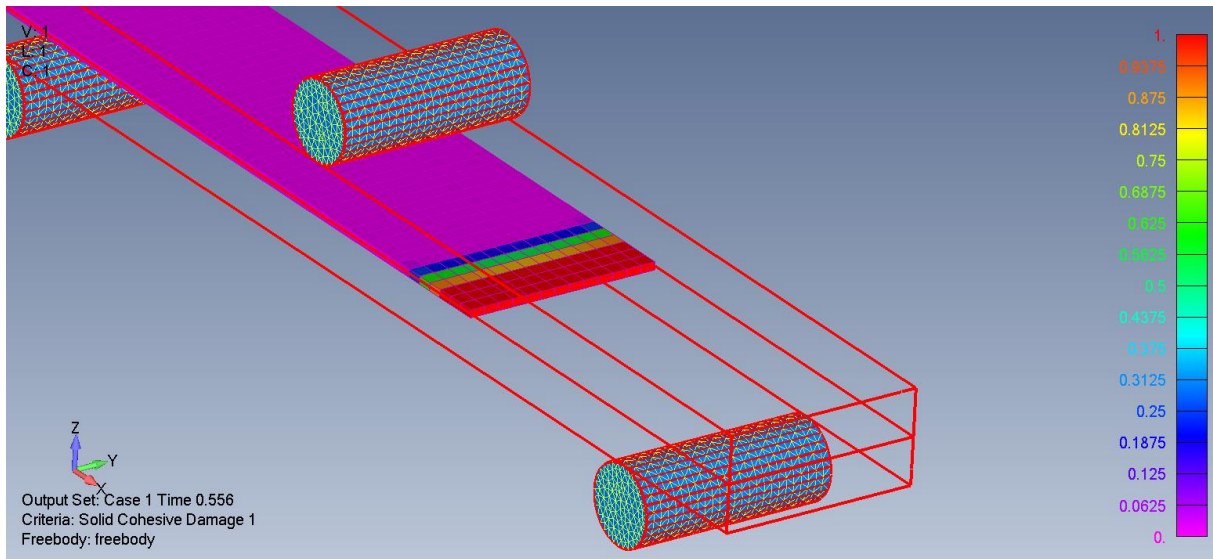


Figure 4.2-10: Plot of the cohesive element damage during the ENF test showing a planar crack propagation.

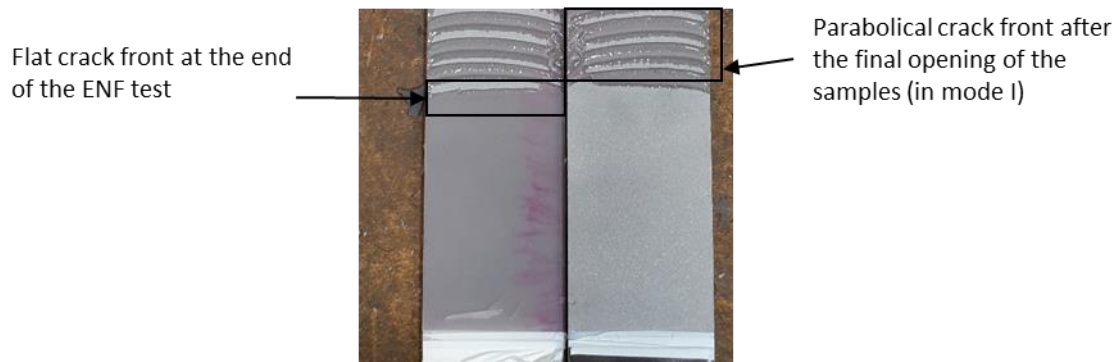


Figure 4.2-11: Crack front observations on an ENF sample at the end of the test.

4.2.4. Model results in mode I

4.2.4.1. Convergence Study

The same analysis of mesh convergence as for the ENF model has been performed for the DCB model. Three mesh sizes in the crack propagation direction were tested: 2 mm, 1 mm and 0.5 mm. Note that the initial crack length was set to 74 mm for this analysis. The resulting load/displacement curves for the three mesh sizes are compared in the Figure 4.2-12.

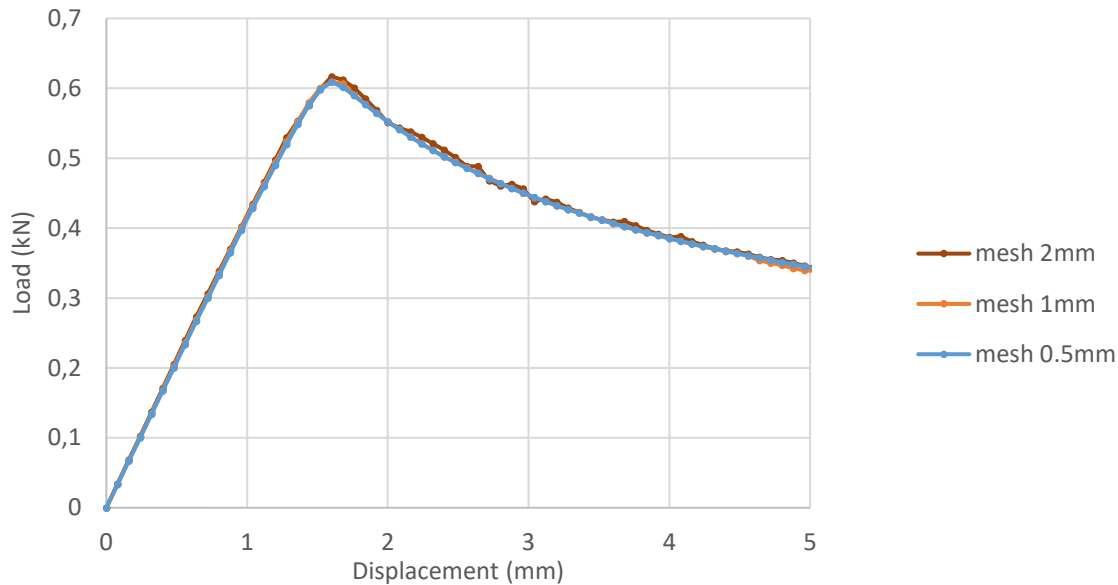


Figure 4.2-12: Load/displacement curves for different mesh sizes for the DCB model.

The three curves show minimum error between each mesh size from 2mm to 0.5mm. The comparison of predicted failure forces for each mesh size is presented in Table 4.2-4.

<i>Mesh size cohesive (mm)</i>	0.5	1	2
<i>Failure forces (kN)</i>	0.609	0.609	0.617
<i>Difference to converged mesh (%)</i>	0.00%	0.06%	1.29%

Table 4.2-4: Failure forces for different mesh sizes for DCB model.

The DCB models have a lower mesh sensitivity than ENF models. The mesh size for the following used characterization was set to an element size of 1mm as the computation time difference between 1mm and 2mm mesh size was not significant. This allowed using similar mesh for DCB and ENF models.

The next step in the indirect method for mode I is to calibrate either the critical peel stress or the cohesive stiffness since the parameter γ_0s was already set in FEMAP from the calibration of the mode II cohesive law.

4.2.4.2. Stiffness sensitivity analysis

This stiffness sensitivity analysis was performed with a mesh size of 1mm. The used cohesive parameters are:

- $G_{IC} = 0.25 \text{ kJ/m}^2$,
- $\sigma_c = 35 \text{ MPa}$, This initial value is obtained from the final value for the cohesive law in mode II,
- $K_I = 13\ 000 \text{ MPa/mm}$, $18\ 560 \text{ MPa/mm}$ (preliminary value), $23\ 000 \text{ MPa/mm}$ and $75\ 000 \text{ MPa/mm}$.

In this analysis, the critical peel stress was taken as constant, as well as the cohesive parameters in mode II. Because of the elastic energy absorbed before damage y_0s (in mode I) and $y_0s \cdot \frac{G_{IIc}}{G_{IC}}$ (in mode II) being fixed and the relation described by the equation 105, the parameter y_0s must be updated for each stiffness. This means that the critical shear stress and therefore the mode II cohesive law has to be updated for each mode I cohesive law tested. The final cohesive laws in mode I and mode II will be summarized in the conclusion.

The load/displacements curves for each mode I cohesive stiffness is shown in Figure 4.2-13. It can be observed that the cohesive stiffness in mode I barely influences the results, the failure forces difference being below 1% for these four results. Thus, the calibration of the mode I cohesive law will only be based on the critical peel stress and the cohesive stiffness will be calculated to maintain a constant value for the parameter y_0s from the mode II cohesive law.

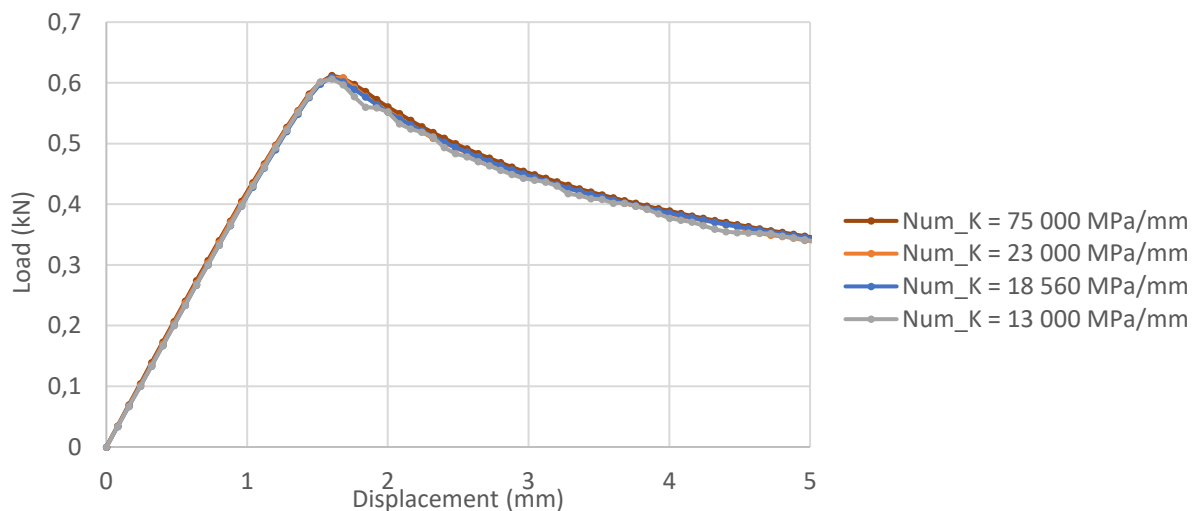


Figure 4.2-13: Numerical load/displacement curves for different cohesive stiffness for DCB models.

4.2.4.3. Critical peel stress sensitivity analysis

This sensitivity analysis was performed with a mesh size of 1mm. The used cohesive parameters are:

- $G_{IC} = 0.25 \text{ kJ/m}^2$,
- $y_0s = 0.047 \text{ kJ/m}^2$, which will fix the stiffness in mode I, it is obtained using the equation (105).
- $\sigma_c = 35 \text{ MPa}$ ($K_I = 12\ 900 \text{ MPa/mm}$), $\sigma_c = 50 \text{ MPa}$ ($K_I = 26\ 350 \text{ MPa/mm}$) and $\sigma_c = 70 \text{ MPa}$ ($K_I = 51\ 650 \text{ MPa/mm}$).

The comparison of load/displacement curves is presented in Figure 4.2-14 for the different critical peel stresses. It can be observed that doubling the critical peel stress barely impacts the failure forces. Furthermore, the difference to experimental failure load is reduced when increasing the critical peel stress. Yet, choosing a value greater than 70 MPa has no physical meaning. Thus, the choice was made to keep a critical peel stress of 35 MPa, equal to the critical shear stress, for the resulting cohesive law.

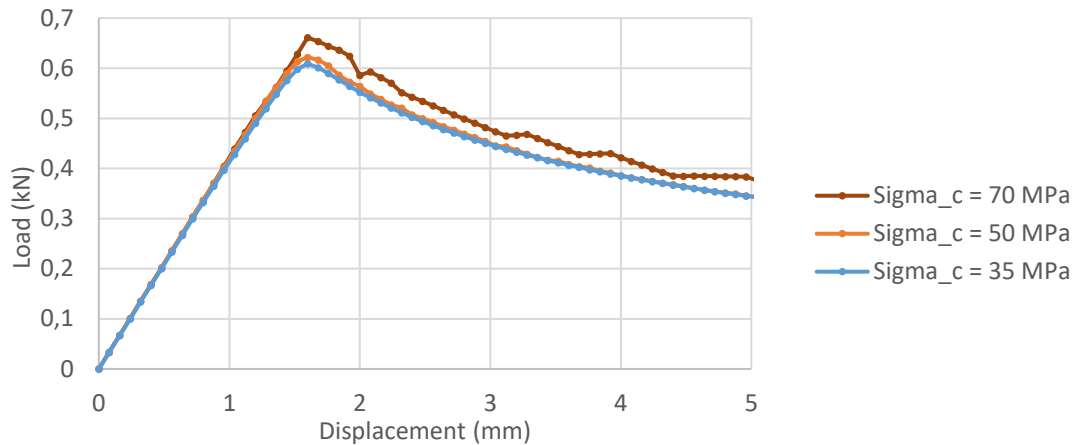


Figure 4.2-14: Comparison of load/displacement curves for different critical peel stresses for DCB models.

Table 4.2-5 presents the final difference between the failure load obtained experimentally and numerically in mode I for different critical peel stresses σ_c . The difference shows that the failure load prediction remained lower than the experimental results (Table 4.2-5). This is supposed to be related to the chosen critical toughness value based on the standard results being conservative. The same analysis performed with the results obtained with the J-integral method may provide better results.

σ_c (Mpa)	Numerical $\sigma_c = 35$	Numerical $\sigma_c = 50$	Numerical $\sigma_c = 70$
Failure load (kN)	0.647	0.661	0.670
Difference to experimental failure load (%)	-15.00%	-13.24%	-12.03%

Table 4.2-5: Comparison of experimental and numerical failure forces for different critical peel stresses for DCB models.

A comparison of the numerical model with a critical peel stress of 35 MPa and experimental load/displacement curves is shown in Figure 4.2-15. It can be seen that, despite being conservative on the failure load (-15%), the crack propagation is well represented on its globality. However, it must be noted that the model does not represent the uncontrolled crack propagation for some of the tests.

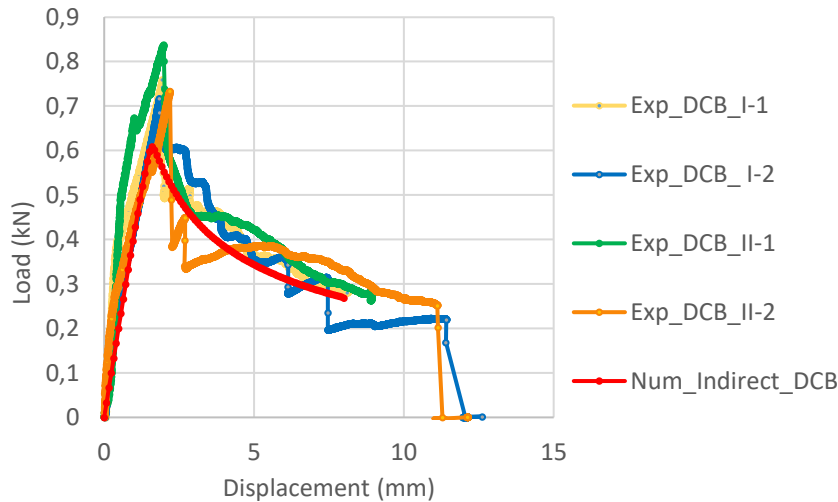


Figure 4.2-15: Comparison of experimental and numerical load/displacement curves of DCB resin B.

The final cohesive parameters for the indirect cohesive law in mode I following the equation (105) are given in Table 4.2-6. The cohesive law is shown in Figure 4.2-16.

<i>Fracture toughness</i>	<i>Cohesive stiffness</i>	<i>Critical peel stress</i>
$G_{Ic} = 0.25 \text{ kJ/m}^2$	$K_I = 12\,900 \text{ MPa/mm}$	$\sigma_c = 35 \text{ MPa}$

Table 4.2-6: Cohesive parameters in mode I for indirect method.

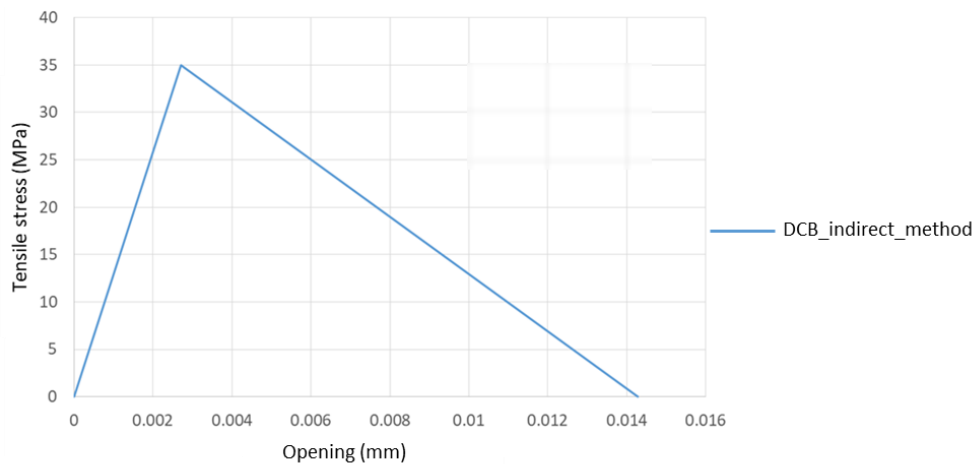


Figure 4.2-16: Resulting indirect cohesive law in mode I for steel-to-steel bonded assembly with resin B.

4.2.4.4. Comparison to 3D model

A 3D model was created to assess the hypothesis of the 2D model which considers a constant crack pattern along the width, but also plane strain conditions. The mesh of the model can be seen in Figure 4.2-17 and the element size in the crack propagation direction is 2mm to save computation time. The nodes along the width for the section at $x=0$ are all pinned at the bottom while a rigid element includes all the top nodes of the same section. The loading is applied on an independent node from this same rigid element. As the computation time is quite long, the model was not run until the end but during a long enough time to obtain a sufficient propagation.

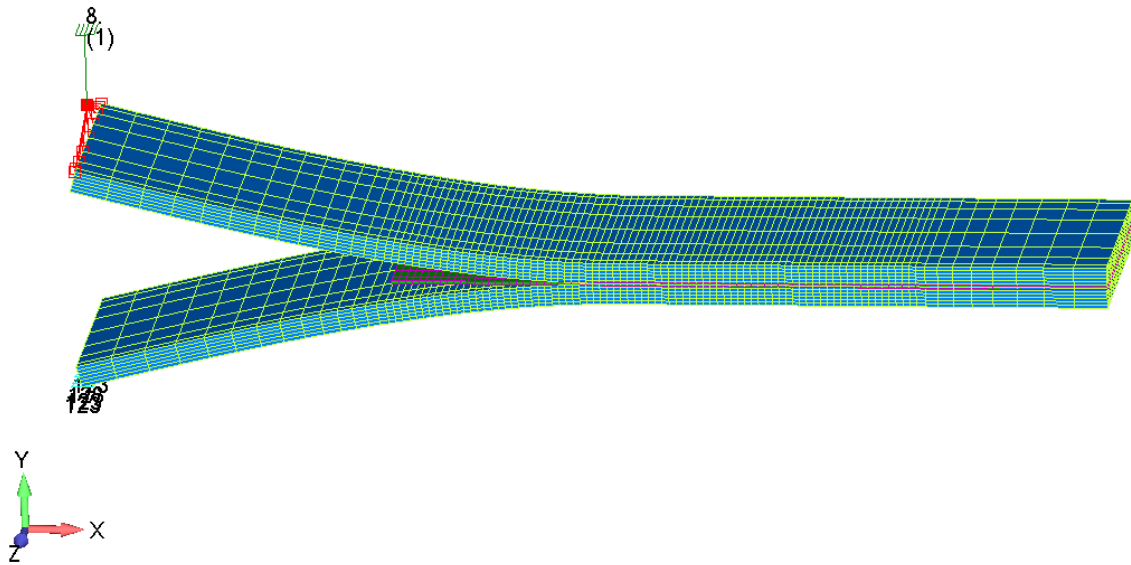


Figure 4.2-17: 3D DCB model.

The cohesive parameters for this simulation were taken from the final cohesive law in mode I. The load/displacement curve comparison between 2D and 3D models (both with same element size in the crack propagation direction) is shown in Figure 4.2-18. It can be seen that the propagation is almost identical in both models, although the 3D curve is smoother. The difference of failure forces is around 4% which validates the hypothesis made in 2D model. Furthermore, the crack propagation pattern is shown in Figure 4.2-19 by considering the damage in the bondline as the crack front shape. It can be compared to experimental observations after failure presented in Figure 3.2-1 that are similar. Thus, a 3D model can be interesting to confirm fracture surfaces but is not necessary for predicting failure forces in this case.

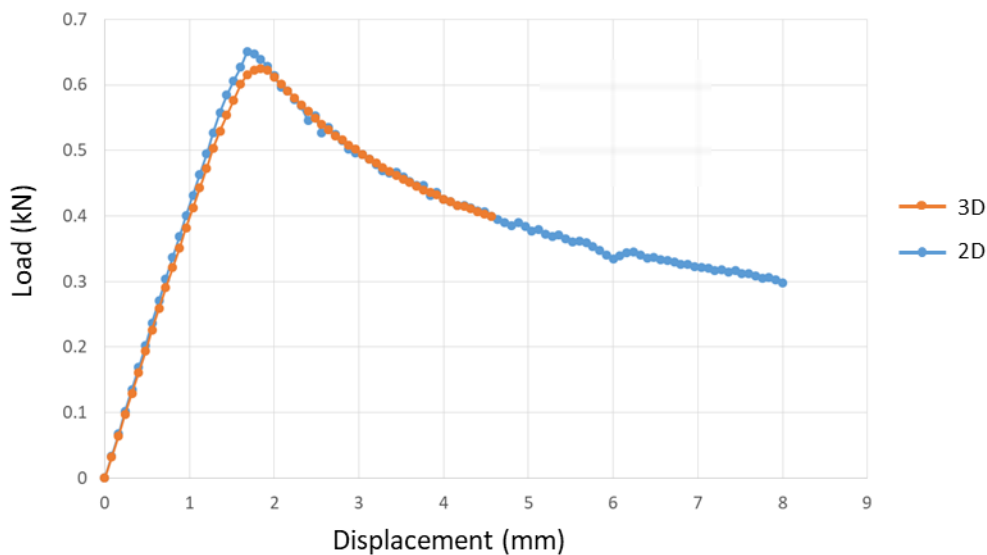


Figure 4.2-18: Comparison of load/displacement curves for DCB model in 2D and 3D with a 2mm mesh size.

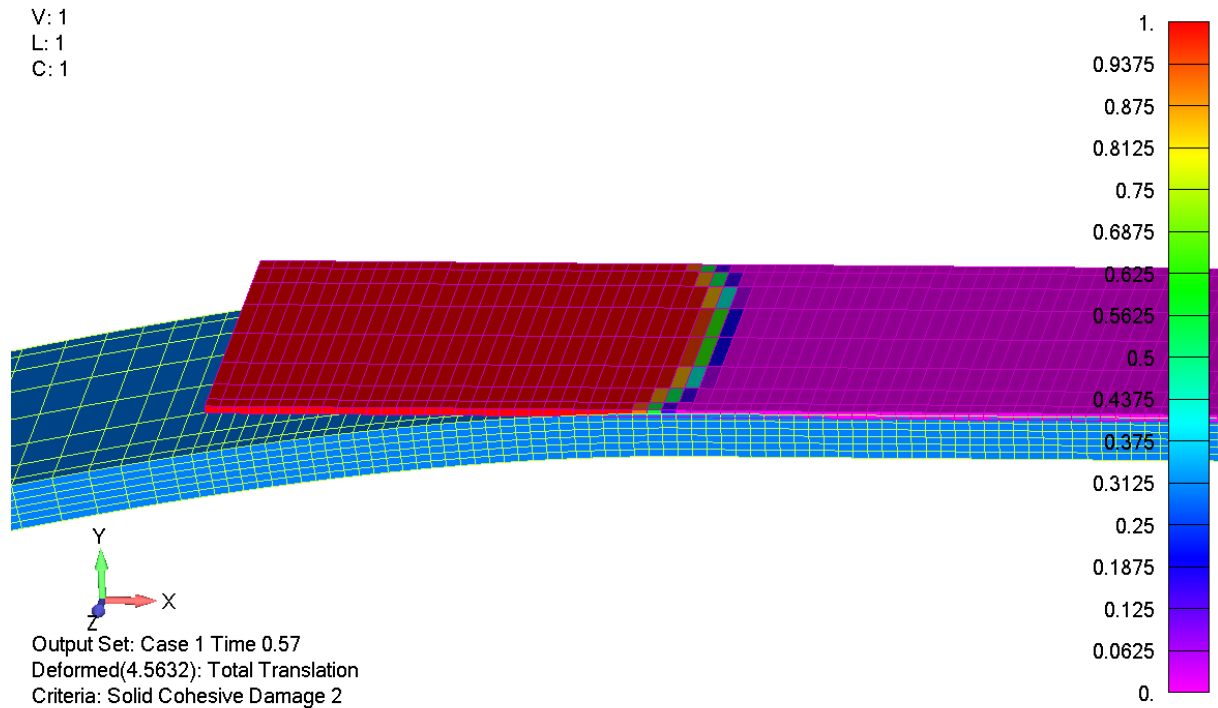


Figure 4.2-19: Fracture surface along the width for the 3D DCB model.

4.2.5. Model results in mixed mode

For the MMB modeling, both mode I and mode II laws obtained previously by the indirect method are used (Figure 4.2-20). The mesh to model the MMB test was the same than the one chosen for the DCB and ENF convergence meshing study, with a mesh size in the crack propagation direction of 1mm. The applied boundary conditions are the same than the one described in the part 4.1.2.

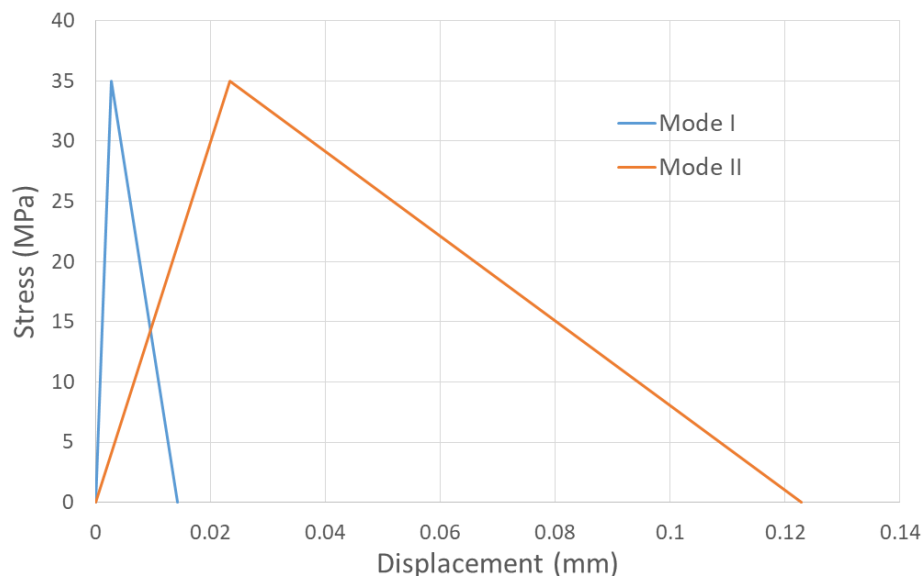


Figure 4.2-20: Indirect cohesive laws obtained in mode I and mode II.

Figure 4.2-21 presents the comparison between the experimental (part 3.2.4) and the numerical results for a mode ratio of 0.7. A series of computation were performed to find the best fit of

the coupling parameter α by varying its value between 0 to 1. The result of this analysis is a final parameter α chosen equal to 0.37. This value was chosen to get the smallest difference between numerical and experimental failure loads as described in Table 4.2-7.

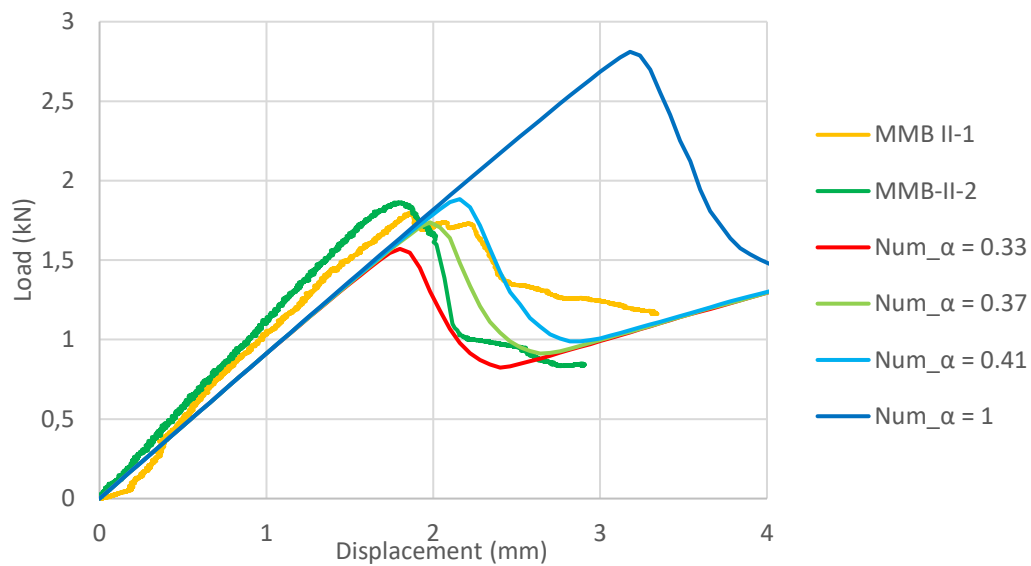


Figure 4.2-21: Comparison of load/displacement curves for MMB experimental test and model with a 1mm mesh size, a mixed mode ratio of 0.7 and different values of the coupling parameter α .

Figure 4.2-22 presents the same model results performed with the same cohesive laws, and the same values of the coupling parameter, compared to the experimental results for a mode ratio of 0.5.

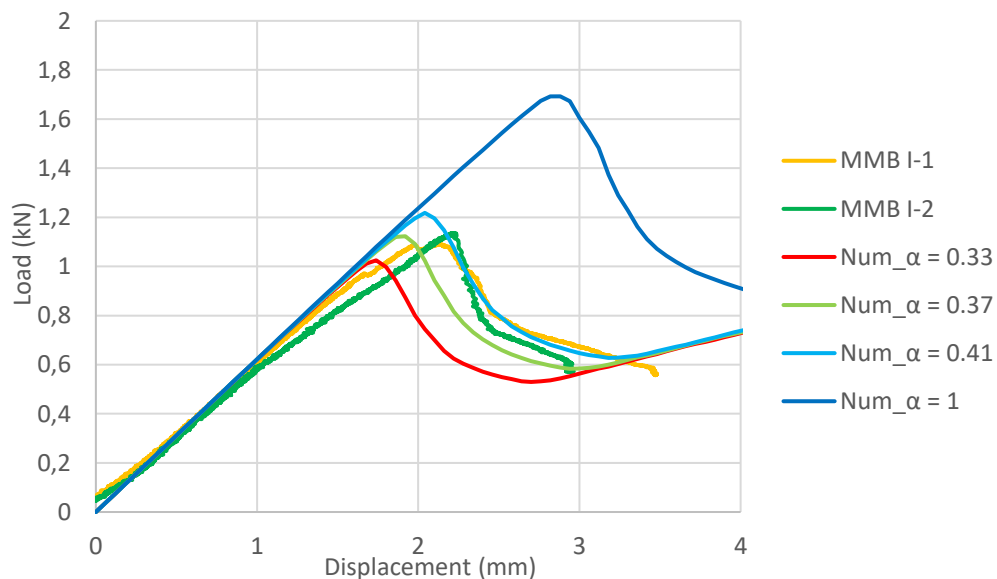


Figure 4.2-22: Comparison of load/displacement curves for MMB experimental test and model with a 1mm mesh size, a mixed mode ratio of 0.5 and different values of the coupling parameter α .

The curves show that the model can reproduce well the maximal load, rigidity and crack propagation. The resulting errors on the maximal load for each mode ratio and each value of the coupling parameter are given in Table 4.2-7.

	<i>MMB 70% mode II</i>				<i>MMB 50% mode II</i>			
<i>Coupling parameter α</i>	<i>1</i>	<i>0.41</i>	<i>0.37</i>	<i>0.33</i>	<i>1</i>	<i>0.41</i>	<i>0.37</i>	<i>0.33</i>
<i>Failure load (kN)</i>	<i>2.811</i>	<i>1.884</i>	<i>1.739</i>	<i>1.571</i>	<i>1.693</i>	<i>1.21</i>	<i>1.12</i>	<i>1.02</i>
<i>Difference to experimental failure load (%)</i>	<i>53.58</i>	<i>2.94</i>	<i>-4.98</i>	<i>-14.16</i>	<i>51.80</i>	<i>9.25</i>	<i>0.71</i>	<i>8.10</i>

Table 4.2-7: Comparison of experimental and numerical failure loads for MMB test for a mode mixity of 50% and 70% and for different coupling parameter values.

In conclusion, this study shows that the cohesive laws determination by using the indirect method (for brittle adhesive) can represent well the behavior of adhesively steel-to-steel bonding assembly with thin adhesive layer (1mm) and thicker adherends, in the full range of studied modes for standard tests. The generalization of this assumption to more complex geometries and loadings will be assessed in the next chapter to validate that this method can be used for full size bonded assembly.

4.3. Cohesive zone model determination using direct method

In the direct method, the cohesive law is measured experimentally in pure mode I (DCB test) and pure mode II (ENF test), based on the J-integral method and the local displacements measurements by DIC. These laws are then directly used in numerical DCB and ENF models with the FEM software FEMAP and no parameter needs to be calibrated in these cases. However, in mixed mode, no cohesive law was measured during the MMB test.

The available experimental results from the ENF test and the numerical cohesive law in pure mode II are plotted in Figure 4.3-1. Likewise, the available experimental results from the DCB test and the numerical cohesive law in pure mode I are plotted in Figure 4.3-2. As the experimental laws are monotonous, it was challenging to introduce a bilinear law based on these results. A bilinear law in the direct method was designed to have similar critical peel and shear stress compared to the experimental cohesive laws (average values). The analysis of part 4.2.2 and 4.2.3 proved that the stiffness had little to no impact on the general behavior. Therefore, its definition is not considered as critical.

Furthermore, in this direct method, it is important to underline that the critical toughness value is based on the value obtained with the J-integral method and consequently, is slightly different to the one used in the indirect method. The cohesive law values used for the direct modeling are summarized in the Table 4.3-1. The fracture toughnesses and critical stresses were kept as close as possible to experimental results and the fitting was mainly made using the stiffness parameter.

	<i>Fracture toughness G_c (kJ/m²)</i>	<i>Critical stress (MPa)</i>	<i>Stiffness K (MPa/mm)</i>
<i>Mode I</i>	<i>0.316</i>	<i>60</i>	<i>8426</i>
<i>Mode II</i>	<i>1.960</i>	<i>53</i>	<i>1060</i>

Table 4.3-1: Cohesive parameters using direct method for mode I and II.

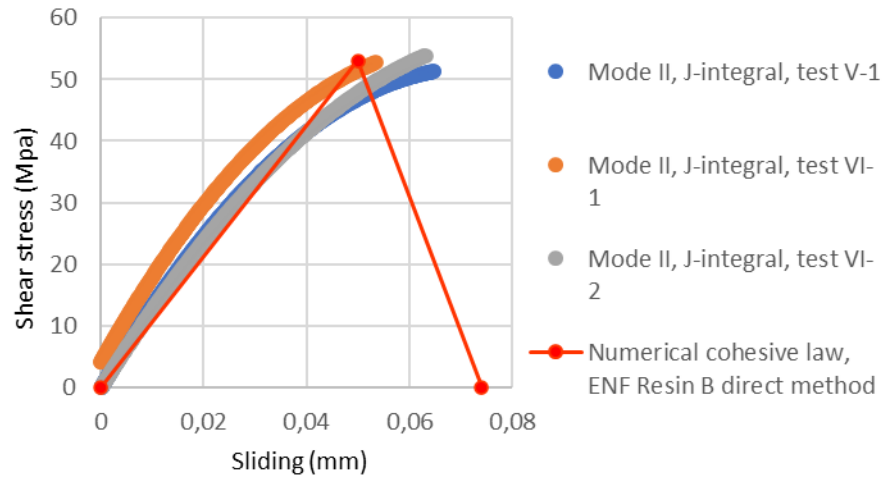


Figure 4.3-1: Experimental and proposed numerical cohesive laws in pure Mode II for ENF test.

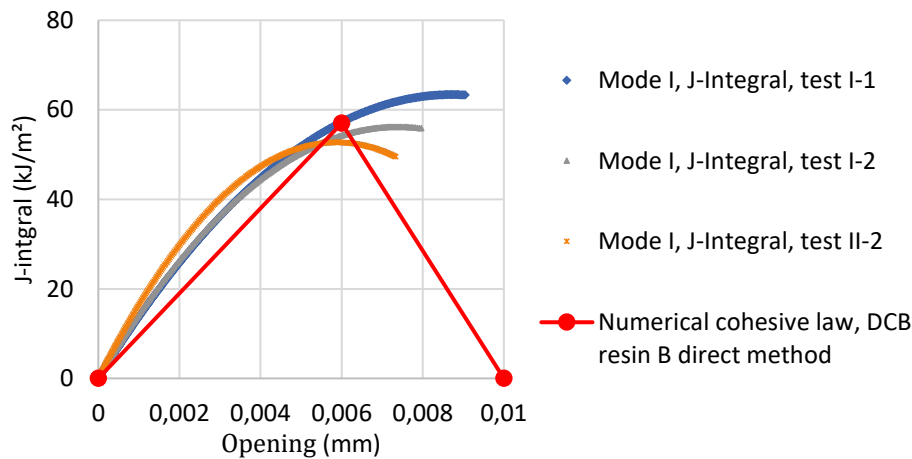


Figure 4.3-2: Experimental and proposed numerical cohesive laws in pure Mode I for DCB test.

4.3.1. Model results in mode II

Based on the mesh sensitivity analysis performed in the part 4.2.3, the 1mm element size was used. The numerical and experimental load/displacement results are plotted for different initial crack length ($a_0 = 59 \text{ mm}, 74 \text{ mm}, 90 \text{ mm}$) in Figure 4.3-3. It can be seen that the stiffness as well as the failure loads are quite close between numerical and experimental results. As the difference in failure loads is below 10% for all the tests, the models using direct cohesive laws can be considered to replicate properly the behavior of bonded assembly in pure mode II.

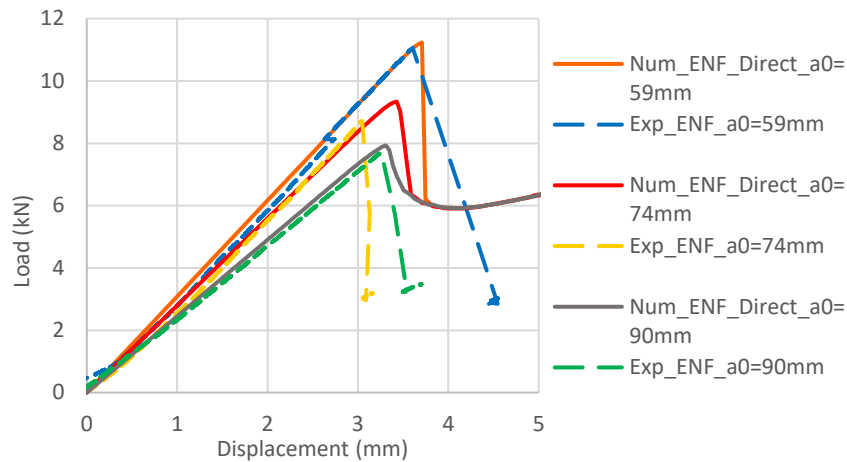


Figure 4.3-3: Numerical and experimental ENF load/displacement curves for different initial crack lengths.

Crack length (mm)	59	74	90
Numerical failure force (kN)	11.235	9.340	7.936
Experimental failure force (kN)	11.06	8.703	7.711
Difference (%)	1.58%	7.31%	2.91%

Table 4.3-2: Comparison of failure loads in mode II obtained numerically by the direct method and experimentally by ENF tests.

4.3.2. Model results in mode I

The comparison of load/displacement curves obtained experimentally and numerically is given in Figure 4.3-4. It shows that the direct method cohesive law predicts a more accurate failure load compared to the indirect method. This implies a more optimistic crack propagation part of the curve. This is supposed to be directly correlated to the higher critical toughness of the cohesive law, which is 0.316 kJ/m² for the direct method, and 0.25 kJ/m² for the indirect one. The values of failure loads are presented in Table 4.3-3 and tend to prove that the value measured with the J-integral computation leads to a more accurate failure prediction than the one obtained with the standard.

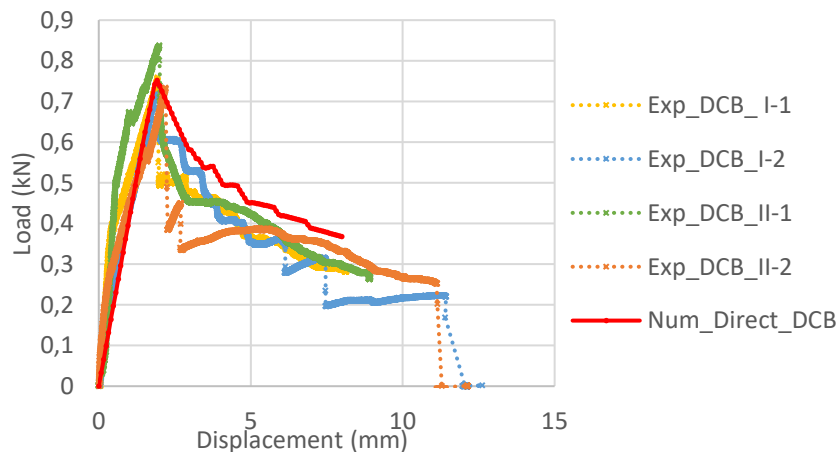


Figure 4.3-4: Numerical direct method and experimental DCB load/displacement curves.

	I-1	I-2	II-1	II-2
Experimental failure force (kN)	0.759	0.717	0.837	0.733
Numerical failure force (kN)		0.752		
Difference to mean experimental (%)		-1.23%		

Table 4.3-3: Comparison of numerical and experimental failure loads for the DCB direct method.

4.3.3. Model results in mixed mode

The cohesive laws determined in pure mode I and II were then implemented in MMB models with an element size of 1 mm in the crack propagation direction. This part will present the calibration of the coupling parameter α for both mixed mode ratio 50% and 70% of mode II. An initial value of the coupling parameter was set at $\alpha = 0.37$ based on the indirect method results.

Results of the coupling parameter calibration are shown in Figure 4.3-5 (for a ratio of 50% of mode II) and Figure 4.3-6 (for a ratio of 70% of mode II). Comparison of numerical and experimental failure loads is presented in Table 4.3-4 (for 50% of mode II) and Table 4.3-5 (for 70% of mode II). The coupling parameter allowing to obtain the closest average failure loads was 0.35. This is close to the parameter found in the indirect method. This parameter seems to be adapted for both mode ratios.

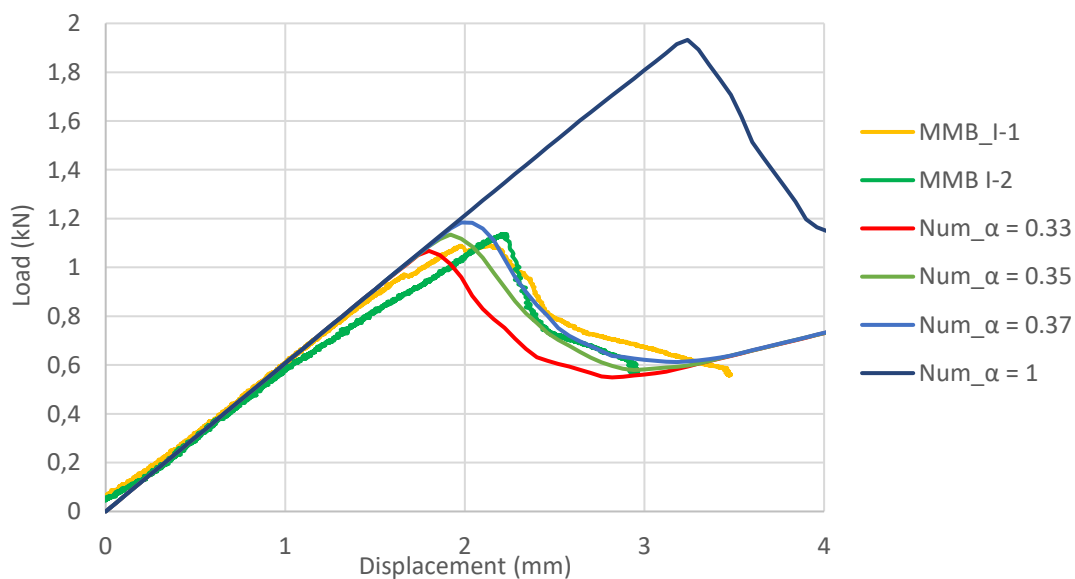


Figure 4.3-5: Comparison of numerical and experimental load/displacement curves for MMB test with 50% of mode II, for different values of the coupling parameter, using direct cohesive law.

Coupling parameter α	1	0.41	0.37	0.35	0.33
Failure load (kN)	1.932	1.290	1.184	1.135	1.068
Difference to experimental failure load (%)	73.30	15.68	6.20	1.75	-4.23

Table 4.3-4: Comparison of experimental and numerical failure loads for MMB test with 50% of mode II, for different values of the coupling parameter, using direct cohesive law.

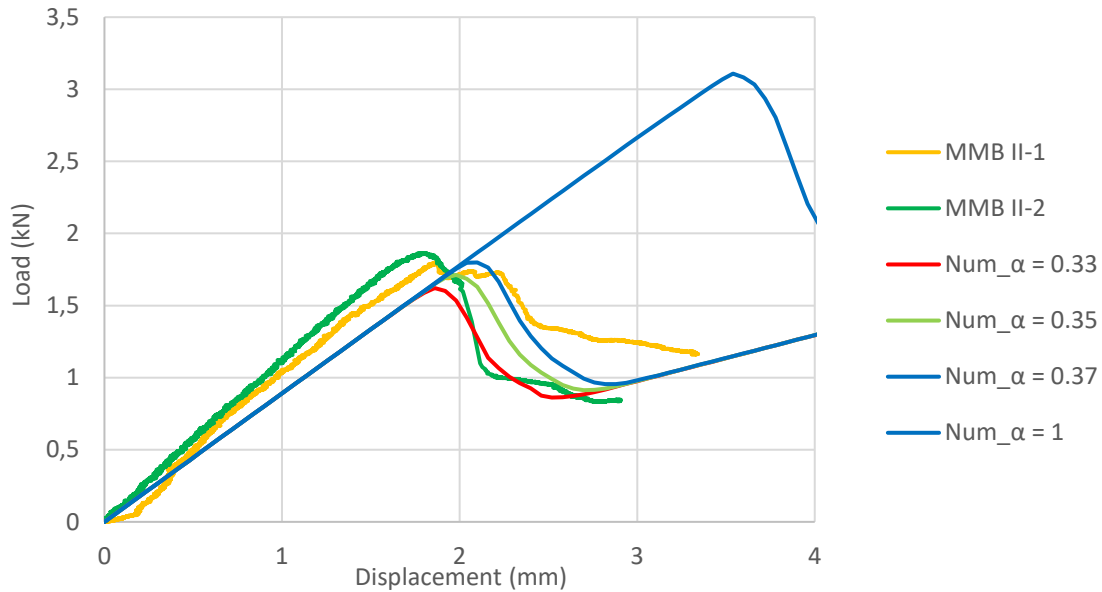


Figure 4.3-6: Comparison of numerical and experimental load/displacement curves for MMB test with 70% of mode II, for different values of the coupling parameter values, using direct cohesive law.

Coupling parameter α	1	0.41	0.37	0.35	0.33
Failure load (kN)	3.109	1.967	1.799	1.713	1.621
Difference to experimental failure load (%)	69.87	7.46	-1.67	-6.38	-11.42

Table 4.3-5: Comparison of experimental and numerical failure loads for MMB test 70% of mode II, for different values of the coupling parameter, using direct cohesive law.

4.3.4. Resulting cohesive law parameters

The final parameters for the calibration of cohesive laws using the direct method for the assembly characterization are given in Table 4.3-6.

	Fracture toughness G_c (kJ/m ²)	Critical stress σ_c (MPa)	Stiffness K (MPa/mm)	Coupling parameter
Mode I	0.316	60	8426	0.35
Mode II	1.960	53	1060	

Table 4.3-6: Resulting parameters of cohesive laws using direct method.

4.4. Discussion

Figure 4.4-1 and Figure 4.4-2 present the final cohesive laws in mode I and II obtained in this chapter using both direct and indirect studied methods. The cohesive laws measured in this part are only valid for the considered assembly with its specific adhesive, adherends, interfaces but also its specific adhesive thickness.

The shape of the direct and indirect laws are significantly different. The initial rigidity are similar, but the difference in the critical toughnesses and the critical stresses obtained for both methods, generate difference in the obtained cohesive law shape. From a physical point of view, the direct method seems more accurate, as brittle behavior has been observed and analyzed in chapter 3 (the area under the curve for the damaged part is lower, which corresponds well to a brittle fracture).

The results obtained with indirect method proved that results from standards (with the help of optical fiber) provided usable data. The indirect approach remains a valid method to obtain the cohesive laws as its implementation in the numerical models proved to lead to results close to the experimental ones, in terms of load/displacement curves for the pure mode I, pure mode II and mixed mode tests.

The results obtained with the direct method proved that the J-integral analysis has provided higher quality data. Yet, this method is more difficult to use, because of the local displacements measurement required to monitor local sliding, opening and rotation. In our case, the DIC was used, but these data could be obtained with much more simple sensor such as LVDT or inclinometer.

Regarding numerical prediction, one major drawback of the indirect method could be the computation time (high number of simulations). The validation of the directly computed cohesive laws requires actually a relatively limited number of models, computation and post process.

Though both approaches lead to rather different cohesive laws, both matched well with experimental results. This is consistent with literature such as in [120] for DCB test or [123] for single-lap test that conclude that the cohesive law shape has little impact on the behavior and the failure load prediction for such bonded assemblies.

The final cohesive model that has been fitted to mode I and II experimental results, should be able to predict correctly the behavior for other types of loading and assembly. The analysis has also shown that the proposed approaches relying on the formulation proposed in FEMAP and a coupling parameter seemed to be satisfactory. The coupling parameter, α , obtained for the direct and indirect method are really similar (respectively 0.35 and 0.37) and the comparisons between experimental and numerical results are very close.

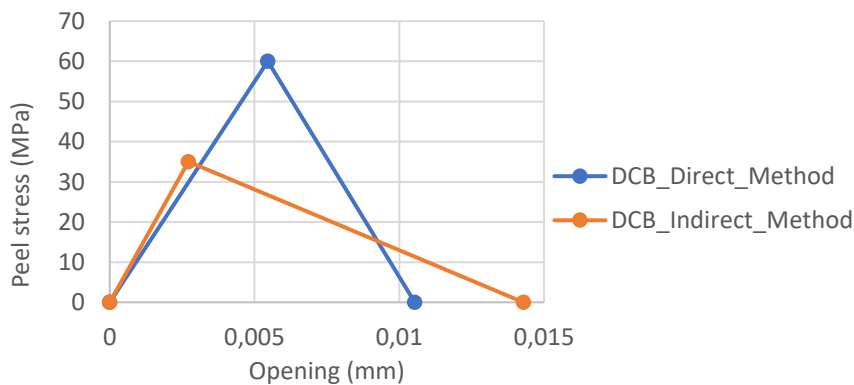


Figure 4.4-1: Final DCB cohesive laws.

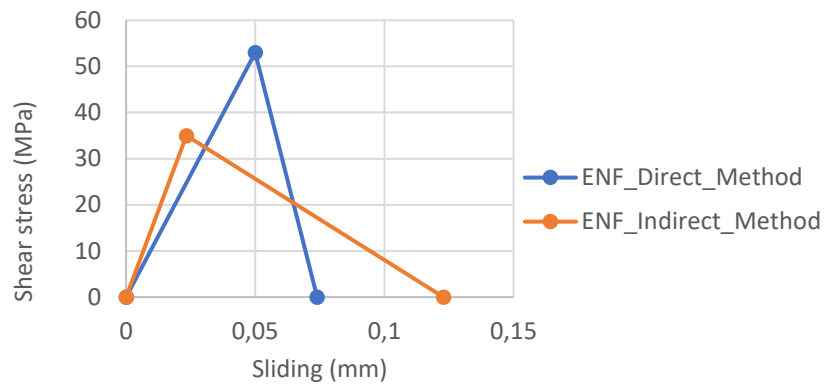


Figure 4.4-2: Final ENF cohesive laws.

In the next chapter, the direct and indirect cohesive laws will be tested to predict the behaviors of full size specimens more representative of real applications.

Chapter 5: Robustness appraisal of the proposed methodology

As the validity of the developed modeling approach (using finite element models and cohesive zone model) was carried out using small scale fracture mechanics investigations in the previous chapter, it was decided to apply it on more realistic samples to verify its adequacy. Thus, real-scale tests with loading conditions closed to reality (most commonly encountered loading situations for ship decks) were realized. In order to assess the efficiency of the proposed methodology and to investigate its robustness, it was decided to compare its performance with an alternative design methodology relying on both continuous and fracture mechanics, the coupled stress-energy-criteria method.

First, the experimental campaign and the obtained results are described. The coupled stress-energy criteria method is then carried out. Thirdly, the developed methodology is applied using both direct and indirect approaches. The final discussion compares the different methods and their ability to predict the studied bonded samples' behavior.

5.1. Experimental campaign at real scale and under most commonly encountered loading situations

5.1.1. Studied samples and instrumentation

To assess the robustness of the different design methodologies (the direct, indirect method, and coupled criteria) for full scale bonded reinforcement, two mostly encountered type of loadings have been chosen. Figure 5.1-1 presents those two load cases. The first one is a typical shear loading of the bonded patch which can be encountered on ship decks. The second one is a three-point bending (bending/tension) test which could be encountered on pressure loaded tanker.

The materials used for the sample manufacturing are medium carbon steel (C45 steel with a yield stress between 600 and 800 MPa, from datasheet) to ensure that no plasticity in the steel will occur during the test, and the adhesive is the resin B previously studied. The design and geometry of the specimens are shown in Figure 5.1-1.

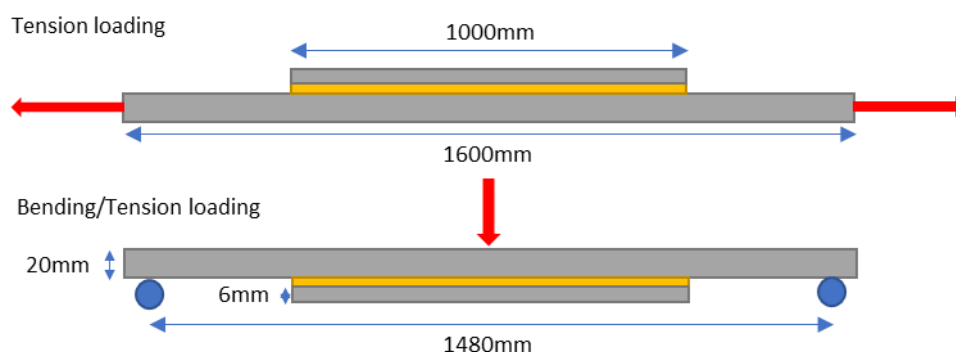


Figure 5.1-1: Full-size test geometries for tension and bending/tension loadings.

The bonding procedure is similar to the one described in chapter 3. The geometry is similar for bending and tension tests. The total length is of 1600 mm with a 1000 mm long bonded patch. The thickness of one of the substrates is 20 mm. The other one (the reinforcement corresponding

to the thinner substrate) is 6 mm thick. No crack initiations are made in these samples. These choices have been made to ensure that:

- the patch is long enough to express the behavior of a full-size patch (transition length should be small compared to the patch length),
- the 20 mm substrate length is long enough to have some distance between the border of the patch and the clamp of the test machine for the tension test, or between the border of the patch and the support for the bending test (20 cm),
- the 20 mm substrate has a standard thickness which can be encountered on ship deck.

This change in shape has introduced much more leakage during the bonding procedure. Thus, the samples were made in two steps with two castings of the resin (using the same batch). Post curing (70°C during 16h) was made after the second casting. The thickness of the bonding layer (1mm) was controlled using 3D printed plastic pieces maintaining the steel plates in place during the casting. The thickness of the adhesive has been controlled after curing, showing that, in the first 20 cm at each border of the bonded patch, the thickness has not change more than ± 0.2 mm. The center section was not measured.

The instrumentation of the specimens is shown in Figure 5.1-2. A set of ten strain gauges were used to obtain local strain measurements on the surface of the specimen. The gauges 1/2/9/10 were used to monitor the bending and tension in the 20 mm substrate due to the off-centered disposition of the 6 mm substrate. The gauges 3/4/7/8 were used to monitor the strain at the border of the patch and obtain information concerning the crack initiation and the corresponding failure load. The gauges 5 and 6 were used to monitor the strain difference in the substrate and the reinforcement. Finally, the continuous optical fiber, placed in the center of the reinforcement substrate (exterior optical fiber), was used to monitor the strain all along the reinforcement length and the crack propagation when it was slow enough. These data have been used to compare the experimental behavior to the ones obtained with the modeling.

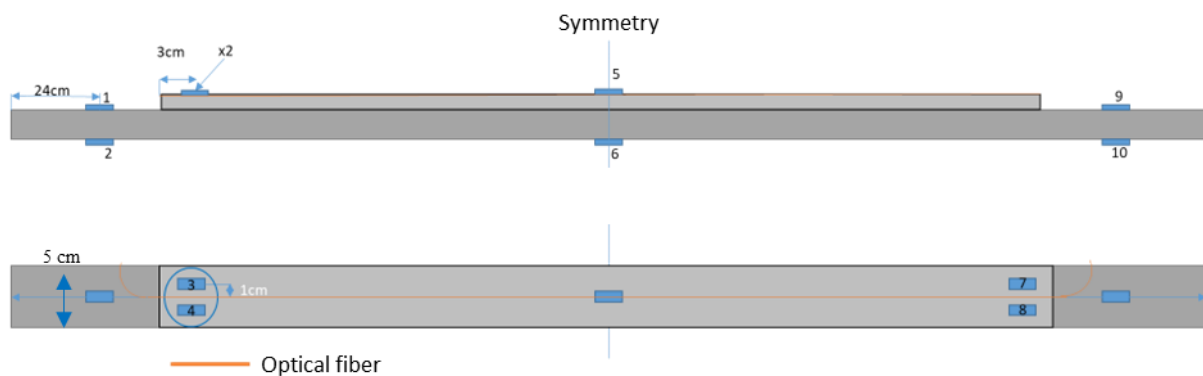


Figure 5.1-2: Full size tension and bending samples instrumentation.

5.1.2. Test protocols

Two sets of three tests were performed:

- 3 tension tests made on a 2500kN Instron test machine (1% error in measurement, 1% error in repeatability). The samples were clamped on a length of 10 cm on each side, leading to a 140 cm tested length (Figure 5.1-3a, b). The used load cell was the one from the machine,
- 3 three-point bending tests made on a 300kN Losen test machine. The test frame was set at a length of 148 cm (maximal test frame allowable length) (Figure 5.1-4). The used load cell was adapted to the expected load during the test (10kN, precision $\pm 0.145\%$).



Figure 5.1-3: a) Initial tension test without instrumentation, b) Tension sample lower end with optical fiber and gauge instrumentation.

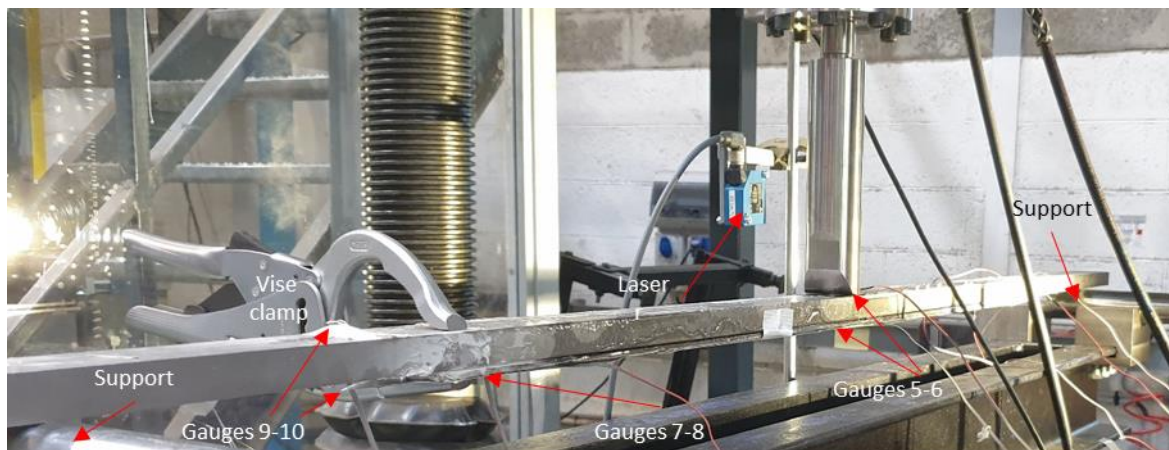


Figure 5.1-4: Bending test with instrumentation.

On Figure 5.1-4, a vice clamp was used at one edge of the bonded area. It was placed to remove the mode I loading at one end of the patch for the tension and bending tests. This allowed ensuring that the crack initiates on the other side of the patch, where the DIC setup was placed. In each case, the clamp was put in place next to the gauges 7 and 8 leading the crack initiation to start in the gauges 3 and 4 area. The tests were conducted up to the total debonding of the patch in tension and in bending.

The analysis of the failure surfaces (visible in Figure 5.1-5) shows that the failure was similar for the six tests and 100% adhesive (Appendix A6). The failure pattern reveals a parabolic crack front shape that corresponds to the propagation. Based on the analysis performed in chapter 4 on the failure pattern for DCB, ENF and MMB tests, this figure tends to attest that mixed mode ratio (G_{II}/G_c) was obtained for the two sets of tests, with at least a ratio of 50%.



Figure 5.1-5: Adhesive failure and crack front shape of the samples.

5.1.3. Strain measurement and load at failure

The next part presents the load/displacement curves and the strain gauges measurements curves for the tension and bending tests.

5.1.3.1. Tension test

Figure 5.1-6 shows the three load/displacement curves obtained for the three traction tests. It can be observed that the curves are initially linear. A second nonlinear part can be seen which might be correlated to the crack propagation occurring in the bondline (in a stable manner, progressive loss of rigidity). Then, the crack propagates violently on the whole bondline length.

In fact, the load/displacement curve of the three tests shows a violent decrease corresponding to the stiffness loss by the debonded adherent (abrupt loss of rigidity around the displacement of 2 mm). For the analysis of these curves and the modeling, the patch is considered to be broken when the crack initiates, i.e. at the first point of non linearity. However, the identification of this point on the curve is not an easy task. The results obtained are summarized in Table 5.1-1 with relatively low confidence.

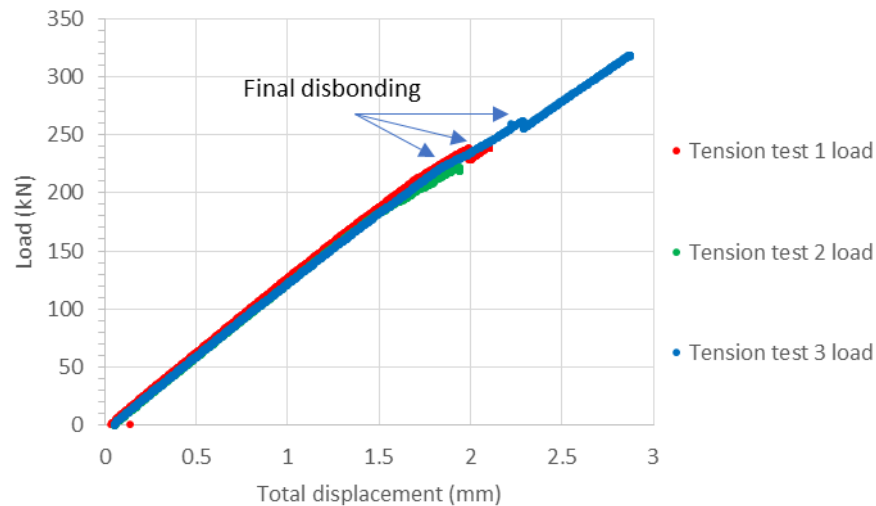


Figure 5.1-6: Tension test load/displacement curves.

To solve this issue, the gauges bonded just near the crack initiation on the sample (gauges 3 and 4, at 3 cm of the border of the adherent) are used as crack time initiation measurement devices. When the gauge curve decreases, the crack is considered to have propagated under the gauges. Figure 5.1-7 displays the gauges 3 and 4 measurements for the three tension tests. It can be seen that during the loading of the bondline, the measurements are really similar for the three tests. At the beginning of the test, an offset of the strain values is visible. It is related to the initial loading of the sample which is not perfectly straight (tightening of the clamps). This may have an impact on the patch's general behavior (small initial torsion or bending). Disbonding occurred in the patch for relatively similar strain measurement of around $350 \mu\text{strain}$ (three tests' mean value) at a load level of around 170kN (three tests' mean value). The precise values are given in Table 5.1-1. These values will be used as comparison with the model results to validate the load at failure predictions.

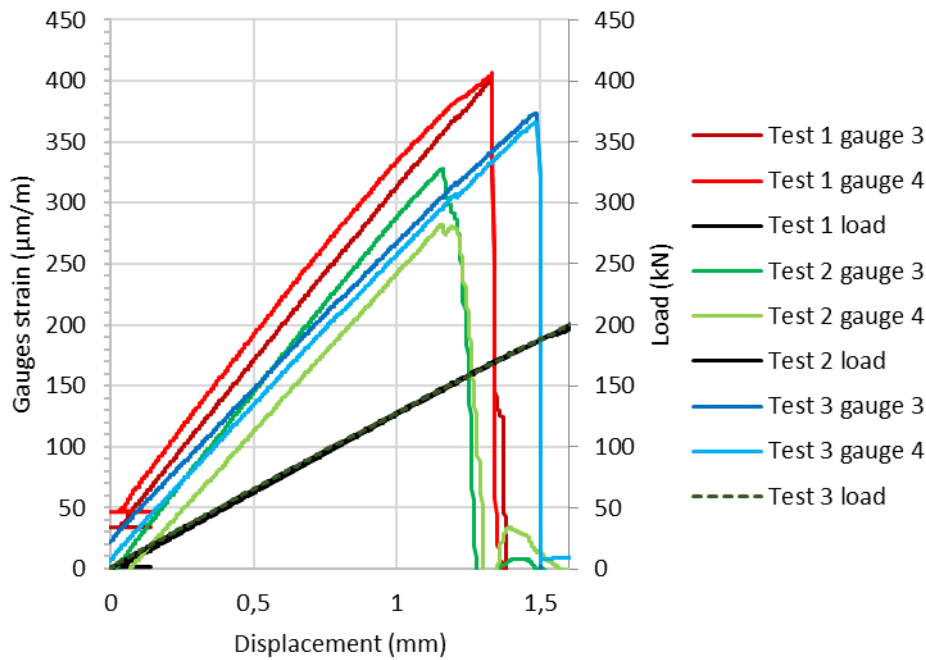


Figure 5.1-7: Gauges 3 and 4 strain measurement for the three samples in tension.

	<i>test 1</i>	<i>test 2</i>	<i>test 3</i>
<i>Gauge 3 max (µm/m)</i>	404	327	375
<i>Gauge 4 max (µm/m)</i>	400	282	366
<i>Mean gauge 3 and 4 max (µm/m)</i>	402	303	371
<i>Load at break (kN) using mean gauge data</i>	170	148	181
<i>Load at failure (kN) using load/displacement non-linearity</i>	160(±10)	140 ±10)	160 (±10)

Table 5.1-1: Strain and load at failure for the tension test.

5.1.3.2. Bending test

Figure 5.1-8 shows the three load/displacement curves obtained for the three bending tests. It can be seen that the curves are initially linear then nonlinear when the crack propagates. The load/displacement curves show an abrupt decrease corresponding to the stiffness loss by the debonded adherent. The same analysis as the tension test is performed on the failure time, and the gauges 3 and 4 are used as crack time initiation measurement devices (Figure 5.1-9). Disbonding occurred in the patch for around 440 µstrain (mean value) at a load level of around 570 daN (mean value). The precise values are described in Table 5.1-2. These values will be compared with the modelling predictions.

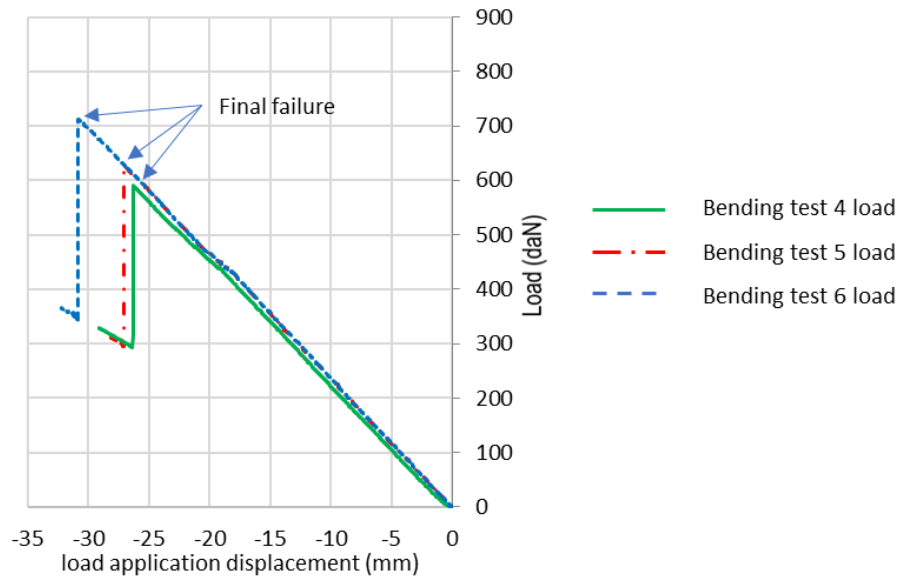


Figure 5.1-8: Load/displacement curves of the bending tests.

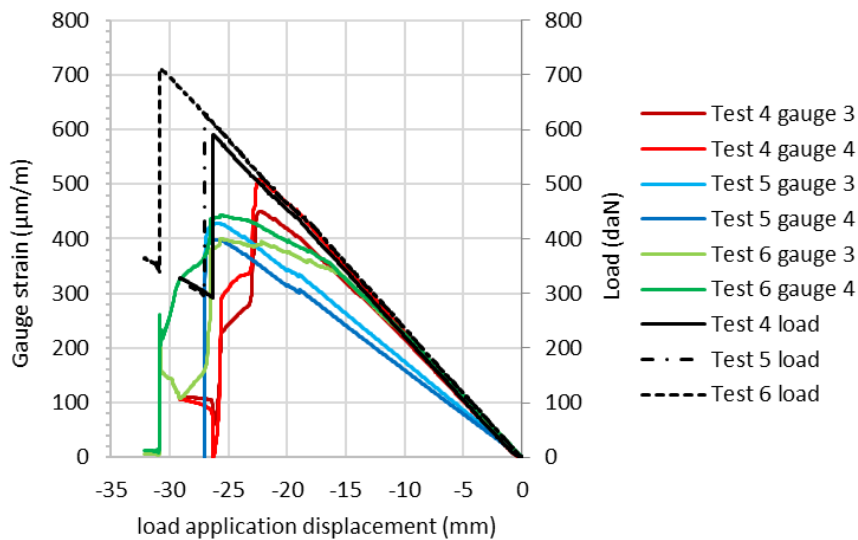


Figure 5.1-9: Gauges 3 and 4 strain measurements during the bending tests.

	test 1	test 2	test 3
Gauge 3 ($\mu\text{m/m}$)	506	427	398
Gauge 4 ($\mu\text{m/m}$)	454	396	441
Mean gauge 3 and 4 (μstrain)	480	411	420
Load at failure (daN) using gauge measurement	500	605	601
Load at failure (daN) using load/displacement non-linearity	450(± 10)	440(± 10)	450(± 10)

Table 5.1-2: Strain and load at failure of the bending tests.

5.2. Stress/energy criteria application to full size model

To check the capabilities of the direct and indirect methodology, the load at failure prediction capability has to be assessed. In our case, it is compared to another method of the literature: the coupled stress energy method. This method has, compared to the cohesive element methods,

limited capacity to express the local behavior of the assembly, but can provide good predictive failure capacities.

This criterion consists in combining the stress and the energy while bypassing the problems:

- of stress concentration at patch border for the stress approaches,
- necessity to have an initial crack to compute the energy approach.

In the coupled criteria the damaged length (a_d) predicted by the stress criterion is compared to the critical crack length (a_c), the minimal crack length required for the crack to propagate predicted by the energy criterion. For a design loading, the coupled stress-energy approach states that the failure (crack initiation and propagation) will occur when both damage and critical lengths become equal as illustrated in the Figure 5.2-1.

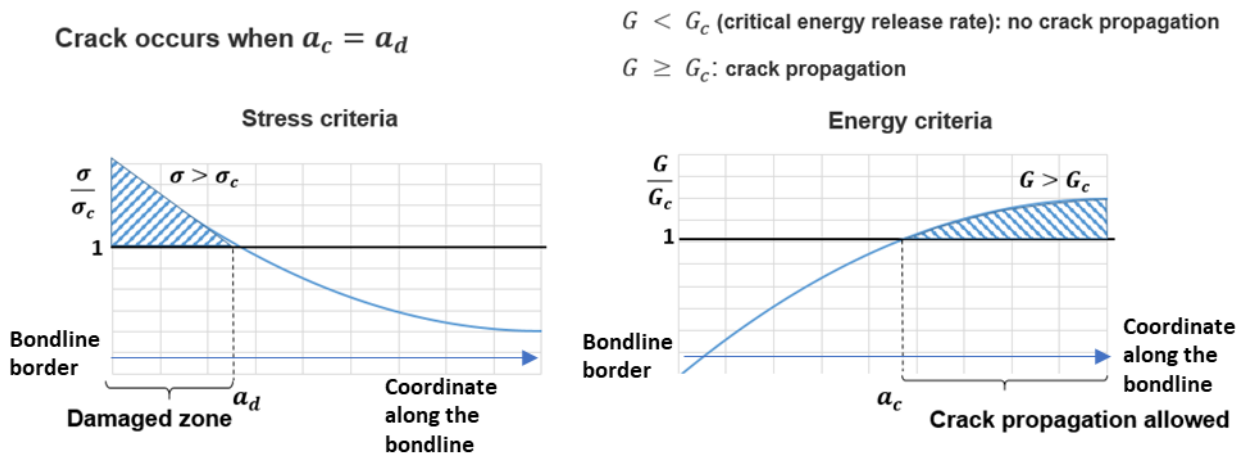


Figure 5.2-1: Stress- energy coupled criteria.

5.2.1. Hypothesis for FE model

X-symmetry was taken into account to model only half of the samples. The material properties were defined as linear elastic for the steel substrates with a Young modulus of 210 GPa, and the adhesive properties were defined as linear elastic with a Young modulus of 3.3 GPa (using bulk test results for resin B - Appendix A4). The applied loading for both models (tension test and bending test) was set from the average experimental failure load. The boundary conditions are shown in Figure 5.2-2 for the tension test. Regarding the bending test, the boundary conditions are described in Figure 5.2-3.

The boundary conditions were applied accordingly with the experimental investigations (same fixed displacement).

For the tension model:

- at the load applications points, y and z displacements were blocked,
- at the symmetry plane, x displacements were blocked.

For the bending model:

- on the sliding pivot, y and z displacements are blocked,
- at the symmetry plane, x displacements were blocked.

The applied loading for both models was realized using the average experimental failure load obtained with the gauges.

The values for the time steps were defined constant during the loading. No convergence issue was observed.

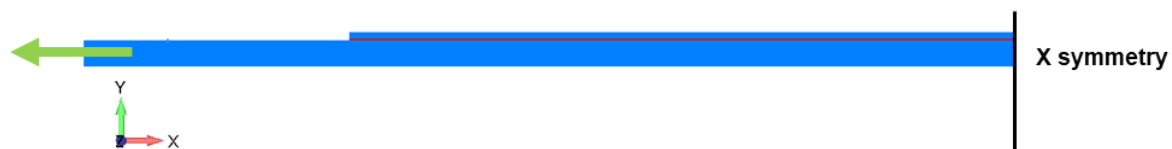


Figure 5.2-2: Finite element model boundary conditions for tension test.



Figure 5.2-3: Finite element model boundary conditions for bending test.

Compared to the previous finite element models described in chapter 4, the 1 mm thick adhesive layer was modelled using 4 elements in the thickness, as visible in Figure 5.2-4. It was made to fit the geometry of the experiments and of the cohesive models.

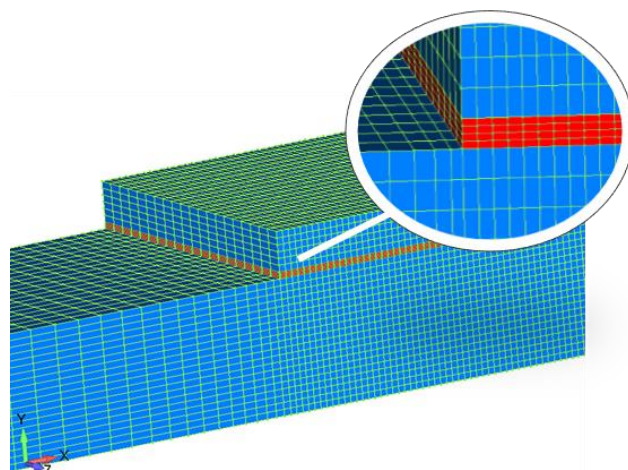


Figure 5.2-4: Stress analysis meshing.

5.2.2. Stress criteria and mesh sensitivity

To be in accordance with the failure mode obtained experimentally, it must be noted that the stress and energy analysis are performed at the resin/steel interface in the model. The stress will be computed in the first element in the thickness and at a centered position in width (where stress is maximal). The strain energy will be considered only at the interface layer to reduce computation time. This approximation is made following the results obtained at chapter 3 (adhesive failure mode).

When using a stress criterion, the predicted failure load is the load at which the monitored stress reaches the critical stress. Two types of critical stresses can be used:

- the stress in the bulk of the adhesive, in case of cohesive failure,
- the interfacial stress, in case of adhesive failure, obtained through standardized test, such as TAST tests.

The stress analysis can be performed at different locations, and on different stresses. The choice of the studied stress is also really important and highly impacts the obtained results. The state of the art has shown that the peel stress, shear stress, and maximal principal stress have been used to predict bonding failure in different application (part 1.3.1). These three stresses will therefore be studied during the mesh sensitivity analysis.

First, a mesh sensitivity analysis was performed on the tension test model. The basic mesh is shown in Figure 5.2-4. The mesh is refined in the first few centimeters of the crack propagation length (in x-direction). The mesh sensitivity results performed for tension test are plotted for the shear stress, peel stress and maximum principal stress, respectively in Figure 5.2-5, Figure 5.2-6 and Figure 5.2-7, in the first element in the thickness of the adhesive.

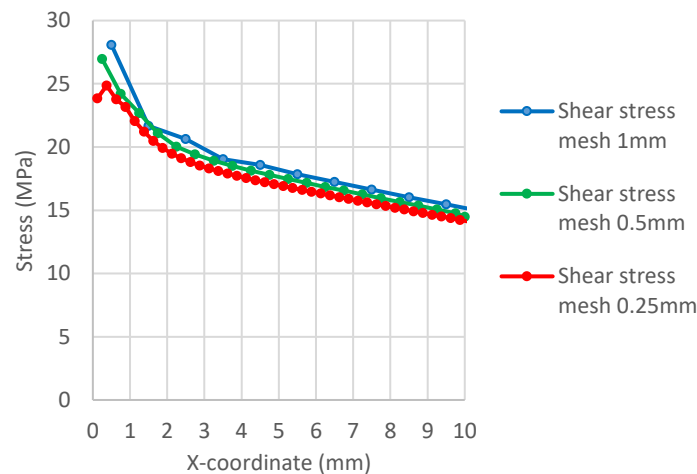


Figure 5.2-5: Mesh sensitivity analysis for the tension test: shear stress.

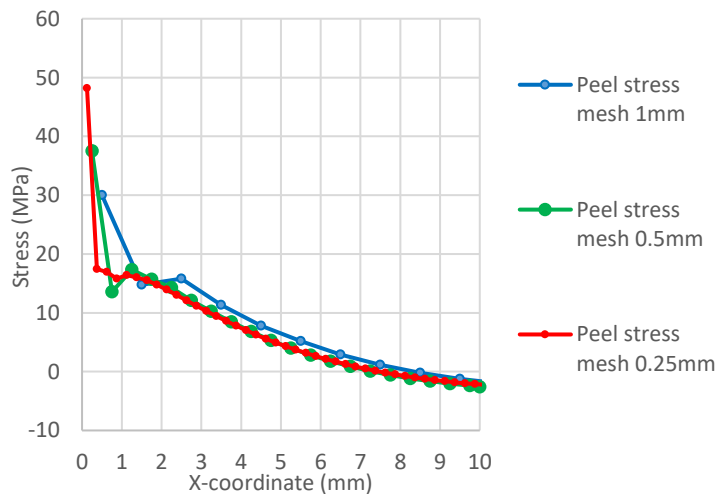


Figure 5.2-6: Mesh sensitivity analysis for the tension test: peel stress.

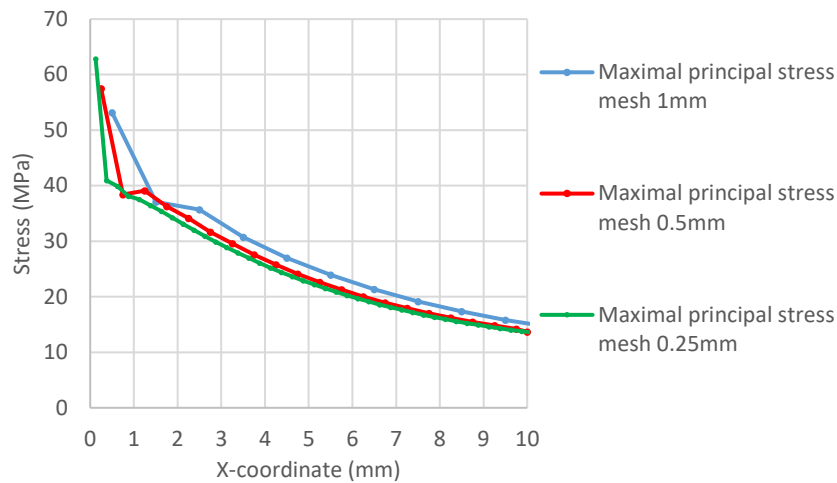


Figure 5.2-7: Mesh sensitivity analysis for the tension test: principal stress.

The mesh sensitivity analysis shows that for the peel stress and the maximum principal stress, the result does not converge around the border of the model (< 2 mm) and stresses tend to infinity as the mesh size decreases because of the stress concentration. Thus, no analysis can be performed using these values. In the case of shear stress, the model is being considered to converge for a mesh size of 0.25mm, except for the initial element. This stress will therefore be used for the stress/energy criteria analysis, with the exception of the first element.

The experimental campaign performed in the chapter 3 has shown that adhesive failure was obtained. In this case, defining the stress criteria from bulk results seems to be inadequate. Therefore, it was decided to adopt the shear strength obtained from TAST test as critical value. The obtained average shear stress at failure was 30.4 MPa (see Appendix A2). The Figure 5.2-8 shows the mesh sensitivity analysis performed for the bending model.

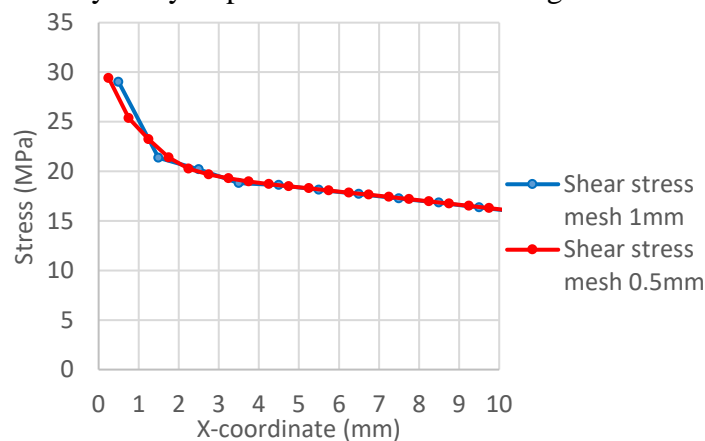


Figure 5.2-8: Mesh sensitivity analysis for the bending test: shear stress.

In the case of bending test, for shear stresses, the model seems to converge for a mesh size of 1mm. Thus, it was decided, because of the low difference in computation time, to keep the 0.5 mm mesh.

Figure 5.2-9 presents the final shear stress curves that will be used for the coupled criteria definition (obtained for a mesh size of 0.25 mm for the tension model, and 0.5mm for the bending test). It can be seen that, despite the two types of loading being really different (tension and bending), the final shear stress curves are close.

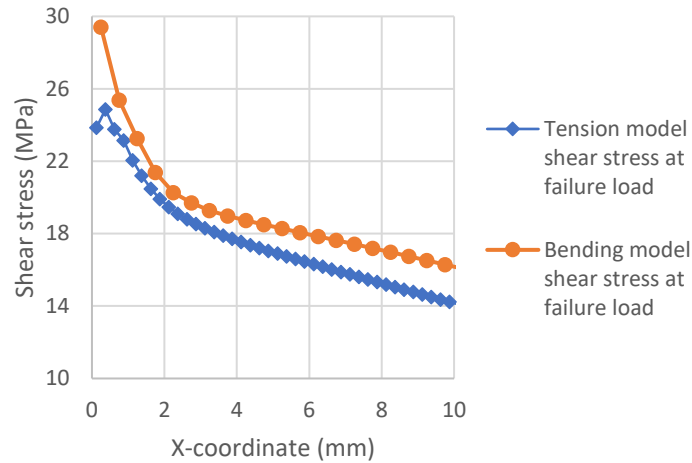


Figure 5.2-9: Tension and bending model shear stress.

5.2.3. Energy criteria

This criterion is based on the measurement of the energy release rate (ERR, described in part 1.3.3). The Virtual Crack Closure Technique (VCCT) can be used to determine it using numerical finite element approach. Several methods can be performed within the VCCT but only the two-step method will be presented here.

The local energy release rate equation used for the VCCT in 2D without any mode III contribution (neglected) is reminded in equation (106).

$$G_t = \frac{1}{2da} [F_{c,x}(u_d - u_c) + F_{c,y}(v_d - v_c)] = G_{II} + G_I \quad (106)$$

In this criterion, the ERR is used and compared to the critical ERR, G_c , of the interface. For a certain level of loading, when $G_t = G_c$, a characteristic length a_c will thus be defined. If the length of the initial crack a_0 is greater than the critical crack length a_c , the crack propagates.

This criterion can be also used in such a way that the ERR is assessed for a step of propagation starting with an initial crack a_0 . If the available energy at the crack tip is greater than the critical ERR, then the crack will propagate.

Alternatively, the ERR can be evaluated as the crack propagates from the initial position to a large distance as illustrated in Figure 5.2-10. Thus, in order to use that criterion, it is necessary to calculate the ERR for different crack lengths.

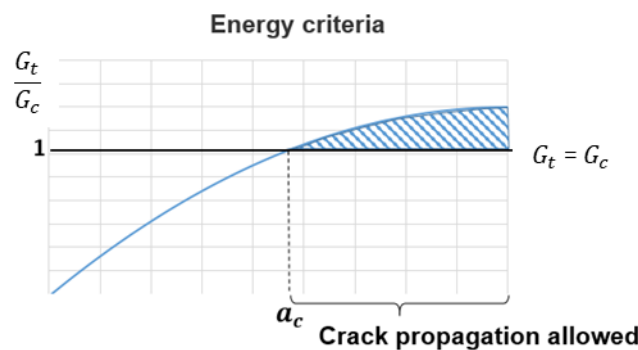


Figure 5.2-10: Illustration of the energy criteria with a critical interface ERR G_c and a characteristic length a_c .

A drawback of the method is the necessity to know the initial crack dimension. This is in general related to inspection techniques.

When the loading induces mode mixity (when the crack is loaded in mode I, II and III simultaneously), the total critical ERR can be defined in several ways. The one that was chosen here (making the assumption of mode I and II only) is the Benzeggagh-Kenane (B-K) criteria. It considers values based on tests in mode I, mode II and mixed mode and interpolates the values with a Power law as shown in Figure 5.2-11. The function used for the interpolation is detailed in equation (107).

$$G_t = G_{Ic} + (G_{IIc} - G_{Ic}) \left(\frac{G_{II}}{G_t} \right)^\eta \quad (107)$$

where η is the only parameter that needs to be characterized. In the presence of mode III, the last term with the power would be $\left(\frac{G_{II} + G_{III}}{G_t} \right)^\eta$.

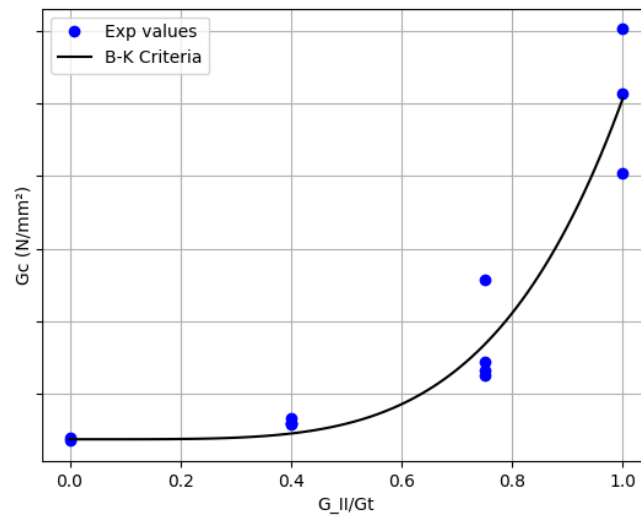


Figure 5.2-11: Example of the definition of the critical ERR with the B-K criterion for a resin C.

5.2.3.1. Elaboration of VCCT in FEMAP

In order to calculate the mode I and II contributions, the VCCT method was used. This method is not available in NASTRAN and was developed using FEMAP API, and PYTHON CODE. Several simulations were performed with the same model by unzipping one node by one node at the adhesive/steel interface. Since it is a tedious task to run each model and post-process it, a small routine (an API) was created in FEMAP to automate it. The routine was written in the VBA language and used in the software as a custom tool. The pseudo-codes main steps for the routine is detailed in the Appendix A5.

5.2.3.2. Energy criteria definition

The B-K criterion was used to define a critical ERR for all mode ratios G_{II}/G_t . This law has been experimentally obtained and already discussed in chapter 3. Figure 5.2-12 presents the final B-K criterion fitting on the experimental data. The results of the resin B were quite particular (compared to Figure 5.2-11) as the results in mixed mode were just equal or slightly

below the results in pure mode I up to relatively high G_{II}/G_t ratio (~ 0.75). The curve was kept as nearly linear until reaching this mode ratio.

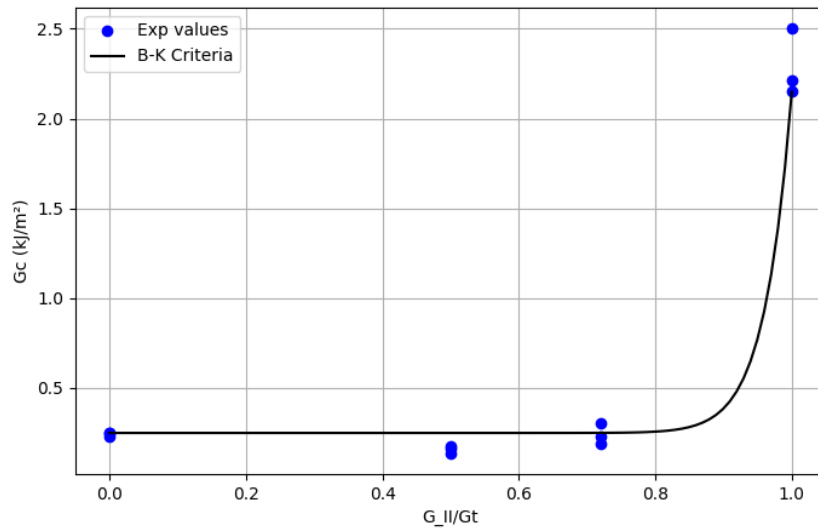


Figure 5.2-12: Resin B fracture test results and B-K criterion fitting.

The results of the VCCT for the converged mesh is plotted in Figure 5.2-13 for the tension model, and in Figure 5.2-14 for the bending model.

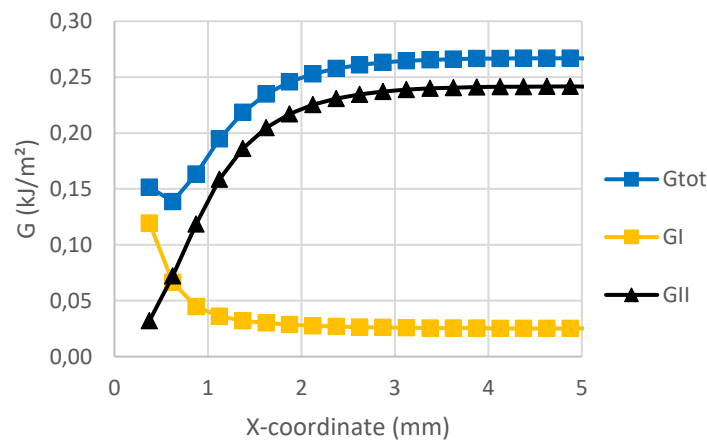


Figure 5.2-13: VCCT energy release rate for the tension model.

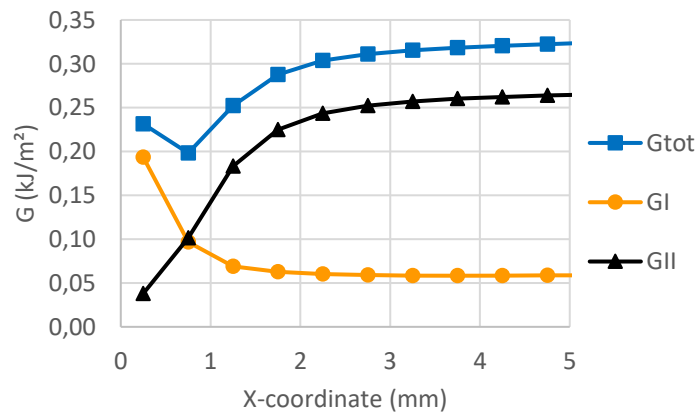


Figure 5.2-14: VCCT energy release rate for the bending model.

It can be seen that the ERR continuously increases except from the first to the second element. The analysis of the first element must be avoided because of this issue. In the following, the analysis will be done starting from the second element. Figure 5.2-15 presents the resulting (from the VCCT) mixed mode ratio along the bondline. It can be seen that the mode I loading is predominant initially (and should not be underestimated) and that the crack propagates mainly in mode II. It can also be stated that, despite the two tests being totally different, the energy at the border of the bondline seems to be close.

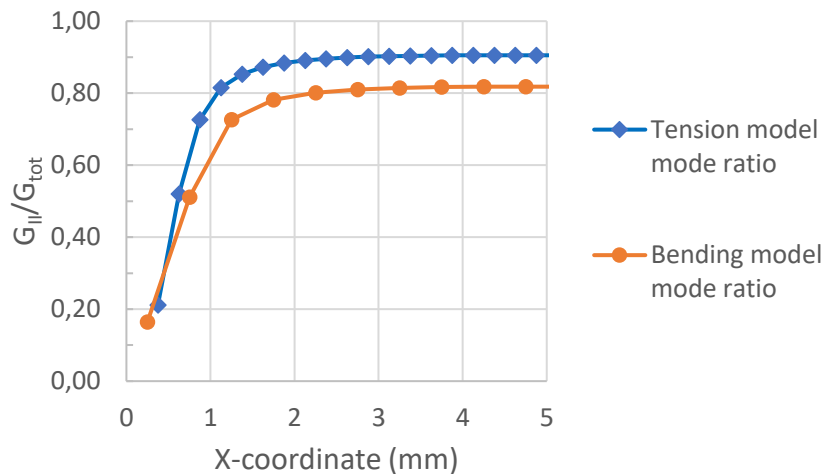


Figure 5.2-15: VCCT G_{II}/G_{tot} mode ratio for the tension and bending model.

5.2.4. Load at failure prediction analysis using coupled stress-energy criteria

Using the shear stress profiles, the shear strength (value from TAST), the energy release rate and the critical toughnesses obtained with fracture mechanics tests for the converged mesh, a numerical failure load can be determined. The coupled criterion at the experimental failure load tests is shown in Figure 5.2-16 for tension test and in Figure 5.2-17 for bending test. It can be noted that depending on the applied load:

- the criteria can intersect each other, without any of them being fulfilled (example: at average experimental failure load),
- the criteria can intersect each other with only one of the criteria being fulfilled (example at 1.15 time the average experimental failure load). In this case, the stress criterion is not fulfilled, and the failure is not predicted to happen,
- the first load where the two criteria are fulfilled, is 1.22 times the average experimental failure load (Figure 5.2-16) in tension, and 1.13 time the average failure load in bending (Figure 5.2-17).

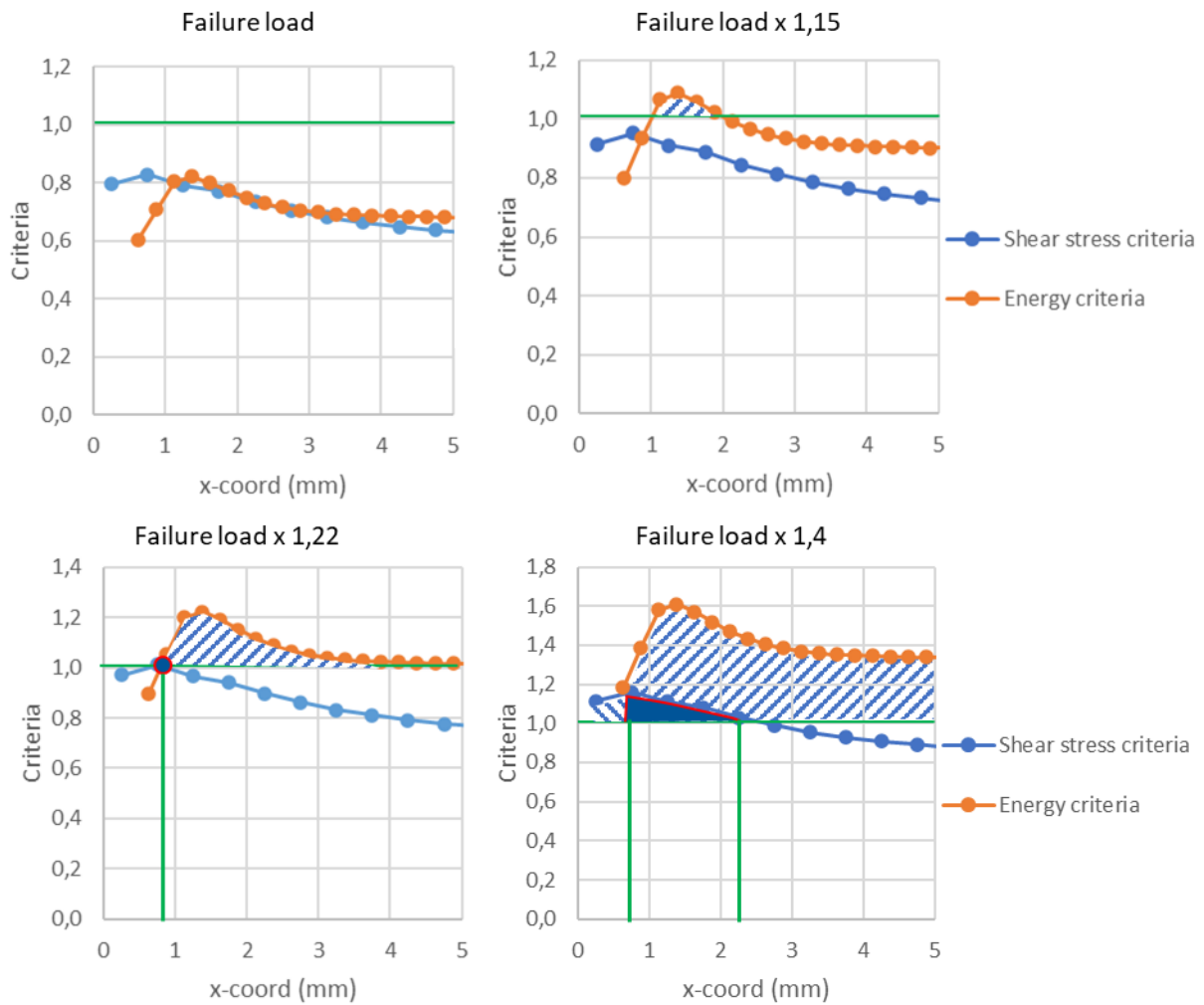


Figure 5.2-16: Tension test coupled stress-energy criterion computation for: a) experimental failure load, b) 1.15 * experimental failure load, c) 1.22 * experimental failure load and d) 1.4 * experimental failure load.

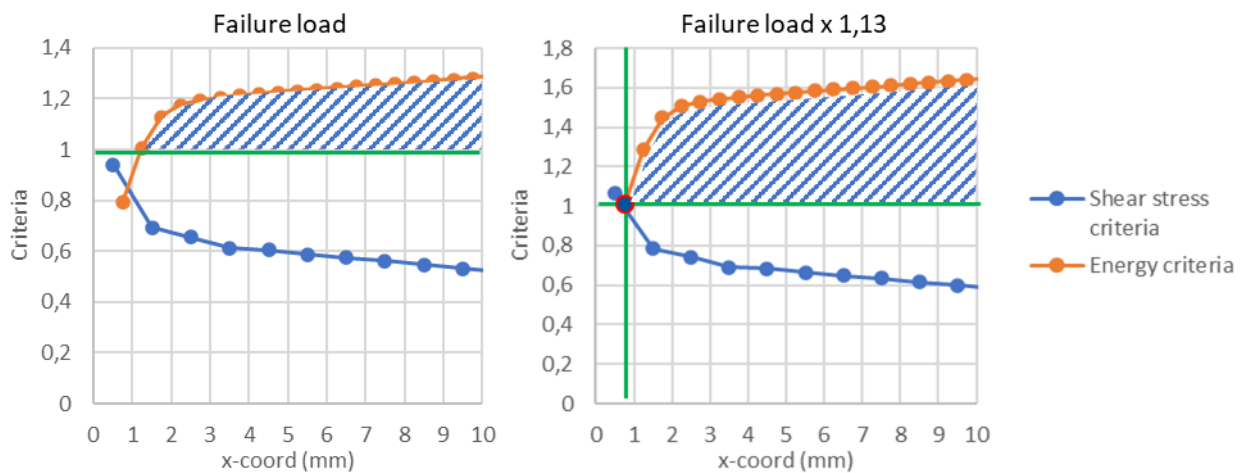


Figure 5.2-17: Bending test coupled stress-energy criterion computation for: a) experimental failure load and b) 1.13 * experimental failure load.

The shape of the energy criteria also provides information on the propagation characteristics. Once the coupled criterion is fulfilled, the crack propagates. Then:

- if the energy criterion decreases at one point, the load should be increased again to continue to propagate, which implies a controlled crack propagation,
- if the energy criterion is always increasing at each crack propagation step (for a fixed load), the remaining energy stored by the bondline is sufficient to allow the propagation to continue. It led to an uncontrolled propagation.

For the tension and bending test, this result is consistent with the visual observations during the test and the load/displacement curves. Actually, the crack initially propagates slowly along a few centimeters and then violently up to the total disbonding.

5.3. Application of the developed methodologies: direct and indirect method failure prediction

This part presents the analysis of the load/displacement curves and the local measurement analysis of the gauges for the tension and bending test obtained by the model both for direct and indirect method. The results are compared to the experimental results to validate if the models predict correct load at failure values, and good bonded patch behavior.

5.3.1. Hypothesis for FE model

The cohesive elements are introduced in the model at the interface between the steel substrate and the steel reinforcement. It was decided to have no volume elements for the adhesive (Figure 5.3-1). This assumption is made to simplify the modeling as in chapter 4. Consequently, the additional momentum generated by the offset of the 1 mm bondline has to be modeled by adding thickness of the cohesive elements. The mesh was changed in one direction compared to the stress energy model. In order to reduce the total number of elements (and therefore the computation time), the number of elements was reduced in the center of the sample (dividing the total number of elements by 3.5).

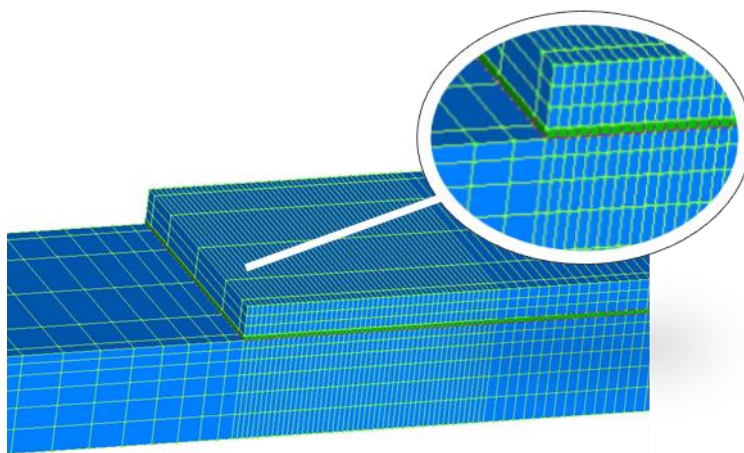


Figure 5.3-1: Cohesive model meshing.

The cohesive properties were taken from the chapter 4 results. The parameters are reminded in Table 5.3-1 and Table 5.3-2.

	Fracture toughness G_c (kJ/m ²)	Critical stress σ_c (MPa)	Stiffness K (MPa/mm)	Coupling parameter
Mode I	0.316	60	8426	0.35
Mode II	1.960	53	1060	

Table 5.3-1: Resulting parameters of cohesive law for resin B steel-to-steel assembly characterization using direct method.

	Fracture toughness G_c (kJ/m ²)	Critical stress σ_c (MPa)	Stiffness K (MPa/mm)	Coupling parameter
Mode I	0.25	35	12 900	0.37
Mode II	2.15	35	1 500	

Table 5.3-2: Resulting parameters of cohesive law for resin B steel-to-steel assembly characterization using indirect method.

5.3.2. Load/displacement curves

Figure 5.3-2a and b display the obtained experimental load/displacement curves for the bending and tension tests compared to FE cohesive models. The overall stiffness is well modeled for bending tests while the difference in the stiffness for the tension tests is around 25%.

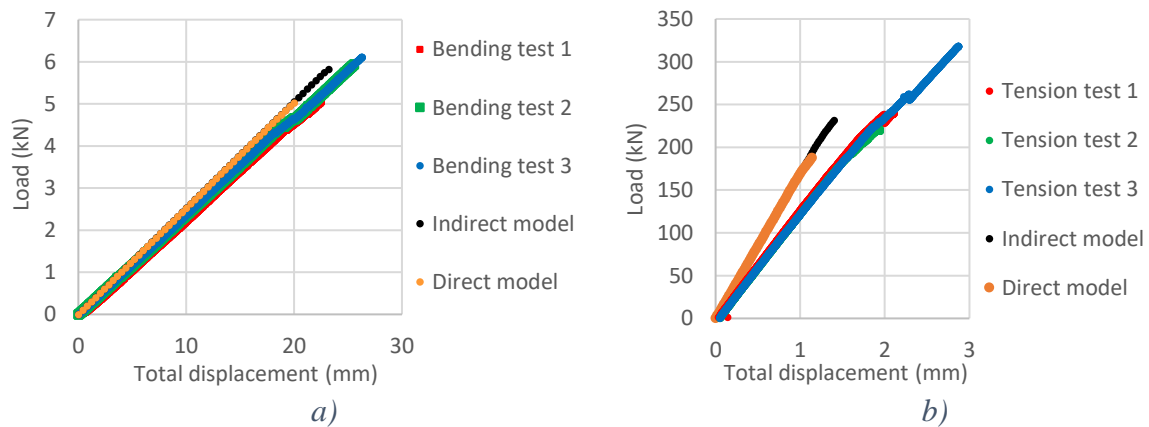


Figure 5.3-2: a) Bending test load/displacement curves, b) Tension test load/displacement curves.

The error in stiffness, depending on the type of loading, can be due to two possible issues. Firstly, it could be related to an approximation or error in the modeling hypothesis which could be translated by a wrong behavior of the model. Secondly, it could be due to an error with the load or displacements measurement during the tests. The meshing and cohesive behavior being the same for the two models, and as good stiffness is observed for the bending test, this may be related to possible sliding in the clamps during the tension tests. This introduces higher displacement than in the model where the displacements are mimicking a perfect clamping at the end of the sample. The analysis of the gauge measurements in the next part will validate this assumption.

5.3.3. Strain measurements analysis during tension tests

5.3.3.1. Gauges data analysis

Based on Figure 5.1-2, the gauges results that are compared to the modeling results are:

- the gauges 3 and 4 that give informations on the capacity of the modeling:
 - to express the transition length impact on the strain in the 6 mm adherent. If the transition length predicted by the model is too long or too short, the gauges measurement will indicate smaller or bigger values compared to experimental values,
 - to give informations on the propagation of the crack at the beginning of the patch failure,
 - to predict the same maximum values as the experimental ones.
- the gauges 1 and 5 related to the global patch behavior during the loading and the crack propagation.

The gauges 7 and 8 will not be described as they were on the side of the vice clamp and as this behavior is not modeled.

Figure 5.3-4, Figure 5.3-4 and Figure 5.3-5 present the gauges 1 and 5 measurement (as function of the load) compared to the results obtained through the developed finite element model at the same position (3 mm from the patch end and in the center of the patch).

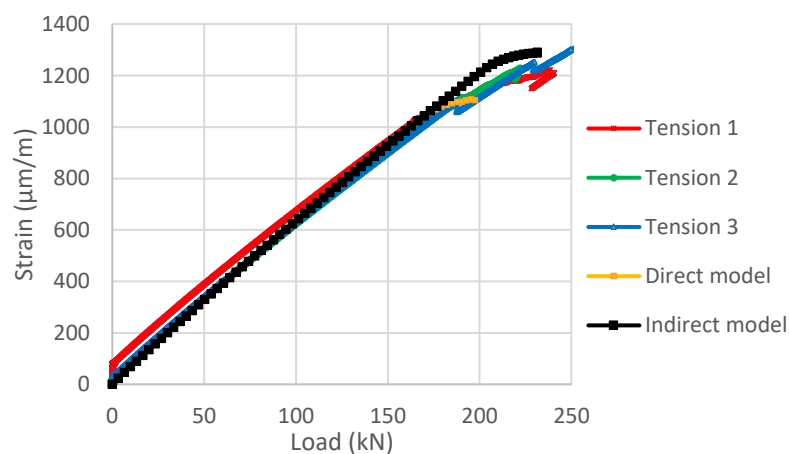


Figure 5.3-3: Experimental and numerical gauge 1 measurements for the tension tests,

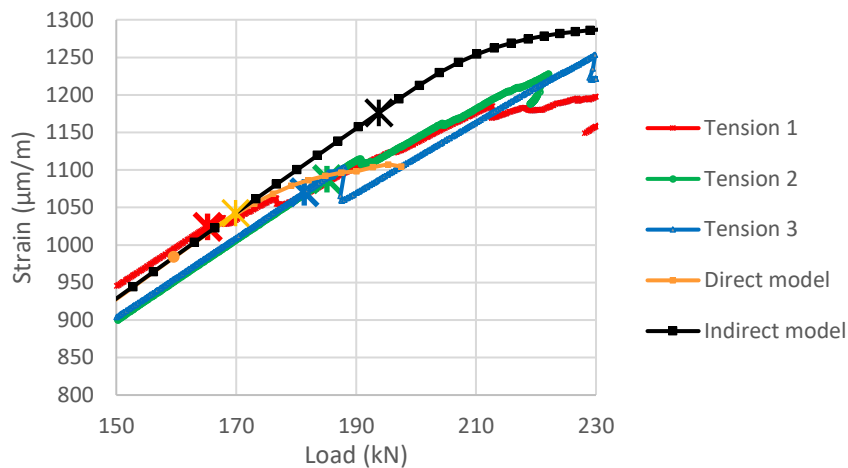


Figure 5.3-4: Zoom on the non-linear part of the curves for gauge 1 measurements for the tension tests.

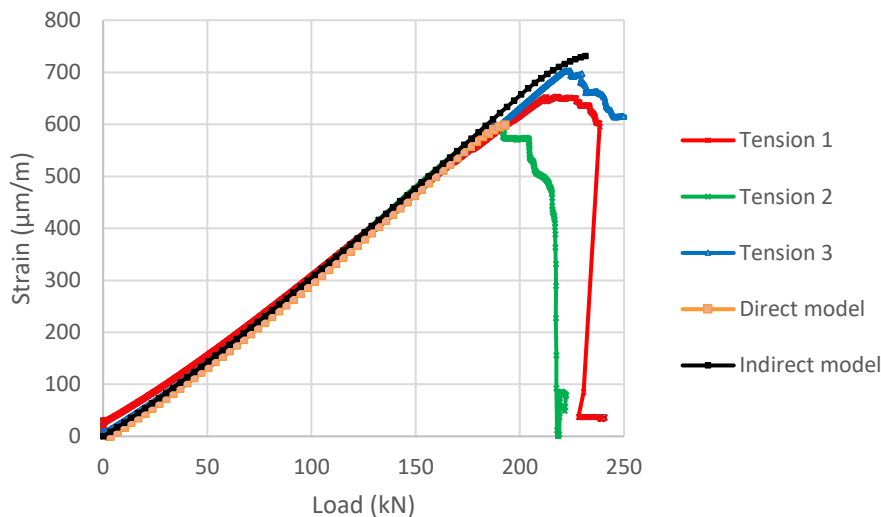


Figure 5.3-5: Experimental and numerical gauge 5 data for the tension test.

The gauge 1 experimental curves are similar to the numerical ones with the same initial slope during the loading of the patch, with close first point of non-linearity for the direct model (Figure 5.3-4, highlighted crosses) and close maximal strains related to crack initiation for both models. A similar loss of stiffness (non-linear part) during the crack propagation is also observed for both models. Thus, the results show that the predictions of the direct and indirect methods are accurate and that the overall behavior of the patch, in the 20 mm adherent, is correctly modeled.

Table 5.3-3 gives the different values obtained for each model and compares them to the experimental ones. It can be observed that the indirect model predicts a non-linearity at a higher strain and load level than the direct model (20% more).

	<i>Initial slope ($\mu\text{m}/\text{kNm}$)</i>	<i>Strain ($\mu\text{m}/\text{m}$) at stiffness change (gauge 1)</i>	<i>Strain ($\mu\text{m}/\text{m}$) at half- length debonding (gauge 5)</i>	<i>Load (kN) at half- length debonding (gauge 5)</i>
<i>Test 1</i>	5.58	1021	640	216
<i>Test 2</i>	5.78	1086	592	188
<i>Test 3</i>	5.79	1071	701	223
<i>Experimental average</i>	5.71	1063	641	209
<i>Direct method</i>	6.15	1042	598	192
<i>Average difference with direct method (%)</i>	(+8%)	(-2%)	(-5%)	(-8%)
<i>Indirect method</i>	6.15	1176	730	231
<i>Average difference with indirect method (%)</i>	(+8%)	(+10%)	(+13%)	(+10%)

Table 5.3-3: Several characteristic values determined through experimental and numerical analyses using the developed cohesive zone approaches (direct and indirect methods) for gauges 1 and 5, for the tension tests.

Figure 5.3-6 presents the results for the gauge 3. The gauge 4 results are similar and are not presented in this document. The initial slopes of the experimental and model results are similar. Table 5.3-4 presents the load at failure predicted for the tension test by the direct method (difference of -4% with experimental results) and the indirect method (difference of +20% with experimental results). This load is defined when the gauge 3 strain measurement is maximal. The results prove that the cohesive law shape (direct method) and the critical toughness value (indirect method) seem to influence mainly the failure load prediction but not the general behavior of the patch.

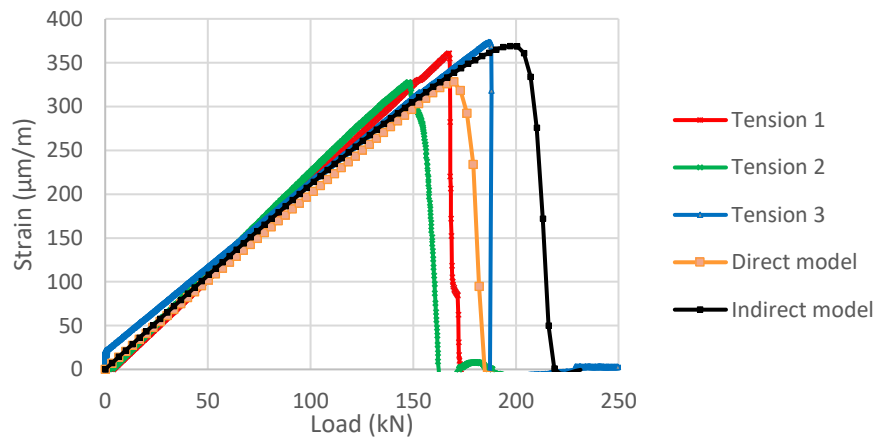


Figure 5.3-6: Experimental and numerical gauge 3 measurements for the tension test.

	<i>Initial slope ($\mu\text{m}/\text{kNm}$)</i>	<i>Strain at failure ($\mu\text{m}/\text{m}$)</i>	<i>Failure load (kN)</i>
<i>Test 1</i>	2.23	354	167
<i>Test 2</i>	2.27	325	148
<i>Test 3</i>	1.91	372	181
<i>Experimental average</i>	2.13	348	165
<i>Direct method</i>	2.01	328	169
<i>Difference with direct method (%)</i>	(6%)	(-6%)	(+2%)
<i>Indirect method</i>	1.99	368	197
<i>Difference with indirect method (%)</i>	(7%)	(+8%)	(+19%)

Table 5.3-4: Several characteristic values determined through experimental and numerical analyses using the developed cohesive zone approaches (direct and indirect methods) for gauge 3, for the tension tests.

5.3.3.2. Optical fiber data analysis during tension test

Figure 5.3-7 displays the experimentally obtained optical fiber strain measurement for the tension test n°3 (the two other tests show similar surface strain measurements), and for different times before and after the crack propagation (from $t = 61.11$ s to $t = 71.05$ s). The absciss of the figure corresponds to the distance from the border of the reinforcement (0 is the border). The blue line shows the position of the gauge 3 and the black line corresponds to the strain profile obtained with the finite element model on the 6 mm adherent surface when numerical maximal strains are measured at the position of gauge 3 (fixed as the experimental crack initiation time).

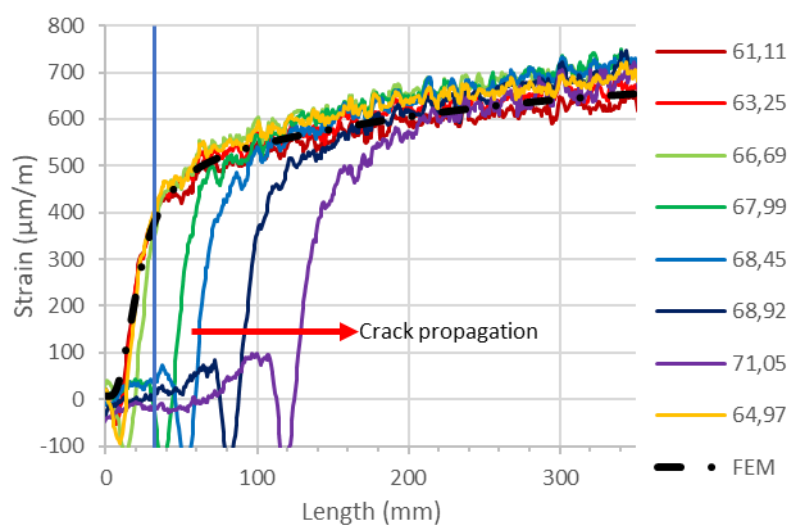


Figure 5.3-7: Experimental optical fiber strain measurements for tension test n°3 and numerical strain profile results.

The curves show that the use of gauge 3 (gauge 4 gives similar results) as crack initiation measurement seems to be consistent. As highlighted by the blue line (gauge 3 position), the strain at this position is maximal just before the beginning of the crack propagation and is similar to the one obtained with the gauge 3 and 4 (~375 μstrain) at crack propagation. A shift of the strain curve is visible after the crack initiation and the measurement of this shift can provide crack propagation curve.

Finally, it can be seen that the finite element model strain profile and experimental one, before crack propagation (orange curve, $t = 64.97$ s), are nearly identical. It validates that the general behavior of the patch and, in particular, the transition length, is well modeled.

All the comparisons between the experimental results and the numerical ones allow to have high confidence into the capacity of the model, and the cohesive methodology (with a limited impact of the cohesive law shape) to be able to predict general bonded patch behaviors.

5.3.4. Strain measurements analysis during bending tests

5.3.4.1. Gauges data analysis

Figure 5.3-8 and Figure 5.3-9 present the gauge 1 and 5 measurements (as function of the load) compared to the results obtained with FE modelling. Table 5.3-5 presents the obtained load and strains at half debonding of the patch measured by the gauges 1 and 5.

The two methods (direct and indirect) predict:

- good global behavior of the patch (slope of the gauge 1 and 5 curves during the loading of the patch),
- underestimated local strains at failure (especially the direct method) (Table 5.3-5)

The direct model predicts lower strain at failure than the indirect one. These different results are consistent with the load at failure obtained from the two models. The results are also consistent with the tension test results and indicate that the overall behavior of the patch is correctly modeled. Again, the shape of the cohesive law does not seem to influence the general behavior, except the load at failure value.

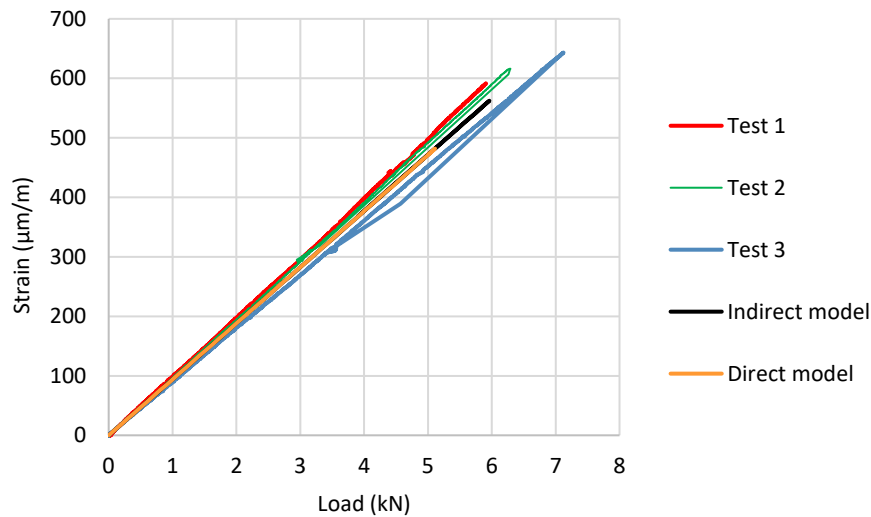


Figure 5.3-8: Experimental and numerical gauge 1 measurements for the bending tests.

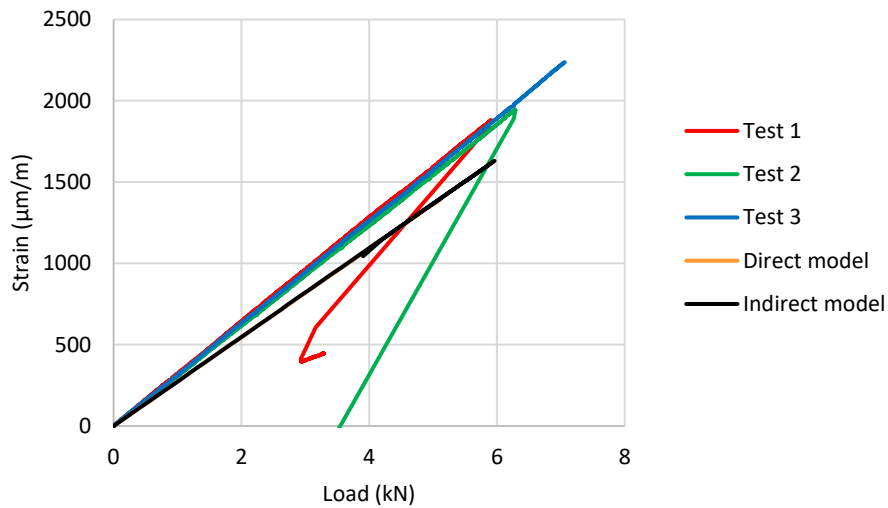


Figure 5.3-9: Experimental and numerical gauge 5 measurements for the bending tests.

	Strain ($\mu\text{m/m}$) at failure (gauge 1)	Strain ($\mu\text{m/m}$) at half debonding (gauge 5)	Load (kN) at half debonding (gauge 5)
<i>Test 1</i>	576	1822	5.87
<i>Test 2</i>	595	1910	6.15
<i>Test 3</i>	645	2210	7.03
<i>Experimental average</i>	605	1980	6.35
<i>Direct method</i>	483	1480	5.2
<i>Difference with direct method (%)</i>	(-19%)	(-25%)	(-18%)
<i>Indirect method</i>	560	1720	6
<i>Difference with indirect method (%)</i>	(-7%)	(-13%)	(-6%)

Table 5.3-5: Several characteristic values determined through experimental and numerical analyses using the developed cohesive zone approaches (direct and indirect methods) for gauge 1 and 5, for the bending tests.

Figure 5.3-10 presents the obtained results for the gauge 3 and Table 5.3-6 presents the results extracted from these data, in the same manner as for the tension tests. The initial slope and load at failure of the experiments show limited difference for the three tests. Model results are similar to experimental ones (direct and indirect methods). The difference of the load at failure predicted by the direct and indirect methods is by 10%, the direct model remaining more conservative. Conclusions are similar to the ones obtained with the gauges 1 and 5.

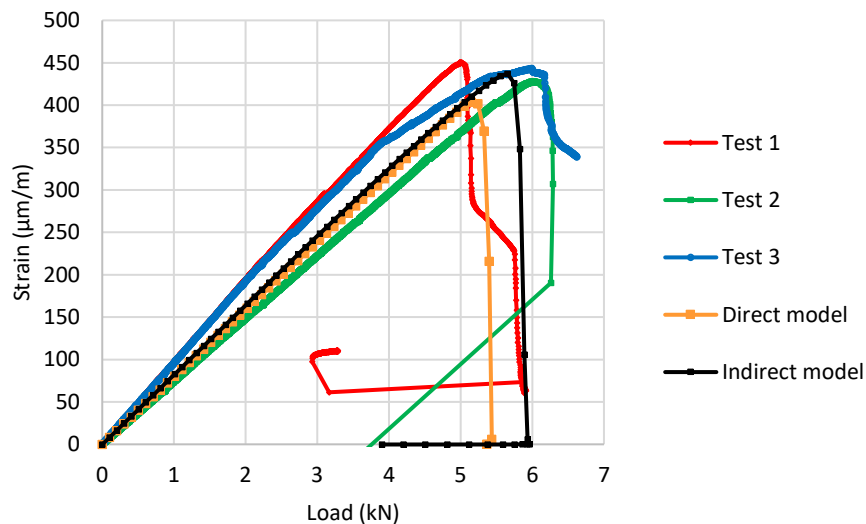


Figure 5.3-10: Experimental and numerical gauge 3 measurements for the bending tests.

	Strain ($\mu\text{m/m}$) at break	Load at break (kN)
<i>Test 1</i>	450	5.0
<i>Test 2</i>	417	6.1
<i>Test 3</i>	438	6.0
<i>Experimental average</i>	435	5.7
<i>Direct method</i>	403	5.15
<i>Difference with direct method (%)</i>	(-7%)	(-9%)
<i>Indirect method</i>	437	5.65
<i>Difference with indirect method (%)</i>	(0.5%)	(0.8%)

Table 5.3-6: Several characteristic values determined through experimental and numerical analyses using the developed cohesive zone approaches (direct and indirect methods) for gauge 3, for the bending tests.

These results demonstrate that the overall behavior of the patch in bending is correctly modeled using the two methods (direct and indirect) with an accurate load at failure prediction.

5.3.4.2. Optical fiber data analysis during bending test

Figure 5.3-11 displays the experimentally obtained optical fiber strain measurements for the bending test n^o2 (the two other tests show similar surface strain measurements), and for different times before and after the crack propagation (from t = 38 s to t = 88.59 s). The absciss of the figure corresponds to the distance from the border of the reinforcement (0 is the border). The blue line shows the position of the gauge 3 and the black line corresponds to the strain profile obtained with the finite element model on the 6 mm adherent surface when numerical maximal strain is measured at the position of gauge 3 (fixed as the experimental crack initiation time, t = 71.73).

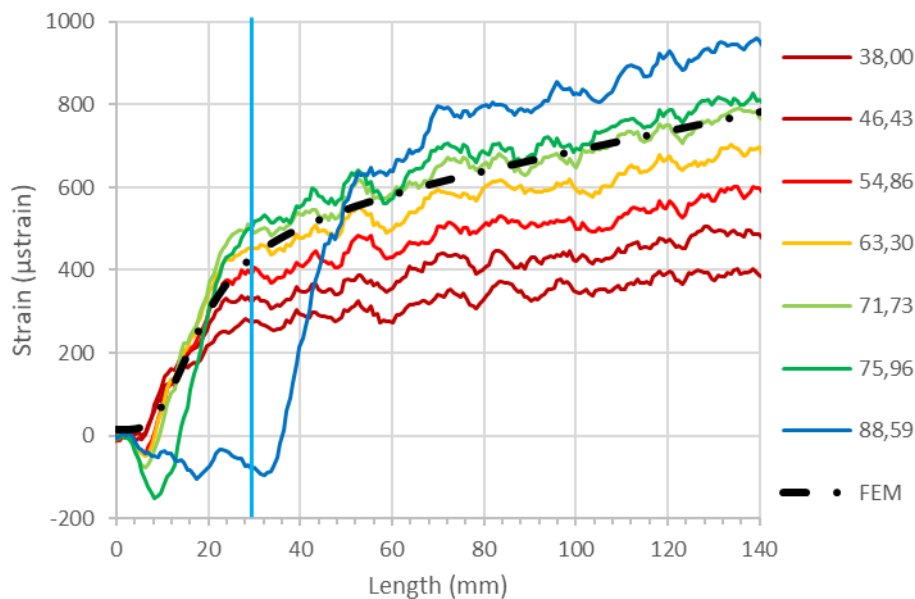


Figure 5.3-11: Experimental optical fiber strain measurements for the bending test n°2 and numerical strain profile results.

The curves show that the use of gauge 3 (gauge 4 shows similar results) as crack initiation measurement seems to be consistent. As highlighted by the blue line, the strain at this position is maximal just before the beginning of the crack propagation. Moreover, a shift of the strain curve is visible after the crack initiation and the measurement of this shift can provide crack propagation curve.

Finally, it can be seen that the finite element model strains profile and experimental measurements before crack propagation (green curve, $t = 71.73$ s) are nearly identical. It validates that the general behavior of the patch is correctly modeled.

All the comparisons between the experimental results and the numerical ones allow to have high confidence into the capacity of the model, and the cohesive methodology (direct and indirect methods), to be able to predict general bonded patch characteristics under monotonous loading.

5.3.5. Crack front shape

The crack front shape analysis performed in chapter 2 and 3 (for different resins) has shown that this shape is dependent on the loading mode. Mode I generates parabolic crack front shape and mode II generates straight crack front shape. These results are in accordance with Griffith theory as described in [124]. The description of the process zone shape for mode II loading shows no difference between plane strain and plane stress. On the contrary, for mode I loading, the process zone for plane strain behavior is much more condensed around the crack tips compared to plane stress loading. Thus, to ensure that the modeling of the bonded patch describes precisely the bonding behavior, a validation of the correct mode ratio in the bondline (represented by a correct crack front shape) is required.

Figure 5.3-12 presents a comparison of the obtained experimental fracture surface and the numerical model damage pattern for a tension test. The same result was obtained for the bending test. The failure was 100% adhesive at the substrate interface. On the figure on the left, some “micro” cracking is occurring inside the bondline up to the interface with the 6mm reinforcement plate (no propagation on the other interface). The shape of these cracks is used

as a measurement of the crack shape in the bondline during the crack propagation. It is compared to the damage distribution in the bondline during the crack propagation of the tension modeling, which represents the numerical crack front shape.

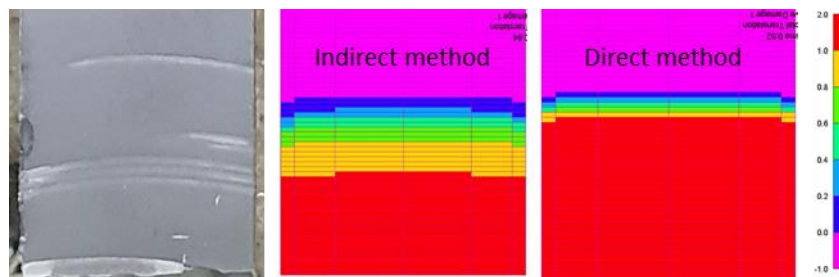


Figure 5.3-12: Experimental crack front shape and FE method crack front shape prediction.

Figure 5.3-12 shows that the crack front shape obtained numerically for the direct and indirect method analysis is in accordance with the experimental results. However, it can be seen that the predicted process zone length by the direct and indirect methodologies are quite different. Studying the shape of the cohesive laws described in the conclusion of the chapter 4, these results are consistent as the energy stored by the damaged part of the cohesive is much smaller in the direct cohesive laws than in the indirect ones.

The relatively flat shape of the parabolic front shape tends to indicate, compared to the chapter 3 results, that the loading mode is mainly mode II (as expected from the loading of the sample). The mode ratio cannot be directly experimentally quantified, but gives informations on the correct interpretation of the experimental results by the model. The bending test has shown similar results and conclusions than the tension test.

5.4. Conclusion

In this chapter, real-scale tests with loading conditions close to reality (most commonly encountered loading situations on ship deck) were carried out. Two types of loading were performed on the same geometry: bending (3 specimens) and tension (3 specimens) loadings.

The three modeling methodologies (direct, indirect and coupled criteria) chosen in the chapter 1 were tested and the patch's behavior and maximal capacity were assessed. The monitoring of the tests with strain gauges and optical fiber was used as reference values. It has helped to validate the capacity of the cohesive element model (with the direct and indirect method) to predict the failure load of the assembly and its local and global behavior. The application of the coupled stress-energy method was also assessed. The definition of each criterion was made using experimental data from adapted and described characterization tests. Final predictions were done using finite element methods and the presented methodologies.

Table 5.4-1 and Figure 5.4-1 present the final comparison of the failure loads predicted by the three methods and the experimental results. They show that, despite the relatively low number of tests that could be made (especially critical toughness determination), the methodologies that have been initially defined were able to predict failure load of bonded patch with good accuracy. The only methodology which proved to have conservative results (and the better accuracy) was the direct one.

	<i>Load at break Bending (kN)</i>	<i>Load at break Tension (kN)</i>
<i>Experimental average</i>	5.7	166
<i>Direct method</i>	5.2	169
<i>Difference with direct method (%)</i>	(-9%)	(+2%)
<i>Indirect method</i>	5.6	197
<i>Difference with indirect method (%)</i>	(-2%)	(+19%)
<i>Coupled criteria</i>	6.32	203
<i>Difference with coupled criteria (%)</i>	(+13%)	(+22%)

Table 5.4-1: Failure load prediction of direct, indirect methodologies and coupled stress-energy criteria compared to experimental results for real-scale investigations.

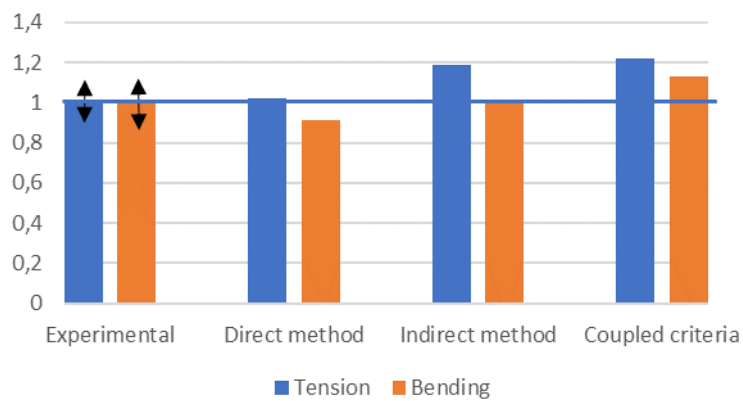


Figure 5.4-1: Normalized failure load predictions of direct, indirect and coupled stress-energy criteria methods compared to experimental results.

General conclusion

This study was part of the Strength Bond project dedicated to the development of a design methodology for bonded reinforcements of corroded steel plates like those that can be found in offshore applications. The absence of effective failure criteria has led to a tendency to oversize bonded joints in industrial applications. A better understanding of the failure of bonded joint and the development of reliable design methodologies are necessary to increase confidence and to lead to more efficient application of composite bonded repairs in offshore applications. In order to design adhesively bonded joints, the mechanical state of the adhesive within the joint (stress, strain, energy) should be well determined and a reliable failure criterion, adapted to the obtained failure mode, should be chosen.

In the first chapter dedicated to the state of the art of bonded assemblies, two main strategies have been detailed for mode I and II failure criteria. The first is based on a stress or strain criterion in relation with continuous mechanics. The second is based on an energetic criterion in accordance with fracture mechanics. Both criteria have advantages and drawbacks. For mixed-mode approaches, the coupled stress-energy criteria can be used as well as the cohesive zone models. This last approach was more deeply studied in this work. Regarding the determination of the mechanical state in a bonded assembly, two main strategies can be considered: the use of analytical methods, or numerical methods. Analytical methods can be an efficient way to obtain fast results that may be valuable in the preliminary design stage, or in case of simple joint design. They allow a good understanding of the behavior of the bonded joints and an identification of the driving parameters. On the other hand, numerical methods allow considering more complex and detailed geometries and the introduction of nonlinear material behavior that could affect the properties of the assembly. It was chosen in this work to rely on the use of finite element modeling so that the developed strategy may be easily applied to alternative geometries. To carry out the design process using cohesive zone approach and finite elements, several steps are needed. First, the critical toughnesses and the cohesive laws must be determined. This is in general done through fracture mechanics investigations. Then, the finite element model can be built and its robustness verified through mesh sensitivity analysis and comparison with experimental results. Finally, it can be applied to different cases.

The second chapter was dedicated to the improvement of the existing fracture mechanics investigations, studying the capacity of distributed optical fiber to monitor crack propagation in bonded assemblies. Resin A (epoxy) was used during those investigations. Several strategies have been assessed through experimental investigations, analytical and numerical modelling. The use of externally surface bonded optical fiber on the adherends proved to be successful for the studied geometries (it was compared to post-failure measurements). The crack monitoring process was settled for mode I, mode II and mixed mode investigations. This technique has several advantages as it is rather easy to settle, it is non-intrusive, it can measure mid-width crack propagation and can be rather easily automated. The use of embedded optical fiber has also been studied but the results were less satisfactory and more investigations seem to be required.

The third chapter presented the realized fracture mechanics investigations using developed methodology relying on continuous optical fiber. It aimed to study the different proposed methodologies for the critical toughness determination, and to present a methodology able to provide cohesive laws from experimental local measurements using digital image correlation.

Those investigations were realized using resin B (epoxy). In the case of uncontrolled crack propagation, the use of continuous optical fiber system was not able to monitor properly the crack (this was the case for ENF and MMB tests), and consequently, only conservative critical initiation toughness values could be determined through standardized approaches. When controlled crack propagation occurred, the continuous optical fiber proved to be able to improve the critical propagation toughness determination (done for DCB tests). The use of the J-integral method also proved to be successful, providing closed results to the critical propagation toughness in mode I. It allowed also to determine cohesive laws shape for mode I and mode II.

Fourth chapter aimed at presenting the chosen finite element modelling strategy relying on the use of FEMAP software. Cohesive laws are implemented in this software and mode coupling is carried out through a coupling parameter that needs to be determined. This software allowed to study two different methodologies to determine the complete cohesive laws (including the coupling parameters) and to compare the numerical expectations with the experimental measurements. The first method is called direct method and consists in using the mode I and II cohesive laws determined through the J-integral approach (described in chapter 3). The second method, called the indirect method, relies on the use of the numerical model to determine all the cohesive parameters (mode I and II laws and the coupling parameter). Both approaches gave satisfactory results in comparison with experimental measurements for the DCB, ENF and MMB tests (presented in chapter 3). The obtained coupling parameters were closed, but the cohesive laws were rather different. Though the cohesive law shape does not seem to have an impact on the studied quasi-static tests, it is important to underline that it could have more influence in the case of durability investigations (creep or fatigue for example). This should be analyzed more deeply.

The last chapter was dedicated to the application of the developed numerical approaches to large-scale experiments on adhesively bonded joints. Samples more representative of industrial applications were studied and tested. The developed numerical methodology was applied with both the direct and indirect method to assess numerical predictions and verify their consistency with experimental measures. The coupled stress-energy approach was also carried out. It proved to be rather difficult as several strong hypotheses had to be settled (choice of the stress and its location, selection of the stress criteria). The obtained results were satisfactory and the direct method proved to be the closest to the experimental results. Table 6.4-1 summarizes the main contribution and drawbacks of each studied methodology. The direct method proved to be the most precise, but requires more instrumentation. The indirect method requires more computation time and less instrumentation. The coupled stress-energy approach is highly dependent upon strong hypotheses particularly related to the stress criteria application.

	<i>Test required</i>	<i>Model computation time (standard test)</i>	<i>Model computation time (full size test)</i>	<i>Model data</i>	<i>Failure prediction</i>
Direct method	DCB/ENF/MMB With special instrumentation (DIC)	2 days	4 days	Complete patch behavior and load at failure	Conservative
Indirect method	DCB/ENF/MMB With standard instrumentation	5-8 days	4 days	Complete patch behavior and load at failure	Non conservative
Coupled criteria	TAST/DCB/ENF/MMB	∅	5-6 days	Load at failure	Non conservative

Table 6.4-1: Comparison of the design methodologies studied.

These results prove that the developed methodologies (direct and indirect methods) can be applied to adhesively bonded composite steel joints.

It would be interesting to carry out similar experiments using ductile adhesive to verify the adequacy of the methodology in this case. In addition, more investigations related to the process zone could be done as the continuous optical fiber measurements seems to be highly sensitive to it. This could maybe provide an alternative method to obtain cohesive laws.

To be extended to adhesively bonded composite patches, it will yet be needed to verify the accuracy of the methodology when multiple layers are present in a single cohesive zone. In fact, in this case, a glass fiber reinforced polymer layer is often inserted between the steel surface and the carbon fiber reinforced polymer, to limit galvanic corrosion risks and to soften the bonded interface.

References

- [1] <https://www.adhesives.org/adhesives-sealants/fastening-bonding/history-of-bonding/bonding-an-ancient-art>.
- [2] Fay P A, Adhesive Bonding, Science, Technology and Applications, Woodhead Publishing Series, vol 2, 3-40, 2021.
- [3] Adams R D, Cawley P, Defect types and non-destructive testing techniques for composites and bonded joints. *Materials Science and Technology*, vol 5, 170-183, 1989.
- [4] Martinez J L, Cyrinoa J C R, Vaz M A, Hernández I D, Perrut V A, Composite patch repair of damaged tubular members from flare boom structures subjected to compressive loads, *Composite Structures*, vol 257, 2021.
- [5] Meniconi L C M, Porciuncula I N, McGeorge D, Pedersen A, Structural Repair at a Production Platform by Means of a Composite Material Patch, Offshore Technology Conference, Houston, Texas USA, 2010.
- [6] McGeorge D, Echtermeyer a T, Leong K H, Melve B, Robinson M, Fischer K P, Repair of floating offshore units using bonded fibre composite materials, *Composites Part A: Applied Science and Manufacturing*, vol 40, 1364-1380, 2009.
- [7] Coldshield tm, <https://www.cold-pad.com/solutions-productandservices-cold-shield>.
- [8] Schindel-Bidinelli E, *Pratique du collage industriel*, Lavoisier, France Paris, 1992.
- [9] Buchan S, Rae W D, Chemical nature of the rubber-to-brass bond, *Rubber Chemistry and Technology*, vol 19, 968-986, 1949.
- [10] McBain J W, Hopkins D G, On adhesives and adhesive action, *The Journal of Physical Chemistry*, vol 29, 188-204, 1924.
- [11] NF EN ISO 8503, Preparation of steel substrates before application of paints and related products - Surface roughness characteristics of blast-cleaned steel substrates - method for the grading of surface profile of abrasive blast-cleaned steel, 2012.
- [12] Wolf A, Buchman A, Eitan A, Fine T, Nevo Y, Heyman A, Shoseyov O, Improved adhesives containing CNT/SP1 nano fillers. *Journal of Adhesion*, vol 88, 435-451, 2012.

- [13] Da Silva L F M, Dillard D, Blackman B, Adams R. Testing Adhesive Joints, Best Practices, Wiley, 2012.
- [14] Adams R D, Comyn J, Wake, W C, Structural adhesive joints in engineering, Elsevier Applied Science Publisher, 2012.
- [15] ISO 11003 Adhesives — Determination of shear behaviour of structural adhesives — Part 2: Tensile test method using thick adherends, edition 3, 2019.
- [16] D5656-10 Standard Test Method for Thick-Adherend Metal Lap-Shear Joints for Determination of the Stress-Strain Behavior of Adhesives in Shear by Tension Loading , ASTM Standard, 2017.
- [17] Volkersen O, Die Niekraftverteilung in Zugbeanspruchten mit Konstanten, Luftfahrtforschung, vol 15, 41-47, 1938.
- [18] McGeorge D, Inelastic failure of adhesively bonded overlap joints, Engineering Fracture Mechanics, vol 77, 1-21, 2010.
- [19] Wong E H, The mechanics of bondline thickness in balanced sandwich structures. International Journal of Adhesion and Adhesives, vol 78, 4–12, 2017.
- [20] Goland M, Reissner E, The stresses in cemented joints, Journal of Applied Mechanics, vol 11, 17-27, 1944.
- [21] Pocius A V, Adhesion and Adhesives Technology An introduction, Hanser, 2012.
- [22] Anyfantis K N, Analysis and Design of Composite-to-Metal, Phd Thesis, National Technical University of Athens, 2012.
- [23] Da Silva L F M, Lima R F T, Teixeira R M S, Puga A, Closed-form solutions for adhesively bonded joints, 2008.
- [24] Hart-Smith L J, Adhesive-bonded double-lap joints, NASA, 1973.
- [25] Gleich D, Stress Analysis of structural bonded joints, Delft University press, 17-19, 2002.
- [26] Adams R D, Harris J A, The influence of local geometry on the strength of adhesive joints, International Journal of Adhesion and Adhesives, vol 7, 69-80, 1987.
- [27] Zhao X , Adams, R D , Da Silva, L F L, Single lap joints with rounded adherend corners, Journal of Adhesion Science and Technology, vol 25, 837-856, 2011.

- [28] Mouton L, Errotabehere X, Paboeuf S, Sayed-Ahmad F, Enhance Reliability of structural bonding: An advance solution of repair for corrosion onboard offshore units, OMAE2018, 2018.
- [29] Kouno Y, Makoto I, Ryutaro H, Masaki O, Fusahito Y, R-curve behavior of adhesively bonded composite joints with highly toughened epoxy adhesive under mixed mode conditions. *International Journal of Adhesion and Adhesives*, vol 105, 2021.
- [30] Xiacong H, A review of finite element analysis of adhesively bonded joints, *International Journal of adhesion and adhesives*, vol 31, 248-264, 2011.
- [31] Banea M B, Da Silva, L F M, Adhesively bonded joints in composites materials: an overview, *Proceedings of the institution of mechanicals engineers Part L, Journal of Materials Design and Applications*, vol 223, 1-18, 2009.
- [32] Koenig H A, *Modern computational methods*, Taylor and Francis, 1998.
- [33] Smith G D, *Numerical solution of partial differential equation; finite difference methods*, Oxford clarendon press, 1985.
- [34] Bigwood D A, Crocombe A D, Nonlinear adhesive bonded joints design analyses, *International Journal of Adhesion and Adhesives*, vol 10, 31-41 1990.
- [35] Chabot A, Hun M, Hammoum F, Mechanical analysis of a mixed mode debonding test for composite pavements , *Construction and Building Materials*, vol. 40, 1076-1087, 2013.
- [36] Pagano N J, Stress fields in composites laminates, *International Journal of Solids Structures*, vol 19, 385-400, 1978.
- [37] Hadj-Ahmed R, *Modélisation des assemblages collés: application à l'optimisation du transfert des effort par cisaillement*, Ecole national des ponts et chaussées, 1999.
- [38] Duong V A, Diaz Diaz A, Chataigner S, Caron J F, A layerwise finite element for multilayers with imperfect interfaces, *Composite Structures*, vol 93, 3262-3271, 2001.
- [39] Da Silva L F M, Carbas R I C, Critchlow G W, Figueiredo M A V, Brown K, Effect of material, geometry, surface treatment and environment on the shear strength of single lap joint, *International Journal of Adhesion and Adhesives*, vol 29, 621-632, 2009.
- [40] Ikegami K, Takeshita T, Matsuo K, Sugibayashi T, Strength of adhesively bonded, *International Journal of Adhesion and Adhesives*, vol 10, 385-400, 1990.

- [41] Chataigner S, Caron J F, Duong V A, Diaz Diaz A, Experimental and numerical investigation of shear strain along an elasto-plastic bonded lap joint, *Construction and building materials*, vol 25, 432-441, 2011.
- [42] John S J, Kinloch A I, Matthews F L, Measuring and predicting the durability of bonded fibre/epoxy composite joints, *Composites*, vol 22, 121-127, 1991.
- [43] Crocombe A D, Global yielding as a failure criterion for bonded joints, *International Journal of Adhesion and Adhesives*, vol 9, 145-153, 1989.
- [44] Adams R D, Harris J, Strength prediction of bonded single lap joints by nonlinear finite element method, *International Journal of Adhesion and Adhesives*, vol 4, 65-78, 1985.
- [45] Wei R P, *Fracture Mechanics: Integration of Mechanics, Materials Science and Chemistry*, Cambridge University Press 1-214 , 2010.
- [46] Wu X-F, Chowdhury U, Fracture toughness of adhesively bonded joints with large plastic deformations, *Engineering Fracture Mechanics*, vol 190, 16-30, 2018.
- [47] Goglio L, Rossetto M, Stress intensity factor in bonded joints: influence of the geometry, *International Journal of Adhesion and Adhesives*, vol 30, 313-321, 2010.
- [48] Griffith A A, The Phenomena of rupture and flow in solids, *Phylosophical transactions of the royal society of london*, vol 221, 163-198, 1921.
- [49] Kanninen M F, *Advanced Fracture Mechanics*, Oxford University Press, 1985.
- [50] Cherepanov G G, Crack propagation in continuous media, *Journal of Applied Mathematics and Mechanics*, vol 31, 476-488, 1967.
- [51] Rice J R, A path independent integral and the approximate analysis of strain concentration by notches and cracks, *Journal of Applied Mechanics*, vol 35, 379-386, 1968.
- [52] Yoda M, The J-integral fracture toughness for Mode II, *International journal of fracture*, vol 16, ,1980.
- [53] Bui H B, Dang Van K, Trois problèmes non linéaire de l'étude mécanique de la rupture des matériaux, *Revue de Physique Appliquee*, vol 9, 605-610, 1974.
- [54] Choupani N, Interfacial mixed-mode fracture characterization of adhesively bonded joints, *International Journal of Adhesion and Adhesives*, 2008, vol 28, 267-282.
- [55] Reeder J R, *3D Mixed-Mode Delamination Fracture Criteria-An Experimentalist's Perspective*, NASA, 2006.

- [56] O'Brien T K, Fracture Mechanics of Composite Delamination, ASM Handbook Composites, vol 21, 242-245, 2001.
- [57] Jamali J, Mechanistic Failure Criterion for Unidirectional and Random Fibre Polymer Composites. Phd Thesis of the University of Ontario, 2014.
- [58] Whitcomb J, Analysis of instability-related growth of a through-width delamination, National Aeronautics and Space Administration, Langley Research Center NASA, 1984.
- [59] Reeder J R, A Bilinear Failure Criterion for Mixed-Mode Delamination, Composite Materials: Testing and Design, vol 11, 303-322, 1993.
- [60] Leguillon, D, Strength or toughness? A criterion for crack onset at a notch, European Journal of Mechanics A/Solids, vol 21, 61-72, 2002.
- [61] Parvizi A, Garret K W, Bailey J E, Constrained cracking in glass fiber-reinforced epoxy cross-ply laminates, Journal of Materials Science, vol 13, 195-201, 1978.
- [62] Irwin G, Fracture I, Handbuch der Physik VI, Flugge Springer Verlag, Berlin, Germany, 558-590, 1958.
- [63] Sha G T, Yang C T, Weight function calculations for mixed-mode fracture problems with the virtual crack extension technique, Engineering Fracture Mechanics, vol 21, 1119-1149, 1985.
- [64] Barenblatt G, The Mathematical Theory of Equilibrium Cracks in Brittle Fracture, Advances in Applied Mechanics, vol 7, 55-129, 1962.
- [65] Dugdale D S, Yielding of steel sheets containing slits, Journal of the Mechanics and Physics of Solids, vol 8, 100-104, 1960.
- [66] Hillerborg A, Modeer M, Petersson P E, Analysis of crack formation and crack growth in concrete by means of fracture mechanics and finite elements, Cement and Concrete Research, vol 6, 773-782, 1976.
- [67] Jouan A, Constantinescu A, A critical comparison of shear tests for adhesive joints, International Journal of Adhesion and Adhesives, vol 84, 63-79, 2018.
- [68] Campilho R D S G, de Moura M F S F, Domingues J J M S, Modelling single and double-lap repairs on composite materials, Composites Science and Technology, vol 65, 1948-1958, 2005.

- [69] Turon A, Camanho P P, Costa J, and Dávila C G, An interface damage model for the simulation of delamination under variable-mode ratio in composite materials, NASA, 2004.
- [70] Sørensen B F, Jacobsen T K, Determination of cohesive laws by J-Integral approach, *Engineering Fracture Mechanics*, vol 70, 1841-1858, 2007.
- [71] Yang Q D, Thouless, M D, Ward S W, Elastic-plastic mode-II fracture of adhesive, *International Journal of Solids and Structures*, vol 38, 51-62, 2001.
- [72] Turon A, Pedro P, Camanho P P, Soto A, Gonzalez E, Analysis of Delamination damage in composite structures using cohesive elements. *Comprehensive Composites Materials II*, vol 8, 136-156, 2018.
- [73] Needleman A, A Continuum Model for Void Nucleation by Inclusion Debonding, *Journal of Applied Mechanics*, vol 54, 525-531, 1987.
- [74] Tvergaard V, Effect of fibre debonding in a whisker-reinforced metal *Material Science and Engineering Part A*, 1990.
- [75] Camacho G T, Ortiz, M, Computational modeling impact of damage in brittle materials, *International Journal of Solids and Structures*, vol 33, 2889-2938, 1996.
- [76] Camanho P P, Dávila C G, Mixed-mode decohesion finite elements for the simulation of delamination in composite materials, NASA, 1-37, 2002.
- [77] Petersson P E, Crack growth and development of fracture zones in plain concrete and similar materials, Report TVBM, 1006, Lund Institute of Technology, 1981.
- [78] Girolamo D, Leone F, Dávila C, Lin S, Ghose S, Carlos G, Characterization of Adhesive Fracture Properties by Digital Image Correlation, SAMPE: Long Beach CA, 2013.
- [79] Alfano G, On the influence of the shape of the interface law on the application of cohesive-zone models, *Composites Science and Technology*, vol 66, 723-730, 2006.
- [80] Marat-Mendes R, Freitas M J, Characterisation of delamination surfaces under mixed mode loading, Iberian Conference on Fracture and Structural Integrity, CIFIE2010, 2010.
- [81] Benzeggagh M L, Kenan M, Measurement of Mixed-Mode Delamination Fracture Toughness of Unidirectional Glass/Epoxy Composites with Mixed-Mode Bending Apparatus, *Composite Science & Technology* vol 56, 439-449, 1996.

- [82] «Sørensen B F, Jørgensen K, Jacobsen T K , Østergaard R C, DCB-specimen loaded, International Journal of Fracture, vol 141, 59-72, 2006».
- [83] Sorensen B F, Cohesive laws for assessment of materials failure: Theory, experimental methods and application, Technical University of Denmark library, 2010.
- [84] Alfred F V, Christopher T, Generation of mixed mode I/II failure criteria from MMB specimens: an experimental study, Materials Research Express, vol 6, 2019.
- [85] Reeder J R, 3D Mixed-Mode Delamination Fracture Criteria-An Experimentalist's Perspective, NASA, 2006.
- [86] D5528 Test Method for Mode I Interlaminar Fracture Toughness of Unidirectional Fiber-Reinforced Polymer Matrix Composites, ASTM Standard, 2014.
- [87] D3433-99 Standard Test Method for Fracture Strength in Cleavage of Adhesives in Bonded Metal Joints, ASTM Standard, 2020.
- [88] Brunner A J, Blackman B R K, Davies P, Fracture Mechanics Testing Methods for Polymers, Adhesives and Composites, Mode I delamination, Elsevier Science , vol 28, 277-305, 2001.
- [89] D7905 Standard test method for determination of the mode II interlaminar fracture toughness of unidirectionnal fibre-reinforced polymer matrix composites, ASTM Standard, 2014.
- [90] Ayatollahi M R, Ajdani A, Akavan-safar A, da Silva L F M, Effect of notch length and pre-crack size on mode II fracture Energy of brittle adhesives, Engineering Fracture Mechanics vol 212, 123-135, 2019.
- [91] Davies P, Blackman B R K, Brunner A J, Fracture Mechanics Testing Methods for Polymers, Adhesives and Composites, Mode II delamination, Elsevier Science , vol 28, 307-333, 2001.
- [92] D6671 Standard Test Method for Mixed Mode I-Mode II Interlaminar Fracture Toughness of Unidirectional Fiber Reinforced Polymer Matrix Composites, ASTM Standard, 2001.
- [93] Kinlock A, Wang Y, Wiiliams J G, Yala P, The mixed-mode delamination of fibre composite materials, Composites science and technology, vol 47, 225-237, 1993.
- [94] Reeder J R, Refinement to the mixxed-mode bending test for delamination toughness, ASTM Journal of Composites technology and Research, vol 25, 191-195, 2003.

- [95] de Barros S, Fadhil B M, Alila F, Diop J, Reis J M L, Using blister test to predict the failure pressure in bonded composite repaired pipes. *Composite Structures*, vol 211,125 - 133, 2019.
- [96] Martin R H, Davidson B, Mode II fracture toughness evaluation using a four point bend end notched flexure test. In, 4th international deformation and fracture of composites conference, London Institute of Materials, 243-253, 1997.
- [97] Davies P, Casari P, Carlsson L A. Influence of fibre volume fraction on mode II interlaminar fracture toughness of glass/epoxy using the 4ENF specimen. *Composites Science and Technology*, vol 65, 295-300, 2005.
- [98] Wang H, Vu-Khang T, Use of end-loaded-split (ELS) test to study stable fracture behaviour of composites under mode II loading, *Composite Structures*, vol 36, 71-79, 1996.
- [99] Blackman B R K, Kinloch A J, The determination of the mode II adhesive fracture resistance, GIIC, of structural adhesive joints: an effective crack length approach, *Engineering Fracture Mechanics*, vol 72, 877-897, 2005.
- [100] Alvarez D, Fracture mechanics of carbon fibre reinforced plastics to ti-alloy adhesive joints, PhD thesis, Imperial college London, 2012.
- [101] Chataigner S, Caron J-F, Benzarti K, Quiertant M, Aubagnac C, Use of a single lap shear test to characterize composite-to-concrete or composite-to-steel bonded interfaces, *Construction and building materials*, vol 25, 468-478, 2011.
- [102] Lepretre E, Chataigner S, Dieng L, Gaillet L, Gagnon A, Roth J, Leroy C, Experimental characterization of different adhesively, HAL, 2017.
- [103] Fernlund G, and Spelt J K, Mixed-mode fracture characterization of adhesive joints, *Composite Science Technology*, vol 50, 441-449, 1994.
- [104] Sørensen B F, Jørgensen K, Jacobsen T K, Østergaard R C, DCB-specimen loaded, *International Journal of Fracture*, vol 141, 59-72, 2006.
- [105] Saeedifar M, Fotouhi M, Najafabadi M A, Toudeshky H H, Prediction of delamination growth in laminated composites using acoustic emission and Cohesive Zone Modeling techniques, *Composite Structure*, vol 124, 120-127, 2015.
- [106] Bernasconi A, Carboni M, Comolli L, Monitoring of fatigue crack growth in composite adhesively bonded joints using Fiber Bragg Gratings. *Procedia Engineering*, vol 10, 207-212, 2011.

- [107] Meadows L, Sullivan R, Brown K, Ranatunga V, Vehorn K, Olson S, Distributed optical sensing in composite laminates. *The Journal of Strain Analysis for Engineering Design*, vol 52, 410-421, 2017.
- [108] Allix O, Ladeveze P, Corigliano A. Damage analysis of interlaminar fracture specimens. *Composite Structures*, vol 31, 61-74, 1995.
- [109] de Barros S, Champaney L, Crack propagation tests: analytical and numerical approaches, *Mechanics of Solids in Brazil*, H.S. da Costa Mattos & Marcílio Alves, 2009.
- [110] Chapeleau X, Bassil A, A General Solution to Determine Strain Profile in the Core of Distributed Fiber Optic Sensors under Any Arbitrary Strain Fields, *Sensors*, vol 21, 2021.
- [111] Östlund S, Nilsson F, Cohesive zone modelling of damage at the tip of cracks in slender beam structures, *Fatigue of Engineering Materials and Structures*, vol 16, 663-676, 1993.
- [112] <http://femap.sigmeo.fr/FEMAP-NX-NASTRAN-V11-1.pdf>.
- [113] Lopes Fernandes R, Budzik M K, Benedictus R, Teixeira de Freitas S, Multi-material adhesive joints with thick bond-lines: Crack onset and crack deflection, *Composite Structures*, vol 226, 2021.
- [114] Monteiro J P R, Campilho R D S G, Marques E A S, da Silva L F M, Experimental estimation of the mechanical and fracture properties of a new epoxy adhesive, *Applied Adhesive Science*, vol 3, 3-25, 2015.
- [115] Leffler K, Alfredsson K S, Stigh U, Shear behaviour of adhesive layers, *International Journal of Solids and Structures*, vol 44, 530-545, 2007.
- [116] Alfredsson K S, On the energy release rate of the end-notch flexure adhesive joint specimen, *International Journal of Solids and Structures*, vol 41, 4787-4807, 2004.
- [117] Leffler K, Shear behaviour of adhesive layers. Thesis for the degree of licentiate of Engineering in Applied Mechanics, Department of Applied Mechanics, Chalmers University of Technology, 2005.
- [118] Högberg J L, Sørensen B F, Stigh U, Constitutive behavior of mixed mode loaded adhesive layer, *International Journal of Solids and Structures*, vol 44, 8335-8354, 2007.
- [119] Li V C, Ward R J, A novel testing technique for post-peak tensile behavior of cementitious materials, *Fracture Toughness and Fracture Energy*, 1989.

- [120] Campilho R D S G, Fernandes R L, Testing different cohesive law shapes to predict damage growth in bonded joints loaded in pure tension, *Journal of adhesion*, vol 93, 57-76, 2016.
- [121] Fernandez-Canadas L, Ivanez I, Sanchez-Saez S, Influence of the cohesive law shape of the composites adhesively bonded patch repair behavior, *Composites Part B: engineering*, vol 91, 414-421, 2016.
- [122] Lemaitre J, Chaboche J-L, *Mécanique des matériaux solides*, Dunod, 1985.
- [123] Campilho R, Testing different cohesive law shapes to predict damage growth in bonded joints loaded in pure tension, *Journal of adhesion*, vol 93, 2016.
- [124] Beom Seon J, Linear fracture mechanics, lecture Note of Eindhoven University of Technology,
<https://ocw.snu.ac.kr/sites/default/files/NOTE/07%20Linear%20fracture%20mechanics.pdf>, 2017.
- [125] Agilent technical datasheet, https://www.agilent.com/cs/library/flyers/public/5991-4123EN_Flyer_4300_MCT.pdf, 2014.
- [126] Boulangé L, Bonin E, Saubot M, Physicochemical characterisations of the bitumen – aggregate interface to get a better understanding of stripping phenomena, *Road Materials and Pavement Design*, vol 14, 384-403, 2013.

Appendix

A1: ENF specimens with primer – observations after failure.

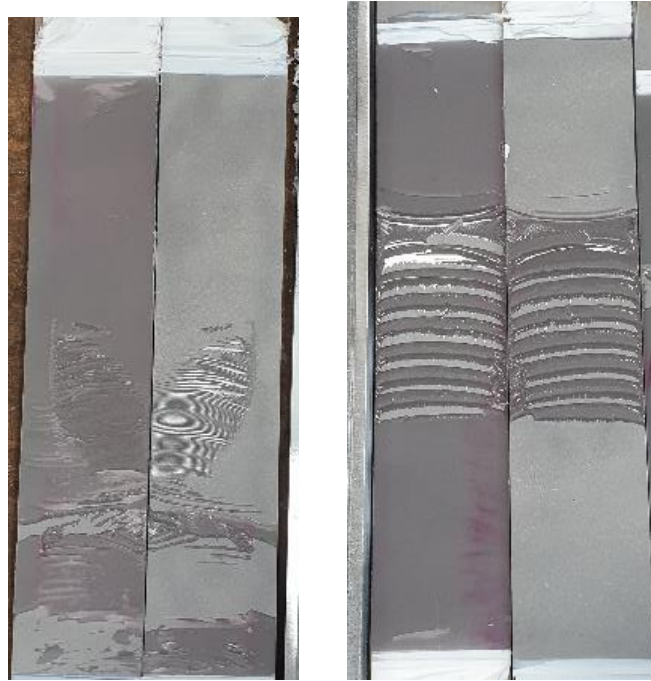


Figure A1-1: ENF failure mode with primer.

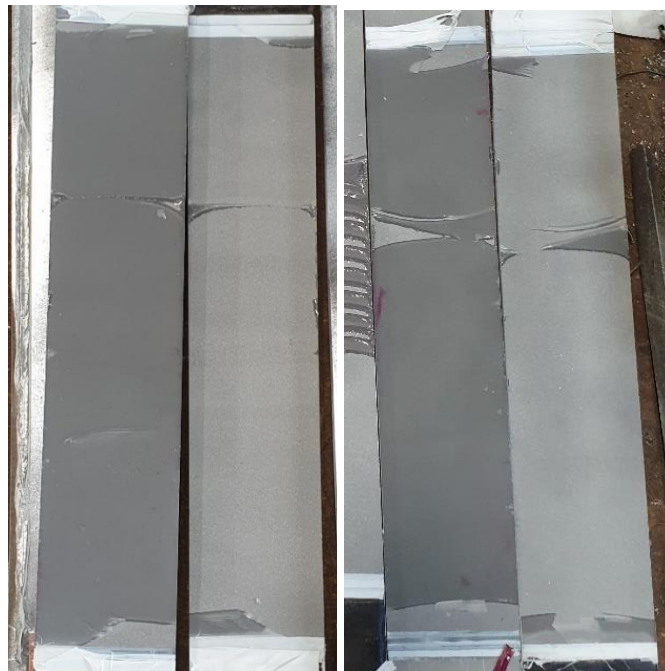


Figure A1-2: ENF failure mode without primer.

A2: TAST test of the resin B with primer.

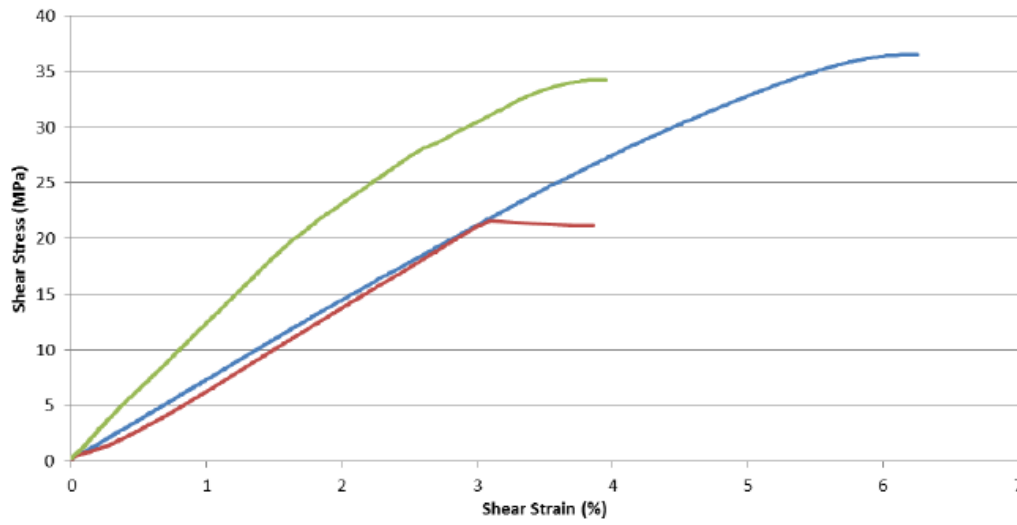


Figure A2-1: Resin B TAST test with primer - load/displacement curves (provided by NavalGroup).

A3: Surface preparation analysis

Surface preparation is of great importance in bonded repairs as described in paragraph 1.1.2. It would be a great advantage to be able to qualify the level of surface preparation carried out on site before bonding to avoid any unanticipated low interface properties. In this application case, samples which have been deliberately degraded (corrosion and pollution) and with several surface preparation methodologies were tested. The quality of these preparations was then assessed using methods that can be implemented on site and that are complementary to more commonly used methods. Two main aspects were investigated: the detection of the residual presence of pollutants through the use of a portable infrared spectrometer and the determination of surface energy after preparation using contact angle and wettability measurement equipment. The objective is to compare the obtained measurements to the critical toughness measurements performed in the previous parts to see if correlation can be made directly with the wettability, chemical properties and mechanical properties.

A3.1 Studied specimens and initial pollution

Fourteen specimens were used for this study and are metallic plates of S235 steel (yield strength ~250MPa). Each specimen was treated as follows:

- initial sandblasting to remove scale and residual oxidation from the manufacturing process (crude steel),
- ageing for two days in an outdoor environment (humidity > 95%) to create a surface corrosion layer,
- pollution of the surface of the specimens with: diesel (four specimens), hydraulic oil (four specimens) or a paraffinic corrosion protection spray (four specimens). Two specimens were left unpolluted and serve as a reference,
- after the pollution of each sample, two more days of ageing in an outdoor environment (humidity > 90%) were observed to recreate a surface corrosion layer.

The resulting specimen are presented Figure A3.1-1 A and B prior and after treatment.

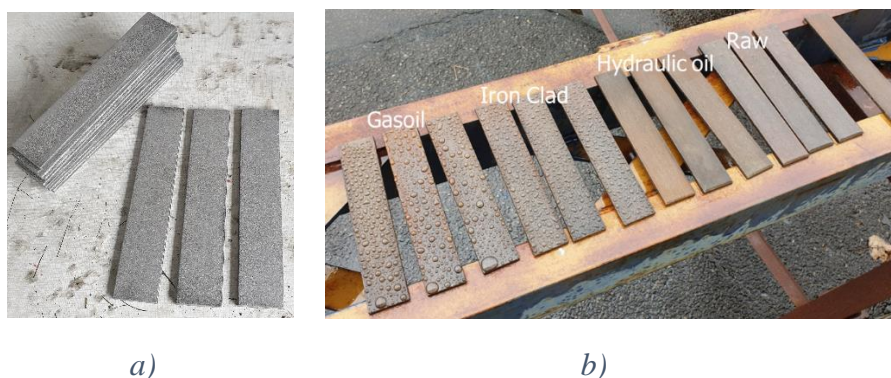


Figure A3.1.1 a) Surface preparation specimens before ageing and pollution. b) Specimens after ageing and pollution.

A3.2 Surface preparations

Four types of surface treatment were carried out for each type of pollution:

- Preparation (A): detergent cleaning,
- preparation (B): detergent cleaning, follows by a sandblasting and then follows by the application of an anti-corrosion primer,
- preparation (C): detergent cleaning, follows by a sandblasting, follows by a solvent cleaning and then follows by the application of an anti-corrosion primer,
- preparation (D): detergent cleaning, follows by a sandblasting and then follows by a solvent cleaning.

The pollution by diesel, hydraulic oil, or paraffin spray used as corrosion protection, were respectively named (1), (2) and (3) while the pollution-free samples were named (4). The different surface preparations of each specimen are summarized in Table A3.2-1 and visible in Figure A3.2-1.

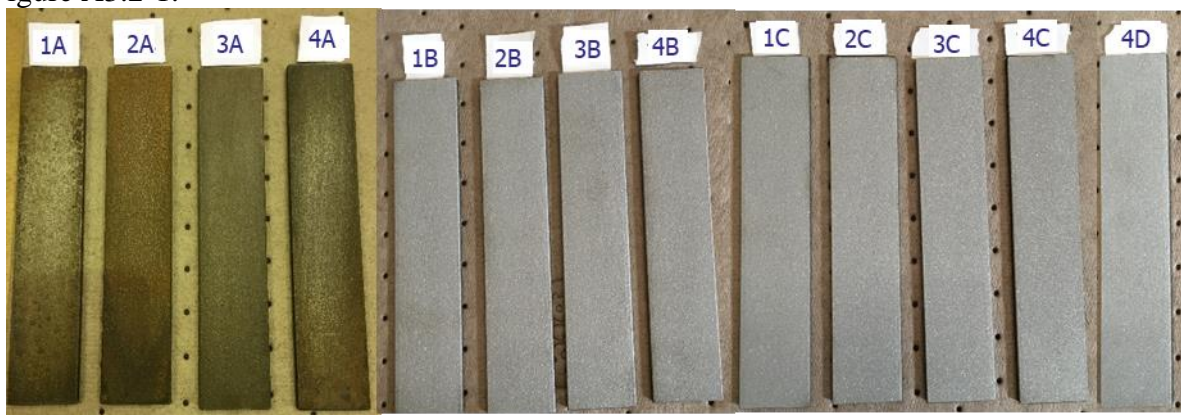


Figure A3.2.1: Surface preparation specimens after surface preparation.

Type of surface treatment	Detergent cleaning	Sand blasting	Solvent cleaning	Anti-corrosion primer	Specimens considered
A	X				4 specimens : 3 polluting agents (1, 2, 3) + Unpolluted reference (4)
B	X	X		X	3 specimens : 3 polluting agents (1, 2, 3)
C	X	X	X	X	3 specimens : 3 polluting agents (1, 2, 3)
D	X	X	X		4 specimens : 3 polluting agents (1, 2, 3) + Unpolluted reference (4)

Table.A3.2.1: Studied surface preparations.

A3.3 Analysis of the presence of pollutants by infrared spectrometer

In order to investigate the ability of the different surface preparations to remove the initially deposited pollutants, an Agilent Technology 4300 infrared spectrometer was used [125]. The spectra obtained for all measurements are shown in Figure A3.3-1, Figure A3.3-2, and Figure A3.3-3. For reasons of clarity, an offset on the absorption values has been artificially introduced in Figure A3.3-1 and Figure A3.3-2 to facilitate the comparison of the obtained spectra.

Figure A3.3-1 shows a comparison of the absorption curves obtained for the specimens with type (A) surface preparation (specimens 1A, 2A, 3A, 4A) and the specimens with type (D) surface preparation (specimen 4D). This figure shows the presence of rust (dome between 3000 and 3500 cm^{-1}) on specimens 1A, 2A, 3A and 4A, as well as the presence of more or less marked pollution (peaks between 2800 and 3000 cm^{-1} , and peaks between 1200 and 1700 cm^{-1}) for the specimens 1A, 2A and 3A. As a result, cleaning with detergent alone does not seem sufficient to remove completely rust and pollutants.

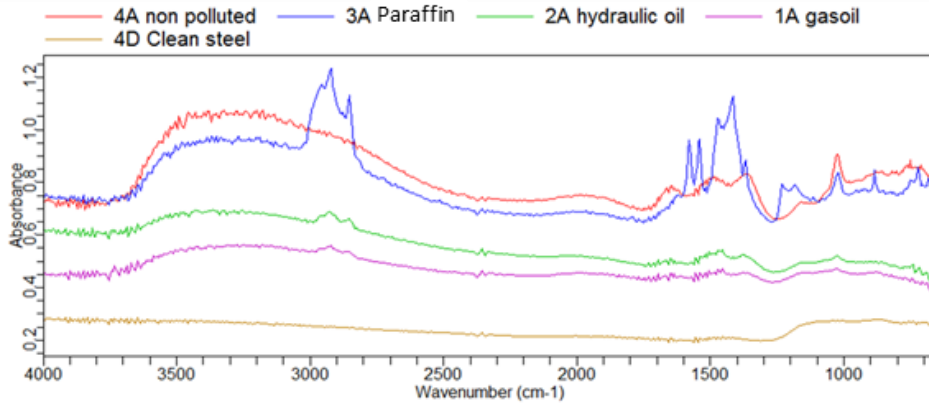


Figure A3.3.1: Influence of initial pollution on infrared spectrometer measurements for type (A) surface preparation.

Figure A3.3-2 shows the absorption curves for the reference specimens (4D) before and after the primer application. As it can be seen, the presence of primer does not seem to affect the measurements in this wavelength range.

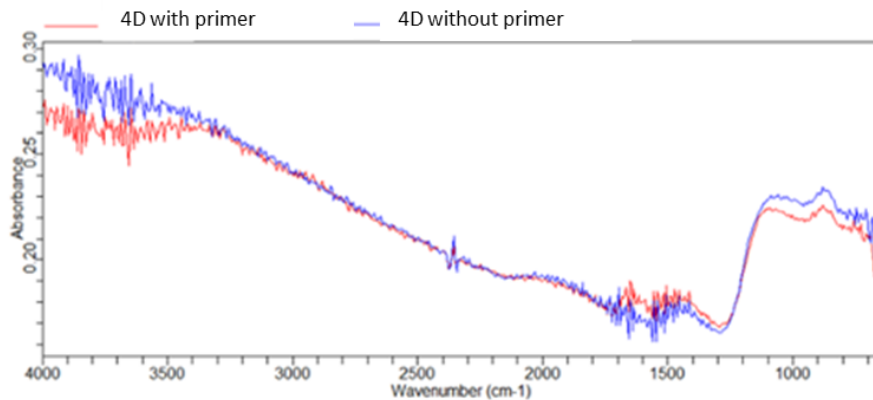


Figure A3.3.2: Influence of the presence of primer on infrared spectrometer measurements.

Finally, Figure A3.3-3 shows a comparison of the absorption curves obtained for the specimens with the different pollutions. It can be observed that the surface preparation of type (B), (C) and (D) (with a sandblasting, followed or not by a solvent cleaning) give similar infrared spectra, independently of the pollution applied. As a result, it is set that sandblasting allows removing rust (which becomes undetectable in the FTIR analysis), but also all the pollution, since it is no longer detectable in the FTIR analysis after sandblasting, whether or not solvent degreasing has been carried out. It therefore seems that solvent cleaning after sandblasting is not necessary to eliminate residual pollutants.

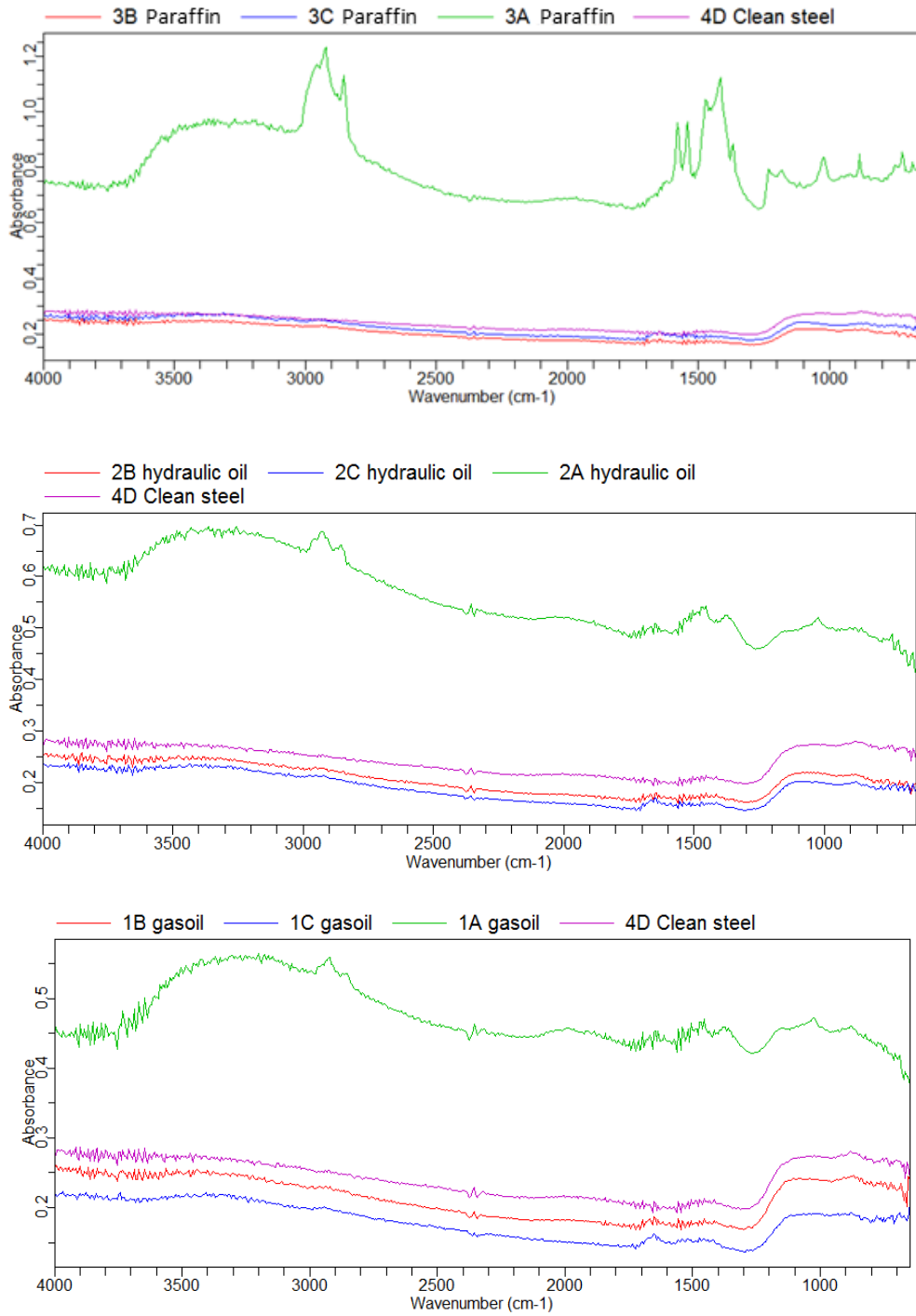


Figure A3.3.3: Comparison of the infrared spectra obtained for the three surface preparation methods studied and the different type pollutions.

A3.4 Surface energy measurements

In this study, surface energy measurements were carried out using:

- the WCA "Water Contact Angle" technique [127]. This technique was carried out using a thermoregulated tensiometer (Kruss DSA100), available at the MIT Laboratory of the Gustave Eiffel University, and for three reference liquids (Water, Ethylene Glycol, Glycerol) deposited in drop on the studied surfaces (Figure A3.4.1a). It should be noted that some of the used liquids (Ethylene glycol and Glycerol) led to a dissolution of the primer. The measurements made with these liquids could therefore not be processed and analyzed,
- spread measurements using wettability measurement inks (Table A3.4.1). The used test inks have a measuring range of 31 to 67 mJ/m² with a step between each ink of 2mJ/m² (any values outside this range cannot be precisely measured).

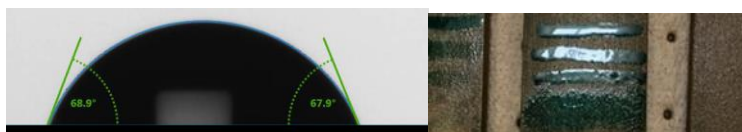


Figure A3.4.1: a) Contact angle measurement b) Use of spread measuring inks.

The results obtained with these two methods are summarized in Table A3.4.1.

Specimens	Wettability ink (mJ/m²)	Contact angle measurement (mJ/m²)
A		
With (1,2,3) and without initial pollution(4)	27 - 35	
B et C		
With (1,2,3) and without initial pollution(4)	36 - 44	40 ± 12
D without pollution	67+	90 ± 10

Table A3.4.1: Presentation of the performed surface energy measurements.

With surface treatment B, C, D, it appears that it is not possible to clearly differentiate between polluted test specimens.

It appears also that sandblasting followed by cleaning with solvent (preparation D) increases significantly the surface energy. The comparison of the surface energies obtained for the type C and D surface preparations shows that the treatment with an anti-corrosion primer of the sandblasted surface strongly reduces the wettability (reducing from - 30% to - 60%).

A3.5 Surface energy analysis: Conclusions

Surface preparation analysis:

Within the framework of the optimization of bonding patch over steel, the carried-out investigations focused on the comparison of different surface preparation methods. The evaluation of the obtained surfaces is carried out using two different methodologies.

The selected pollutants represent a sample of probable pollution on a ship or offshore unit, plus a product used to maintain a corrosion-free surface.

The study showed that cleaning with detergent does not remove the rust, nor the pollutants since they were clearly detected with the FTIR spectrometer, and surface energy of the steel remains very low. This preparation is insufficient. The study did not highlight specific interest of solvent

cleaning after grit blasting as neither FTIR nor surface energy measurement showed significant differences.

The obtained results indicate that solvent cleaning plus sandblasting removes all measurable traces of rust and pollutant, and increase the surface energy of the specimens. The application of the primer significantly degrades the energy of the prepared surfaces. It should be checked that this degradation remains sufficiently low so as not to diminish the capacities of the interface between the patch and the steel substrate. Methods FTIR, WCA, and wettability inks are available in portable format, and seem to bring an interesting information on the quality of the surface preparation. However no direct relation between the measured wettability and critical toughness can be made. In this series of tests, the impact of the primer was not measured as damageable for the toughness compared to bare steel specimens, where high decrease of the wettability was measured.

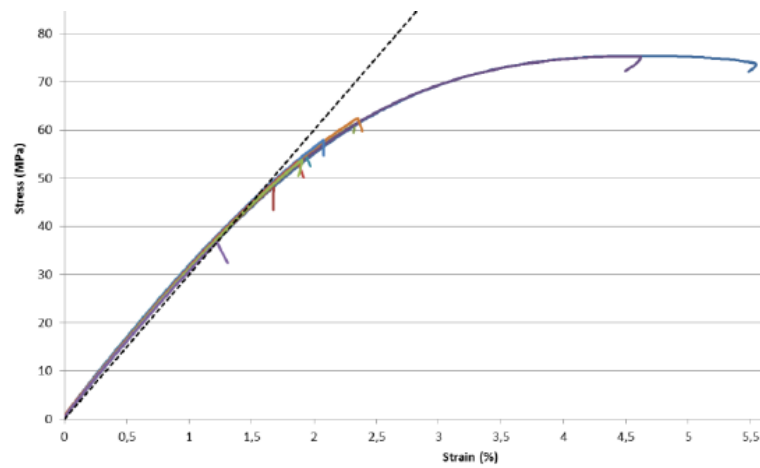
A4: Tensile test result on resin B (bulk samples)

Figure A4.1: Tensile test result on resin B, Load/displacement curves (provided by NavalGroup).

Specimen	Maximum Stress (Mpa)	Maximum strain (%)	Young modulus (Mpa)	Poisson's coefficient
Resin B-1	75,44	5,54	3225	0,42
Resin B-2	48,35	4,68	3298	0,31
Resin B-3	61,08	2,32	3296	0,38
Resin B-4	75,30	4,62	3347	0,39
Resin B-5	54,78	1,93	3381	0,33
Resin B-6	62,44	2,35	3245	0,43
Resin B-7	57,90	2,06	3301	0,44
Resin B-8	53,46	1,87	3243	0,57
Resin B-9	53,82	1,90	3240	0,6
Resin B-10	36,79	1,22	3221	0,43
Average	57,94	2,55	3280	0,43
Resin B-9	11,06	1,32	54,39	0,09
Resin B-10	19%	52%	2%	20%

Table A4.1: Tensile test result on resin B, material properties (provided by NavalGroup).

A5: VCCT routine

Step 1:

The nodes and elements along the interface (so where the crack would propagate) are put in a group.

Step 2:

Pick the direction the crack would propagate.

Step 3:

Renumber the nodes at the interface (based on the crack direction) so that the crack would propagate in the order of the nodes.

Step 5:

Unzip all the nodes and create constraint equations so that the nodes from both materials along the interface will still have the same displacements.

Step 6:

Copy the original constraint set but delete the first 3 constraint equation (the equation will be x, y and z displacements of both nodes at the crack tip). That means the crack will propagate 1 element. Since the nodes were renumbered, the constraint equations are also ordered so that it is easier to know which one to delete.

Step 7:

Do a loop to create as many constraints set as there are elements on the crack.

Step 8:

Create a multi-case analysis where each case will perform the simulation for 1 constraint set.

Step 9:

Run the analysis.

A post-process routine (that needs mode I and mode II direction to input) then recovers only the constraint forces and displacements from the nodes at the edge of the crack in order to use the VCCT, where the rest of the calculations were done with a Python script.

This routine greatly improved the time of modeling and post processing. If done manually, the evolution of the ERR as the crack propagates took half a day, since a lot of simulations had to be performed and post-processed. Moreover, the ERR was not calculated at each element (several elements were unzipped between 2 simulations). With the routine, all the simulations were done really fast, depending on the length of the entire crack the simulations alone took from 5 to 20 minutes to perform (from 100 to 500 nodes unzipped so the same number of cases), while it took 35 seconds for each manual simulation. The routine was especially efficient since the stiffness did not have to be recalculated at each case. The post-process was also immediate based on the API and the Python script.

A6: Full size tension and bending tests – observations after failure

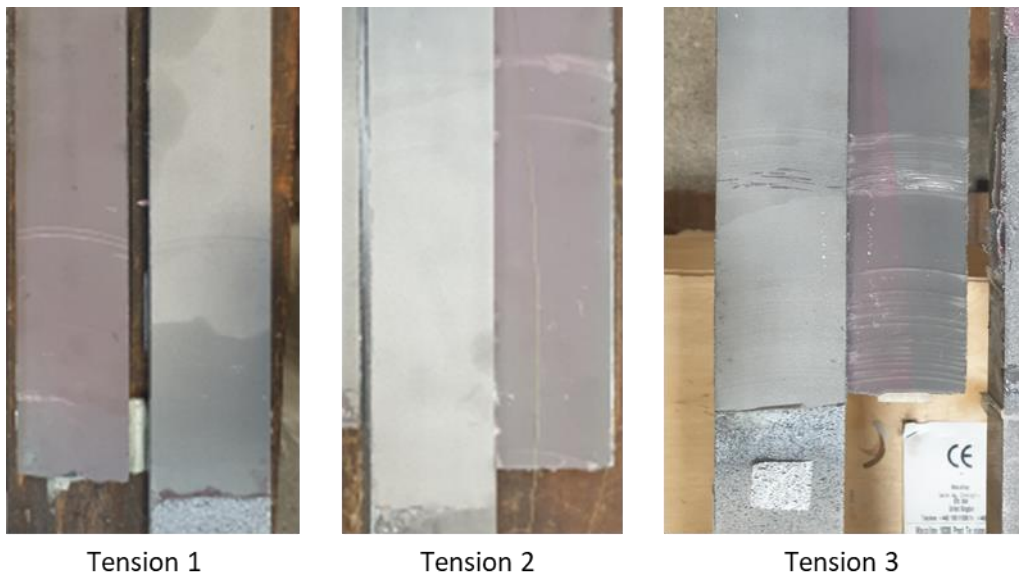


Figure A6.1 Full size tension failure mode.

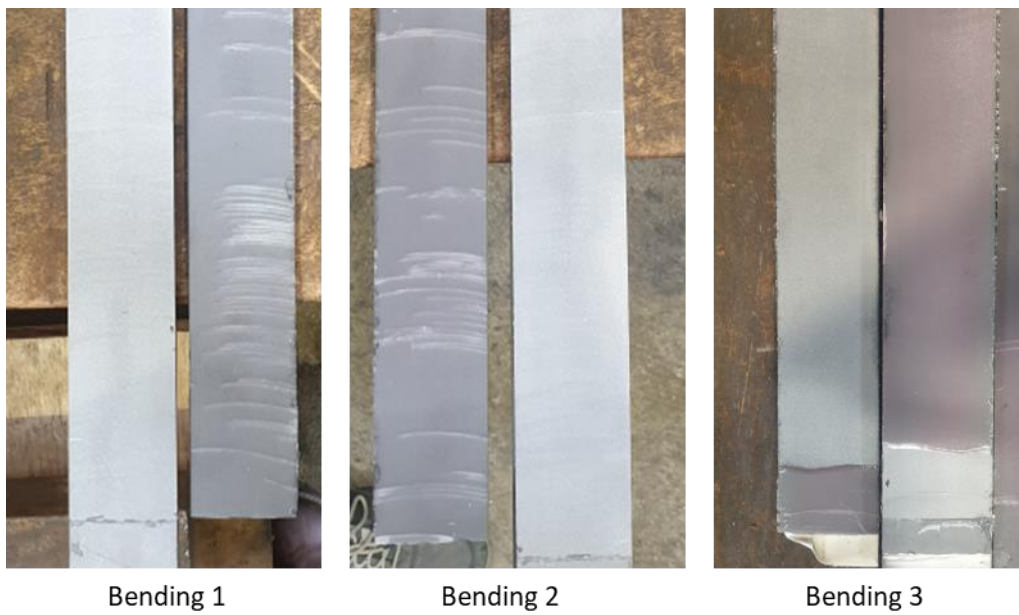


Figure A6.2 Full size bending failure mode.